THE MICROSTRUCTURE AND CORROSION PROPERTIES OF LASER PROCESSED ALUMINIUM ALLOYS

Thesis submitted in accordance with the requirements of the University of Liverpool
for the degree of Doctor of Philosophy
by
Martin Andrew McMahon

Department of Materials Science
and Engineering

April 1994

ABSTRACT

Laser surface melting (LSM) treatments were applied to 2014 and 7075 Al alloys, and laser surface alloying (LSA) with Mo was applied to 2014 Al alloy. Potentiodynamic anodic polarization and extended immersion tests were carried out in chloride electrolytes to investigate the correlation between the corrosion properties and the microstructure. In addition, residual stress measurements were carried out by X-ray diffraction to find the effect on the corrosion resistance of the laser surface melted alloys.

The microstructure after both the LSM and LSA treatments consisted of columnar grains that had solidified by cellular dendritic growth. It is also shown that the grains grew epitaxially from the substrate alloys. Solidification is shown to have started with a planar front region of 2 - 5 μm followed by cellular dendrites 1 - 3 μm in size, corresponding to cooling rates of the order of 10^6 K/s. A banded structure was observed, which was attributed to instantaneous halts during the cellular dendritic solidification, and resulted in local solute enrichment. The solid solubility of Mo in Al was found to increase to ~1.5 wt.% Mo after LSA. However, most of the Mo was contained in the intermetallic particles that formed from the melt. After solidification these intermetallic particles mapped out the convection contours. In the LSM alloys it was found that the surface residual stresses were tensile and that these stresses increased with increasing laser scan velocity and intertrack advance. However, the stress distribution through the melt depth was found to be non-uniform and the maximum stress (~ 220 MPa), which was approximately half the yield stress in the case of the 2014 alloy, coincided with the maximum melt depth.

The effect on the corrosion properties of 2014 alloy and 7075 alloy after LSM was different. For the 2014 alloy there was a marked increase in the anodic passive potential range (E_{PD}), that was as much as 430 mV, as a result of a decrease in the free corrosion potential (E_{corr}) and an increase in the pitting potential (E_{pit}). In the case of the 7075 alloy there was not such a large increase after LSM. Instead, the result was the elimination of the anodic current density transient observed for the as-received alloy. The general corrosion properties were found to be dependent on localised changes in the solute concentration associated with the cellular dendrite boundaries, banded structure, grain boundaries, and the track/track interfaces. In the case of LSA with Mo into the 2014 alloy, it was found that increases in E_{pit} of upto 200 mV were achieved. Pitting was found to initiate only in the presence of intermetallic particles and not within the cellular dendritic structure as in the case of the LSM alloys.

ACKNOWLEDGEMENTS

The financial support for this project was provided by Brite-EuRam Project BE 4305.

The work in this project was carried out under the supervision of Dr K.G.Watkins whom I would like to thank for his support during the preparation of this thesis. My thanks also to Prof. W.M.Steen for allowing me to use the laser lab in the Department of Mechanical Engineering. I acknowledge the help and assistance of all the staff in the Department of Materials Science but special thanks to Dr Arthur 'It'll Be Alright' Green for his invaluable help in keeping my experimental work ticking along. Thanks are also due to Dr F.W.Noble for his advice during the preparation of this thesis.

I would also like to thank my friends for their encouragement and support over the years. In particular Iain for spurring me ever onward during the pursuit of this, the final goal, my Ph.D, for introducing me to real ale and crispy dumplings, and for the walks. Also Eddie, Cheng and Mike, my office sparring partners, together we solved the mysteries of life, the universe, and everything...NOT! Also Simon and Neil, for Batman, Zig and Zag, and yet more beer. Last but not least, all my friends in Portugal, Nunu, Amelia, Marcio, Patricia and Manuela for making my visits there so enjoyable.

Finally, I would like to thank my parents and my sister, to whom this thesis is dedicated, for never losing faith in my abilities and constantly giving me encouragement to carry on.

CONTENTS

I got nothing to say I ain't said before
I bled all I can, I won't bleed no more
I don't need no one to understand
why the blood run, hold
The highered hand
On heart
Hand of God.
Floodland and driven apart
Run cold
Turn
Cold
Burn
Like a healing hand

Sing CORROSION....

Sisters of Mercy, Corrosion from the album Floodland.

1. INTRODUCTION

In recent years two techniques have been successfully used in the treatment of stainless steel to improve the corrosion resistance of the surface. These are laser surface melting (LSM) and laser surface alloying (LSA); reviews of this work include Draper and Poate (1985) and Steen and Watkins (1992). In LSM a very shallow surface layer can be melted followed by rapid solidification. On stainless steels homogeneous corrosion resistant surface layers have been achieved because of the dissolution of the second phase particles and the even redistribution of the alloying elements. Furthermore, corrosion resistance is improved because LSM results in a finer microstructure. In LSA the addition of alloying elements to the melt pool results in the formation of a surface layer that has a different composition to that of the base alloy. In type 304 stainless steels small amounts of Mo have been added to form a homogeneous layer similar to the more corrosion resistant type 316 stainless steel. The use of LSM and LSA in the treatment of Al and its alloys to improve corrosion resistance has until now been very minimal.

Aluminium alloys are extensively used today in a wide variety of applications. The great advantage of using Al alloys is that high strength can be achieved while maintaining relatively low density when compared to steel. However, there is a limit to the usage of aluminium alloys due to the fact that the corrosion and wear resistance of the alloys are comparably less than those of alloy steels. Usually the alloying elements added to Al are chosen so that small amounts can be used to impart high strength to the alloy with only small deleterious effects on the overall density of Al; this is especially important for the aerospace industry. However, the alloying elements that have been found to give high strength also lead to increased susceptibility to pitting corrosion, intergranular corrosion and stress corrosion cracking (SCC). Furthermore, the elements added to stainless steels to impart good corrosion resistance (Cr and Mo) do not readily form solid solutions with Al under normal near equilibrium conditions.

The corrosion resistance of Al and its alloys is determined by the structure and properties of the oxide film that covers the surface. However, aluminium alloys are strengthened by the formation of second phase precipitates during heat treatment, that act as barriers against the movement of dislocations. The problem of reduced pitting corrosion resistance arises because the precipitates can affect the structure and properties of the oxide film. Firstly, the precipitates can interfere with the coverage of the surface by the oxide and secondly they quite often have different electrochemical potentials to that of the Al matrix solid solution. Corrosion is, therefore, locally accelerated whenever one of the precipitates and the surrounding matrix are exposed simultaneously to an aggressive aqueous environment. Intergranular corrosion is caused by the formation of a precipitate free zone (PFZ) adjacent to grain boundaries due to solute migration to the grain boundaries during the heat treatment of the alloys. The result is that there is a potential difference between the grain boundary and the PFZ. During corrosion there is a galvanic couple and selective dissolution occurs in the region that has the lowest potential. In simple terms SCC is an extension of intergranular corrosion, where grain boundary cracking can occur at lower stresses than normal due to the effect of corrosion. In all of the above cases, however, corrosion is initiated at the surface.

There have been various treatments developed for the protection of aluminium against corrosion. Probably the most common is anodising. This involves polarising the alloy in sulphuric acid solutions to artificially thicken the oxide film on the surface. Chromate or molybdate oxide conversion treatments can also be carried out after anodising which further increases the corrosion resistance. However, the effectiveness of these treatments is governed by the lifetime of the film and whether it has the ability to self heal when damaged. In stainless steels, for instance, the oxide is self healing because the chromium from the base metal always oxidises to form a very stable film, even when the surface suffers from mechanical damage such as scratches. The oxide treatments on Al alloys do not facilitate this type of healing unless the treatment is repeated periodically.

Recently, work has been carried out involving non-equilibrium alloying of transition metals Cr, Mo, W, and Zr with Al by ion implantation and sputter deposition. This work, which has been recently reviewed by Szklarska-Smialowska (1992), has shown that the pitting corrosion resistance of Al alloys can be improved if the elements are retained in solid solution with the Al. Other methods that can be used to form surface alloys include plasma spraying and electrodeposition. However, electrodeposited layers are prone to porosity and more so plasma sprayed coatings because they are not fully dense. Hence, both of these techniques cannot be relied upon to deposit surface alloys, that are chosen for their corrosion resistant properties, on Al.

It has, therefore, been the main aim of the present work to investigate whether LSM and LSA (using Mo) treatments can be used to improve the corrosion resistance of Al alloys. In order to do this, two high strength alloys, 2014 and 7075, were firstly surface melted with a 1.5 kW CO_2 laser and the resulting structures and properties were characterised using a range of techniques. Optical microscopy, scanning electron microscopy (SEM), and transmission electron microscopy (TEM) were used to study the microstructure. The composition of the surface melted layers was measured using energy dispersive X-ray (EDX) analysis and by wavelength dispersive spectroscopy (WDS). The phases were identified by X-ray diffraction and electron diffraction techniques. Residual stresses in the resolidified layers were measured by X-ray diffraction techniques. The corrosion properties of the alloys were then investigated by carrying out anodic potentiodynamic polarisation in aqueous chloride solutions, and by monitoring the free corrosion potential, E_{corr}, during total immersion tests over periods of up to two weeks. In addition to this qualitative determination of the composition of the surface oxide was achieved by X-ray photoelectron spectroscopy (XPS). Secondly Mo was surface alloyed into the 2014 alloy and the structure and properties were characterised using the same techniques as for the LSM alloys. Central to the aim of the project has, therefore, been to correlate the observed corrosion properties to the changes in the microstructure of the alloys after the laser surface treatments. Furthermore, special regard has been given to the effect of residual stress on the corrosion resistance, particularly in the case of the LSM alloys.

2. LITERATURE REVIEW

2.1. INTRODUCTION

In this chapter the theory behind the principal subjects of the research undertaken during the present work will be explored. The results and observations of other workers who have carried out similar investigations will also be examined. After this introduction the chapter is divided into six further categories. The first category presents a brief introduction to laser processing and introduces aspects of melt pool solidification related to the microstructure and state of residual stresses that are pertinent to understanding the subsequent corrosion properties of laser surface treated Al alloys. This is followed by an introduction to the metallurgy of the two Al alloys used in this study. An elementary description of the development of the alloys is presented, and is followed by an account of the precipitation sequences that can occur in each of the alloys. The next two categories review the work that has been carried out to date on laser surface melting (LSM) and laser surface alloying (LSA) of Al alloys. In the fifth category an introduction to the corrosion of Al alloys is given, concentrating on the present position of the theory of pitting corrosion. However, susceptibility to other forms of attack is also reviewed. The last category then examines the work to date involving the corrosion properties of LSM and LSA Al alloys.

2.2. LASER PROCESSING

2.2.1. Introduction

The word laser is derived from Light Amplification by Stimulated Emission of Radiation. Einstein first showed that the lasing action should be possible in 1917 but it was not until 1960 when the first laser, which used a ruby rod, was successfully built by Theodore Maiman . In the years since then a great variety of substances have been made to lase. The most common commercial lasers today are the ruby, CO_2, Nd-Glass, Nd-YAG, He-Ne, diode and Excimer lasers; this work is only concerned with the CO_2

laser.

Lasers are used today for a great deal of applications where a high level of accuracy is required. In industry lasers are now used for welding, cutting, drilling, and surface treatment of metals and alloys in place of tungsten inert gas (TIG) welding or metal inert gas (MIG) welding, oxyacetyline gas torch or saws, drills, and furnace heat treatments respectively. The actual use of lasers for any given operation is governed by the laser beam diameter, focal length and wavelength, and material parameters, reflectivity, composition and thickness, but in general can be summarised as in Figure 2.1.The area of most interest is the shaded band in Figure 2.1 covering all treatments that actually involve melting the workpiece, and in particular surface treatments.

The advantages that are gained by using lasers for surface treatments instead of more conventional techniques are listed below (Steen, 1986):

(1) laser processing is a chemically clean process,
(2) thermal penetration and therefore component distortion is controllable,
(3) thermal profile can be controlled and therefore the shape, size, and location of the heat affected zone,
(4) less machining is required after laser processing,
(5) remote noncontact processing is possible,
(6) there is relative ease in automating the process.

Probably the most important advantage of laser processing is the ability to completely change the physical and chemical nature of relatively thin layers without affecting the bulk material properties. This is particularly the case for the production of corrosion resistant surfaces. In a recent publication Steen and Watkins (1992) summarised the advantages of using lasers to produce corrosion resistant surfaces compared with more conventional techniques. These were:

(1) pore free surface layers,

(2) bonding between the surface layer and the substrate is complete,
(3) no deleterious effects to bulk mechanical properties,
(4) special environments are not required,
(5) there is no fundamental restriction on component shape,
(6) the production of novel microstructures such as microcrystallinity or amorphous surfaces,
(7) limited areas can be treated so that laser processing of critical regions of a component can be achieved.

Two of the principle techniques of laser surface modification are Laser Surface Melting (LSM) and Laser Surface Alloying (LSA). LSM involves a high intensity, rapid scan with no additional elements added. Power densities of 10^7 W/cm^2 can be used, which produces shallow melt depths typically $\leq$ 1 mm, and cooling rates of between 10^4 - 10^8 Ks^{-1} can be obtained. LSA usually involves melting the surface to a depth of 150 - 2000 μm and adding elements to form a completely uniform surface layer, see Figure 2.2. For LSA good mixing is required with minimal loss of alloying elements through vaporisation or dissolution in the substrate by controlling melt pool turbulence, plasma formation and gas shrouding (Draper and Poate, 1985). Some techniques that are used to add the elements are predeposited coatings or blown gas powder injection. The main types of lasers used to carry out these treatments are the CO_2 laser and the Nd:YAG laser which are both capable of delivering very high power densities, of the order of 10^{10} W/cm^2, at very fast speeds.

2.2.2 The CO_2 laser

The CO_2 as its name suggests uses CO_2 gas but today all CO_2 lasers have a gas mixture of approximately CO_2: N_2: He = 0.8: 1: 7. The nitrogen and helium are added to improve the efficiency and output power of the laser and to stabilize and aid conduction of the plasma respectively. This type of laser operates in the infra-red at a wavelength of 10.6 μm and can be used in either continuous wave (CW) or pulsed (P) modes. From the energy diagram shown in Figure 2.3 the quantum efficiency, taken as the ratio of the energy in going from the upper state to the intermediate state over the energy required to raise the molecule to the upper state or (A-B)/A, is 45 %. However, the efficiency of the process from electric discharge to optical power is between 15 - 20 % and the wall plug efficiency, defined as the (optical energy out) / (total electrical energy into the system), is only 12 %. Even with such a low value the CO_2 laser remains the most efficient of the main industrial lasers used today.

2.2.3. Laser- Material Interactions

The incident laser intensity, Ho, may be much higher than the actual absorbed intensity, H (Roessler, 1986). A coupling coefficient, γ, can be defined to represent the ratio of the absorbed intensity to the incident intensity.

$$\gamma = \frac{H}{H_0} \tag{2.1}$$

For samples that are sufficiently thick and absorbing γ is 1-r where r is the reflectivity of the surface. The reflectivity can be seen to be a function of incident wavelength as shown in Figure 2.4, which also shows that the reflectance for aluminium is very high at 10 μm, near the output wavelength of the CO_2 laser. As radiation time increases, however, the substrate does warm up, which is believed to be due to the formation of a partially ionised gas plasma which increases coupling. Hence, the reflectivity decreases which leads to further substrate heating due to an increase in the absorptivity. Furthermore the reflectivity can be decreased by using surface pretreatments. In the case of aluminium and its alloys surface pretreatments like sand blasting (Hegge and De Hosson, 1990, and Leech, 1989), sooting (Luft et al, 1987), and grinding with 600 grit paper (Lasek et al, 1992) have been successfully used.

2.2.4. Melt Pool Solidification

2.2.4.1. Introduction to solidification

The morphology of the solid phase that forms from the liquid can be either planar, cellular, or dendritic depending on factors such as solute concentration, solidification rate and temperature gradient. Due to solute rejection at the solid/liquid interface there is a composition profile ahead of the interface in the liquid, as shown in Figure 2.5 (a). However because of this, the actual temperature of the liquid just ahead of the solidification front can be lower than the equilibrium liquidus temperature, Figure 2.5 (b). This region is then constitutionally supercooled which encourages the growth of irregularities such as cells or dendrites into the liquid. The different solidification morphologies are summarised in Figure 2.6 as a function of temperature gradient, G, and solidification rate, R. For high values of G and low R a stable planar front can exist. As G decreases and R increases, first cells can form and then eventually dendrites can grow. This can be represented mathematically as follows:

Assuming there is no convection in the liquid phase the gradient of the solute concentration in the liquid at the interface is given by the mass balance relationship:

$$\left(\frac{dC_L}{dx}\right)_{x=0} = -\frac{R}{D_L}C_L^*(1-k) \qquad (2.2)$$

The limit before the onset of constitutional supercooling is defined as:

$$G = \left(\frac{dT}{dx}\right)_{x=0} = m_L\left(\frac{dC_L}{dx}\right)_{x=0} \qquad (2.3)$$

where

C_L = Solute concentration in the liquid

T = Temperature (°C)

R = Rate of solidification (ms^{-1})

D_L = Diffusivity (m^2s^{-1})

C_L^* = Liquid concentration in equilibrium with solid
concentration C_S^* at the solid/liquid interface

k = Partition coefficient C_S^*/C_L^*

m_L = Slope of the liquidus

G = Thermal gradient (°Cm^{-1})

x = Distance perpendicular to the melt front (m)

Combining equations 2.2 and 2.3 then gives the condition for planar front growth:

$$\frac{G}{R} \geq \frac{-m_L C_S^*(1-k)}{kD_L} \tag{2.4}$$

Thus the ratio G/R should be large for a stable planar front solidification mechanism. Equation 2.4 is then the mathematical equivalent of Figure 2.6.

Inversely the scale of the structure can be used to estimate the cooling rate. If the dendrite or cellular structure is fine enough it is possible to approximate the liquid between the cells as being like in a small tank whose composition is determined by the rate of solute diffusion out of the cell. This diffusion is in fact governed by Fick's Second Law:

$$D_L \frac{\delta^2 C_L}{\delta y^2} = \frac{\delta C_L}{\delta t} \tag{2.5}$$

where y is in the transverse direction across the cell.

Now:

$$\frac{dC_L}{dt} = \frac{dC_L}{dT} \cdot \frac{dT}{dx} \cdot \frac{dx}{dt} = -\frac{G \cdot R}{m_L} \tag{2.6}$$

Thus, substituting for dC_L/dt and integrating across the cell width, λ, we obtain:

$$\left[\frac{\delta C_L}{\delta y}\right]_{y=0} = -\frac{G \cdot R\,\lambda}{m_L D_L} \tag{2.7}$$

and

$$\Delta C_{L_{max}} = -\frac{G \cdot R\lambda^2}{2m_L D_L} \tag{2.8}$$

Hence the cooling rate GR in $^\circ Cs^{-1}$ is inversely proportional to the square of the cell spacing, λ.

2.2.4.2. Solidification in laser melt tracks

For an initial consideration equilibrium phase diagrams can give a good indication of the likely constituent phases in a solidified laser melt track. However, it is usual that the laser melt pools are resting on a cool substrate, which is very thick relative to the melt depth and can cool the melt at very high rates. Typically cooling rates can be achieved from around 10^2 to 10^6 $^\circ Cs^{-1}$. Therefore, supercooling is likely to occur and hence, metastable phases may become thermodynamically possible. Constitutional supercooling does not occur, however, until there is a sufficient build up of solute atoms in the liquid in front of the solid/liquid interface which initially grows as a stable planar front. At very high cooling rates, >> 10^6 $^\circ Cs^{-1}$, absolute stability is possible because there is insufficient time for diffusion to occur. Under these conditions the whole melt solidifies very rapidly as either a planar front, or as a very fine microcrystalline structure, or even as a glass.

A characteristic feature of solidification in laser melt tracks is that the solid grows epitaxially from the unmelted parent material. The intimate contact between the melt pool and the partially melted grains in the substrate means that solidification starts by heterogeneous nucleation and, hence, the pre-existing grains continue to grow into the liquid. Savage and Aronson (1966) have shown by means of X-ray diffraction that continuous grains across the fusion boundary for welds in pure metals have identical orientations. Munitz (1980) later showed that epitaxially growth can also occur in laser melted alloys, even when the composition of the melt pool differs from the parent metal by adding elements to the melt.

2.2.5. An Introduction to Residual Stresses Induced by Solidification

Munitz (1980) found from electron channelling patterns that there were high strains near the fusion line in resolidified layers on laser melted Al alloys. He also proposed that the strains could cause cracking near to the fusion line. Residual stresses arise because of the volume changes that occur during solidification and cooling (Pumphrey and Lyons, 1948, Clyne and Davies, 1978). Detailed analysis of the origin of residual stresses can be found in the literature (Beck and Ericsson, 1986, Solina et al, 1984), but for simplicity the explanation of Steen (1986) is used here. If we consider a melt track on the surface of a cool substrate then there is no stress when the track is liquid. On cooling the melt shrinks and the stress builds up because the substrate is already cold and acts as a restraint on the contraction of the prior molten track. This situation is illustrated in Figure 2.7. For a fully restrained melt track the tensile strain is approximately given by:

$$\sigma/E = dl/l = \beta\Delta T \tag{2.9}$$

where

σ = thermal stress (Nm^{-2})

E = Young's Modulus (Nm^{-2})

dl = thermal expansion over length, l

β = coefficient of thermal expansion

ΔT = temperature change (°C)

In particular, during laser surface melting tensile residual stresses will always be present because the melt pool is restrained by the substrate (Solina et al, 1984). These tensile stresses remain provided there is no subsequent volume phase change such as the martensitic transformation that can occur in steels (Lamb et al, 1986, Pilloz et al, 1992, Van Brussel and De Hosson, 1993). The stress in some cases reaches values of the same order as the yield stress, or higher, which means that plastic deformation takes place in order to relieve the stress. Matsunawa et al (1990) have showed that the deformation can then take the form of microcracks that form along grain boundaries in the centre of the melt zone of Nd:YAG laser spot welded Al-Cu alloy.

When there are overlapping melt tracks there are further effects. For instance, the tensile ‘bow wave’ of an overlapping run can add to the prior residual stress and cause more deformation. However, there are also two heating effects that could potentially relieve the residual stress level. Firstly there is the part of the prior melt track that lies within the heat affected zone of the overlapping melt track, and secondly there is the effect due to substrate heating. Lamb et al (1986) have attributed both of these effects to thermal stress relief associated with tempering.

2.3. ALUMINIUM ALLOYS

2.3.1. Introduction to the 2xxx and 7xxx Series Alloys (Van Lanker, 1967)

Aluminium is now a very widely used metal in engineering applications probably second only to iron. It is favoured because of its low density and ease of formability. On its own however its mechanical strength is very poor. In order to improve the strength of aluminium, alloying elements such Si, Cu, Mg, Zn, Fe, Zr and Li have been added to form a whole range of engineering aluminium alloys. One way in which these elements strengthen aluminium is that they facilitate precipitation reactions within the alloy during ageing. These precipitates generally hinder the movement of dislocations within the alloys and hence improve the mechanical properties of the alloy.

The alloys that are in use nowadays are classified by the International Alloy Designation System (IADS) with a four figure number according to their main type, or types, of alloying elements. This scheme was implemented in 1970 and was based on the system used by the Aluminium Association of the United States (Polmear, 1989). For instance, alloys where Cu is the main addition are called 2xxx (2000) series alloys and those with mainly Mg and Zn are called 7xxx (7000) series alloys, and the type of alloy dictates the type of precipitate found within them. Traditionally the 2xxx series alloys are strengthened by $CuAl_2$ (θ) or $CuMgAl_2$ (S) and the 7xxx series alloys by $MgZn_2$ (η), however, further alloy developments have led to the formation of different types of precipitates. A further complete history of the development of these alloys can be found in the literature.

2.3.1.1. Microstructure of the as-received 2014 alloy

In the Al-Cu binary alloy the equilibrium precipitate is θ ($CuAl_2$) as shown by the phase diagram in Figure 2.8. The presence of > 1 wt.% Mg promotes the formation of S phase (Silcock, 1960-61) and also allows the possibility of the formation of Mg_2Al_3 (Van Lanker, 1967); a small addition of 0.2 wt.% Si promotes the formation of Mg_2Si (β phase), and $Al_5Cu_2Mg_8Si$ (Q) (Gupta et al, 1987). 2014 is a heat treatable wrought aluminium alloy with the nominal composition: 3.9-5.0 Cu, 0.5-1.2 Si, 0.7 Fe, 0.4-1.2 Mn, 0.2-0.8 Mg, 0.25 Zn, 0.1 Cr, 0.15 Ti, 0.2 max Zr; all the figures are quoted in weight percent, wt.% (Polmear, 1989).The precipitation sequence in the binary alloy is:

$$\alpha\text{-Al (solid solution)} \rightarrow \text{GP zones} \rightarrow \theta'' \rightarrow \theta' \rightarrow \theta\ (CuAl_2)$$

However, in 2014 alloy there can be several types of precipitate present in the alloy, depending on the heat treatment condition and the different ratios between Cu, Mg, and Si. The mechanical properties depend on the heat treatment condition and the most common heat treatment for this alloy is solution treatment followed by quenching and then artificial ageing. Alloys in this condition are recognised by the suffix T6 after the alloy number.

In this condition the microstructure of 2014 alloy, solution treated in the range 460-500 °C, water quenched and aged at 175 °C (Polmear, 1989), consists of grains of α-Al with a fine dispersion of $CuAl_2$ (θ' and θ'') and $CuMgAl_2$ (S'). As well as the precipitates a larger insoluble $CuAl_2$ phase exists randomly distributed within the grains and at grain boundaries. The segregation of Cu to grain boundaries often leads to an area within the grain adjacent to the grain boundaries denuded in fine θ' and S' precipitates. This is known as the precipitate free zone (PFZ).

2.3.1.2. Microstructure of the as-received 7075 alloy

7075 is an age hardenable wrought aluminium alloy with the nominal composition: 5.1 - 6.1 Zn, 2.1 - 2.9 Mg, 1.2 - 2.0 Cu, 0.5 Fe, 0.4 Si, 0.3 Mn, 0.18 - 0.28 Cr, 0.2 Ti, 0.25 (Zr +Ti); all the figures are quoted in wt.% (Polmear, 1989). The equilibrium precipitate for the ternary alloy is $MgZn_2$ (η), shown by the phase diagram for Mg-Zn in Figure 2.9, and is formed by the following sequence:

$$\alpha\text{-Al (solid solution)} \rightarrow \text{GP zones} \rightarrow \eta' \rightarrow \eta\ (MgZn_2)$$

this precipitate is usually found regardless of the other alloying additions, unless the Cu content is higher than the Mg content and then $CuAl_2$ or $CuMgAl_2$ can be precipitated (Mondolfo, 1976). However, in the case of 7075 Cu is present in smaller quantities than the Mg, and its main effect is that it accelerates precipitation (Livak and Papazian, 1984). The presence of Si in the alloy also means that the β phase (Mg_2Si) may precipitate from the solid solution, if the ratio of free Mg:Si is greater than 1.73, by the following sequence (Mondolfo, 1976):

$$\alpha\text{-Al (solid solution)} \rightarrow \text{GP zones} \rightarrow \beta'' \rightarrow \beta' \rightarrow \beta\ (Mg_2Si)$$

Although precipitation is normally induced by heat treatments, following solution treatment and quenching, 7075 alloy has the ability to age naturally at room temperature. However, in the T6 condition the microstructure consists of a fine dispersion of η–$MgZn_2$ (Polmear, 1989).

2.4. REVIEW OF LASER SURFACE MELTED ALUMINIUM ALLOYS

2.4.1. Aluminium-Copper Alloys

The solidification microstructures of surface melted single crystal Al and Al- 2 wt.% Cu alloys have been studied by Simidzu et al (1990) and Katayama et al (1991) using Nd:YAG lasers. In both cases the surfaces of the alloys to be melted were orientated in a specific crystallographic plane to investigate the orientation relationship between the substrate and the solidified melt pool. It was found that the alloys resolidified epitaxially with planar front growth which became cellular dendritic towards the surface. They found that copper formed $CuAl_2$ in the dendritic boundaries, and the amount of Cu in solid solution was about 1.5 wt.% which was higher than the amount predicted from the phase diagram (0.3 wt.%). These workers reported that planar front growth was thicker for the pure Al than the alloy because the transition to cellular dendritic growth in the alloy was easier due to constitutional supercooling. The cellular dendrites grew away from the planar front but whereas in the alloy they grew straight, in the pure Al the growth tended to shift away from the preferred direction towards the direction of heat flux resulting in curved dendrites.

Munitz (1980, 1985) has carried out a detailed investigation of the epitaxial growth and microstructure of laser surface melted Al- 4.5 wt.% Cu alloy using CO_2 lasers operating at 6 kW and 1.7 kW, respectively. In his work he showed clearly that grain boundaries in the substrate are continued through the fusion zone into the resolidified layer and that the resolidified grains had the same preferred orientation as the grains in the substrate. However, Munitz also found that even though the growth was epitaxial there were large residual strains at the fusion line that could cause cracking adjacent to this region.

At the substrate/melt pool interface there was a region of planar front solidification that contained no precipitates. The solidification of columnar grains after the planar front region proceeded by cellular dendritic growth. He observed that there were 'circular stripes' (usually referred to as solute banding) within the structure that resulted from differences in microstructure of the precipitated interdendritic phase. The precipitated phase was identified as $CuAl_2$ and the microstructural changes in this phase, that cause bands was attributed to variations in solidification rate induced by changes in the local heat flux. Composition profiles also revealed that there were macroscopic changes in Cu concentration due to the banding structure. Another form of banding was identified by Munitz caused by the rapid solidification of the back flow of the melt from the solidifying front which forms the rippling commonly observed on the surface.

Reznicek et al (1989) also studied the microstructure of an Al- 4.5 wt.% Cu alloy (designated CSN42 4201) surface melted with a CO_2 laser operating at 2 kW. They found that the structure consisted of α-Al dendrites surrounded by $CuAl_2$ - Al eutectic. The dendrites were well defined at the maximum melt depth and their size decreased in the direction of the surface. Furthermore, Kaech and Epprecht (1978) characterised the microstructure of a 4.6 wt.% Cu alloy surface melted with a nanosecond pulsed CO_2 laser operating at 8 J/pulse. The substrate alloy was solution treated at 535 °C and quenched to room temperature prior to surface melting so that the microstructure consisted of an even distribution of GP zones. After single and double pulses the GP zones were replaced by smaller precipitates, and a uniform distribution of spherical and elliptical coherent precipitates, respectively. These precipitates were found to be dissimilar to the usual GP zones and θ'' precipitates obtained after conventional heat treatments. For further melting with 3 to 10 pulses these workers reported the formation of a metastable amorphous layer in the top 1 μm of the melted layer, which was observed to crystallise during transmission electron microscopy.

In addition to the above binary alloys laser surface melting has also been carried out on 2024 Al alloy (Al- 4.4 wt.% Cu- 1.5 wt.% Mg- 0.6 wt.% Mn). Kim and Weinmann (1978) have studied the formation of porosity during solidification after melting with a microsecond Nd:Glass laser. More recently, Milewski et al (1993) used an Nd:YAG laser and the microstructures were similar to those in the work reported by Munitz (1985) mentioned previously. Noordhuis and De Hosson (1993) studied the nucleation of precipitates in this alloy after surface melting with a 1.3 kW CO_2 laser. They noted that nucleation could be induced by shot peening for as little as 10 s after laser surface melting.

Other work concerning Al-Cu alloys has involved eutectic (Zimmerman et al, 1989) hypoeutectic (Gill et al, 1992) and hypereutectic (Gill and Kurz, 1993) compositions. Zimmerman et al (1989) using a 1.5 kW CO_2 laser observed that the microstructure of a Al- 32.7 wt.% Cu eutectic alloy melted at various scan velocities was dependent upon the local growth velocity and direction which was calculated according to the following relationship (see Figure 2.10):

$$V_s = V_b \cos\theta \tag{2.10}$$

where

V_s=Local growth rate.

V_b=Laser scan velocity.

θ= Angle between V_b and the direction of the solidifying structure.

Using Equation 2.10 they showed that for $V_s < 200$ mm/s the microstructure was a regular lamellar eutectic consisting of α-Al and θ (Al_2Cu), for 200 mm/s $< V_s <$ 500 mm/s a wavy eutectic of α-Al and θ′ was observed, and for $V_s > 500$ mm/s a banded structure of alternating supersaturated α-Al and the wavy eutectic was formed. The lamellar spacing, λ, of the eutectic obeyed the relationship $\lambda^2 V_s$ = constant for low growth rates but for growth rates above 200 mm/s this relationship did not hold. Gill et al (1992, 1993) obtained similar results using Al-Cu alloys with 26 - 28 wt.% Cu and 36 - 44 wt.% Cu, respectively. However, they found that at growth rates of between 50 mm/s and 600 mm/s a cellular dendritic structure could form. Gill and Kurz (1993) also showed, for the same alloy as Gill et al (1992, 1993), that planar front solidification could be achieved when the growth velocity was much higher than 1 m/s.

2.4.2. Aluminium-Silicon Alloys

Hegge and De Hosson (1990) used a 1.5 kW CO_2 laser to melt the surface of Al-Si alloys containing 4, 7, 12 and 20 wt.% Si. At scan velocities of 1 - 250 mm/s the 4 and 7 wt.% Si alloys showed microstructures which were cellular at the bottom of the track, became dendritic and finally cellular dendritic towards the surface. There was an interdendritic eutectic phase of Si plates in Al. At scan velocities of less than 5 mm/s the structure in the 12 wt.% Si alloy was totally eutectic but between 5 - 50 mm/s the structure changed from eutectic to dendritic. A cellular dendritic microstructure was observed just below the surface which increased in depth with increasing scan rate up to 200 mm/s. At scan velocities higher than 200 mm/s the microstructure of the entire melt depth was cellular dendritic.

Leech (1989), Luft et al (1987) and Lasek et al (1992) have also used CO_2 lasers operating at 6.4 kW/cm^2, 2 and 4 kW, and 2.5 kW respectively to surface melt Al-Si alloys of similar composition. Leech (1989) observed a dendritic microstructure at 100 mm/s which changed to a fine filamentary eutectic at 413 mm/s in Al- 13 wt.% Si. Luft et al (1987) and Lasek et al (1992) reported eutectic structures for Al- 12 wt.% Si alloys surface melted at 40 mm/s and 1 - 10 mm/s respectively.

The structure of the fourth alloy, 20 wt.% Si, investigated by Hegge and De Hosson (1990) started dendritic, turned eutectic and finished as cellular for the whole range of scan velocities. They also reported that large areas of pure Si were found at the bottom of the melt pool in the 20 wt.% alloy. Pierantoni et al (1992), on the other hand, showed that the structure of Al- 20 wt.% Si melted at 100 mm/s with a CO_2 laser at 1.5 kW was initially columnar grains of fine eutectic, turning to α-Al dendrites plus interdendritic fibrous eutectic. They showed that the transition from eutectic to dendritic occurred when the local growth rate increased to greater than 70 mm/s and that the transition growth rate decreased with decreasing silicon content.

2.4.3. Aluminium-Zinc Alloys

Lasek et al (1991, 1992) and Synecek et al (1992) have used CO_2 lasers operating at 200 - 1400 W to melt the surface of Al-Zn alloys. The solidification structures were characterised in terms of the heat affected zone (HAZ) in the substrate, original substrate composition and the transition from planar front growth to dendritic growth. In addition Lasek et al (1991) and Synecek et al (1992) studied the effect of additional heat treatment on the microstructure. In the HAZ of laser melted Al- 30 wt.% Zn small spherical GP zones were seen to form in the partially melted grains (Lasek et al, 1991). Epitaxial planar front solidification was seen to occur at the maximum melt depth. The transition from planar front solidification to dendritic growth in an Al- 30 wt.% Zn alloy was preceded by a region of planar front growth that also contained solute enriched droplets that solidified and precipitated β-Zn spheroids on final cooling (Lasek et al, 1991). In alloys containing 1, 6 and 10 wt.% Zn Lasek et al (1992) observed a banded structure (the phenomenon of banding will be reviewed in more detail in the next section, 2.3.4). For an alloy of Al- 1 wt.% Zn melted at 0.05 m/min they also found that there was no cellular structure at all within the resolidified layer.

The presence of high residual stresses concentrated in the HAZ and at grain boundaries was also inferred by Lasek et al (1991) because of the existence of shear bands in grains within the HAZ and also because of cracking along the grain boundaries into the melted region. As a result of grain boundary cracking a high density of lattice defects near to grain boundaries was observed and this enabled the heterogeneous nucleation of equilibrium β–Zn particles during room temperature ageing.

After subsequent heat treatment of the surface melted Al- 30 wt.% Zn alloy the cellular dendritic structure transformed firstly by coarsening of the interdendritic phase at the cell boundaries followed by nucleation of β phase within the grains (Synecek et al, 1992). After the full transformation sequence the structure was found to consist of β–Zn in a stable α solid solution similar to that of conventionally quenched and aged alloys. The GP zones observed by Lasek et al (1991) in the HAZ transformed into metastable α′ phase and stable β- Zn.

Roosz et al (1993) have also used a CO_2 laser operating at 1 kW with scan velocities of 1, 2.08, 4.16, 8.33 and 16.66 mm/min to surface melt an Al- 6 wt.% Zn- 2 wt.% Mg alloy. The microstructure of the resolidified layer consisted of a planar front region at the maximum melt depth extending into the melt by as much as one quarter of the total melt depth (~40/150 μm). The remainder of the melt zone solidified with a coarse cellular dendritic structure.

2.4.4. Aluminium-Iron Alloys

Gremaud et al (1990) used a CO_2 laser operating at 1.5 kW to laser surface melt Al-Fe alloys with 0.25 to 8 wt.% Fe at scanning speeds between 100 mm/s and 6 m/s. Similar overall microstructures were observed to those reported previously for Al-Cu, Al-Si and Al-Zn alloys. Carrard et al (1991) using similar alloys and laser operating conditions, later studied in detail the structure of the intercellular precipitates formed in alloys with between 0.5 and 8 wt.% Fe. They found that the precipitates were quasicrystalline in nature but were unable to actually identify the type of precipitate. They also showed that the precipitates formed without any apparent orientation relationship with the α-Al cells. The size and morphology of the precipitates was dependent on concentration and growth rate and they appeared as globules in some cases. In particular, however, Gremaud et al (1990, 1991) attempted to explain the phenomenon of solute banding.

In their first investigation Gremaud et al (1990) found that for alloys containing up to 8 wt.% Fe, laser melted at scan rates between 100 mm/s and 6 m/s, banded structures would generally form at growth rates higher than 500 mm/s. The actual value of the growth rate at which banding occurred was dependent on the alloy composition and it coincided with the limit of absolute stability. The bands were shown to consist of an alternating structure of precipitate free α-Al solid solution an a fine dendritic structure.

In later work Gremaud et al (1991) showed that two different banded structures could be formed. These were called low-velocity bands and high-velocity bands depending on the laser scan velocity. The low-velocity bands were stated as being due to surface effects and convection, and the contrast was essentially due to a difference in spacing of the same growth morphology grown at different rates. However, it was shown that for high-velocity banding there was a critical growth rate at which the cellular dendritic structure was replaced by a succession of light bands, of planar front growth, and dark bands, of ultra-fine cellular dendritic growth.

The extent of low-velocity banding was shown to be dependent on composition: in Al- 8 wt.% Fe, low-velocity bands existed up to laser scan rates, V_b = 150 mm/s while, in Al- 0.5 wt.% Fe, they disappeared at rates above 50 mm/s. The actual presence of low-velocity banding was, however, independent of composition, and for a given composition the band spacing was independent of V_b. Instead increasing V_b decreased the spacing of the cellular-dendrites within the two bands.

For high-velocity banding the critical growth rate, V_s, for the appearance of banding was found to be dependent on composition and ranged between 300 mm/s for Al- 0.5 wt.% Fe and 4 - 5 m/s for Al- 8 wt.% Fe. The concentration of alloying elements within the light bands was found to be uniform, independent of growth rate, and close to the nominal composition of the individual alloys. They explained the presence of high-velocity banding in terms of the localised acceleration and deceleration of the growth velocity up to the point where the mean velocity reached the limit of absolute stability.

2.4.5. Summary of Other Surface Melted Al Alloys

Luft et al (1987) have made a general study of laser surface melting on various Al-Trans (Cr, Mn, Fe, Ni, Ti, and Zr) alloys using a CO_2 laser operating up to a maximum of 6 kW. In all cases they found increased solid solubility in the α-Al of the transition metal and the increase was dependent on V_b. Due to the differences in the melting temperatures of the individual intermetallic compounds the extent of their dissolution and redistribution was different for each alloy. In Al- 1.5 wt.% Ti and Al- 1.5 wt.% Zr alloys, which had the highest melting point intermetallics ($TiAl_3$, $ZrAl_3$), melting was incomplete but the partially melted particles were redistributed by convection resulting in a finer microstructure with a more even distribution of smaller intermetallic particles. For an Al- 6 wt.% Cr alloy complete dissolution of the second phase was achieved and the melt resolidified as $CrAl_7$ dendrites in an aluminium matrix. Similar dendritic structures were observed for Al- 6 wt.% Mn and Al- 6 wt.% Fe; not in an aluminium matrix but in their respective eutectics instead. In the Al-Fe alloy some of the intermetallics at the limit of the melt depth had not been melted completely, and instead a feathery eutectic was observed for an Al- 6 wt.% Ni alloy but this alloy could only be shallow melted after a graphite coating pretreatment.

McCafferty et al (1981) used a pulsed CO_2 laser with maximum power density of 10^8 W/cm^2 to surface melt 3003 (Al- 1.2 wt.% Mn) alloy. The melt depth was only ~10 μm and the microstructure was found to consist entirely of a banded structure alternating between pure Al and the $MnAl_6$ phase. Juarez-Islas (1991) has also studied laser surface melting of Al-Mn alloys, comparing the resulting microstructure to that from unidirectional solidification (UDS), and tungsten inert gas (TIG) weld traversing techniques. He found that it was only possible to form extended α-Al solid solution without any microsegregation by laser surface melting techniques. The cell spacing of the α-Al dendrites was smaller in the LSM alloys than in the TIG welded and UDS samples, demonstrating that much higher growth rates can be achieved by LSM techniques.

Lastly, an insight into the glass forming ability of several binary alloys is given by Alonso and Lopez (1986). Jost and Rasche (1990) and Jost and Haddenhorst (1991) have used millisecond pulsed Nd:YAG lasers to surface melt Al-Ni-Y alloys in order to study the formation of amorphous phases. They found that the resolidified layers consisted of an outer layer that was fully amorphous, an intermediate layer that contained crystals in an amorphous matrix with the crystallinity increasing with depth, and an under lying layer of eutectic growth down to the maximum melt depth.

2.5. REVIEW OF LASER SURFACE ALLOYED ALUMINIUM

2.5.1. Nickel-Based Surface Alloys

The structure of surface alloys on aluminium is mainly controlled by the solubility of the alloying element(s) being added. Unfortunately, for the transition metals (Ni, Cr, Mo) that impart good wear and/or corrosion resistance the solubility under equilibrium conditions is very low and intermetallic phases usually form instead of supersaturated solid solutions, as illustrated by the phase diagram for Al-Ni in Figure 2.11. Gaffet et al (1989) have used a 3.6 kW CO_2 laser to surface alloy a predeposited electrolytic layer of Ni into an Al-based alloy. They reported a dendritic structure of primary Al_3Ni in an Al matrix for thin Ni coating (25 μm) and dendrites of Al_3Ni_2 plus Al_3Ni for thick coatings (50 μm). Similar results were obtained by Pelletier et al (1991) and Jobez et al (1988, 1990) using CO_2 lasers operating at 3.5 and 4 kW, respectively. However these workers reported that there was no extension of the solid solubility of Ni in Al as a result of laser alloying and Gaffet et al (1989) measured the Ni content in the matrix or interdendritic material to be no higher than 1.3 at.% in solid solution.

Houndri et al (1992) preheated Al-Si alloy substrates electrolytically coated with a 180 μm layer of Ni at 500 °C for 5 hrs prior to surface alloying using a 3.2 kW CO_2 laser.

They found that the heat treatment enhanced the formation of AlNi phase during surface alloying. Without the preceding heat treatment they found that the mixing was very poor, and a layer structure existed with globular Al_3Ni_2 in the top layer and fine dendritic Al_3Ni in the underlying layer. Conversely, Das et al (1992) used a 120 W pulsed laser to surface alloy pure Al with a predeposited 50 μm plasma sprayed Ni coating and subsequently heat treated the alloy at 500 °C for 2 hrs. The microstructure produced by this method consisted of primary Al_3Ni dendrites and a eutectic of α-Al and Al_3Ni.

2.5.2. Chromium-Based Surface Alloys

Jain et al (1981) used a nanosecond pulsed Nd:Glass laser operating at 2 J/pulse to surface alloy pure Al precoated with vacuum-deposited chromium films 650 and 1350 A° (angstroms) thick. They found that homogeneous surface layers could be produced for very shallow melt depths (< 3 μm). In contrast, Hagens and Yates (1989) used a Q-switched Nd:YAG laser to surface alloy sputter coated 400-600 A° films of Cr (and Mo) on Al, and observed inhomogeneous layers for melted depths up to 5 μm.

Crooks and Hornbogen (1989) reported the feasibility of alloying by irradiating chromium powder coatings on aluminium alloys with a 1.5 kW CO_2 laser. The microstructure consisted of an inhomogeneous distribution of coarse lamellar and fine globular intermetallic particles. In addition, they found that the hardness of the surface alloyed layer could be increased to values greater than 1100 Hv. Consequently the layers also exhibited a high degree of cracking. Similar results were observed by Volz (1991), who electroplated an Al-Mg-Si alloy with a 150 μm layer of Cr and then carried out surface alloying using a CO_2 laser operating at 1.7 and 3 kW. Recently Li et al (1993) surface alloyed with Cr by a blown powder injection technique using a 2 kW CO_2 laser. The microstructure consisted of dendrites of $CrAl_7$ in an α−Al solid solution. They found that the solubility of Cr was increased to 1.33 wt.% Cr in Al for a surface alloy with average composition 5.4 wt.% Cr.

Lastly, Petrov and Dimitroff (1993) have used an electron beam operating at 3.7 kW to surface alloy Ni-Cr, Fe-Cr and Co-Cr plasma sprayed coatings on an Al- 10.5 wt.% Si- 5.7 wt.% Cu alloy. They observed microstructures that were dendritic in nature but consisted of numerous intermetallic phases. Of these phase, those containing Cr were $CrAl_7$ and more commonly $(CrFe)_4Si_4Al_{13}$ or $(CrFe)_5Si_8Al_2$. At cooling rates greater than 10^5 K/s they found that the Cr in solid solution with α-Al was up to 10 wt.%.

2.5.3. Other Surface Alloy Systems

The two previous sections describe the general microstructural features reported for LSA treatments of Al alloys. This section serves to illustrate the diversity of the other work involving LSA of Al. Gjonnes (1991), and Pierantoni and Blank (1990) have studied LSA of plasma sprayed and electrodeposited Fe coatings, respectively. Hegge and De Hosson (1991) have used a 1.5 kW CO_2 laser to incorporate Mn, Co, and Ni into Al, and in particular studied the effect of convection on the distribution of alloying elements; homogeneous mixing was not observed.

Two further works have involved alloying with more complex systems, Yulong et al (1991) used a 2.8 kW CO_2 laser to LSA an Al- 25 wt.% Si- 10 wt.% Cr- 10 wt.% Ce alloy powder on a cast Al-Si (ZL108) alloy. After the LSA treatment the alloys were aged under various conditions and the effect on wear resistance was investigated. They found that the alloys produced by the laser processing technique were more wear resistant than a similar alloy produced by conventional means. Takeda et al (1992) used a 5 kW CO_2 laser and alloyed a Cu based alloy, an Fe based alloy, and a Co based stellite alloy into the surface of cast AC2B Al alloy by a blown powder injection technique. They reported that an almost homogeneous alloyed layer was obtained when the Fe based alloy powder was first mixed with pure Al powder before being injected into the melt pool, and concluded that convection played no part in the role of homogeneous mixing.

2.6. INTRODUCTION TO CORROSION

2.6.1. Aqueous Corrosion

2.6.1.1. Introduction

Metals corrode in aqueous environments by electrochemical reactions. On the surface of a corroding metal at any one time there are a number of anodic and cathodic sites at which these reactions occur. Oxidation occurs at the anodic sites involving the loss of electrons, e, and dissolution of the metal, M, which can be represented by the simplified reaction:

$$M - ze \text{ ---> } M^{z+} \text{ (ionised in solution)} \qquad (2.11)$$

in which the number of electrons taken from each atom is governed by the valency of the metal; usually z=1, 2 or 3. In order for this reaction to occur, however, a reduction reaction must occur at a cathodic site. The cathodic reaction involves the consumption of those electrons produced by the oxidation reaction and in aerated aqueous solutions can, for example, lead to either the reduction of oxygen or the evolution of hydrogen, shown below respectively:

$$O_2 \text{ (in solution)} + 4e + 2H_2O \text{ ---> } 4OH^- \text{ (in solution)} \qquad (2.12)$$

$$2H^+ \text{ (in solution)} + 2e \text{ ---> } H_2 \text{ (evolved from metal surface)} \qquad (2.13)$$

The deposition of metal can also occur at the cathodic sites but in corrosion the two above reactions are simplified forms of the usual mechanisms of electron consumption.

In the solution the metal ion can react with the hydroxyl ion to form an insoluble hydroxide which can then be precipitated on to the surface of the metal; this can be depicted in the simplest form as follows:

$$M^{z+} + zOH^{-} \text{ ---> } M(OH)_z \qquad (2.14)$$

Evans and Hoar (1932) were the first to quantitatively demonstrate the electrochemical reactions during aqueous corrosion by measuring the current flow when a piece of steel was immersed in a 3% potassium chloride solution. The weight loss of the anodic portion of the steel was found to be electrochemically equivalent to the current flow. This was taken as proof of the electrochemical mechanism of aqueous corrosion.

2.6.1.2. Electrode potentials

During the dissolution of a metal atom by aqueous corrosion, the atom goes from the metallic state on the surface, to a desorbed ion in the double layer, and eventually becomes a hydrated cation in solution, as illustrated by Figure 2.12. Accompanying this reaction is a change in the free energy, G, of the atom equal to ΔG. This is depicted by the energy diagram in Figure 2.13. However, the free energy of a reaction is also related to the potential of the reaction, E_0, according to Faraday's Law:

$$\Delta G = -zE_0F \qquad (2.15)$$

where F is the charge transported by one mole of electrons and is known as the Faraday constant with the value 96,494 C/mol, and E_0 is the standard potential for unit activity of the metals ions in the solution.

Under equilibrium conditions when a metal is immersed in an aqueous solution the anodic and cathodic reactions occur at the same rate and there is an overall steady state potential at which this occurs related to the net free energy change in the system. However it is not possible to measure the potential differences between the individual anodic and cathodic reactions. To overcome this a standard reference electrode is used to measure the overall reaction potential which is more commonly known as the free corrosion potential, E_{corr}. The potential of the reference electrode is defined as zero so that the absolute potential of the metal in the electrolyte is measured relative to the reference electrode. The standard electrode potentials at 25 °C for some of the more common metals are shown in Table 2.1, measured against a standard hydrogen electrode (SHE).

However, when the corrosive solution does not contain unit activity of the metal ions the dissolution will take place at a different potential, E_M, given by:

$$E_M = E_0 + \frac{RT}{zF} \ln a \qquad (2.16)$$

where R=gas constant= 8.32 J/mol.K, T=absolute temperature, and a is the activity of the dissolved M^{z+} ions originating from the metal.

2.6.2. Corrosion of Aluminium Alloys (Van Lanker, 1967)

Aluminium and its alloys are relatively stable in most environments due to the rapid formation of a protective oxide film on the surface. During exposure to a corrosive environment if the oxide film fails by some mechanism the alloy will suffer from localised attack at the point where the oxide is breached. Localised corrosion of aluminium alloys usually appears as pitting, crevice corrosion, or stress corrosion cracking (SCC). All these forms of corrosion occur as a multi-step process. Differences of opinion among investigators occur when an attempt is made to single out the importance of an individual step in relation to the whole process, implying that the significance of this single step overshadows all of the other steps. From the literature, however, there is a general acceptance that localised corrosion is determined by the physical, chemical, electrical and mechanical properties of the passive film on the surface.

2.6.2.1. Pitting theory

Work involving the investigation of passive film formation and breakdown leading to pitting is still very much at the forefront of corrosion science. The various mechanisms of passive film formation according to current theory are covered in the reviews by Hoar (1970) and Kruger (1988). A good review of the current status in the understanding of passive film breakdown or pitting for aluminium alloys in chloride electrolytes has been written by Foley (1986). In this review the now generally accepted theory of pitting for Al alloys is described as involving a multi-step process consisting of the following four steps.

1. The adsorption of the reactive anion on the oxide covered aluminium. This is a competitive process where the aggressive ion, such as chloride ion, is adsorbed competitively with hydroxyl ions or water molecules that would tend to promote passivity. Adsorption is nonuniform because of surface heterogeneity causing enhanced adsorption and surface activity at the imperfections or flaws in the oxide film.

2. The chemical reaction of the adsorbed anion with the aluminium ion in the aluminium oxide lattice or the precipitated aluminium hydroxide. During this stage stoichiometric compounds are formed by chemical reaction as opposed to loosely held chemisorbed species.

3. The thinning of the oxide film by dissolution. This step has also been described as penetration of the oxide film by the aggressive anion. Penetration here does not mean the diffusion of the chloride ion through the aluminium lattice but the formation of soluble compounds or transitory species at critical sites within the oxide lattice. Surface heterogeneities, being preferred sites for adsorption, become active centres which in turn are sites for accelerated film thinning.

4. Pitting propagation by direct attack of the exposed metal by the anion, possibly assisted by an anodic potential. Rapid attack can occur because of the high degree of

reactivity of metallic aluminium. Pit propagation is schematically shown in Figure 2.14. The significance of the heterogeneous nature of aluminium alloys is made clearer by Figure 2.14. The presence of second phase particles enhances pitting corrosion because of localised galvanic couples between the matrix solid solution and the particles (Hubler and Wranglen, 1964).

Any one of the above steps can be the rate determining step that is associated with the characteristic potential at which spontaneous dissolution of metal atoms occurs. This is then called the pitting potential which is commonly written as E_{pit}.

Measurement of the pitting potential can be carried out using a potentiometer and a three electrode cell, as described elsewhere in the literature and later in chapter 3.3. However, Hoar and Mears (1966) have proposed a method for testing the passivity of metals, which they applied to various stainless steels, by measuring the free corrosion potential, E_{corr}, over a period of time when the metal is completely immersed in an electrolyte. They proposed that if E_{corr} stays below the measured value of E_{pit} then the metal will not pit. Furthermore, the shape of the E vs time graph can be used to characterise the type of corrosion. This is illustrated in Figure 2.15, where curve (a) represents general corrosion when the potential reaches a steady value, and the dissolution of metal ions occurs uniformly over the whole surface; curve (c) depicts the behaviour of a metal that passivates, at E_{pass}, after the formation of a protective film; curve (b) indicates that pitting has occurred as E_{corr} first tends towards E_{pass} but breakdown occurs when E_{corr} is greater than E_{pit}. In curve (b) the alternating maxima and minima are due to the accumulative effect of the numerous local passivation and pitting events over the whole surface of the metal. However, the interpretation of these curves does not necessarily take into account the effect of such factors as surface topography and composition of the metal, therefore, this is presented below. In fact, the corrosion properties of Al alloys have been shown, in recent years, to be dependent on temperature (Bozack and Beshears, 1993), solution chemistry (Carroll et al, 1993), pH (Ambat and Dwarakadasa, 1992), and surface charge (Natishan et al, 1988); the details of which can be found in the literature.

2.6.2.2. The effect of surface topography on pitting

Wu and Wu (1992) have shown that the type of surface finish can affect the pitting characteristics of 7075 Al alloy. They found that on polished surfaces pitting was initially less severe than on roughly abraded surfaces but after prolonged immersion the polished samples showed more localised deeper pits than on the abraded samples. The initial higher corrosion rate for the abraded samples was attributed to a higher total surface area and surface defect density. The decrease in the corrosion rate was said to be due to the fact that on abraded surfaces continuous paths of susceptible material (grain boundaries) are broken up so that during prolonged exposure the corrosion rate is controlled by the dissolution of precipitates. Atomically flat surfaces are also prone to pitting because sites where dislocations emerge and surface vacancies, known as 'monotomic pits', are potential pit nuclei (Van Lancker, 1967). Yasuda et al (1990(a)) have showed that pitting on pure aluminium single crystals is dependent on the crystallographic orientation of the surface. The pitting potential, E_{pit}, showed a small dependence on surface orientation in the order $(E_{pit})_{\{001\}} > (E_{pit})_{\{011\}} > (E_{pit})_{\{111\}}$. They also showed that the presence of copper raised the pitting potential but reduced the dependence of E_{pit} on surface orientation.

2.6.2.3. The effect of composition on pitting

Composition is probably the most important factor controlling corrosion behaviour of aluminium alloys. Yasuda et al (1990(b)) showed that due to segregation pitting occurred in Al-Cu bicrystals at sites of minimum copper concentration. This arises because Al is anodic to Cu and hence Al corrodes preferentially in the presence of Cu. In fact, all the elements used in Al alloys to improve their mechanical properties via precipitation hardening increase the susceptibility to pitting, intergranular corrosion and stress corrosion cracking (SCC). For instance, the presence of certain precipitates at the surface, such as $CuAl_2$ in 2014 alloy, provides points at which the surface oxide film is weak. Scully et al (1993) have shown that the oxide over large second phase $CuAl_2$ particles is effectively thinned because of the presence of metallic copper in the normally insulating oxide. The metallic copper then enhances the the electron transfer reactions across the oxide into the electrochemical double layer.

2.6.3. Stress Corrosion Cracking

From an everyday engineering perspective SCC is probably the most serious form of attack and it has been shown to be linked directly to the presence of grain boundary precipitates. Cathodic second phase particles like $CuAl_2$ not only cause general pitting but as Urushino and Sugimoto (1979) have shown when segregated to grain boundaries in 2017 and 2024 alloys they can cause intergranular SCC. This is due to preferential attack of the precipitate free zone and thus renders the alloy vulnerable to SCC. Similar observations were made by Pickens and Langan (1987) when the anodic η-$MgZn_2$ phase in Al-Zn-Mg alloys was found to precipitate at grain boundaries during heat treatment.

2.6.4. The Effect of Transition Metals on Pitting in Al

It is well known that transition metals such as Cr, Mo and W enhance the corrosion resistance of stainless steels by altering the composition of the surface oxide film, and it is believed that the same effect should be observed in aluminium. This can be achieved by either chemical conversion treatments, such as those proposed by Shaw et al (1990) to incorporate Mo into the oxide layer by molybdate treatment, or by alloying with the bulk alloy. The corrosion resistance is maintained so long as the elements are contained in solid solution. However, the solid solubility of these elements in Al is extremely low (<< 1 atom percent, see Figure 2.16), and at these concentrations they have little or no influence on corrosion behaviour. These passivity enhancing elements have recently been used to improve the localized corrosion resistance of Al through non-equilibrium alloying techniques such as, ion implantation, and sputter deposition. A summary of the most recent work is given here but a more detailed review can be found in the literature (Szklarska-Smialowska, 1992).

The criteria used by Natishan et al (1986, 1988, 1991) for choosing the transition elements was that they had a low pH of zero charge. The pH of zero charge (pH_{pzc}) of an oxide is the pH at which the surface of the oxide has a net zero charge. At pH's lower than the pH_{pzc} the surface has a net positive charge and anions are electrostatically attracted to the surface and can absorb. It was shown that additions of 4 at.% Mo or 12 at.% Cr to aluminium raised the pitting resistance to chloride electrolytes by as much as 750 mV although typical values were around 100 - 125 mV. They proposed that the passive range, when compared to that of Al, in the Al-Cr and Al-Mo alloys was extended because a portion of the aluminium-oxygen bonds in the passive film were replaced with bonds formed between oxygen and the implanted ions, and this had the effect of interfering with the adsorption characteristics of the oxide by changing its surface charge. The actual concentration of the implanted ions in the oxide film was reported to be only 0.4 - 2.0 at.% even when the nominal alloy concentration was as high as 20 at.%. These results have recently been summarised by McCafferty et al (1993), and are shown in Table 2.2. Frankel et al (1989), Moshier et al (1986), and Davis et al (1990) have also reported increases in the pitting potentials, for 5 - 8 at.% Mo alloyed into Al, by about 500 mV, 400 mV, and 550 mV, respectively. In addition Frankel et al (1993) have shown that E_{pit} increases with increasing Mo concentration.

The surface chemistry of the passive films formed on Al-Mo and Al-Cr alloys has been studied by Moshier et al (1989). They found that after polarization in 0.1N KCl Mo was present in the oxide as a film in the form of MoO_4^{-2} and that it impeded the ingress and movement of the Cl^- anion in the film. Cr on the other hand formed a CrOOH barrier layer that inhibits the oxidation of the Al and restricts the Cl^- anions from reaching the metal/film interface. Pitting occurred in the Al-Mo alloys when MoO_4^{-2} was replaced by hydrated Mo^{+4} compounds and in the Al-Cr alloys when Cr^{+3} is oxidised to soluble Cr^{+6}. Mo^{+4} was also found in the air formed oxide and was suggested to be in the form of MoO_2. Shaw et al (1990, 1991) observed large increases in the pitting potential for Al-W alloys and characterised the oxide as containing WO_2

and WO_3. They proposed that the small amount of W in the passive film interacts synergistically with the hydrated aluminium oxide structure to form a more protective film. This type of enhanced protection was also reported by Davis et al (1991) for Al-Mo where the structure of the passive film was modified by the incorporation of Mo. After analysis they found that the passive film on Al-Mo resembled that of the α-Al_2O_3/AlOOH series in comparison to the γ-Al_2O_3/AlOOH series formed on pure Al. The α family contains only octahedrally coordinated Al atoms and is very stable. The γ family also includes tetrahedrally coordinated Al atoms in the lattice which are attributed to increasing the reactivity of passive films on pure Al.

2.7. THE CORROSION OF LASER SURFACE TREATED ALUMINIUM ALLOYS

2.7.1. Laser Surface Melting

There is little available information covering the corrosion behaviour of laser processed surfaces on Al alloys. Furthermore, there is contradiction in the literature as to whether LSM treatments can improve the corrosion resistance of Al alloys in the manner that has been reported for stainless steels; reviewed by Steen and Watkins (1992). Moore et al (1977) was apparently the first to study, by LSM using a CO_2 laser, the effect of surface modification on the pitting behaviour of 2024 Al alloy. However, they found no improvement in the pitting resistance after LSM because of cracks and pores that were presence in the surface. Bonora et al (1980) were the first to study the effect of LSM on the corrosion behaviour of pure Al. They used a Q-switched nanosecond pulsed ruby laser with energy densities at the surface between 1 and 5 J/cm^2 giving estimated cooling rates of the order of 10^{11} K/s. The pitting potential was unchanged after LSM but the current density was lower under both potentiostatic and potentiodynamic control. These workers concluded that the lower corrosion rates were due to a chemically inert amorphous aluminium surface caused by LSM. This effect was also observed by Hagans and Yates (1989) for pure Al in a boric-borate solution containing 1 g/l NaCl, surface melted using a Q-switched Nd:YAG laser with 4 mJ/ pulse, 5 ns pulses.

McCafferty et al (1982) studied the effect of laser surface melting on the electrochemical behaviour of 3003 Al alloy. They melted the surface with a single pulse CO_2 laser in a vacuum and corrosion tested the samples in sodium citrate, hydrochloric acid and sodium chloride solutions. Their overall findings were that laser melting improved the resistance to general corrosion in 0.1M sodium citrate and 0.1M hydrochloric acid solutions. They noted that the free corrosion potential was higher for the laser melted samples by 100 mV in 0.1M sodium citrate. In anodic polarization tests they observed that the rate of anodic dissolution was less for the melted samples. However, the pitting resistance in deaerated 0.1M NaCl was not improved and E_{corr} was increased by 300 mV; having the effect of decreasing E_{PD}. Further to this, Opara et al (1985) reported that the current density increased, or corrosion resistance decreased, with increasing specific energy input for a LSM Al-Si alloy tested in a 5% NaCl solution. Virtanen and Bohni (1993) have reported that the dissolution rate of Al-Si alloys at the free corrosion potential in 0.1M NaCl solutions was decreased after laser surface melting. For pure Al the reduction was only slight after surface melting with a laser. However, Virtanen and Bohni (1993) also reported that the pitting potential was increased for Al- 7 wt.% Si and Al- 12 wt.% Si after laser surface melting but not for Al- 17 wt.% Si.

2.7.2. Laser Surface Alloying

To date there has only been a very small amount of reported work concerning LSA of Al for enhanced corrosion resistance. Hagans and Yates (1989) have studied the effect of LSA with thin Mo and Cr films on Al, using a Q-switched Nd:YAG laser operating between 2.8 and 4.5 mJ/pulse with 5 ns pulses, on the corrosion resistance. They found that the resistance to both general corrosion and pitting was increased after surface alloying. The pitting potential was increased by up to 600 mV in a boric-borate solution containing 1 g/l NaCl for the LSA with Cr.

In the case of pure Mo and the Mo layer (unalloyed) they showed that the Mo pitted after a low overvoltage and that the underlying Al spontaneously pitted. The laser alloyed surface was shown to have a similar free corrosion potential to that of the unalloyed layer but there was an increase in the pitting potential of approximately 300 mV indicating an enhancement of the corrosion resistance. From a.c. impedance measurements they were also able to show that the dissolution rate for the alloyed surface was about half that of the bare substrate. These tests also revealed that different corrosion mechanisms were taking place for the alloyed Mo and Mo metal in contact with Al. Dissolution of Mo was not observed for the laser treated sample which suggested that the electrochemical behaviour of the surface alloy was similar to that of pure Al. They thus attributed the increase in the pitting resistance to the structural and/or chemical form of the Mo/Al layer.

For the unalloyed Cr layer a much greater passive range than the unalloyed Mo layer was observed. The two metals had similar pitting potentials but the free corrosion potential of the Cr was over 100 mV lower than for the Mo. After laser surface alloying the pitting resistance was shown to be far superior to that of the Al base alloy and that of the surface alloyed Mo. Small surges in the current density were observed in these alloys at potentials close to the pitting potential of the unalloyed layer but were believed to be caused by small regions of incompletely mixed Cr. The surface alloy repassivated before reaching the true pitting potential which was reported to be as high as +830 mV versus the standard hydrogen electrode (SHE).

Li et al (1993) have used a 2 kW CO_2 laser to LSA Cr into 7175 Al alloy substrate by a blown powder injection technique, and studied the corrosion behaviour in deaerated 3% NaCl. They found the pitting potential was increased after LSA and that it increased as a function of the Cr content. For a surface alloy containing 5.4 wt.% Cr the reported value of E_{pit} was -274 mV (SCE) compared to -730 mV (SCE) for the untreated 7175 alloy. Lastly, Petrov and Dimitroff (1993) used a 3.7 kW electron beam to surface alloy Ni-Cr and Fe-Cr alloys into an Al- 10.57 wt.% Si- 5.7 wt.% Cu alloy. Before corrosion testing the alloys were aged at 200 °C for 2 hrs. Anodic current densities were measured in a 5% NaCl solution and it was found that the corrosion resistance was lower (the current densities were higher) after the surface alloying treatment. The decrease in corrosion resistance was related to the increased potential difference between the intermetallic phases and the α-Al solid solution.

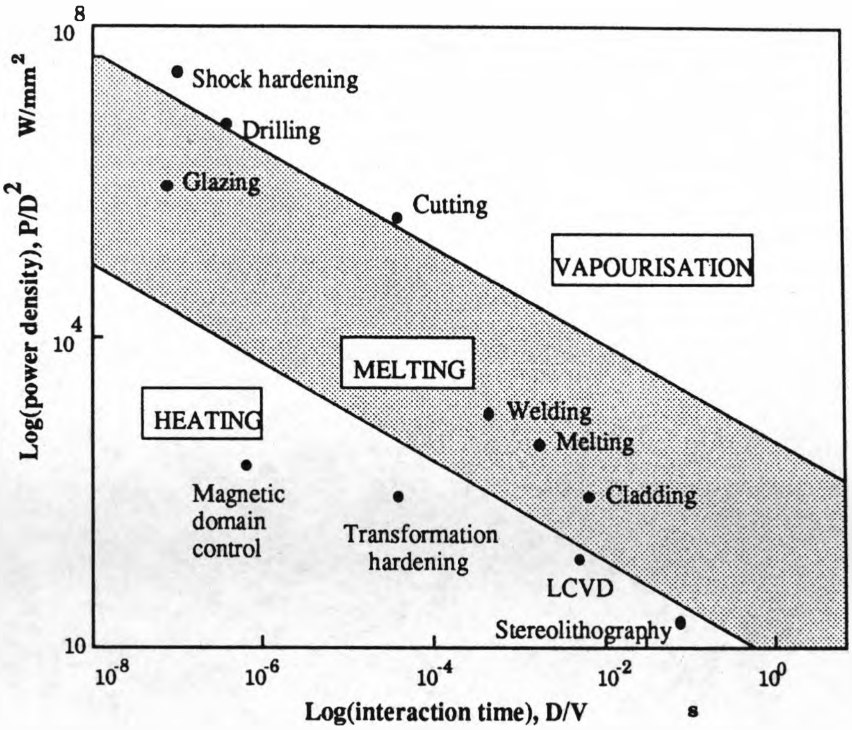

Figure 2.1. Plot of power density versus interaction timefor a range of laser processes (Steen, 1991).

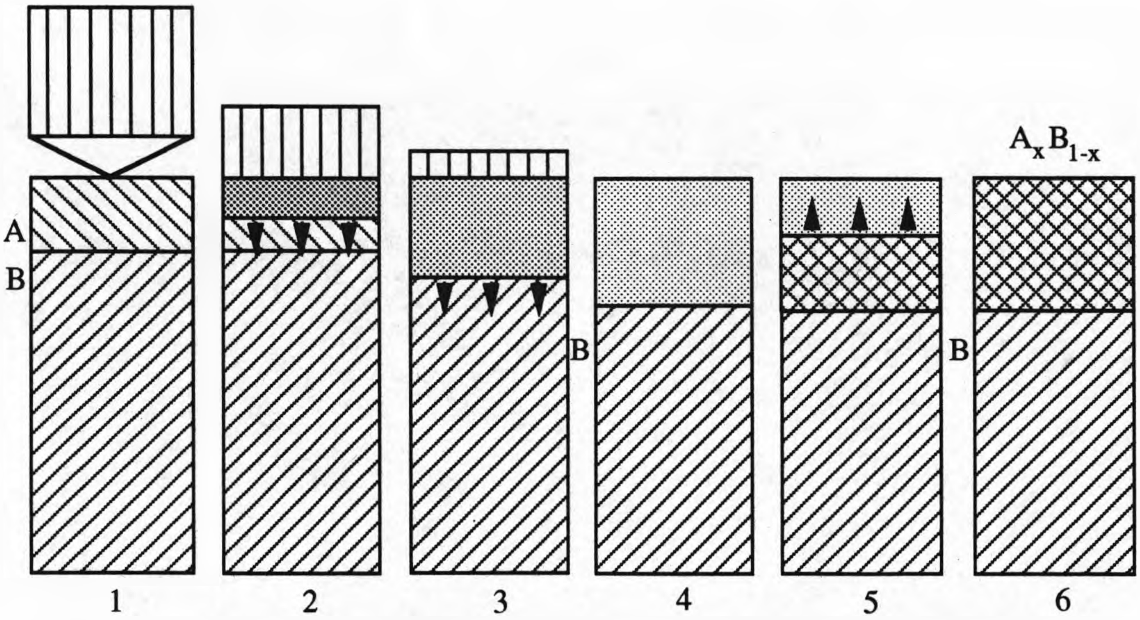

Figure 2.2. Stages involved in laser surface alloying: 1. Layer of A on substrate of B; 2. Laser impinges with layer A and begins to melt the surface; 3. Layer A is fully melted and melt pool extends into B; 4. Maximum melting with B mixing with A in the liquid; 5. Alloy layer solidifies epitaxially on B; 6. Final alloy layer with composition $A_x B_{1-x}$ (Draper and Poate, 1985).

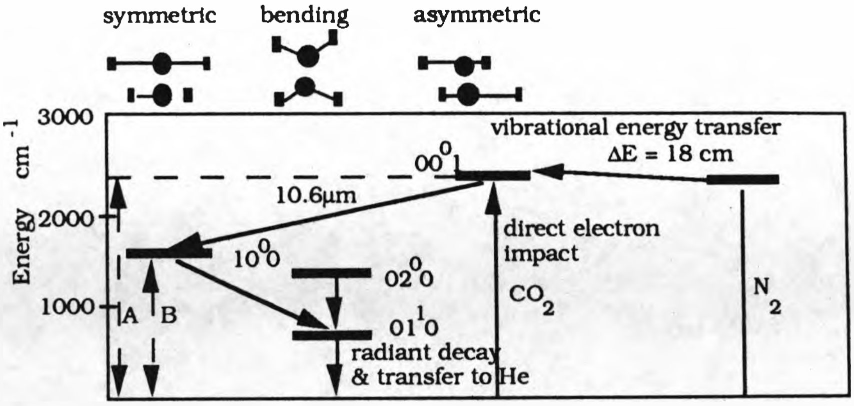

Figure 2.3. Energy levels of the carbon dioxide molecule, associated with lasers (Steen, 1991).

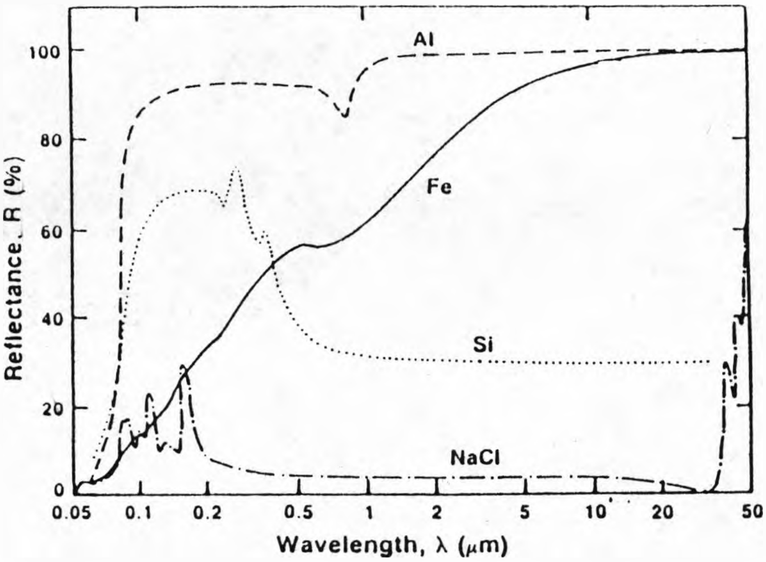

Figure 2.4. The reflectivity of some common elements (Al, Fe, Si) and NaCl (Roessler, 1986).

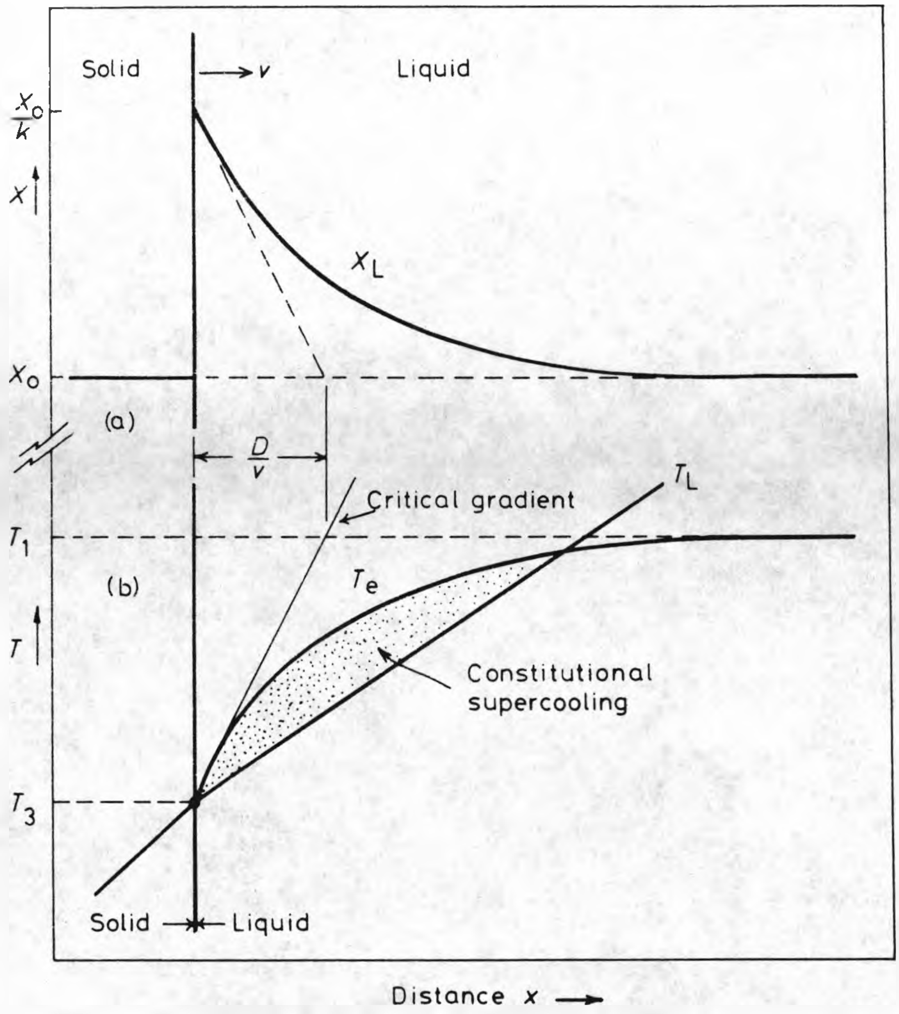

Figure 2.5. Constitutional supercooling ahead of a planar solidification front. (a) Steady-state composition profile across the solid/liquid (S/L) interface. The dashed line shows the actual change in composition dX_L/dx at the S/L interface. (b) T_L shows the temperature profile of the liquid ahead of the solidification front. The equilibrium liquidus temperature of the liquid is given by the line T_e. Constitutional supercooling occurs when T_L lies under the critical gradient (Porter and Easterling, 1988).

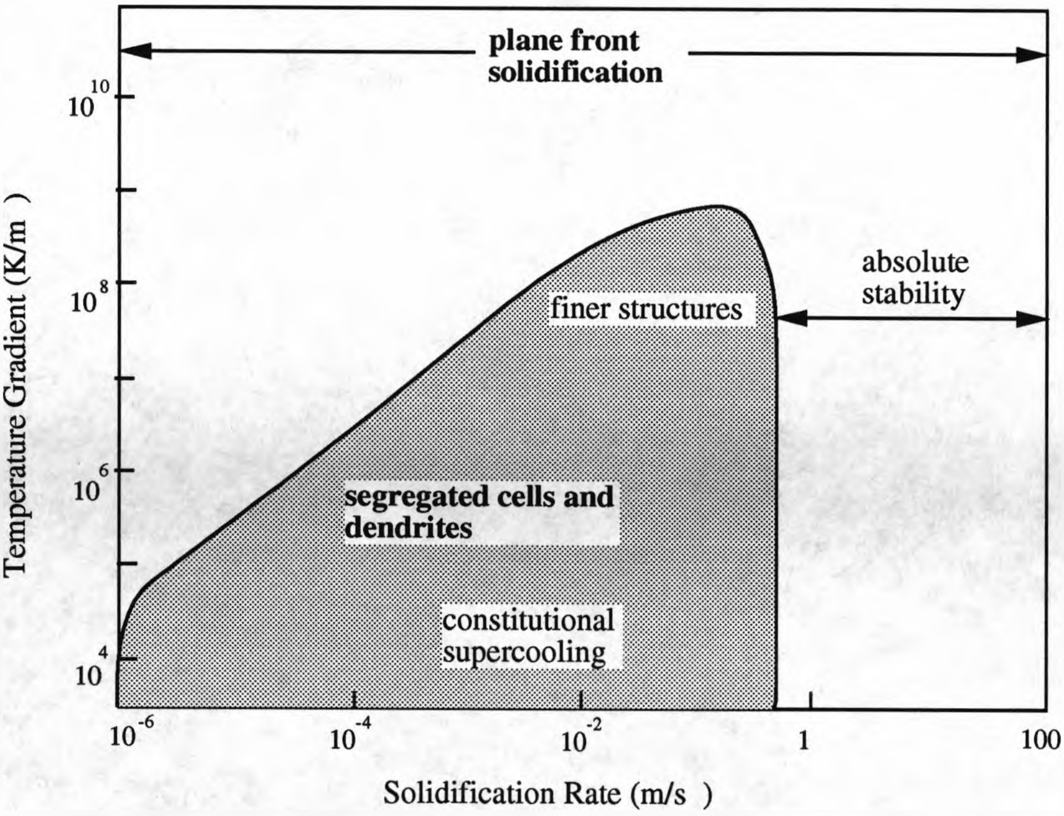

Figure 2.6. Schematic illustration of the plot of temperature gradient versus solidification rate, showing possible alloy solidification morphologies (Steen, 1991).

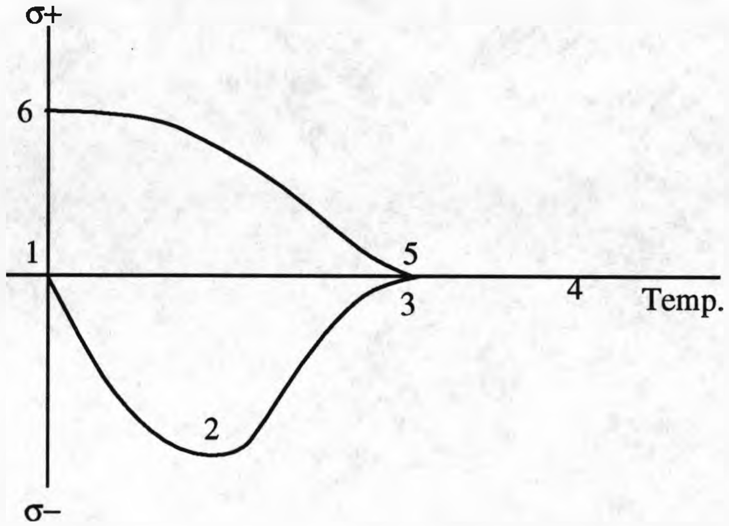

Figure 2.7. A schematic illustration of the stress-temperature relationship during laser surface melting. Point 1: starting temperature; Point 2: stress starts to fall due to plastic flow; Point 3: yield stress falls to zero at the melting point; Point 4: there is no stress in the melt pool; Point 5: on cooling stress starts to build up as the structure solidifies and the yield stress increases; Point 6; stress increases up to the final residual stress (Steen, 1986).

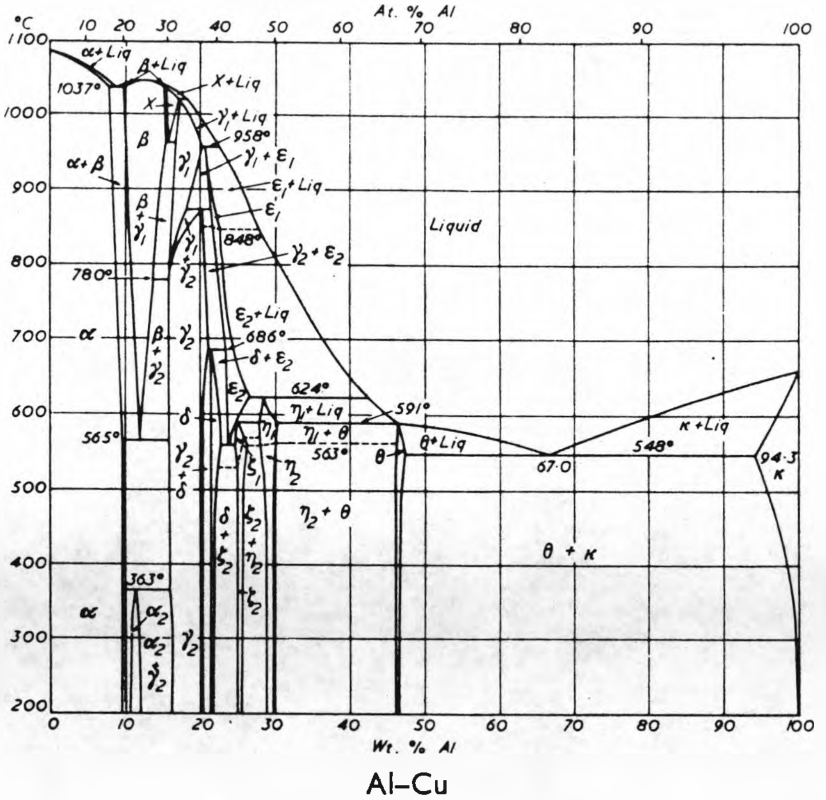

Figure 2.8. Aluminium-copper phase diagram (Mondolfo, 1976).

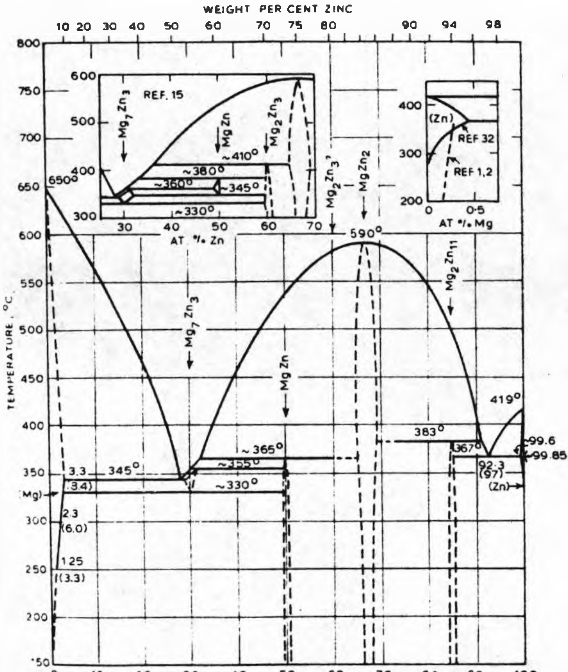

Figure 2.9. Magnesium-zinc phase diagram (Van Lancker, 1967).

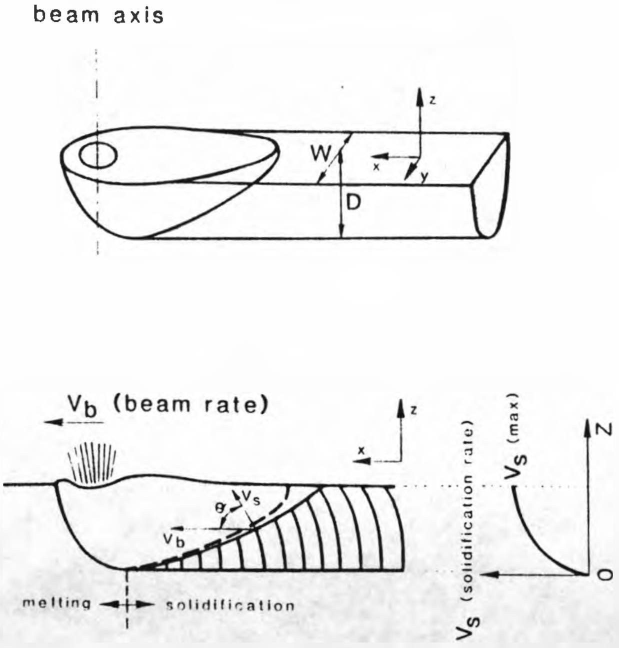

Figure 2.10. Schematic diagram showing the relationship between growth rate, R, and laser scan velocity, V_s (Gremaud et al, 1990).

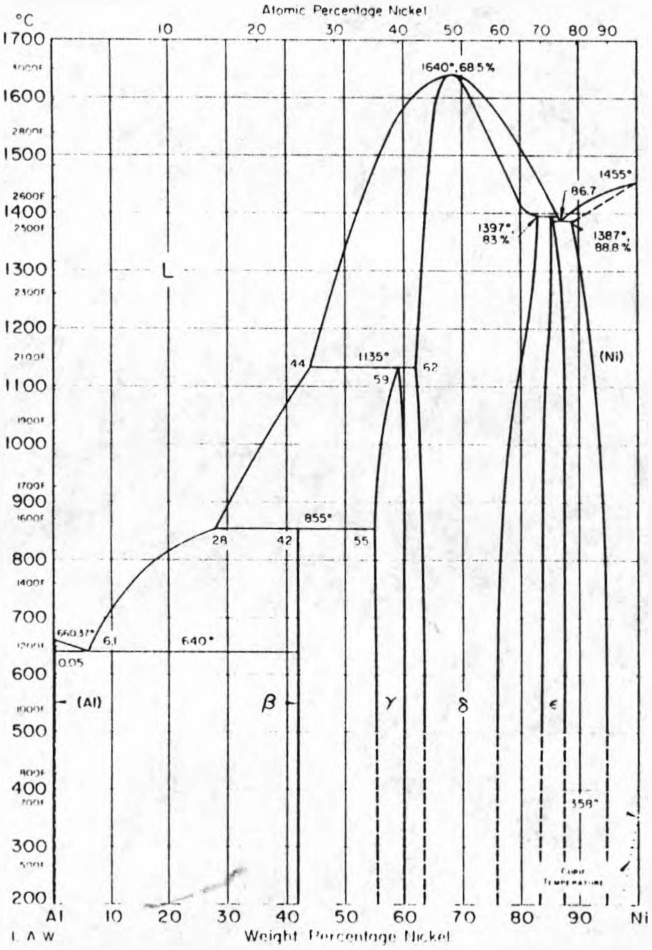

Figure 2.11. Aluminium-nickel phase diagram (Metals Handbook, ASM)

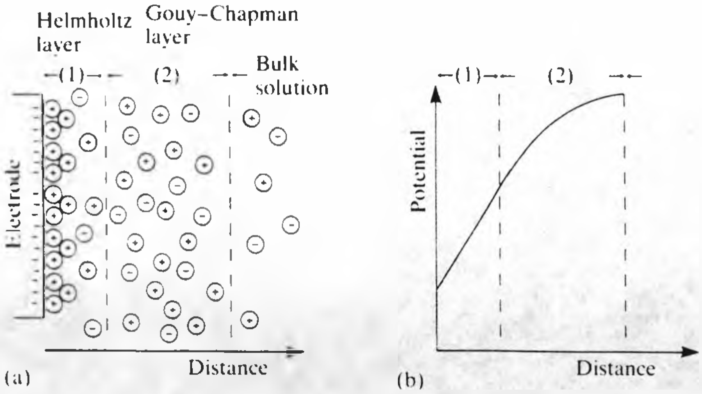

Figure 2.12. The electrochemical double layer. (a) Distribution of ions in solution adjacent to the anode. (b) Variation in potential with distance for the situation in (a) (Tretheway and Chamberlain, 1988)

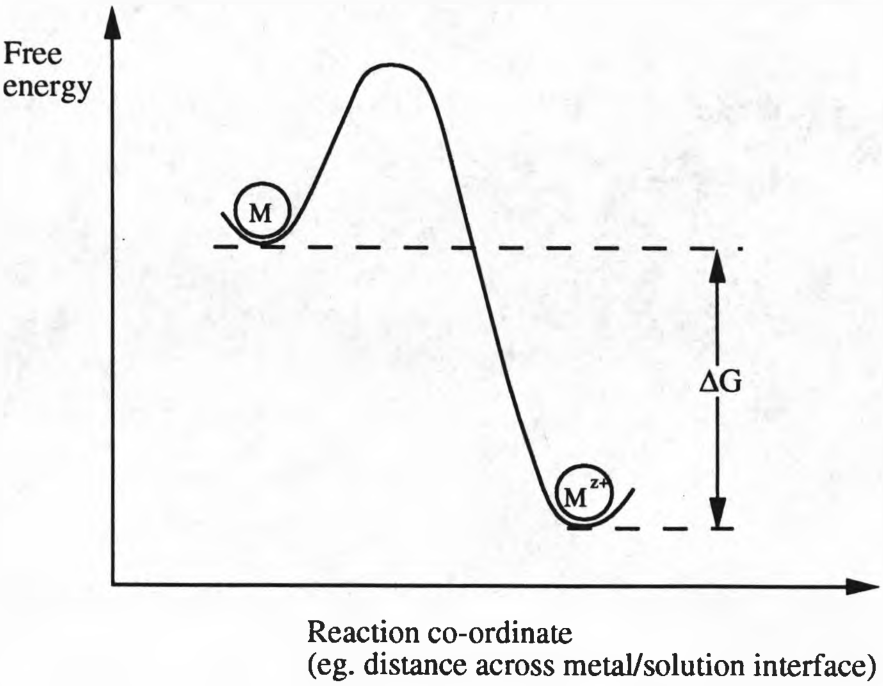

Figure 2.13. Schematic free energy profile representing the dissolution of a metal atom from in the lattice (M) to in the solution (M^{z+}).

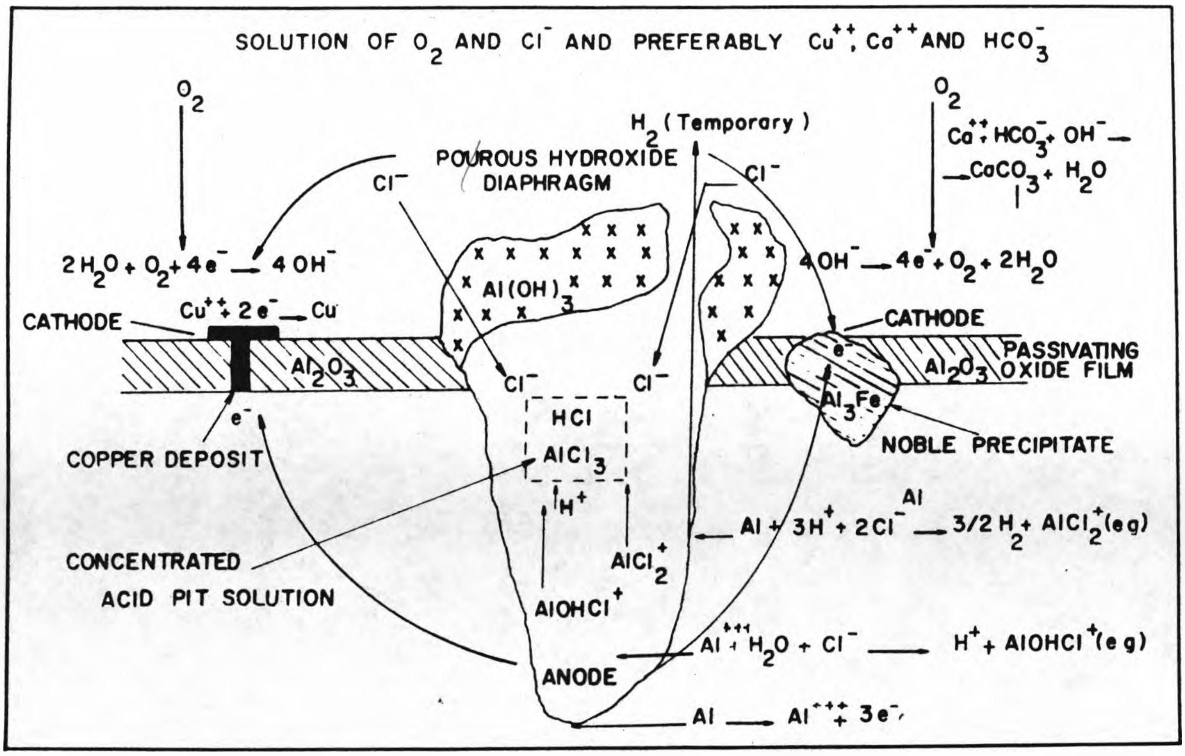

Figure 2.14. Multiple reactions occurring in an aluminium pit during autocatalytic growth (Hubler and Wranglen, 1962).

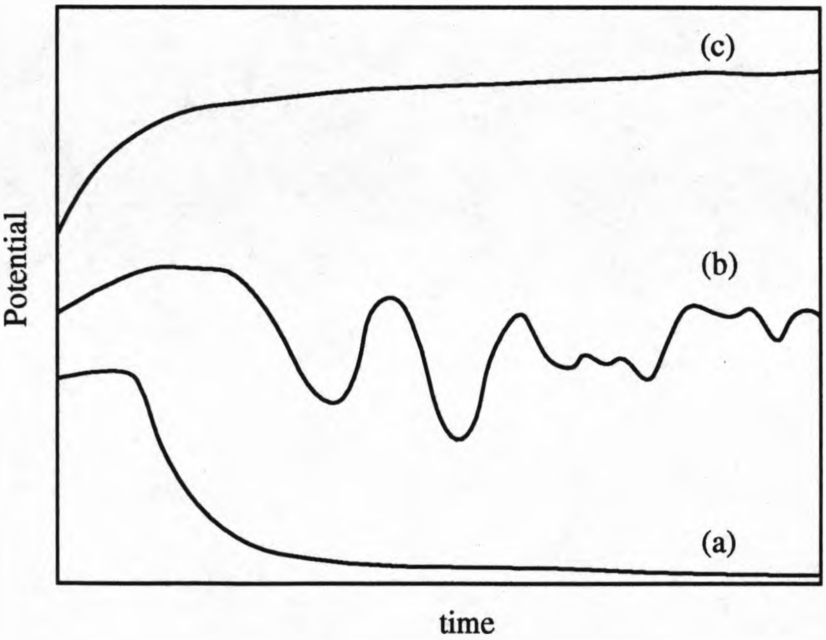

Figure 2.15. Schematic potential versus time curves: (a) general corrosion; (b) pitting corrosion; (c) passive film forms and remains intact (Hoar and Mears, 1966).

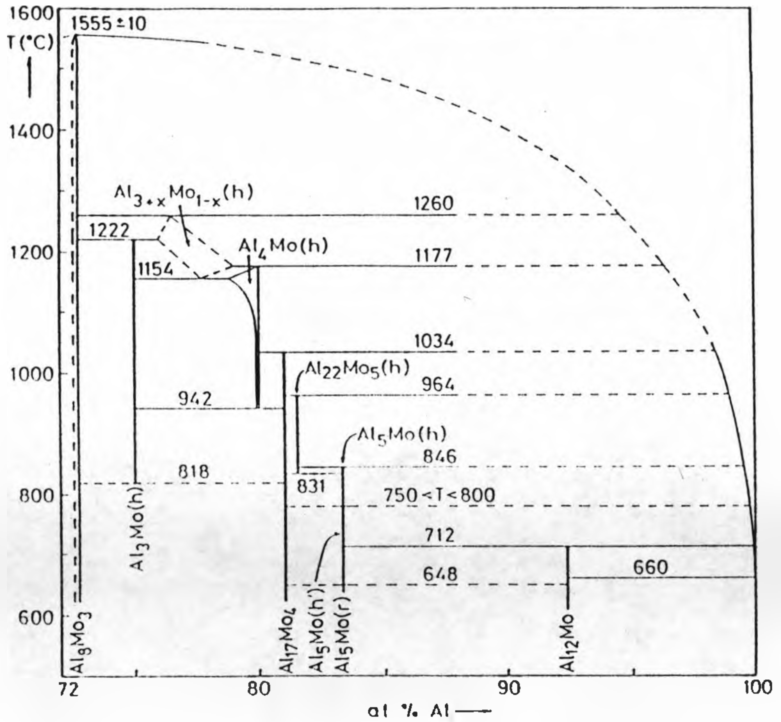

Figure 2.16. Aluminium-molybdenum phase diagram (Schuster and Ipser, 1991).

	Metal-metal ion equilibrium (unit activity)	Electrode potential vs. normal hydrogen electrode at 25°C, volts
↑	Au-Au^{+3}	+1.498
	Pt-Pt^{+2}	+1.2
Noble or	Pd-Pd^{+2}	+0.987
cathodic	Ag-Ag^{+}	+0.799
	Hg-Hg$_2^{+2}$	+0.788
	Cu-Cu^{+2}	+0.337
	H$_2$-H^{+}	0.000
	Pb-Pb^{+2}	−0.126
	Sn-Sn^{+2}	−0.136
	Ni-Ni^{+2}	−0.250
	Co-Co^{+2}	−0.277
	Cd-Cd^{+2}	−0.403
	Fe-Fe^{+2}	−0.440
	Cr-Cr^{+3}	−0.744
	Zn-Zn^{+2}	−0.763
Active or	Al-Al^{+3}	−1.662
anodic	Mg-Mg^{+2}	−2.363
	Na-Na^{+}	−2.714
↓	K-K^{+}	−2.925

Table 2.1. Standard emf series for some pure metals (Fontana, 1987).

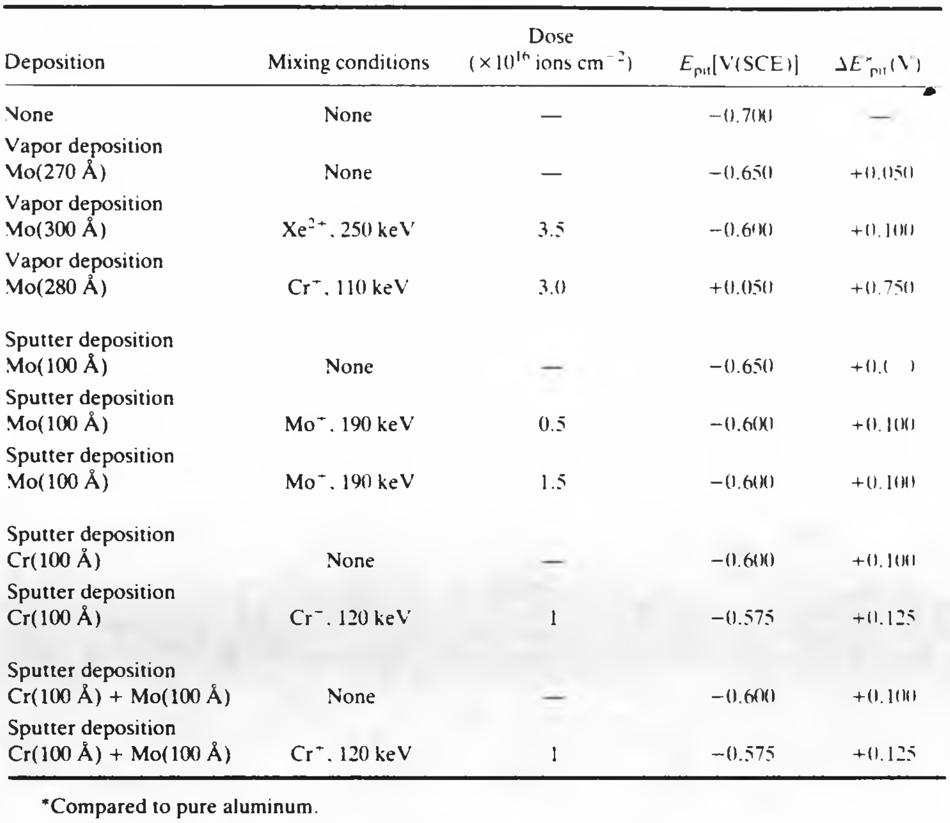

Deposition	Mixing conditions	Dose ($\times 10^{16}$ ions cm^{-2})	E_{pit}[V(SCE)]	ΔE^{*}_{pit}(V)
None	None	—	−0.700	—
Vapor deposition Mo(270 Å)	None	—	−0.650	+0.050
Vapor deposition Mo(300 Å)	Xe^{2+}, 250 keV	3.5	−0.600	+0.100
Vapor deposition Mo(280 Å)	Cr^{+}, 110 keV	3.0	+0.050	+0.750
Sputter deposition Mo(100 Å)	None	—	−0.650	+0.0[illegible]
Sputter deposition Mo(100 Å)	Mo^{+}, 190 keV	0.5	−0.600	+0.100
Sputter deposition Mo(100 Å)	Mo^{+}, 190 keV	1.5	−0.600	+0.100
Sputter deposition Cr(100 Å)	None	—	−0.600	+0.100
Sputter deposition Cr(100 Å)	Cr^{+}, 120 keV	1	−0.575	+0.125
Sputter deposition Cr(100 Å) + Mo(100 Å)	None	—	−0.600	+0.100
Sputter deposition Cr(100 Å) + Mo(100 Å)	Cr^{+}, 120 keV	1	−0.575	+0.125

*Compared to pure aluminum.

Table 2.2. Summary of the results of McCafferty et al (1993); ion beam mixing conditions and anodic pitting potentials in 0.1 M NaCl.

3. EXPERIMENTAL PROCEDURES

3.1. MATERIALS

3.1.1. Substrate Alloys

Two aluminium alloys, 2014 and 7075, have been used as substrate materials in this investigation. These were supplied by Apollo Metals (UK) Limited. The composition in weight percent and heat treatment conditions of the as received alloys are shown in Table 3.1.

Table 3.1. Composition of the substrate alloys (Wt.%).

Alloy	Treatment	Al	Cu	Mg	Zn	Si	Fe	Mn	Cr	Ti
2014	T651	Bal.	4.65	0.54	0.113	0.755	0.119	0.624	0.003	0.012
7075	T6	Bal.	1.63	2.65	5.91	0.04	0.17	0.03	0.2	0.03

3.1.2. Metal Powders

Metal powders were used for some of the laser surface alloying experiments (see section 3.2.2.). Pure Al and Mo powders were obtained from William Roland Ltd. The powders were stored in a desiccator in order to minimise the absorption of water from the atmosphere.

3.2. LASER PROCESSING

3.2.1. Laser Surface Melting

Laser surface melting (LSM) was carried out using an Electrox 2 kW CO_2 laser. This is a fast axial flow laser with four discharge tubes. A CO_2: N: He gas mixture in the ratio 0.8: 1: 7 with a flow rate of 20 - 40 l/min was used. The output radiation of the CO_2 laser had a wavelength of 10.6 µm.

Prior to laser melting with the CO_2 laser the surface of the alloys had to be pretreated to increase the absorptivity of the aluminium surface. Various treatments were investigated including painting, inking and grinding but the most successful were immersing in a 1M NaOH solution or by coating with carbon soot. A 150 mm focal length ZnS lens was used focus the laser onto the work piece. The laser was operated at an output power giving approximately 1.5 kW. The laser beam was stationary which meant that a computer controlled CNC table had to be used to move the specimen through the beam, all further mention of laser scan velocity refers to this method. The laser was scanned across the surface at different heights above the specimen, between ~ 5 - 15 mm below the focus to avoid plasma formation. The maximum spot size was thus ~ 1 mm. The laser scanning speed, denoted by V_s in this work, was varied between 2 mm/s and 500 mm/s, the maximum speed of the x - y table. Thus, the effect on the melt depth and melt width, and the occurrence of porosity were investigated. Argon gas was used to shroud the melt pool to prevent excessive oxidation of the melted layer. A water cooling system was used to prevent excessive heat from building up in the substrate. A schematic diagram of the laser work station is shown in Figure 3.1.

3.2.2. Laser Surface Alloying

In attempts to find the best procedure for alloying Mo into both the 2014 and 7075 alloy substrates two separate coating strategies were investigated. The first method involved alloying with preplaced metal powders and the second with plasma sprayed coatings. The preplaced powder technique is described below. However, for the subsequent characterisation work only the surface alloys produced by the plasma sprayed coating technique were investigated, and to further simplify the work only the 2014 alloy was used as the starting substrate alloy. This decision was taken because of the difficulty encountered in achieving homogeneous mixing in the laser melt pool, due to the high concentration of Mo in the preplaced powder coatings. Furthermore, preliminary corrosion experiments carried out on these alloys showed that the inhomogeneous surfaces exhibited no resistance to attack in chloride electrolytes.

3.2.2.1. Preplaced powder technique

The powders were placed on the substrate alloys in separate layers as illustrated schematically in Figure 3.2. The aluminium alloy substrates were pretreated with a fixing spray and then the Mo powder was sprinkled onto the surface. This first layer was compacted for a day under a heavy load and then the process was repeated for the Al powder. After a second day under a heavy load the substrates were heated at 100°C to 'burn off' the excess adhesive. The double layer thus consisted of approximately 50 % by volume of Mo and Al.

During laser surface alloying argon gas was continuously used to shroud the melt pool to prevent oxidation. The laser scan velocity was varied between 15 and 50 mm/s for a constant overlap of 0.4 mm, and the overlap was varied between 0.2 and 0.6 mm for a constant laser scan velocity of 20 mm/s. The focussing distance was adjusted so that the laser spot size was between ~ 0.8 and 1.5 mm. In some cases the surface alloys were rescanned to attempt to improve mixing.

3.2.2.2. Plasma sprayed coating technique

Coatings for surface alloying were produced by Plasma Technics Ltd. on the aluminium alloy substrates. Initially attempts were made to laser surface alloy with three different plasma sprayed coatings; pure Mo, 75 wt.% Mo- 25 wt.% Al, and 25 wt.% Mo- 75 wt.% Al. However, it was found that it was not possible to produce surface alloys with the first two plasma sprayed coatings, pure Mo and 75 wt.% Mo- 25 wt.% Al respectively, because the aluminium in the substrate boiled before the Mo in the coating layer melted. For this reason the subsequent work, for which the results are presented later, involved laser surface alloying with a 25 wt.% Mo- 75 wt.% Al plasma sprayed coating layer only. The substrates were laser surface alloyed using laser scan velocities of 20, 50 and 70 mm/s operating under the same conditions as in surface melting. Again some of the surfaces were rescanned to try to increase the homogeneity of the surface layer.

3.3. CORROSION ANALYSIS OF ALUMINIUM ALLOYS

3.3.1. Specimen Preparation

A wire was inserted into a hole in the back of sectioned samples of each of the alloys as illustrated in Figure 3.3, these were then mounted in Scaniplast cold setting resin. Up to two hours before testing the samples were first abraded to 1200 grit SiC paper, washed with soap, rinsed with distilled water and dried with hot air. The areas chosen for testing, between 0.4 and 1.5 cm^2, were marked out using either Lacomit or Alcomit varnish.

3.3.2. Test Electrolytes

The chloride electrolytes used for testing were made from distilled water and either GPR or AnalaR grade NaCl and KCl. The concentration of the electrolytes used were 0.1, 0.5 and 1 molar solutions, and 3 % NaCl pH 8. During testing the electrolyte was maintained at a temperature of 30 °C by means of a thermostatically controlled water bath. Some of the tests involved using deaerated solutions, which were obtained by passing pure nitrogen through the electrolytes for at least two hours prior to testing. During the tests the cells were sealed to prevent the ingress of air.

3.3.3. Electrochemical Measurements

Resistance to pitting was measured in both the as received and laser processed conditions using a three electrode cell arrangement; see Figure 3.4. Potentiodynamic and potentiostatic polarization measurements were carried out in accordance with

ASTM G5-69. A Thompson Electrochem Ltd. Autostat or a Sycopel Scientific Ltd. Autostat was used. Both autostats were run under computer control. Potentiodynamic anodic pitting scans were usually run from 0 mV to 1000 mV at a scan rate of 10 mV/min. Scan rates of 30 and 100 mV/min were also used in the preliminary tests in the 3 % NaCl pH 8 solution. However, it was found that increasing the scan rate decreased the corrosion resistance, especially at the track/track interfaces. Subsequently, the majority of the work was carried out using the slower scan rate of 10 mV/min. The upper potential limit of the scan was on occasion lower than 1000 mV so as to obtain a better resolution at potentials near to the pitting potential. Prior to starting the tests the free corrosion potential (E_{corr}) was monitored in the test electrolyte for half an hour. Potentials were measured against a saturated calomel electrode (SCE) and a platinised titanium rod was used as the auxiliary electrode.

3.3.4. Free Corrosion Experiments

Measurements of free corrosion potentials versus time in accordance with ASTM G-69 were obtained using a CIL A to D converter, multiple channel data logging card fitted to an Amstrad 3086 personal computer. This was carried out to investigate the type of corrosion as proposed by Hoar and Mears (1966); described in the literature in section 2.6.2.1. Logging was carried out for time periods of 150 hours and in excess of 300 hours (2 weeks). A 1 molar NaCl solution was used for each of the immersion tests and the temperature was kept at 30 °C by using a thermostatically controlled water bath.

3.4. METALLOGRAPHIC EXAMINATION

Surface samples and cross-sections were examined by optical microscopy and in a Philips 501 SEM. Micrographs were taken on the SEM using either a 35 mm camera attachment or by Polaroid self-developing film. Further detailed microstructural and compositional examinations were carried out on a Philips EM400 TEM, a JEOL 2000FX TEM with Scanning mode attachment, a VG Scientific Scanning Auger microscope with x-ray photoelectron spectroscopy (XPS), JEOL JXA-50A electron probe microanalyser, and a computer controlled McLean diffractometer.

3.4.1. Specimen Preparation

3.4.1.1. Preparation for optical and SEM photomicrography

Samples for photomicrography were sectioned and mounted in black conductive Bakelite. The specimens were ground to a 1200 grit finish before polishing to 1 μm and final polishing using Struers OP-S suspension. Etching was carried out on the freshly polished samples using one of three different solutions.

Etchant 1:	10 g NaOH 100 ml distilled water
Etchant 2:	10g NaOH 10g $KMnO_4$ 100 ml distilled water
Etchant 3: (Keller's etch)	1.5 ml HCl 2.5 ml HNO_3 1 ml HF 95 ml distilled water

In order to improve the etch, on occasion the samples were slightly warmed and prewetted using warm water.

3.4.1.2. Preparation of TEM specimens

(i) Surface sectioned specimens

3 mm discs were trepanned from thin surface sections of both as received and surface

treated samples by spark erosion, see Figure 3.5. Initial thinning was achieved by grinding with 1200 grit SiC paper. The final thin area was achieved by either electropolishing, with one of two electrolytes, using a Struers Tenupol or by ion beam thinning using a Gatan ion mill.

Thinning solution 1:	70% Methyl alcohol 30% Conc. Nitric acid Cooled with Liq. nitrogen to -20 °C, 40 V.
Thinning solution 2:	20% Perchloric acid 80% Ethanol Water cooled, 10V- 30V.

The thinned samples were washed in ethanol and air dried.

(ii) Cross sectioned specimens

The laser treated surfaces were sliced away from the substrate, at a depth of no more then 1.5 mm, using a diamond wafering blade, and then cut in half. The two half sections were then glued together so that the top laser treated surface of each was adjacent to the other and in the same orientation, and so that the cross section thickness was < 3 mm, see Figure 3.6 (a). The glue used for this was Araldite that had also been mixed with SiC to make it more resistant to the ion beam used for thinning the specimens. The glue was also heated slightly to make it flow better and to increase the adhesion between the two sections; heating also decreased the setting time. A thin piece of glass slide was then glued to one of the transverse cross section ends of the small block (see Figure 3.6 (b)). A thin slice (~1.5 mm thick) was then cut through the cross section; the glass prevented the two individual pieces from separating during this procedure. (Araldite was used in the above steps because it is insoluble in acetone). The glass slide was then glued, using an adhesive which was soluble in acetone such as Superglue, to a larger block of alloy and the thin cross section was polished so that it was less than 1 mm thick (Figure 3.6 (c)). The glass slide was then loosened using acetone and reglued to the alloy block on the side with the specimen on. The glass slide was then carefully ground away, leaving only the specimen on the polishing block. The cross section specimen was then further polished down so that the thickness was less than 50 µm. Small squares (~2 mm x 2 mm) were then cut from the cross section and glued to a copper TEM grid (Figure 3.6 (d)). The final thin area was achieved either by electropolishing as described previously followed by ion beam thinning using a Gatan ion beam mill or just by repeated ion beam thinning.

3.4.1.3. Preparation for X-ray photoelectron spectroscopy (XPS)

A square approximately 8 mm x 8 mm and < 1 mm thick was cut from the surface of each of the specimens using a diamond cut-off wheel. In most cases the surfaces were polished to 1200 grit or better except when the as-laser processed surface was to be analysed. In all cases the samples were cleaned, firstly in acetone and then rinsed in distilled water and dried by hot air. The surfaces to be examined were either allowed to oxidise naturally in air or were polarised in 1M NaCl. After polarisation the specimens were rinsed in distilled water and dried by hot air. Typically the time elapsed between polarising the specimens and insertion into the microscope was 10 minutes. The effect of NaOH on the oxide of the as received material was also investigated. Prior to immersion the specimens were prepared in the same way as the naturally oxidised specimens and after immersion rinsed in distilled water and hot air dried. The specimens oxidised in air and in the NaOH were stored in sealed plastic bags inside a desiccator prior to examination.

3.4.2. Analysis of Microstructure and Composition

3.4.2.1. Transmission electron microscopy

The structures of the phases present in the laser treated materials were studied using TEM techniques. A Philips EM400 and JEOL 2000FX were used to obtain transmission electron micrographs and selected area electron diffraction (SAD) patterns from the materials. It was possible to take dark field electron micrographs by centring a diffracted beam and choosing an objective aperture so that the illumination came from only the selected beam. The composition was measured by energy dispersive X-ray (EDX) microanalysis in the STEM mode on the JEOL 2000FX using Link System software. A windowless detector was used and Al was chosen as the standard. Each analysis was carried out for 100 s and the dead time was not allowed to exceed 15%. X-ray element mapping was also performed by setting energy windows corresponding to the peak energies of the elements of interest.

3.4.2.2. Compositional analysis using the electron microprobe

The JEOL JXA-50A electron microprobe was used to carry out quantitative compositional analysis by both EDX and wavelength dispersive spectroscopy (WDS). In the case of the EDX a Co standard was used for calibration and Link Analytical QX200 data analysis software was used to calculate the composition. Each analysis was carried out for 100s with the dead time kept below 15%. For a greater level of accuracy WDS measurements were carried out. Pure standards were used for each of the elements concerned. The counts were collected for 100 seconds at the maximum pulse height position and at +0.5° and -0.5° background positions for each of the elements concerned and their standards. The X-ray intensity ratios or K values were obtained from the count data for each of the elements and used to calculate the respective weight percentages. The ZAF correction programme used was a version of the Frame 3 programme described in NBS Technical Note 796. X-ray element maps were also obtained on the JEOL JXA-50A electron microprobe by WDS.

3.4.2.3. X-ray diffractometry

Phase analysis was carried out from X-ray spectra obtained using a McLean diffractometer. A voltage of 40 kV and a current of 35 mA was used to produce monochromatic Cu X-rays ($\lambda = 1.5405$ A). The incident beam was focussed using a solar slit collimator and 2° front slit to give an area of ~1 cm^2 in the plane of the sample surface. A Ni foil was used to filter the diffracted beam to eliminate Kβ radiation. Computer software running on a Philips P 3302 personal computer was used to drive the diffractometer and to collect and plot the X-ray diffraction data from the scans. The general scans were carried out at diffraction angles of between 15° and 150° 2θ with a step size of 0.03° and for 2 sec/step. The time at each step was increased for more detailed scans at specific ranges of 2θ. Where possible the peaks were indexed by comparison with the data from powder diffraction files.

3.4.2.4. Scanning Auger microscopy and XPS

A VG Scientific scanning Auger electron microscope was used to carry out surface analysis. The incident beam consisted of Al X-rays (λ = 8.339 A) operating at 15 kV and 20 mA. A Pass Energy (PE) of 100 eV was used for general scans between Binding Energies (BE) of 1300 eV and 0 eV with a step size of 1 eV. For scans of the individual elements PE = 10 - 20 eV, the step size was 0.05 - 0.1 eV and a minimum of 30 scans were collected for each analysis; in some cases 60 scans were collected to enable clear resolution of the peak position. In all cases the dwell time of each step was 200 ms.

3.5. HARDNESS AND RESIDUAL STRESS MEASUREMENTS

The mechanical properties of the materials were investigated indirectly by carrying out microhardness measurements and residual stress measurements. This was carried out so that the effect of residual stress on the corrosion properties could be investigated.

3.5.1. Microhardness Measurements

A Leitz Wetzlar diamond indentation machine was used to measure the microhardness of the samples. Hardness vs depth profiles were carried out on polished x-sections. All measurements were made using a 50 g load.

3.5.2. Residual Stress Measurements

A McLean Diffractometer was used to carry out multi-exposure X-ray diffractometry in order to calculate the residual stresses in the as laser processed surface layers, as described in the SAE technical report J784a. The background to this technique is described in Appendix A. The diffracted (422) aluminium peak at $2\theta = 138°$ was used for the measurements. The (422) plane was chosen because it was the plane with the smallest planar spacing that was within the maximum range of 2θ of the machine. A small planar spacing was needed so that any changes were easily detected. The range of the scans was from $2\theta = 135°$ to $2\theta = 141°$ in increments of 0.03° and at count intervals of between 4 - 30 seconds.

First of all a scan was carried out with the specimen in the normal orientation, $\psi = 0$, see also Figure 3.7. Next, the specimen orientation was changed so that $\psi = \psi_1$, where $\psi_1 = 45°$ in most cases, and a second scan was performed. The shift in the 2θ value of the (422) peak between the two specimen orientations, $\Delta 2\theta$, was used to calculate the residual stress, σ_ϕ, using Equations 3.1 to 3.3 below:

$$\sigma_\phi = \frac{\Delta 2\theta \cdot E \cdot \cot\theta}{2(1+\upsilon)\sin^2\psi} \tag{3.1}$$

or

$$\sigma_\phi = K_1 \Delta 2\theta \tag{3.2}$$

where

$$K_1 = \frac{E\cot\theta}{(1+\upsilon)} \cdot \frac{\pi}{180} \quad \text{when} \quad \psi = 45° \tag{3.3}$$

and E = Young's modulus and υ = Poisson's ration.

When ψ was not equal to zero the detector needed to be refocussed so that the diffracted X-rays were collimated correctly. In order to do this the detector had to be moved in the radial direction by a distance D given by Equation 3.4, see also Figure 3.7.

$$\frac{D}{R} = 1 - \frac{\cos[\psi + (90 - \theta)]}{\cos[\psi - (90 - \theta)]} \tag{3.4}$$

Where R= the distance from the specimen to the X-ray source (S). Values of D are shown in Table 3.2.

Depth profiles of the residual stresses were obtained qualitatively by measuring the diffraction angle for different specimen orientations, ψ = 10, 20, 30, 40, 50, and 60, and the results of these measurements were plotted on a graph of 2θ versus $\sin^2\psi$. A quantitative depth profile was also obtained by calculating the residual stress after successive layer removal by electropolishing. Layers of between 20 - 60 μm were removed at each step until the unaffected substrate alloy was exposed. The solution and conditions used for electropolishing was:

70% Methyl alcohol
30% Conc. Nitric acid
Cooled with Liq. nitrogen, 20 V.

3.5.2.1. Correction to X-ray stress measurements

The measurement of residual stresses by X-ray diffractometry is subject to a large amount of minor errors, such as absorption and Lorentz polarisation, which have been ignored in these procedures. These factors are discussed in detail by Cullity (1978). However, in the depth profile measurements a significant error is introduced due to the removal of material from the surface, which causes stress relaxation. The stress measurements were corrected for stress relaxation due to layer removal using the following equations from the SAE technical report J784a, see also Figure 3.8:

$$\sigma(z_1) = \sigma_m(z_1) + c(z_1) \tag{3.5}$$

and

$$c(z_1) = -4\sigma_m(H)\frac{\Delta z_1}{H} \tag{3.6}$$

where

$\sigma(z_1)$ = the true stress

$\sigma_m(z_1)$ = the measured stress

$c(z_1)$ = the value of stress correction

$\sigma_m(H)$ = the true surface stress

Δz_1 = the thickness of the removed layer

H = the original substrate thickness.

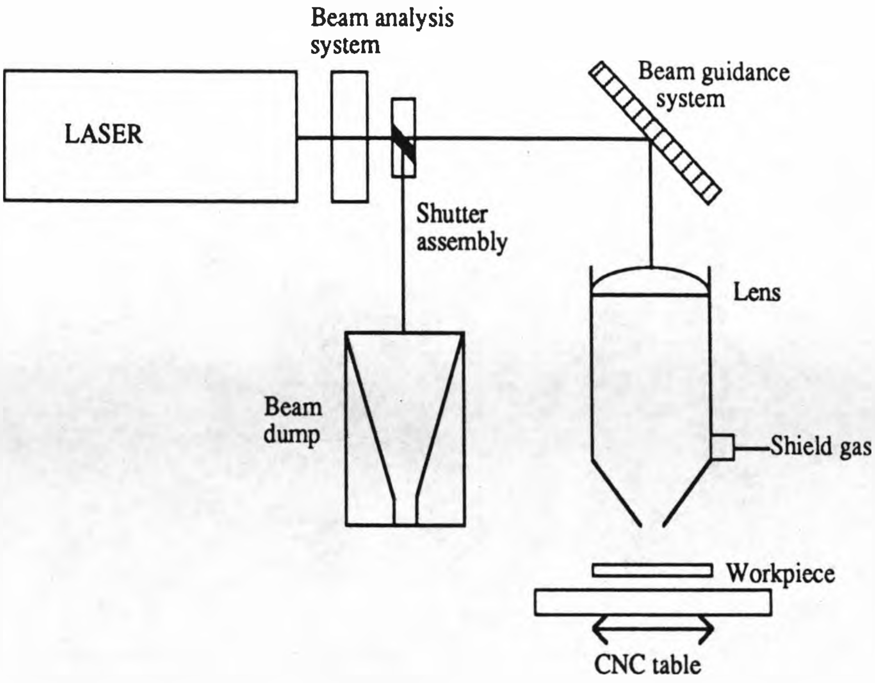

Figure 3.1. Schematic diagram of the laser work station

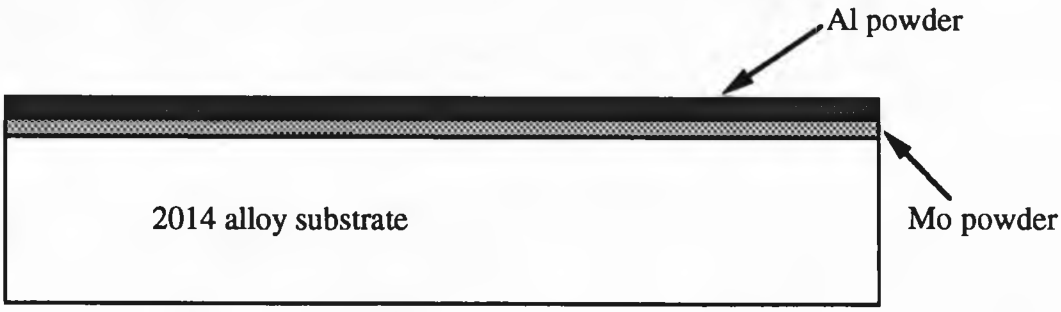

Figure 3.2. Schematic representation of preplaced powder technique. 1. Mo powder affixed with spray adhesive and compacted for 24 hrs. 2. Al powder placed on top of Mo powder and compacted for 24 hrs. 3. Heated at 100 °C for 1 hr. 4. Laser surface alloyed with CO_2 laser.

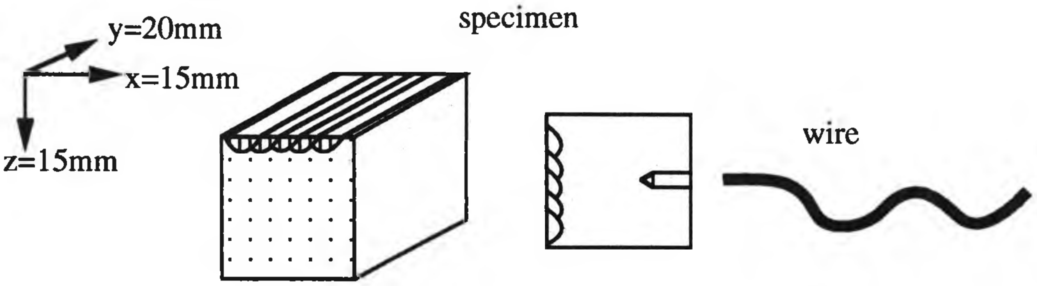

Figure 3.3. Specimen preparation prior to being set in cold setting resin for corrosion test samples. Axes show the approximate size of each sample.

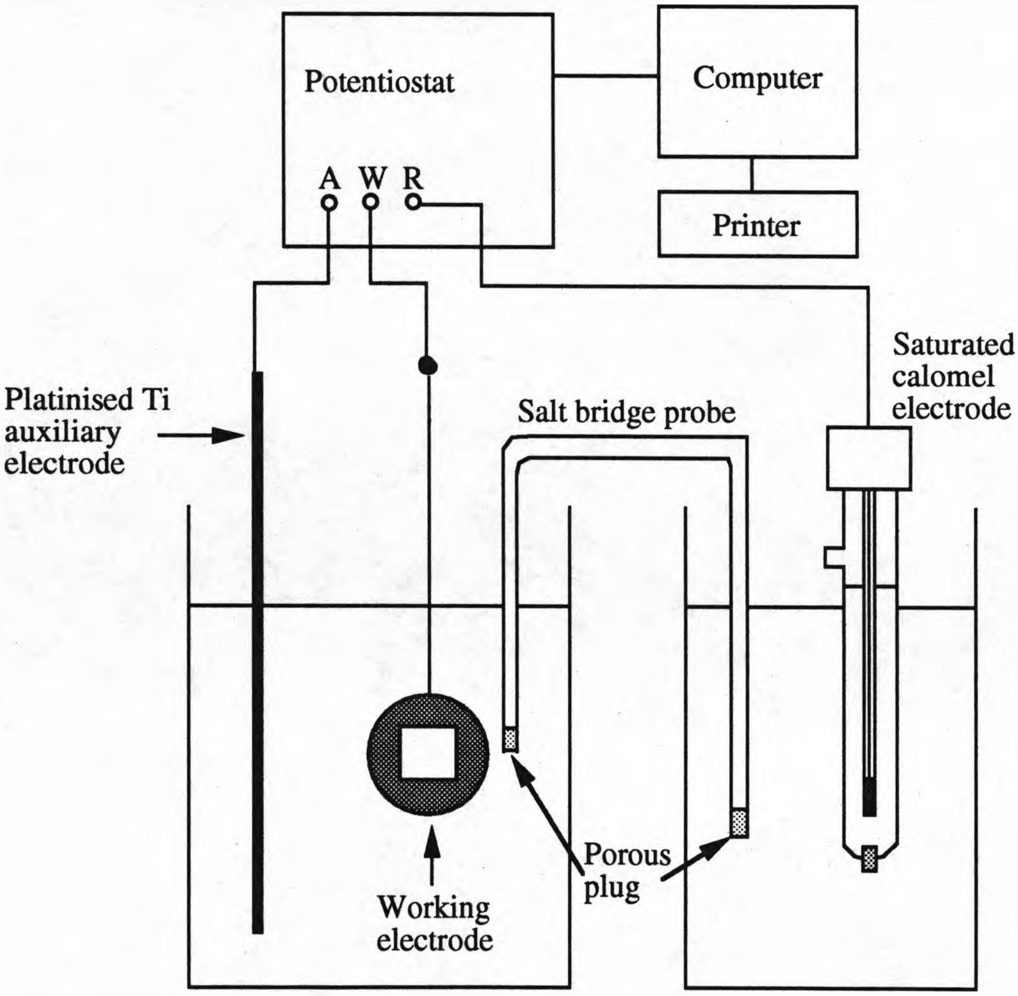

Figure 3.4. Schematic diagram of the three electrode cell arrangement used to obtain anodic polarization curves.

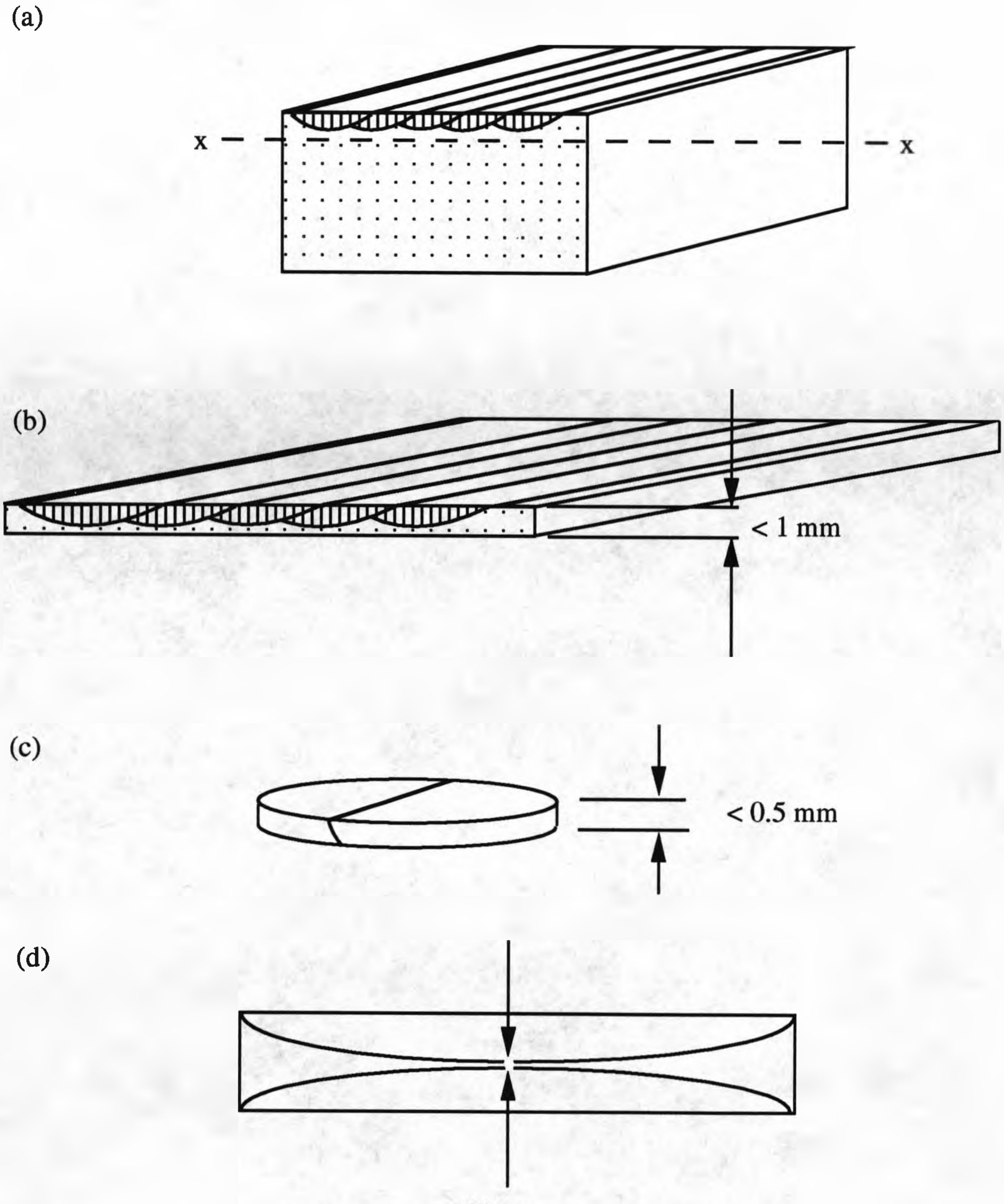

Figure 3.5. Preparation of TEM specimens from an xy section of laser processed surface. (a) Layer removed by wire spark erosion; (b) polished to less than 1mm in thickness; (c) disc trepanned by either spark erosion or mechanical stamping; (d) disc polished and final thin area achieved by electrolytic thinning.

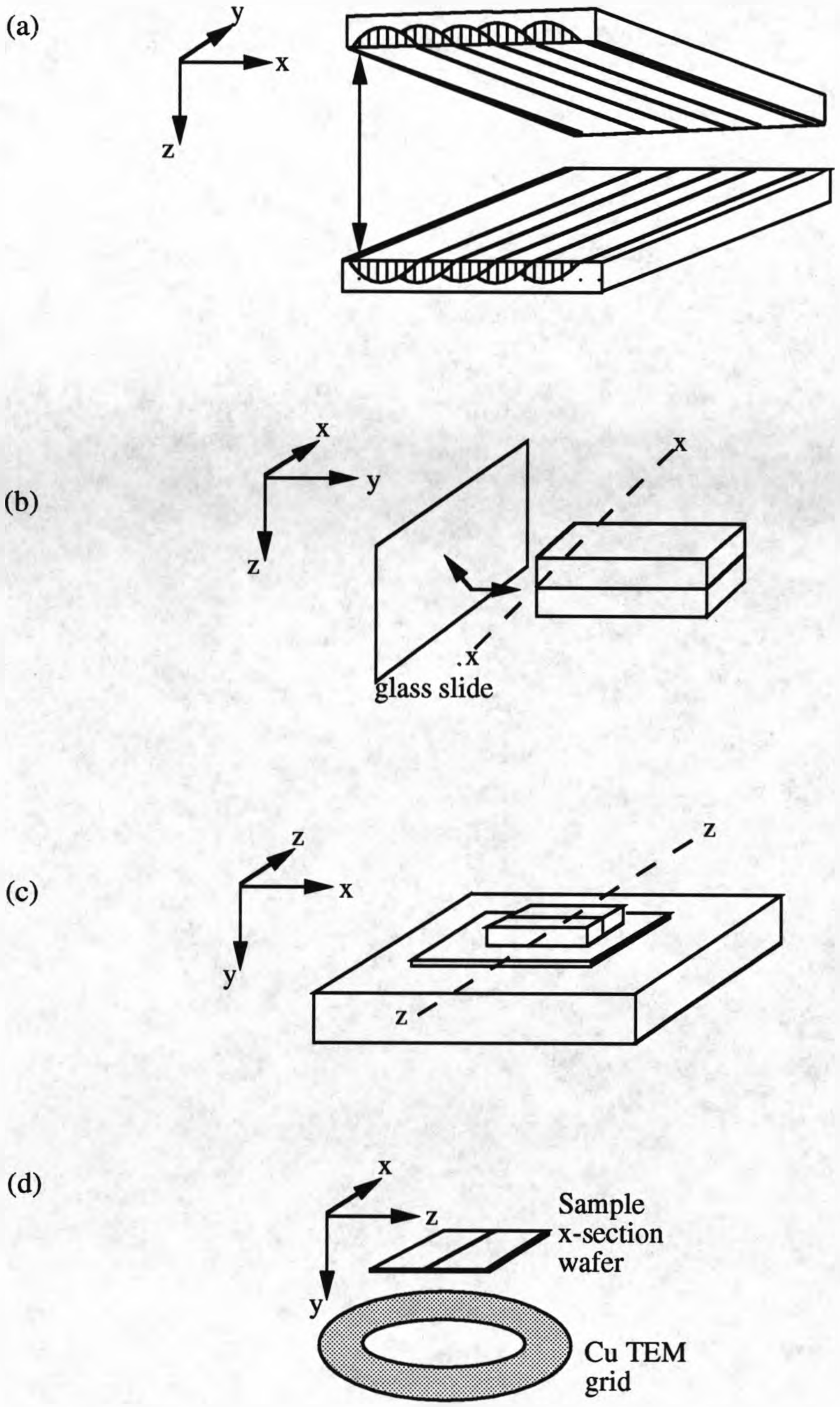

Figure 3.6. Preparation of TEM cross section samples. (a) Two surface layer sections are glued together; (b) a glass slide is glued to one end and then an end section is cut; (c) the glass slide is glued to a larger block and the end section is polished to < 100 μm, repeat (c) on the reverse side to remove the glass and further polish to ~ 50 μm; (d) glue the wafer cross section sample to Cu TEM grid and carry out final thinning by ion beam milling.

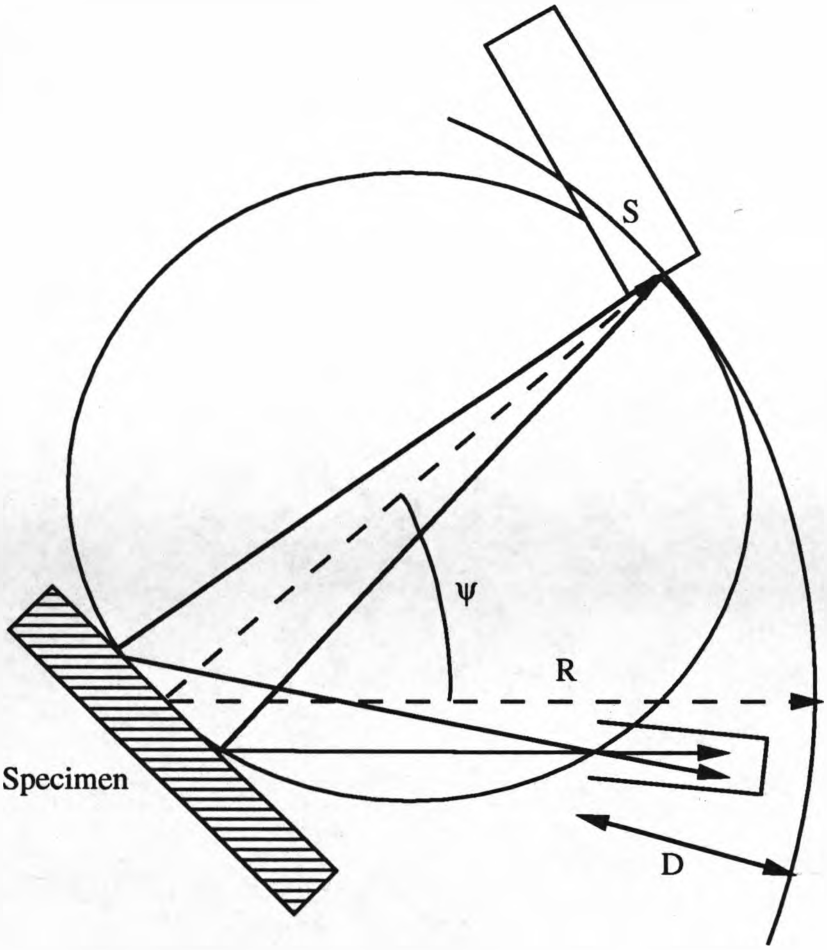

Figure 3.7. Schematic diagram of experimental setup for carrying out residual stress measurements by X-ray diffraction

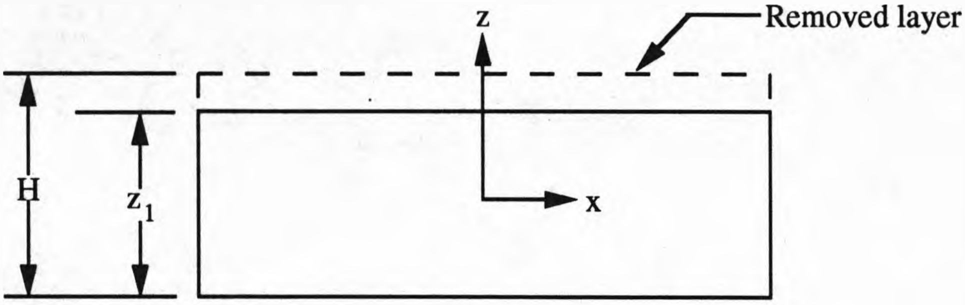

Figure 3.8. Illustration of layer removal in depth profile X-ray diffraction stress measurements

Specimen Orientation, Ψ (deg.)	Focussing Distance, D (mm)
10	28.25
20	54.58
30	80.71
40	108.29
45	121.13
50	139.39
60	177.14

Table 3.2. Diffractometer focussing distances for X-ray stress measurements; D calculated from Equation 3.4, where $R = 220$ mm and $\theta = 69$ deg.

4. RESULTS OF LASER SURFACE MELTING

Experimental results obtained using the procedures described in the previous chapter are presented here for both the aluminium alloys. This chapter has been divided into three general categories. The first category, microstructure and solidification, includes characterisation of the solidification microstructure, quantitative analysis of the composition, and identification of the major phases. The next category, corrosion, includes results from potentiodynamic anodic polarization and potential versus time measurements, and analysis of the surface oxides. The last category, mechanical properties, includes results from hardness tests and residual stress measurements.

4.1. MICROSTRUCTURE AND SOLIDIFICATION

4.1.1. General Characteristics

4.1.1.1. Melt depth

Laser surface melting caused very localised heating of the substrate so that the maximum depth of the melt pool was of the order of a few hundred microns. The actual dimensions of the melt pool depended on the surface pretreatments, laser power, and the laser scanning velocity and the results are shown in Figures 4.1 and 4.2. In general the higher the heat absorption of the surface (for example after blackening with graphite paint) coupled with slower scanning velocities resulted in increased melted depths. However, painting with graphite and deposition of carbon soot resulted in uneven melting due to non-uniform coatings. Unless stated otherwise, all subsequent results are presented for laser surface melting where immersion in NaOH solution was used as the surface pretreatment.

4.1.1.2. Porosity within the melted layer

Pores were found in some of the samples, most commonly when area coverage was achieved by overlapping laser melt tracks. However, porosity was less of a problem in the 7075 alloy. The pores were spherical, varied in size, and were concentrated at the fusion boundary of each laser melt track; this can be seen in Figure 4.3. It was found that there was a critical laser scanning velocity above which the majority of the porosity was eliminated. For both of the aluminium alloys this velocity was about 12 mm/s so that at a scanning velocity of 15 mm/s in general there was no porosity.

4.1.2. 2014 Aluminium Alloy

In the as received T651 (peak aged) condition the microstructure consisted of elongated grains orientated in the rolling direction as illustrated by the optical micrograph in Figure 4.4. The principal age hardening precipitate formed during the T6 heat treatment is θ'- ($CuAl_2$) and appears as the short fine lines in the TEM micrograph in Figure 4.5. The results in this section relate to this structure and the modifications brought about by laser surface melting, in particular the redistribution of the alloying elements.

4.1.2.1. Solidification structure of the melted layer

After laser surface melting (LSM) the microstructure consisted of columnar grains that had grown epitaxially from the unmelted substrate alloy as is shown in the optical micrograph in Figure 4.6. At the fusion boundary there was a very small region of planar front solidification which is illustrated in Figure 4.7. The conditions for planar front solidification only existed for a very short time so that the width was only 3-5 μm. After the short period of planar front solidification columnar grains started to grow with a cellular dendritic substructure which is shown in the TEM micrograph in Figure 4.8. The cellular dendrites grew in the general direction of heat flow causing the grains to grow towards the top and centre of the melt pool. This meant that the grains grew into each other which is referred to as competitive growth. Near to the surface the orientation of the grains tended to be in the x-y plane but growth was still towards the centre of the melt pool as shown in Figure 4.9. From the relationship between cell spacing and cooling rate given in Equation 2.8 it is shown in Figure 4.10 that the cooling rate, given by the measured cell spacings at the maximum melt depths, increased from 2 x 10^6 K/s to nearly 7 x 10^6 K/s as the laser scan velocity was increased from 20 mm/s to 400 mm/s. Figure 4.11 shows that as the cooling rate increased with decreasing melt depth the microstructure became finer.

Figure 4.8 also indicates that there was no precipitation in the α-Al (lighter regions) which means that the majority of the alloying additions must have been segregated to the interdendritic phase (dark regions). The interdendritic region did not seem to consist of a single continuous phase. Selected area diffraction indicated the presence of individual particles that were orientated slightly differently from each other. This is illustrated by Figure 4.12, but the individual particles could not be resolved visually in either bright field or dark field transmission. As well as the segregation to cell boundaries there was also a large amount of segregation of alloying elements to grain boundaries which is evident in Figure 4.6.

When the laser scanning velocity was less than 120 mm/s a banded structure was observed in the microstructure. This can also be seen in Figure 4.6. The bands form almost concentric arcs in the resolidified layer and appear as faint dark contours in Figure 4.6. The cell spacings of the dendrites occurring immediately before and after a band were not the same. The width of the dendrites preceding a banded structure was slightly less than that of the dendrites that formed immediately after the band. The structure of a typical band is shown in Figure 4.13. It is shown that the bands were very narrow and the cell spacing inside them seemed to be slightly coarser than either the cells before or after. The actual structure of the cells tended to resemble that of the first cells that formed adjacent to the planar front region at the start of solidification. At scanning velocities greater than 120 mm/s the banding structure was not observed and the cellular structure within the columnar grains was very fine with little variation in the cell spacing from the start to finish of the individual grains.

Where area coverage was achieved by multiple overlapping laser melt tracks the cellular dendritic structure was partially transformed within the region that corresponded to the heat affected zone (HAZ) caused by the overlapping melt track. The transformation caused the formation of blocky particles of θ phase within the grains adjacent to the new fusion zone (Figure 4.14 (b)). The corresponding grain boundaries were also thicker than the grain boundaries in the unaffected melt zone.

The grains in the HAZ of the substrate forming part of the fusion boundary region (FBR) contained coarsened θ ($CuAl_2$) precipitates, as shown in Figure 4.15, and solute enriched grain boundaries that had a large precipitate free zone (PFZ) around them (Figure 4.16). Both these effects were caused by solute diffusion, at the expense of the θ´ and θ´´, during the heat cycle in the HAZ. In addition, partial melting of the large $CuAl_2$ particles in the HAZ and the subsequent resolidification resulted in the formation of eutectic "Chinese script" type structures, shown in Figure 4.17. If the particles resolidified on or immediately adjacent to the fusion line then they seemed to assist the formation of the cellular dendritic structure without any prior planar front solidification taking place. The actual size of the HAZ was very small, less than 100 µm, thus indicating that the heating during melting was very localised and existed for very short periods of time.

4.1.2.2. Compositional analysis of the melted layer

The composition throughout the melted layer was not uniform but instead showed a dependence on the structure so that variations occurred across the fusion zone and the bands. A composition profile across the fusion zone, measured by WDS using an electron microprobe, is given in Figure 4.18. In the unmelted substrate the concentrations remain fairly constant and close to the equilibrium values. The kink in the lines for Cu and Si at about 20 µm corresponded to a grain boundary in the HAZ. The next change in composition occurred at the fusion line where the sudden decrease in Cu concentration to ~2.5 wt.% marked the onset of planar front solidification. After only a few microns the Cu concentration increased sharply marking the end of planar front solidification and the start of cellular dendritic growth. An X-ray map for Cu across the planar front region is shown in Figure 4.19. This clearly shows that the concentration of Cu increases at the end of the planar front growth. Subsequent increases and decreases in composition were caused by the banded structure with the maximum Cu contents detected at the bands. This point is better illustrated in Figure 4.20 where it can be seen that in places where the line marking out the profile intersects a band (Figure 4.20 (a)) there is a corresponding peak in the composition profile for Cu (Figure 4.20 (b)).

As mentioned above the composition profiles were taken using an electron microprobe but the minimum effective area of the probe was ~2 μm which was larger than most of the important features of the melt zone. In order to have better resolution EDX analysis using STEM was carried out. A composition profile across a cellular dendrite is shown in Figure 4.21. From this it is possible to see that the Cu in solid solution in the α-Al was below the solubility limit (5.7 wt.%) and so did not form a supersaturated solid solution. The Mg and Zn concentrations in the α-Al were both close to the alloy equilibrium concentrations but Si was not detected in the α-Al. The concentration of all the alloying elements increased in the interdendritic phase but it was the Cu concentration that showed the most dramatic change which can also be seen from the X-ray maps presented in Figure 4.22. From the peak concentration value for Cu in Figure 4.21 it can be seen that the composition of the interdendritic phase was comparable to that of θ phase (33 wt.% Cu). Figure 4.22 shows that the distribution of Mg was very uniform throughout the dendritic microstructure with only very slight increases in the interdendritic region. Si was detected in only very small concentrations and was unevenly distributed in the interdendritic regions.

4.1.2.3. Phase identification

The θ´ ($CuAl_2$) precipitates in the as received 2014 alloy shown in Figure 4.5 were identified in the TEM by electron diffraction techniques and were also detected by X-ray diffraction as indicated in Figure 4.23. The X-ray diffraction data for Al and the $CuAl_2$ phase are summarised in Table 4.1. The other precipitates shown in Figure 4.5 were not detected by X-ray diffraction. The X-ray diffraction profile for the laser surface melted 2014 aluminium alloy is shown in Figure 4.24. Three additional peaks were noticed for the LSM 2014 profile when compared to the untreated alloy. The plane d-spacings and diffraction angles are presented in Table 4.1. Candidate phases with d-spacings that showed a close match with the experimental results are also included in Table 4.1.

4.1.3. 7075 Aluminium Alloy

The subgrain microstructure of the as-received 7075 alloy is illustrated in the TEM micrograph in Figure 4.25. The precipitates seen here have been identified from the literature as η-phase ($MgZn_2$) and possibly β-phase (Mg_2Si). The grains in the bulk alloy were elongated and orientated in the rolling direction which resulted in strong texturing in the (200) plane. The results in this section give an account of the effect of laser surface melting on this structure with a particular reference to the redistribution of alloying elements and the formation of precipitates in the melted layer.

4.1.3.1. Solidification structure of the melted layer

The microstructure of the LSM 7075 alloy was essentially the same as that of the LSM 2014 alloy, see Figure 4.26. Solidification was epitaxial starting with a very narrow region of planar front growth which changed to cellular dendritic in the main body of the melt zone. The cellular dendritic structure is shown in Figure 4.27 and the transformation of the interdendritic phase due to overlapping melt tracks is shown in Figure 4.28. Once again evidence was obtained showing that the interdendritic phase was not a single continuous phase but instead consisted of randomly orientated precipitates located between the cellular dendrites. Figure 4.29 contains SAD patterns from the α-Al only, Figure 4.29 (a), and from the interdendritic region plus the α-Al in Figure 4.29 (b). In both cases the beam direction was [013] and the spots from the Al were clearly identified but in 4.29 (b) there was multiple diffraction coming from the interdendritic phase. Inspection of longitudinal cross-sections also revealed that the cellular dendritic growth stopped before reaching the surface in some regions and at these points clusters of fine precipitates were observed just ahead of the dendrites and the remaining few microns to the surface appeared to be a solid solution. As with the 2014 no precipitation was observed in the as melted layer within the actual α-Al cells.

The way in which the microstructure of the laser melted 7075 alloy differed from that of the 2014 alloy was that there were three features that were observed in the initial structure of only the surface melted 7075 alloy. The first was a form of localised banding within some of the grains in the centre of the melt zone, the second was nanometre sized equiaxed grains that formed at the surface of the melted layer, and the third was the occurrence of star shaped particles frozen randomly into the structure. The SEM micrograph in Figure 4.30 shows the banded structure observed from a longitudinal cross-section of the melted layer on the 7075 alloy. Previously banding was observed in the 2014 alloy for laser scanning velocities below 120 mm/s and was caused by slight variations in the size of the cellular dendrites; this type of macro-banding was also found in the 7075 alloy. However, Figure 4.30 shows that the structure of the new bands did not involve cellular dendritic growth and therefore occurred by a totally different growth mechanism. This new type of micro-banding was only observed in the 7075 aluminium alloy samples melted at scanning velocities greater than 20 mm/s. However, the band morphology became more irregular with increasing scanning velocity. The structure consisted of alternating α-Al (grey areas) and intermetallic layers (lighter areas). The α-Al layers were approximately 3-5 μm in width and appeared to be essentially free of precipitates. The banded structure occurred randomly along the length of the melt tracks but was not observed in any of the transverse cross-sections.

The second feature mentioned above was the presence of nanometre sized equiaxed grains at the surface of the resolidified layer. Figure 4.31 shows a TEM micrograph with the corresponding SAD pattern of a nanocrystalline region from an XY surface section. As illustrated by the diffraction pattern the solidifying grains grew at random orientations to each other. The exact structure of the layer was not identified but the plane spacings calculated from the ring pattern shown in Figure 4.31 are listed in Table

4.2. Analysis of the composition of the grains showed that the concentration of Mg was about 20 - 25 wt.% and that there was a very low Zn concentration. By considering the size of the grains (<100 nm) it was deduced that the cooling rate of the the top layer must have been greater than 10^6 K/s.

The last of the three different structural features found in the laser surface melted 7075 was the occasional appearance of star shaped particles. It is shown in Figure 4.32 (a) that the particles formed by dendritic growth with six primary dendrite arms radiating at 90° to each other. The SAD pattern shown in Figure 4.32 (b) was indexed for a cubic structure observed from the $[\bar{2}55]$ beam direction. The dark field electron micrograph shown in Figure 4.32 (c) was taken using the beam from the (511) reflection from the SAD pattern and shows that the particle was completely illuminated at that orientation. Analysis of the composition showed that the particles were in fact oxides with the formula $MgAl_2O_4$. Comparison of the results from the electron diffraction with X-ray powder diffraction data verified the particles as being the spinel $MgAl_2O_4$.

4.1.3.2. Compositional analysis of the melted layer

The composition of the melted layer differed considerably from that of the unmelted substrate. It was found that after laser surface melting the zinc concentration was much lower than the magnesium concentration. The concentration profiles measured by WDS for magnesium and zinc along a line from the substrate up through the melted layer to the surface are shown graphically in Figure 4.33. The initially high concentrations at the start of the graph corresponded to a partially melted second phase particle in the HAZ of the substrate. The actual melted region started at approximately 40 microns on the graph in Figure 4.33 where there was a sudden drop in composition. The subsequent changes resulting in the small peaks in the graphs between 50 μm and 220 μm were due to the macro-banding in the structure of the melted layer. From a depth of 220 μm to the surface the composition remained steady except for a very slight decrease just below the surface.

The composition across a cellular dendrite in the melted layer was measured by EDX using STEM techniques. The line profiles for Cu, Mg and Zn are shown in Figure 4.34. Where previously the microprobe WDS results indicated a very low concentration of zinc the STEM EDX results show that in the α-Al the concentration of zinc was approximately equal to the specified alloy composition of 5.6 wt.%. The higher concentrations of magnesium recorded by WDS were not apparent from the EDX results which showed that the maximum concentration, which actually corresponded to the interdendritic phase, was only ~8 wt.%. Figure 4.34 also shows that the composition of the interdendritic phase was below that of the equilibrium η precipitate ($MgZn_2$, ~ 85 wt.% Zn) that is found in the as received 7075 aluminium alloy.

4.1.3.3. Natural ageing in the melted layer

There were no precipitates found in the 7075 alloy in the as melted condition that were not part of the interdendritic phase. However, six months after the initial surface melting operation a new structure started to appear in the α-Al and this is shown in Figure 4.35 (a). The TEM micrograph shows an array of dislocations at which the nucleation of the precipitates seemed to have occurred. Figure 4.35 (b) shows an α-Al [112] SAD pattern but also shows some electron diffraction from the precipitates. After a further 12 months the structure had changed to give the precipitates shown in Figure 4.36 (a). The accompanying SAD pattern in Figure 4.36 (b) is an α-Al [110] pattern that shows the electron diffraction from the orthorhombic structure of the precipitates in the [112] direction. The precipitates in Figures 4.35 and 4.36 shall be referred to as P1 and P2 from here on.

Figure 4.37 shows X-ray maps taken using STEM of an area containing some of the naturally aged P2 precipitates. It can be seen that during the nucleation and growth of the precipitates copper diffused in from the surrounding material and that there was only a slight enrichment of magnesium compared to the matrix. There was, however, no apparent increase in the zinc concentration in the precipitates when compared to the matrix. The composition range of the P2 precipitates shown in Figure 4.36 was 10-20 wt.% Cu, 5-15 wt.% Mg, 3-7 wt.% Zn, with very small amounts of Fe and Si, with the balance being Al. A feature that seemed to coincide with the growth of the precipitates, and illustrated in Figure 4.38, was the breakup of the interdendritic phase and the diffusion of the solute atoms to form small particles in the adjacent α-Al. This effect was only noticed after the appearance of the precipitation from the matrix. A large number of dislocation loops can also be seen adjacent to the interdendritic boundary, and Figure 4.38 also shows that as the particles formed away from the interdendritic region a hole was subsequently left in the structure. When similar investigations were carried out on fresh thin area samples from the laser surface melted layers on the bulk alloys that had been left for equal times and under the same conditions no evidence of precipitation was found. Neither was any diffusion from the interdendritic phase observed in the bulk samples.

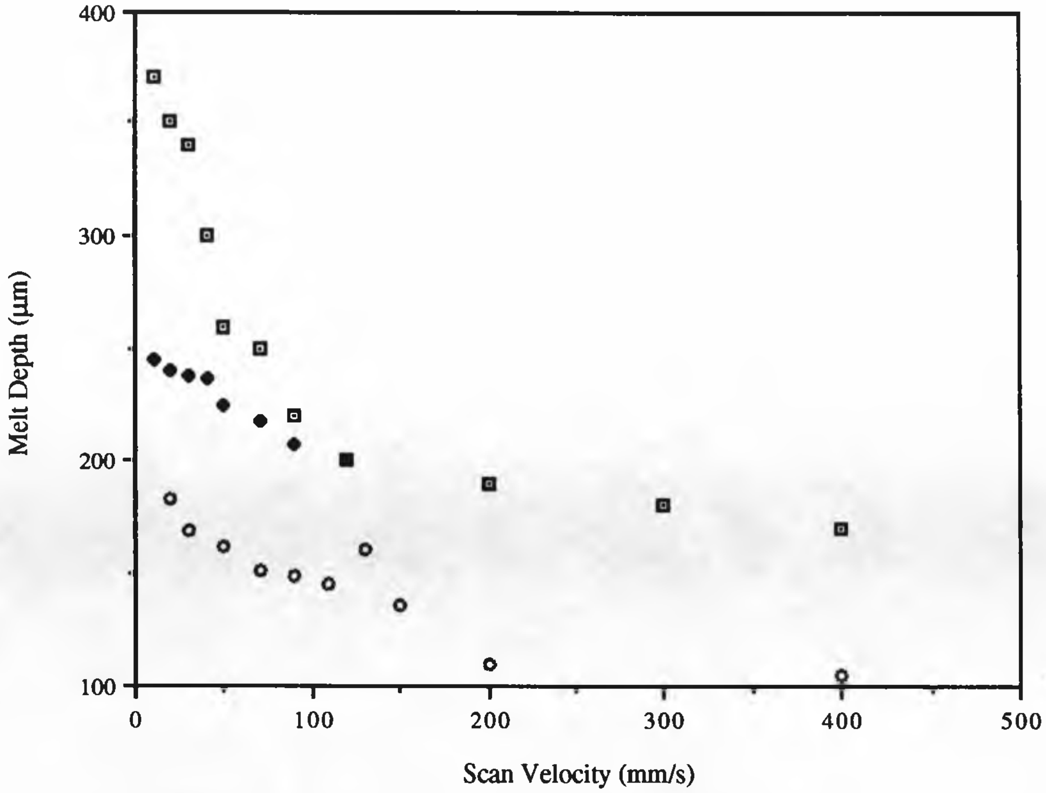

Fig.4.1. Melt depth versus laser scan velocity; laser output power=1.5kW. The three sets of data are for the 2014 alloy treated by immersion in NaOH.

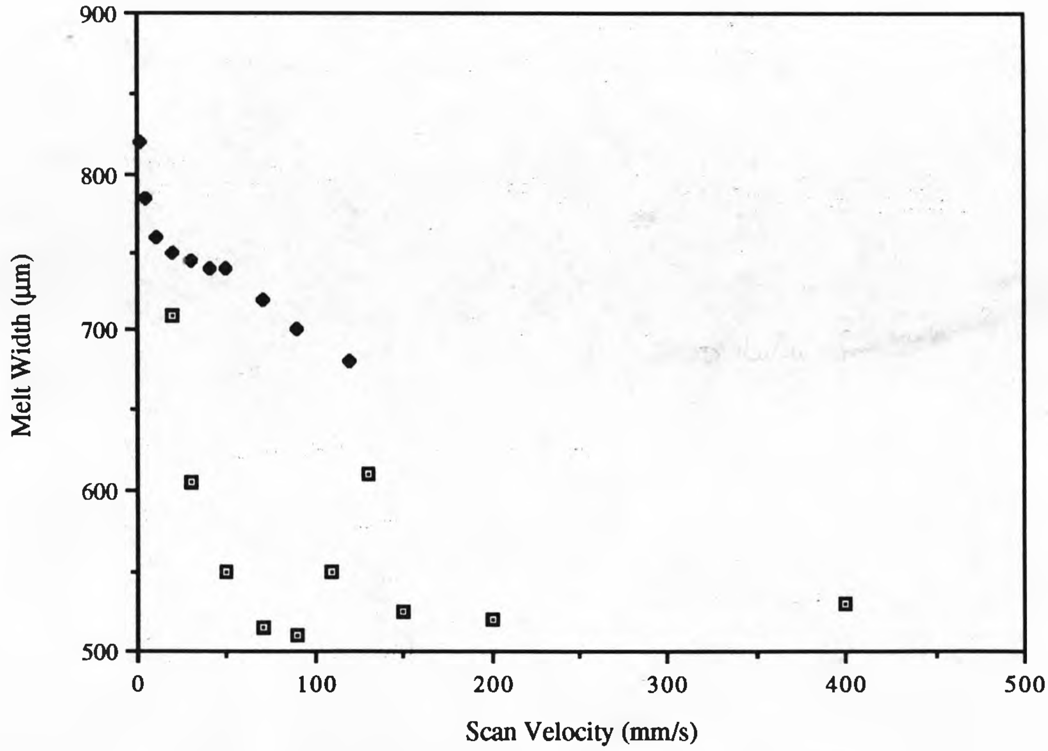

Fig.4.2. Melt width as a function of laser scan velocity, P=1.5kW; two individual sets of data for the same operating conditions.

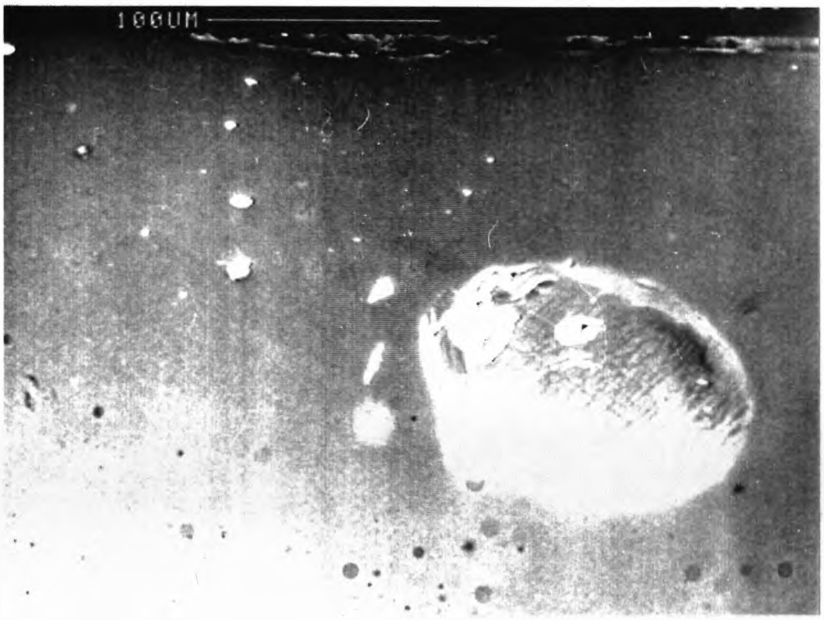

Figure 4.3. Large gas pore in the centre of the melt zone of LSM 2014 alloy and smaller pores at the fusion boundary; laser scan velocity = 8 mm/s.

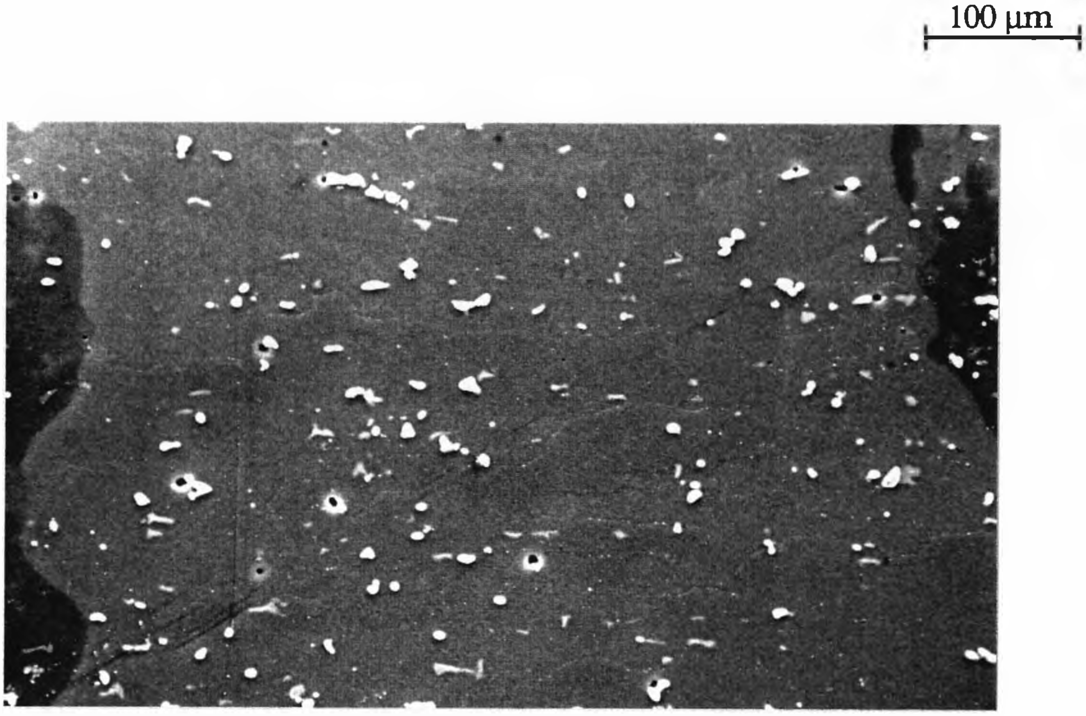

Figure 4.4. SEM micrograph showing the microstructure of the as-received 2014 T6 alloy.

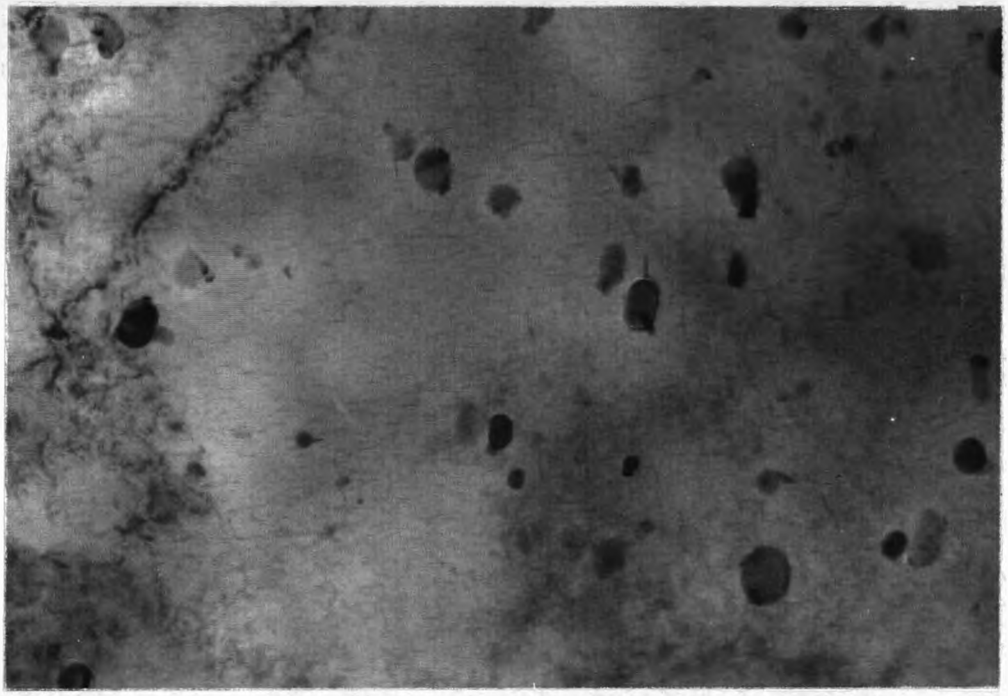

Figure 4.5. TEM micrograph of as-received 2014 alloy showing a uniform distribution of θ', that appears as the fine lines, and possible equilibrium $CuAl_2$.

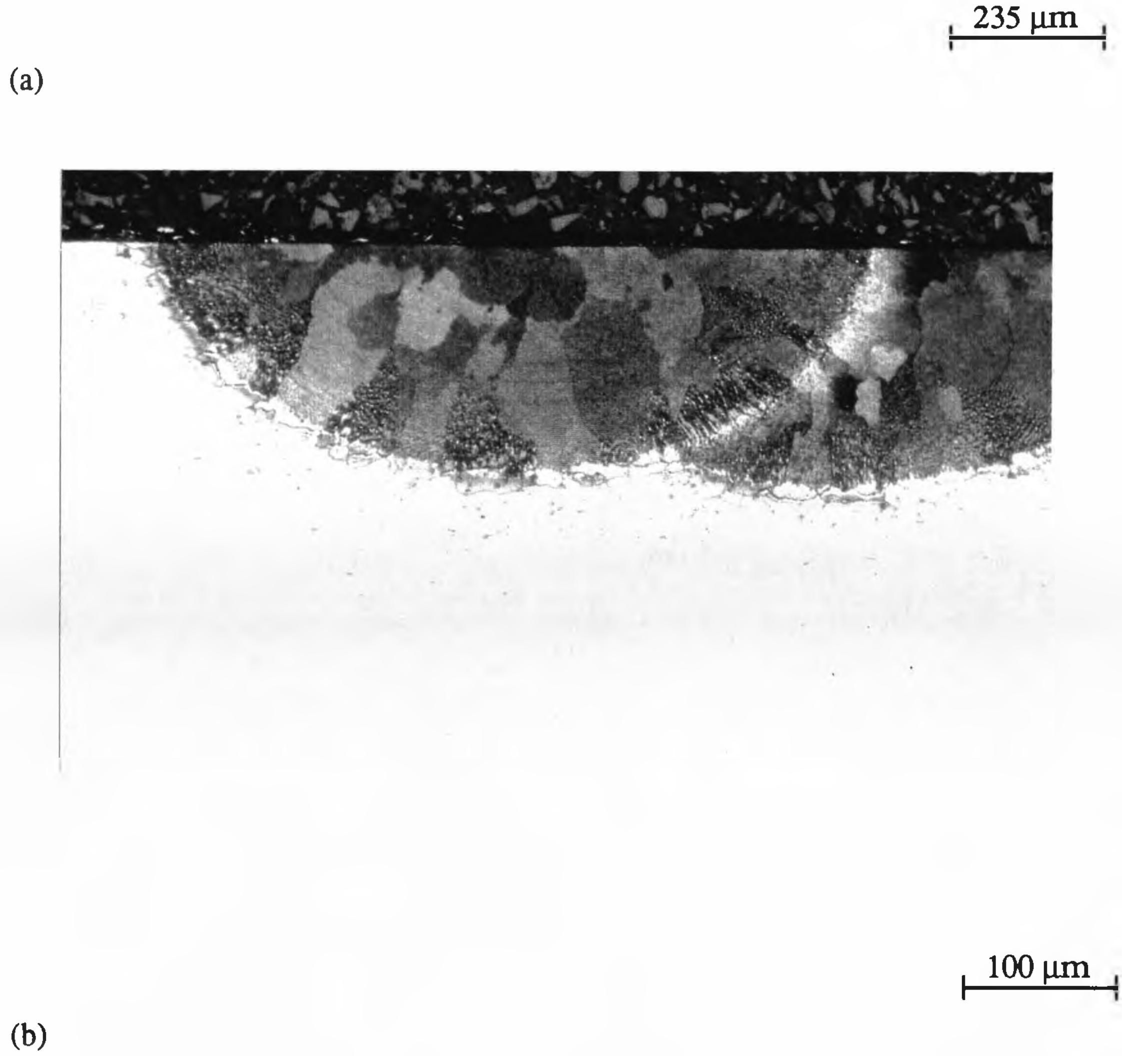

Figure 4.6. (a) Optical micrograph of LSM 2014 alloy showing the large columnar grains in the melted layer; V_s = 15 mm/s. (b) SEM micrograph of the melted layer showing the epitaxial regrowth of the columnar grain more clearly; V_s = 50 mm/s.

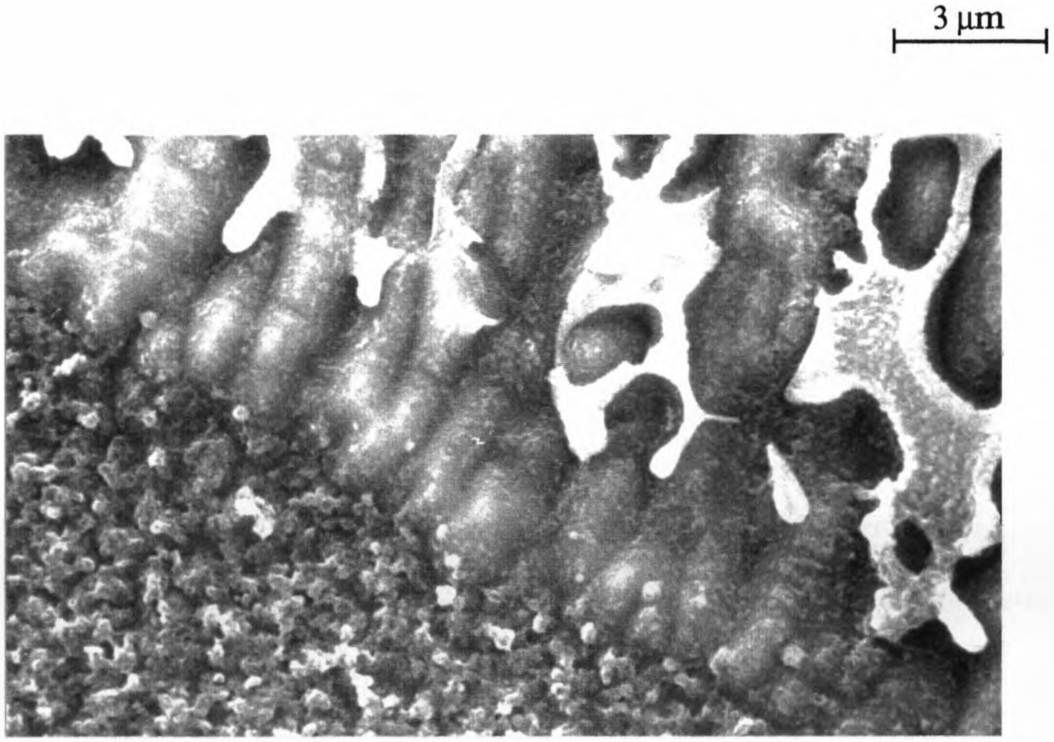

Figure 4.7. SEM micrograph showing the planar front region at the maximum melt depth in LSM 2014 and also the onset of cellular dendritic growth.

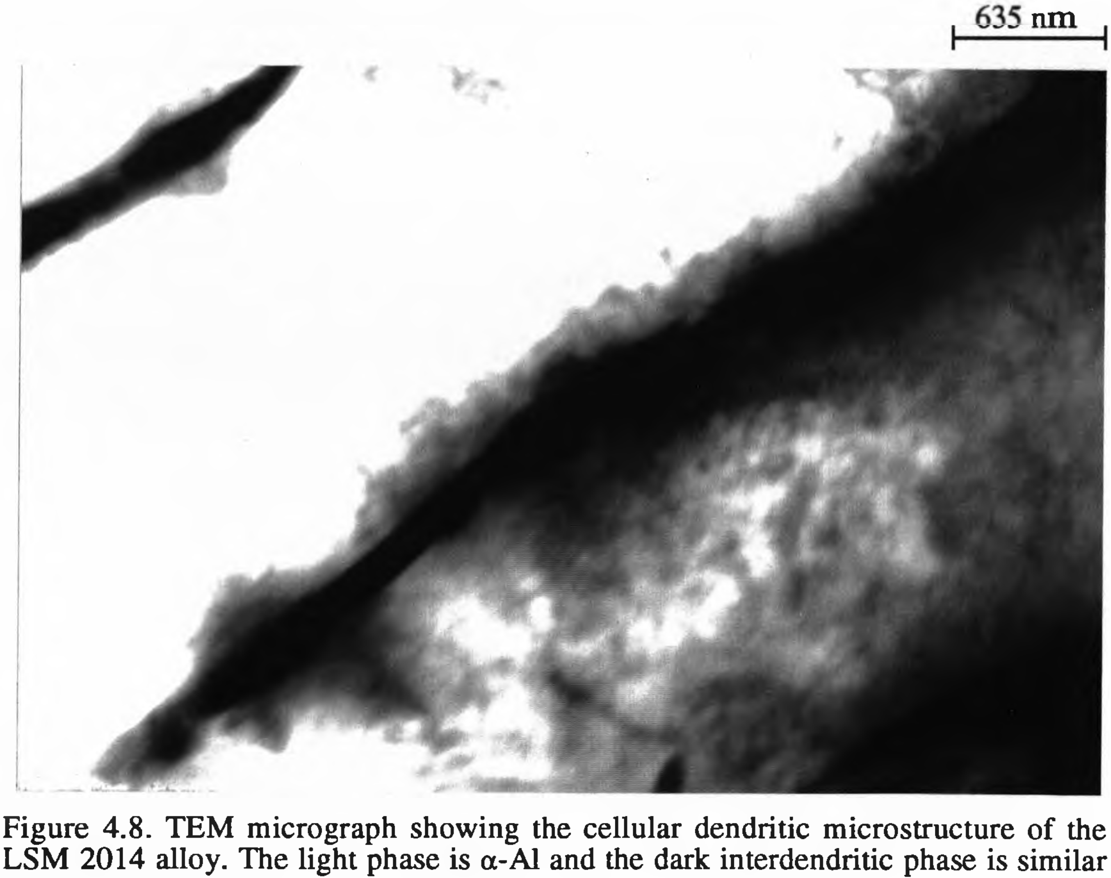

Figure 4.8. TEM micrograph showing the cellular dendritic microstructure of the LSM 2014 alloy. The light phase is α-Al and the dark interdendritic phase is similar to $CuAl_2$.

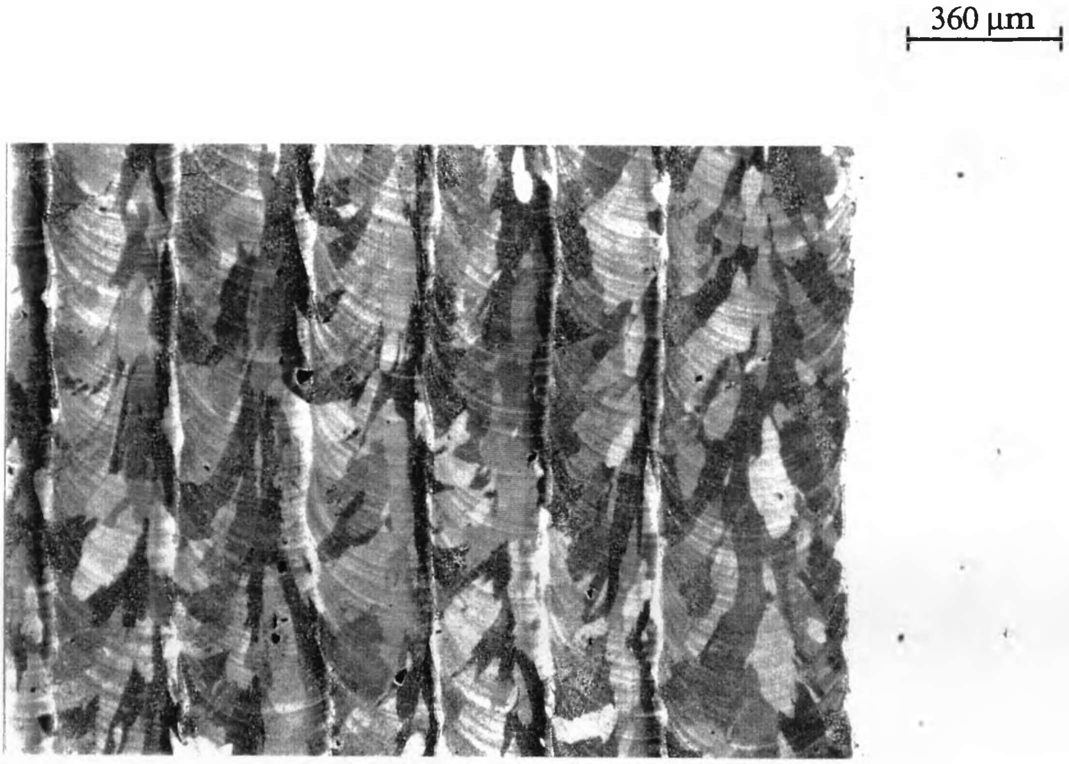

Figure 4.9. Optical micrograph showing a surface (x-y) section of LSM 2014 alloy. The columnar grains have grown from from the edge of the melt track towards the centre and in the direction of the laser scan.

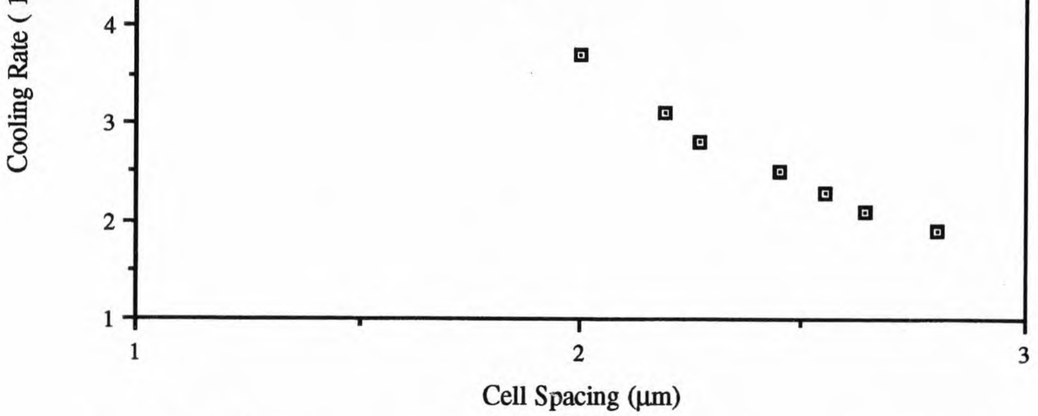

Fig.4.10. Cooling rate as a function of cell spacing at the maximum melt depth.

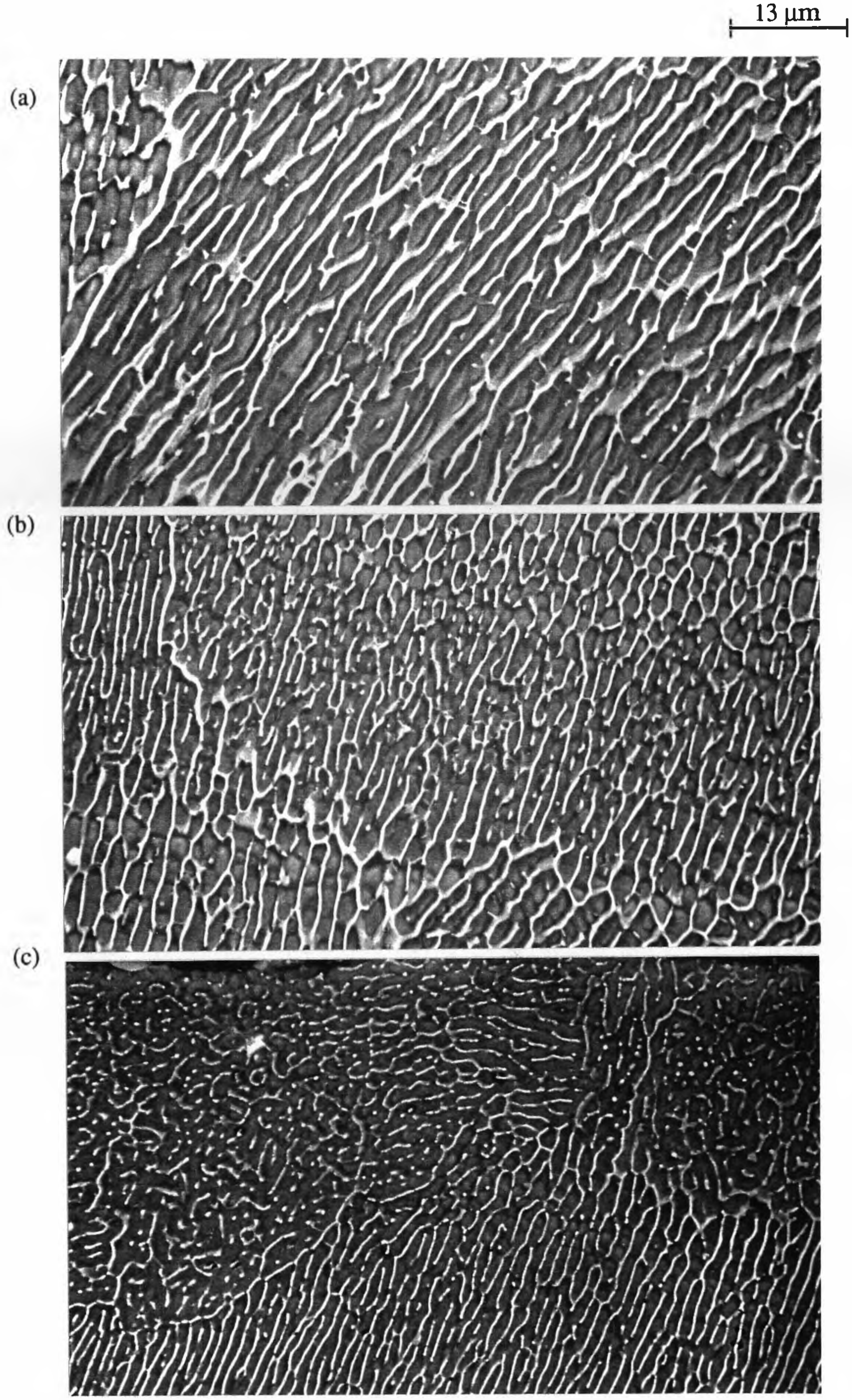

Figure 4.11. SEM micrographs showing the change in microstructure with depth and hence local cooling rate for LSM 2014 melted at 20 mm/s: (a) adjacent to the FBR; (b) centre of melt zone; (c) just below the surface.

Figure 4.12. SAD pattern of interdendritic boundary showing multiple diffraction by the θ (112) planes.

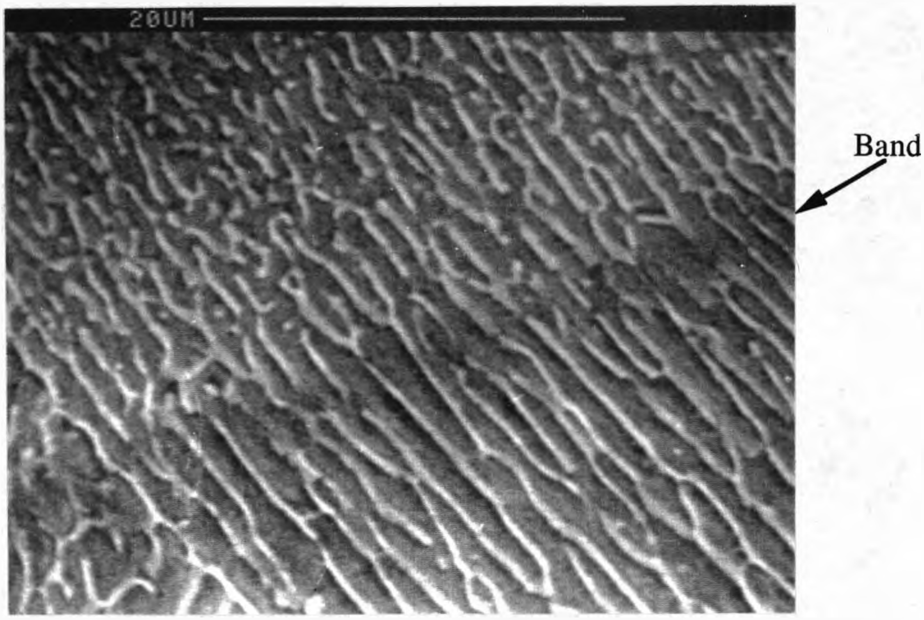

Figure 4.13. SEM micrograph illustrating the change in microstructure caused by solute banding.

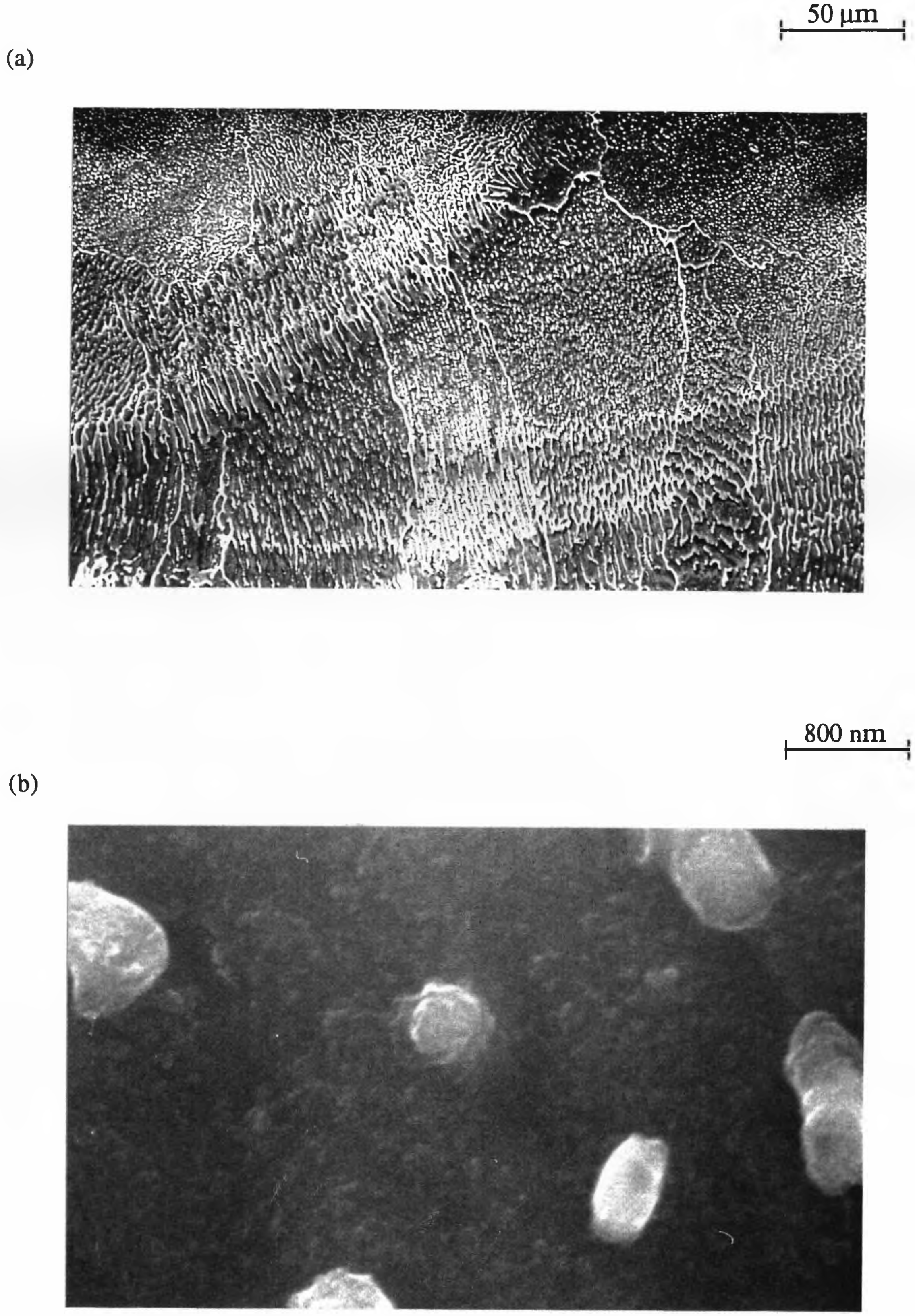

Figure 4.14. (a) SEM micrograph showing the change in microstructure at the track/ track interface of LSM 2014 alloy. (b) Same as (a) but at higher magnification, the interdendritic phase has transformed to globular particles.

Figure 4.15. TEM micrograph showing the microstructure of the partially solution treated grains in the FBR. Larger $CuAl_2$ particles have grown at the expence of the θ´ precipitates.

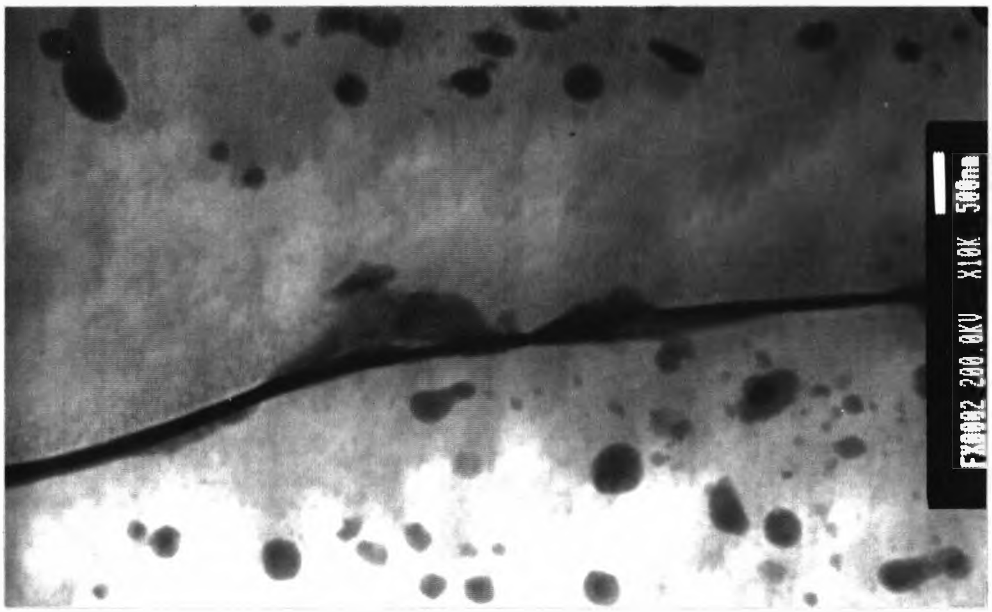

Figure 4.16. TEM micrograph showing the precipitate free zone adjacent to the grain boundaries in the HAZ of the unmelted substrate in 2014 alloy.

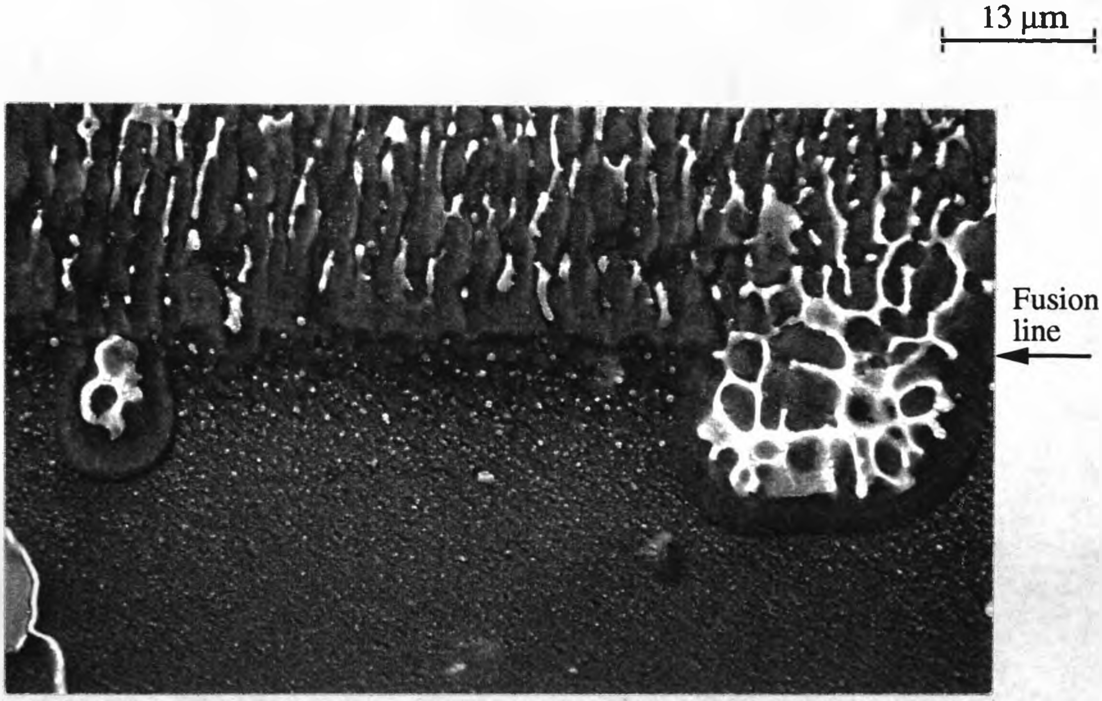

Figure 4.17. SEM micrograph illustrating how partially melted $CuAl_2$ particles at the fusion line, resolidifying as eutectic chinese script structures, can initiate cellular dendritic growth in the melted layer.

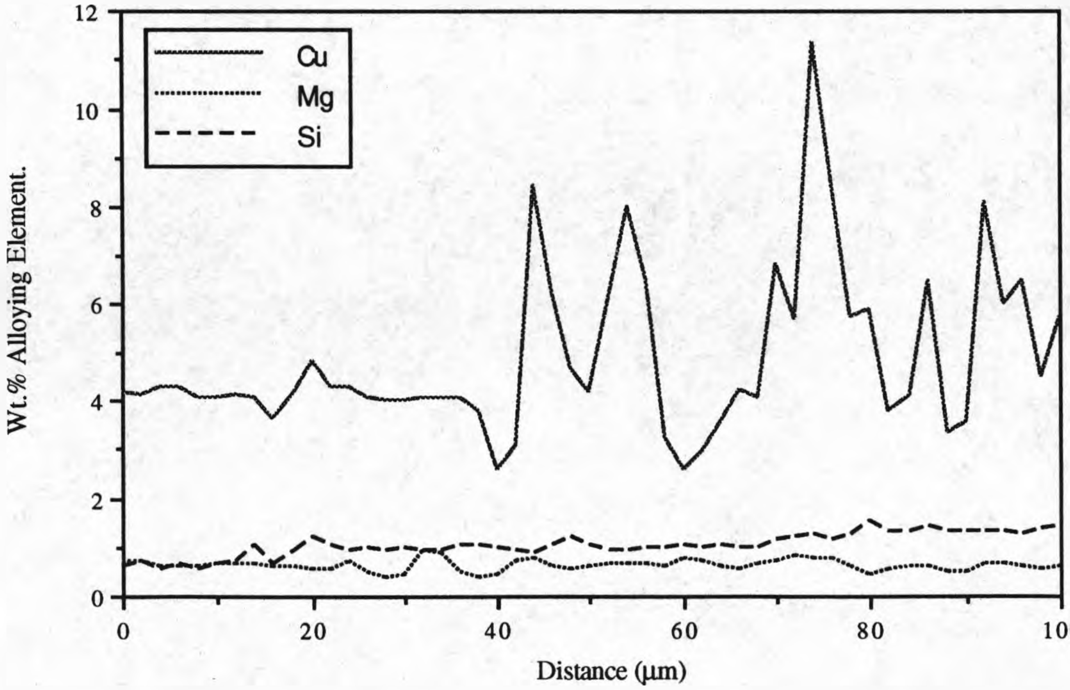

Figure 4.18. ZAF corrected WDS composition profiles from the substrate (0 µm) across the fusion line (40 µm) and into the melt zone of LSM 2014 alloy.

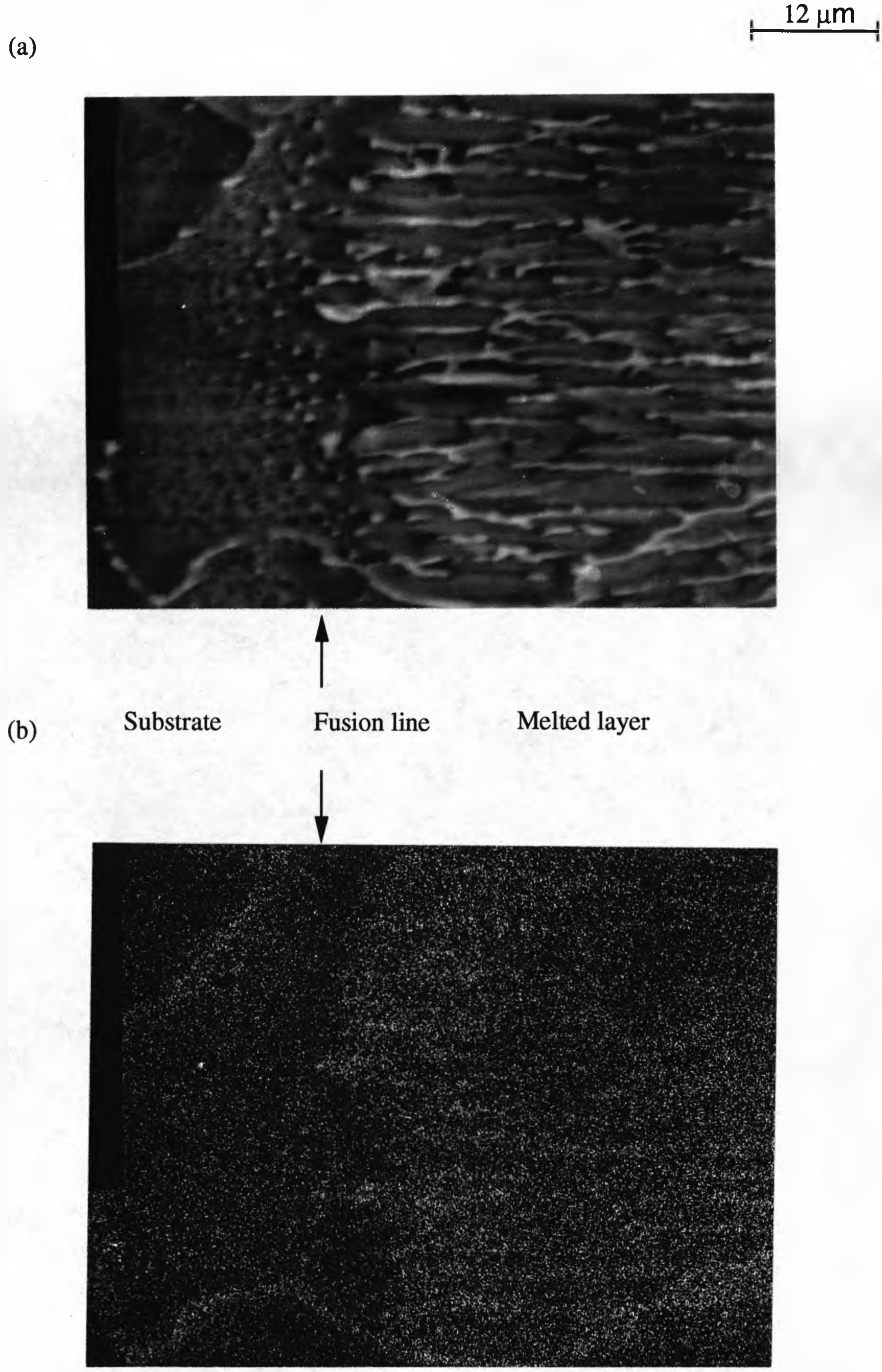

Figure 4.19. (a) Back scattered electron micrograph from the electron microprobe showing the FBR in LSM 2014 alloy; (b) Cu X-ray map corresponding to (a), solute enrichment can be seen in the grain boundaries and immediately after the planar front region.

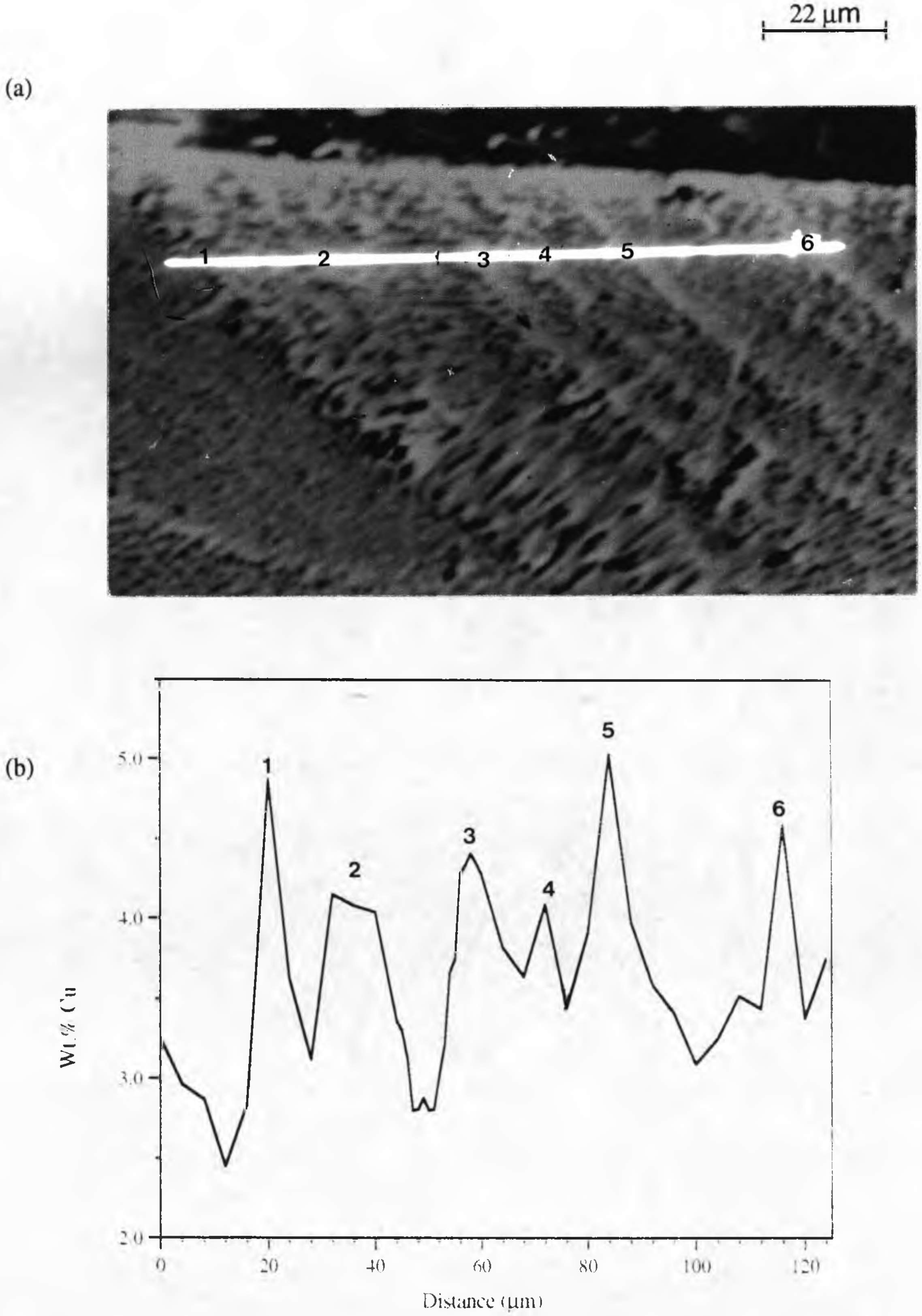

Figure 4.20. (a) Scanning electron microprobe image of a transverse (x-z) cross section of LSM 2014; (b) the peaks in the Cu profile for the line shown in (a) correspond to the numbered bands.

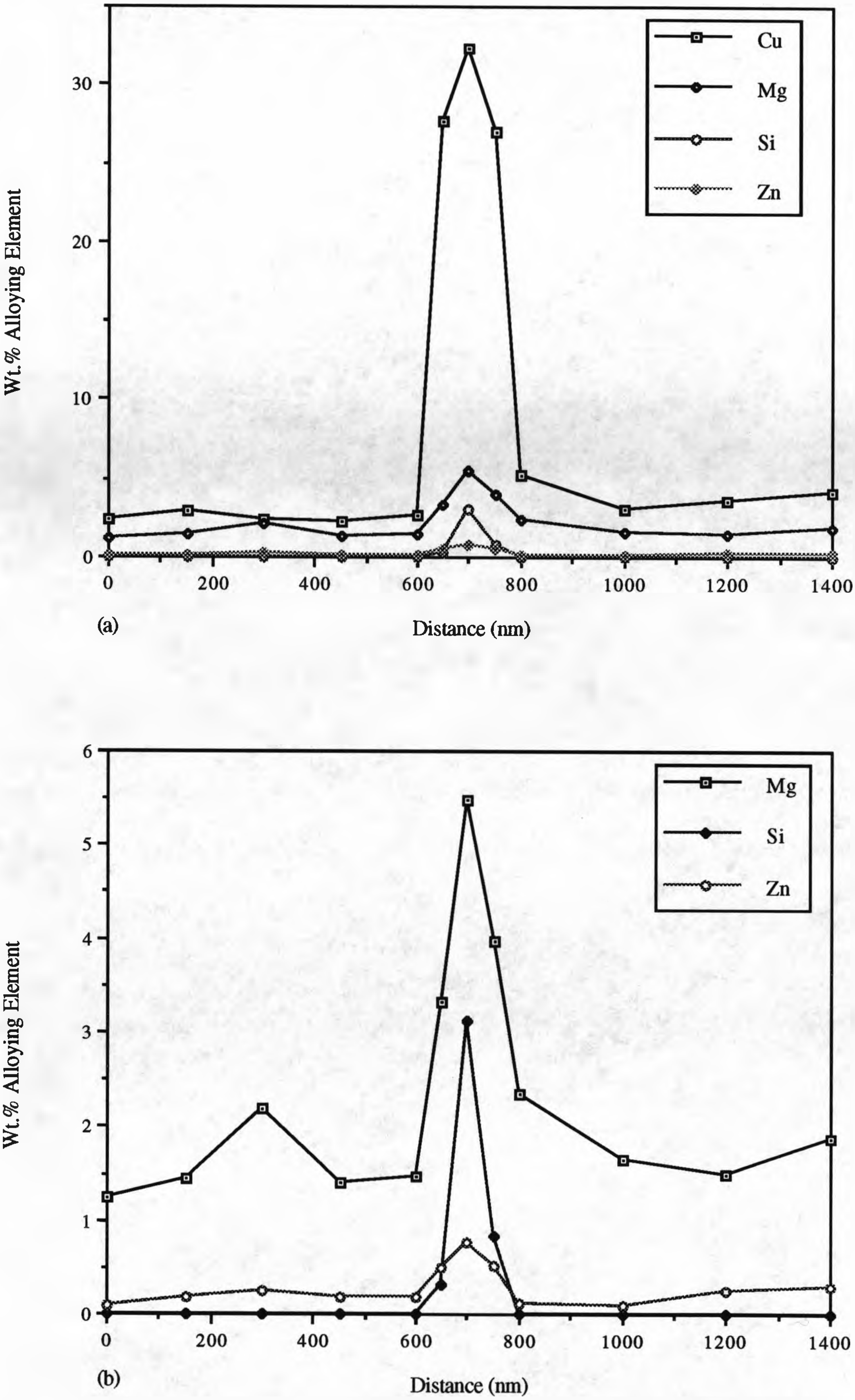

Fig.4.21. Variation in composition across a dendrite in laser surface melted 2014 alloy, analysis by STEM.

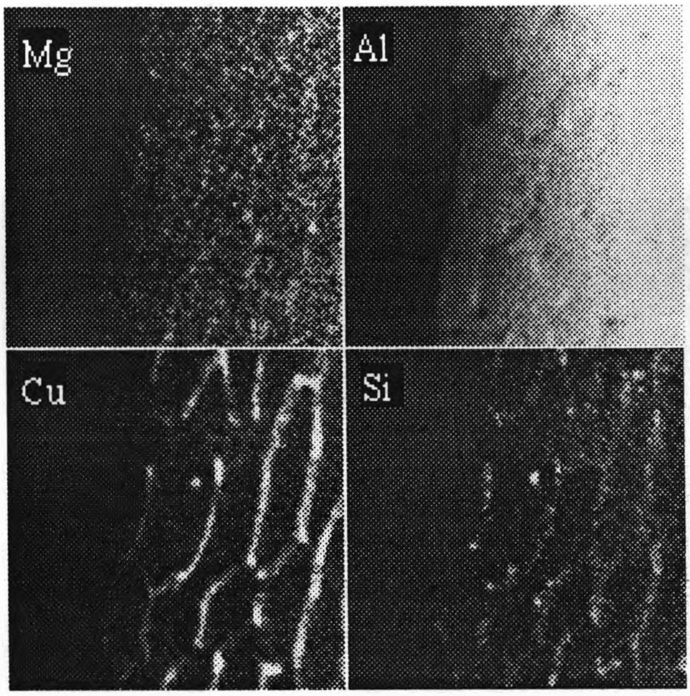

Figure 4.22. X-ray maps from thin foil samples of LSM 2014 alloy showing that Mg, Cu and Si are segregated to the interdendritic regions.

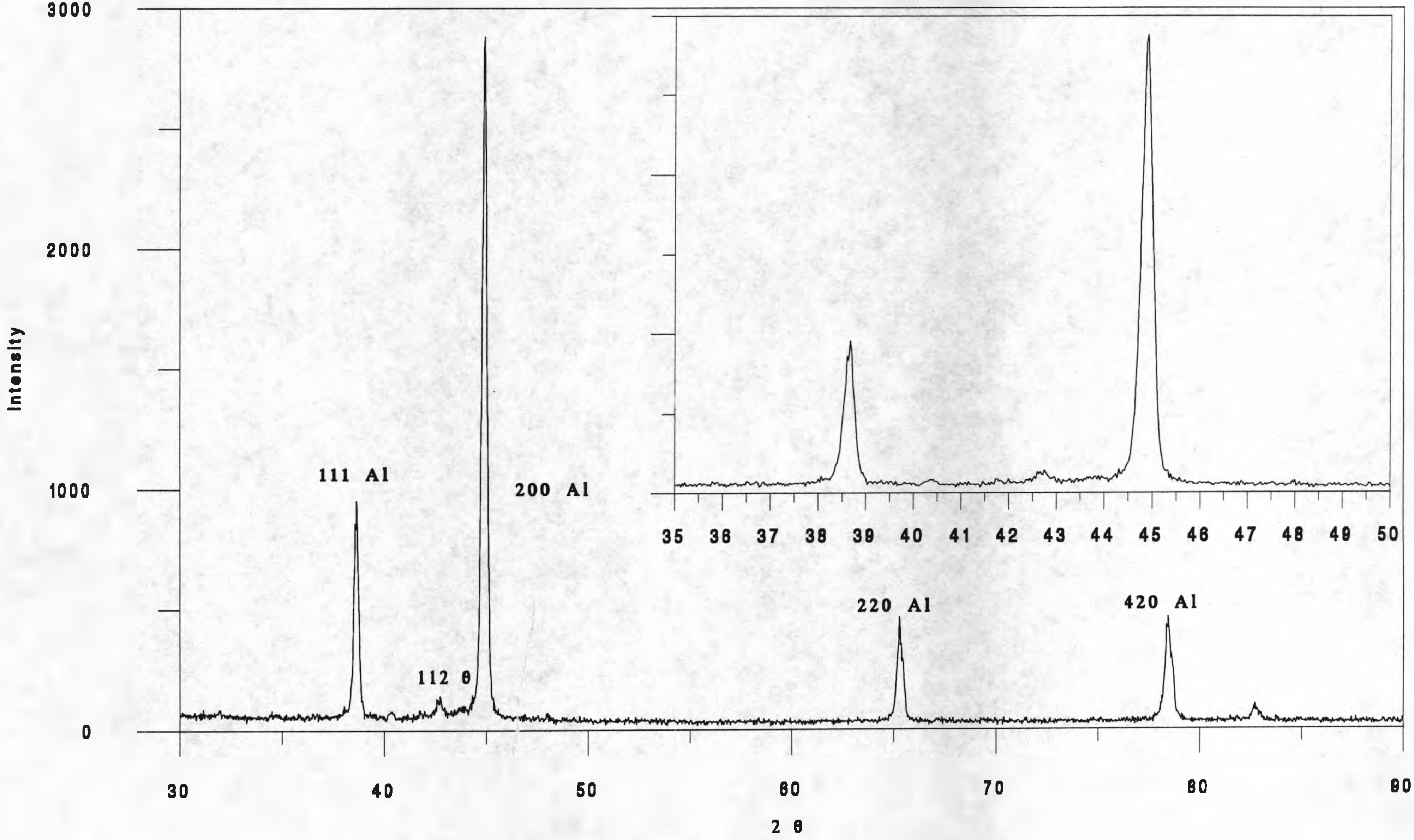

Figure 4.23. X-ray diffraction profile for as-received 2014 alloy.

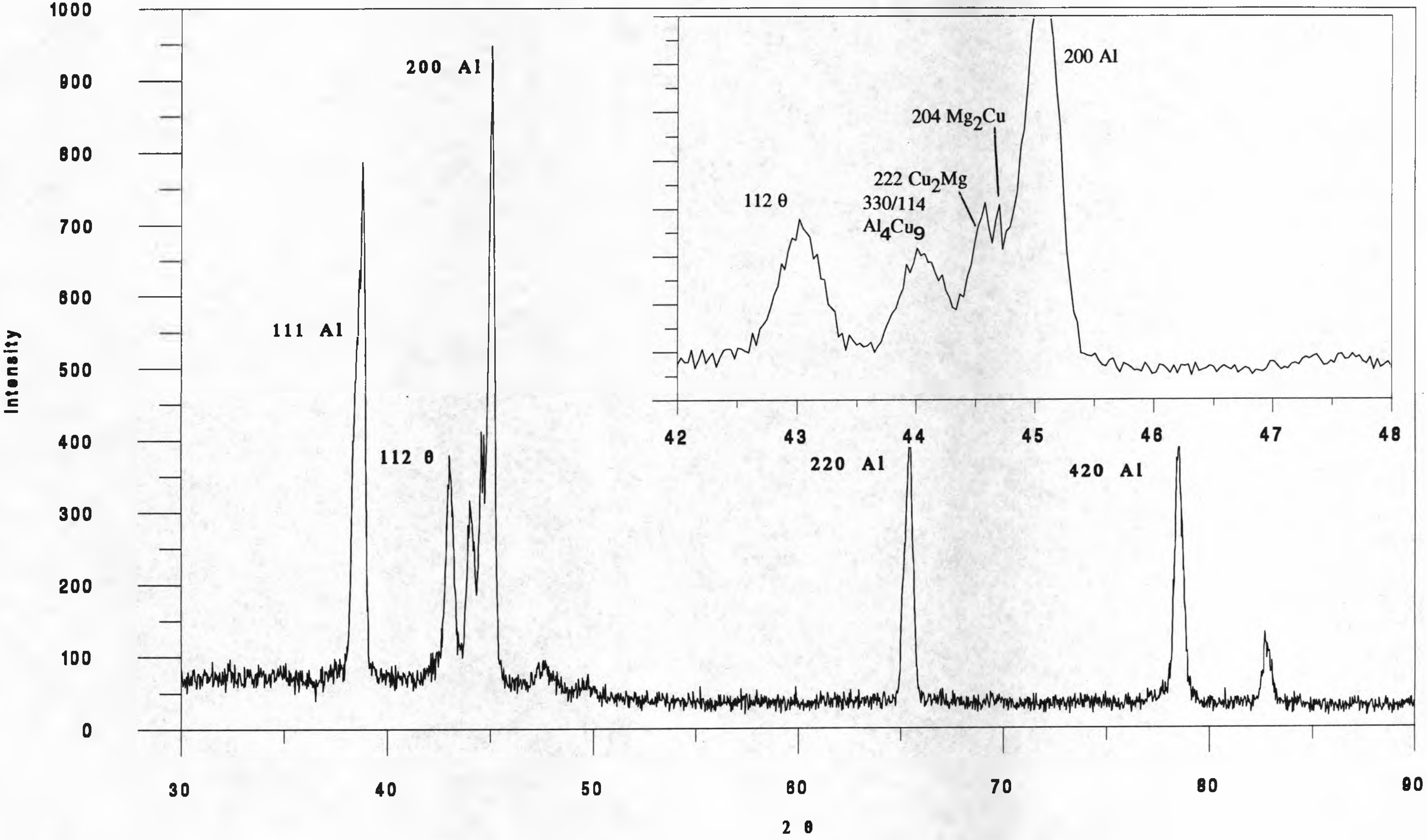

Figure 4.24. X-ray diffraction profile for LSM 2014 alloy.

As-received 2014		LSM 2014		Phase (hkl)
2θ	d - spacing (ang.)	2θ	d - spacing (ang.)	
38.496	2.3385	38.656	2.3292	Al (111)
40.208	2.2428			unknown
42.544	2.1249	43.040	2.1016	$CuAl_2$ (112)
		44.048	2.0558	Al_4Cu_9 (330/114)
		44.560	2.0334	Cu_2Mg (222)
		44.688	2.0278	Mg_2Cu (204)
44.736	2.0258	45.056	2.0121	Al (200)
65.180	1.4313	65.376	1.4275	Al (220)
78.320	1.2208	78.522	1.2182	Al (420)

Table 4.1. X-ray diffraction data for 2014 alloy before and after LSM.

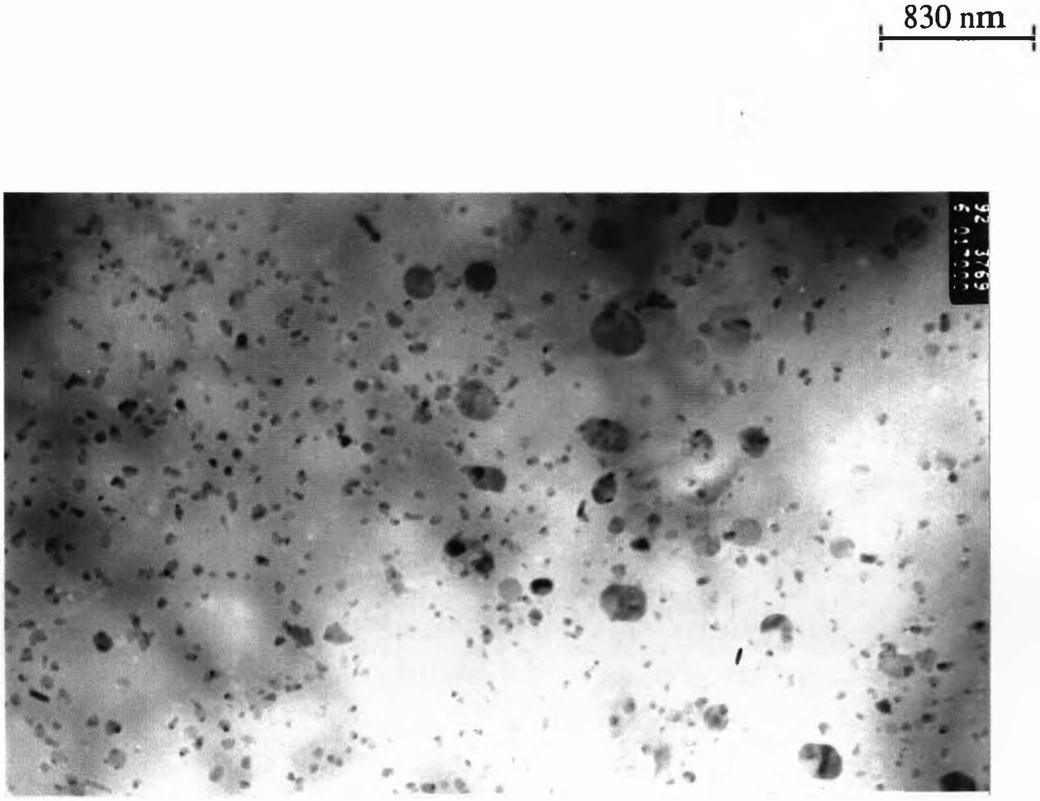

Figure 4.25. TEM micrograph showing the distribution of η precipitates in the microstructure of the as-received 7075 T6 alloy.

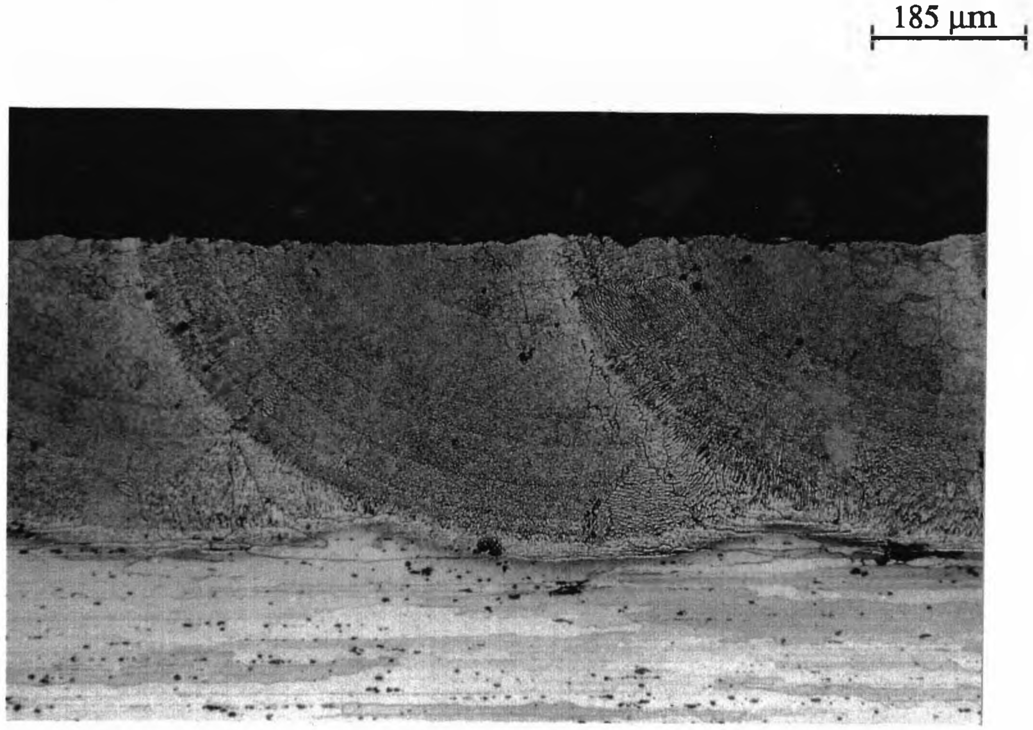

Figure 4.26. Optical micrograph taken of a transverse (x-z) cross section of LSM 7075, showing the microstructural change from the unmelted substrate. A banded structure is also clearly visible.

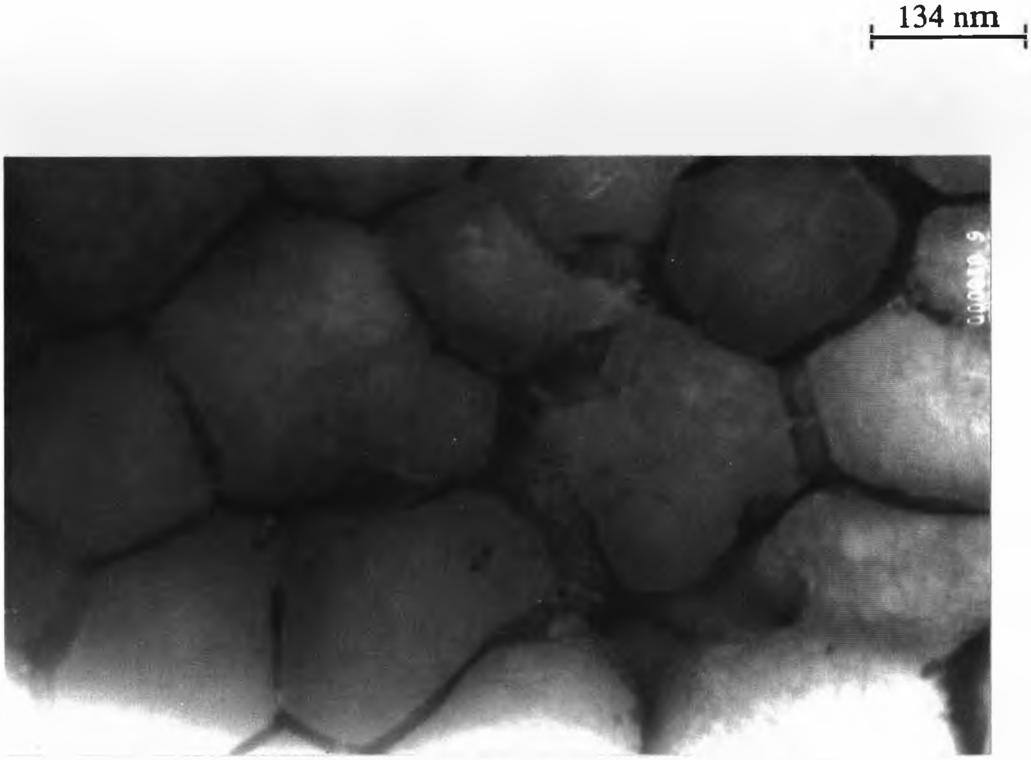

Figure 4.27. TEM micrograph showing the cellular dendrites in the LSM 7075 alloy.

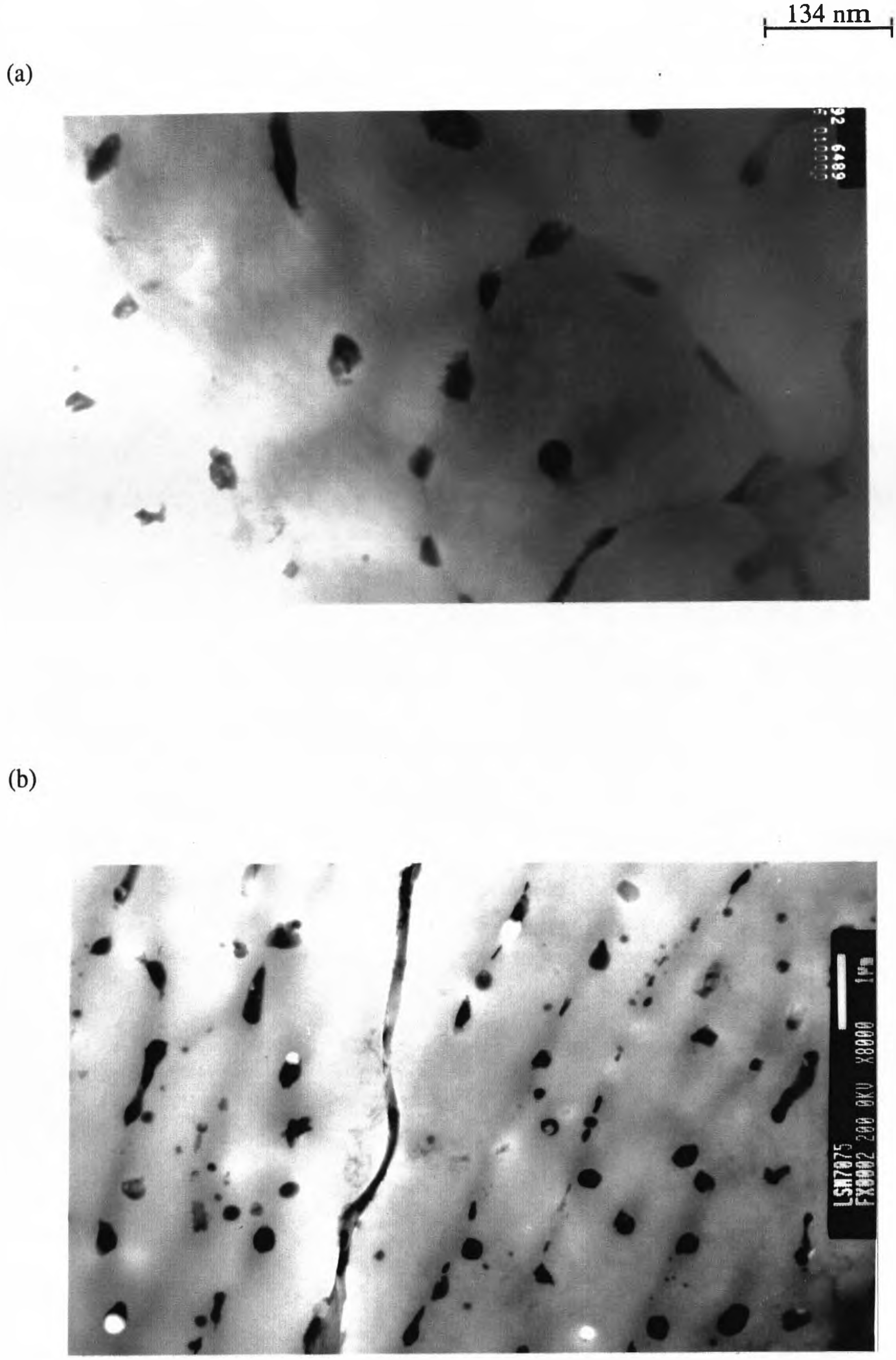

Figure 4.28. (a) TEM micrograph showing a transverse view of the cellular dendritic microstructure in the HAZ of overlapping laser melt tracks in LSM 7075. (b) As (a) but a longitudinal view, the interdendritic phase has transformed to globules.

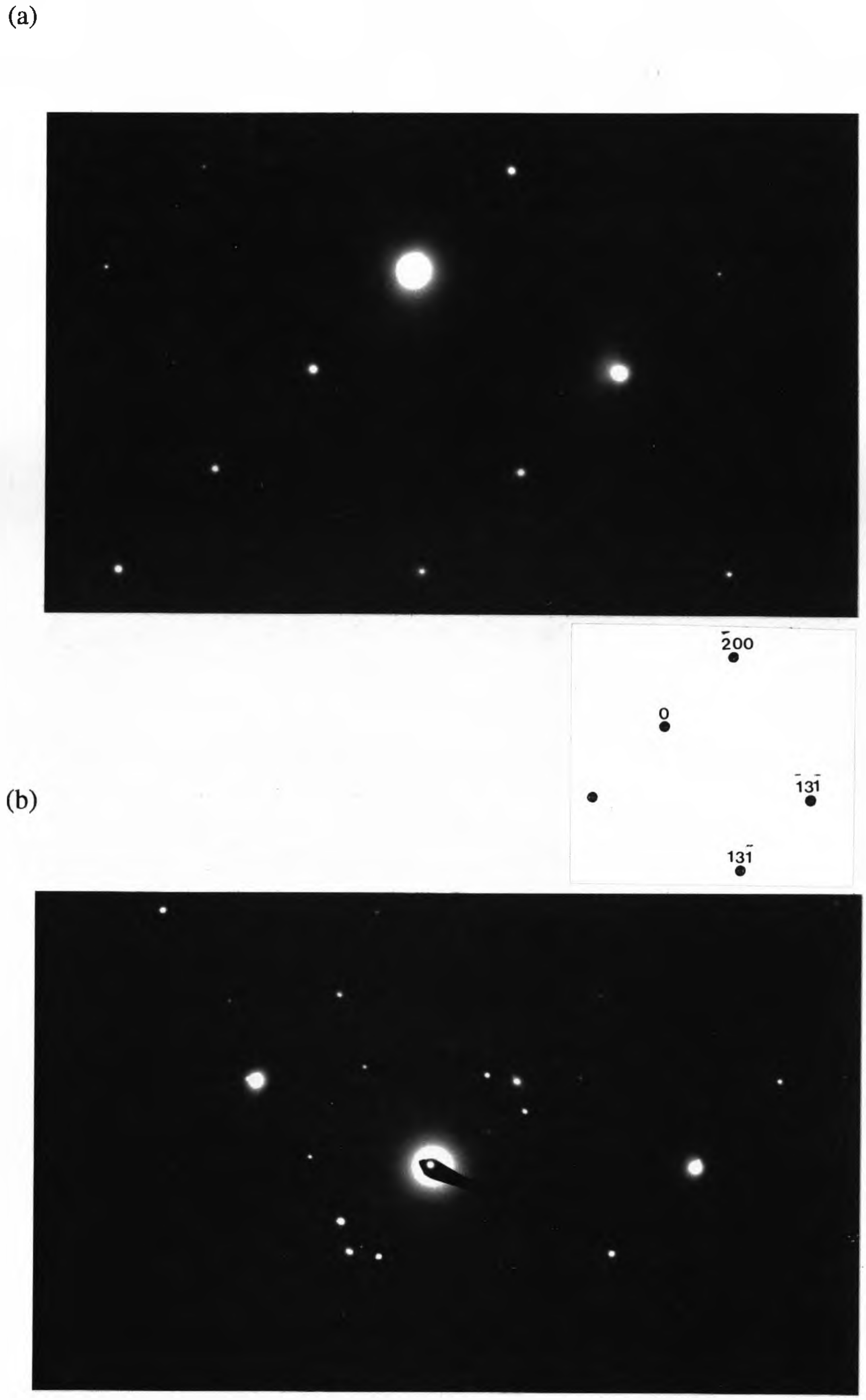

Figure 4.29. $[013]_{Al}$ SAD patterns from LSM 7075 alloy: (a) from the α-Al dendrite arm; (b) as (a) but including the interdendritic region.

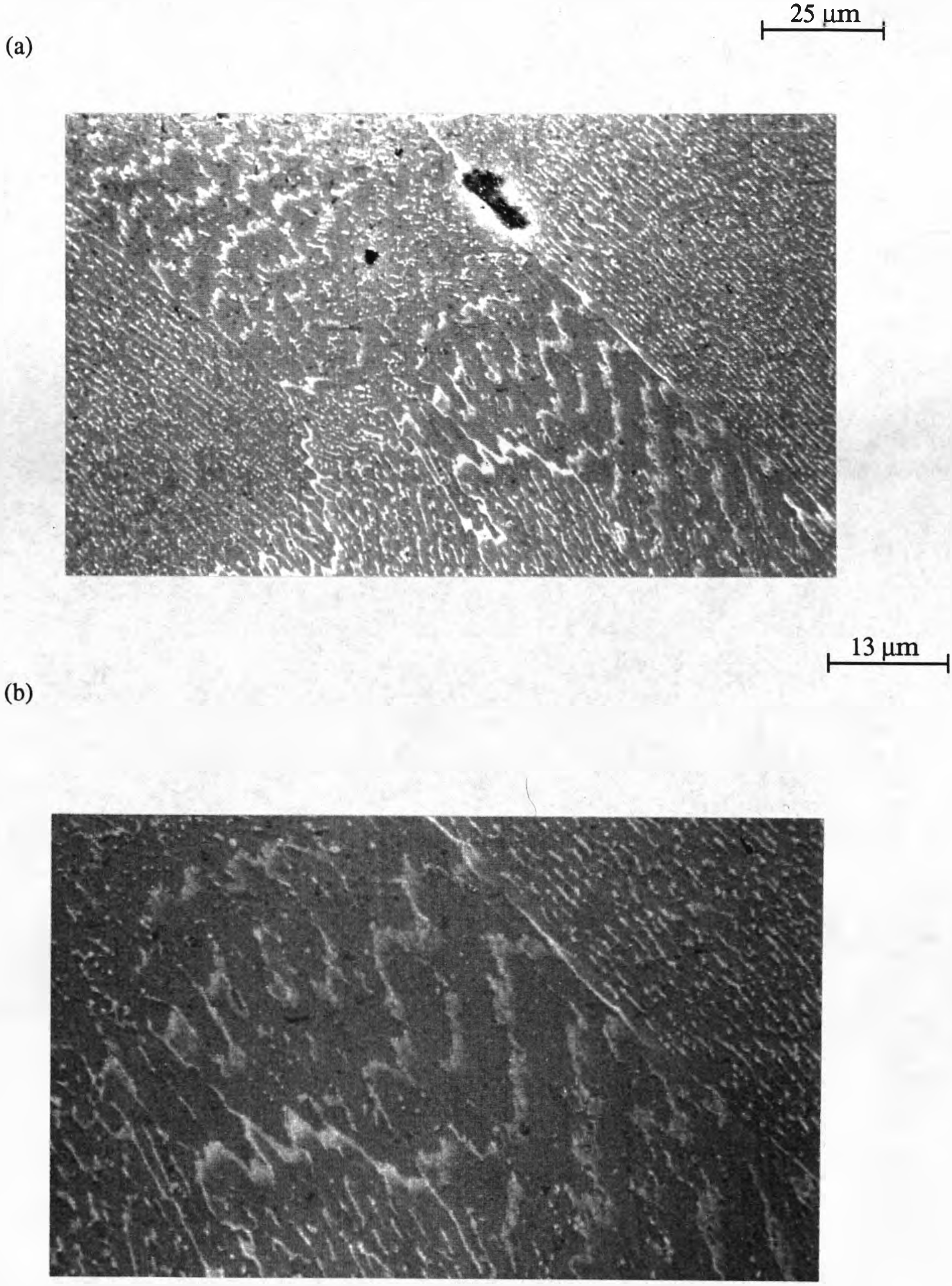

Figure 4.30. (a) SEM micrograph of a y - z section showing a second form of banding in the LSM 7075 alloy; (b) higher magnification image from (a) showing apparent planar front growth alternating with the precipitation of an intermetallic phase.

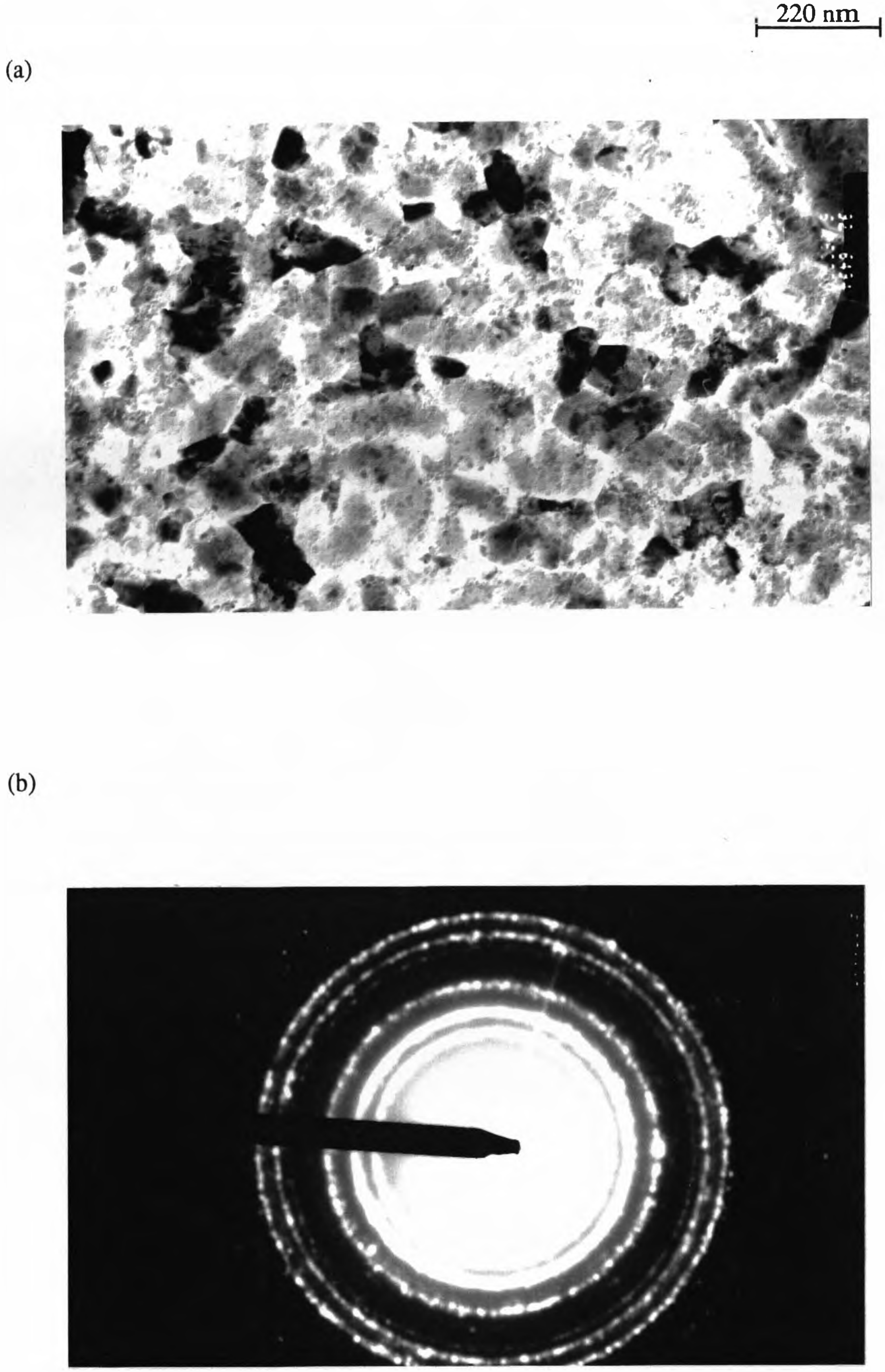

Figure 4.31. (a) TEM micrograph showing the nanocrystalline layer at the surface of LSM 7075 alloy; (b) convergent beam diffraction pattern from (a).

Ring no. about central spot	Diameter (mm)	d - spacing (ang.)
1	15.6	4.9244
2	25.2	3.0484
3	29.7	2.5866
4	36.0	2.1338
5	44.1	1.7420
6	47.0	1.6344
7	51.0	1.5062
8	59	1.3020
9	62.45	1.2302
10	69	1.1134

Table 4.2. Electron diffraction data from the ring pattern obtained from the nanocrystalline layer in LSM 7075 alloy.

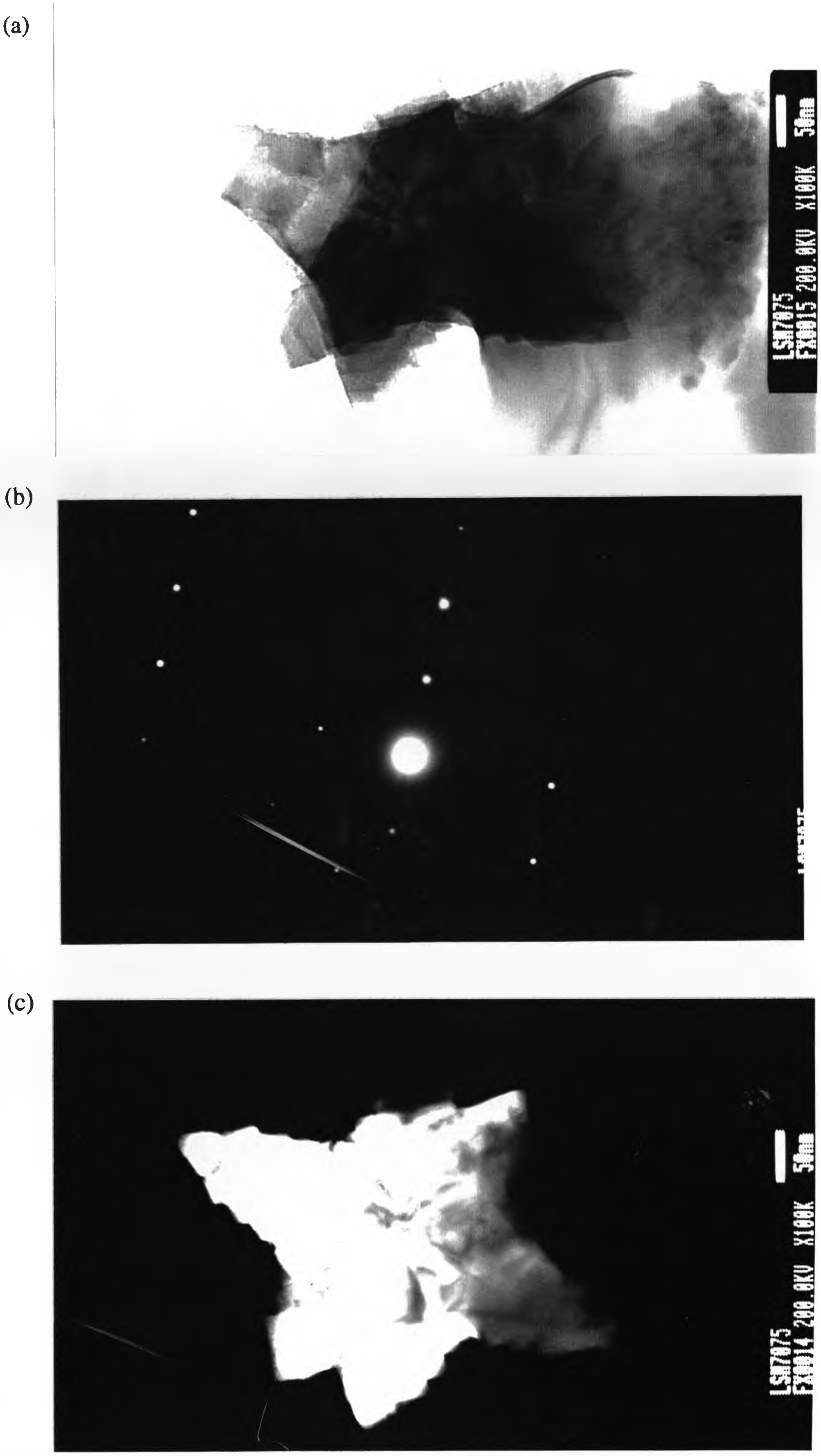

Figure 4.32. TEM micrograph of the Al_2MgO_4 particle found in LSM 7075: (a) Bright field image; (b) SAD pattern from (a), B = [$\bar{2}55$]; (c) dark field image.

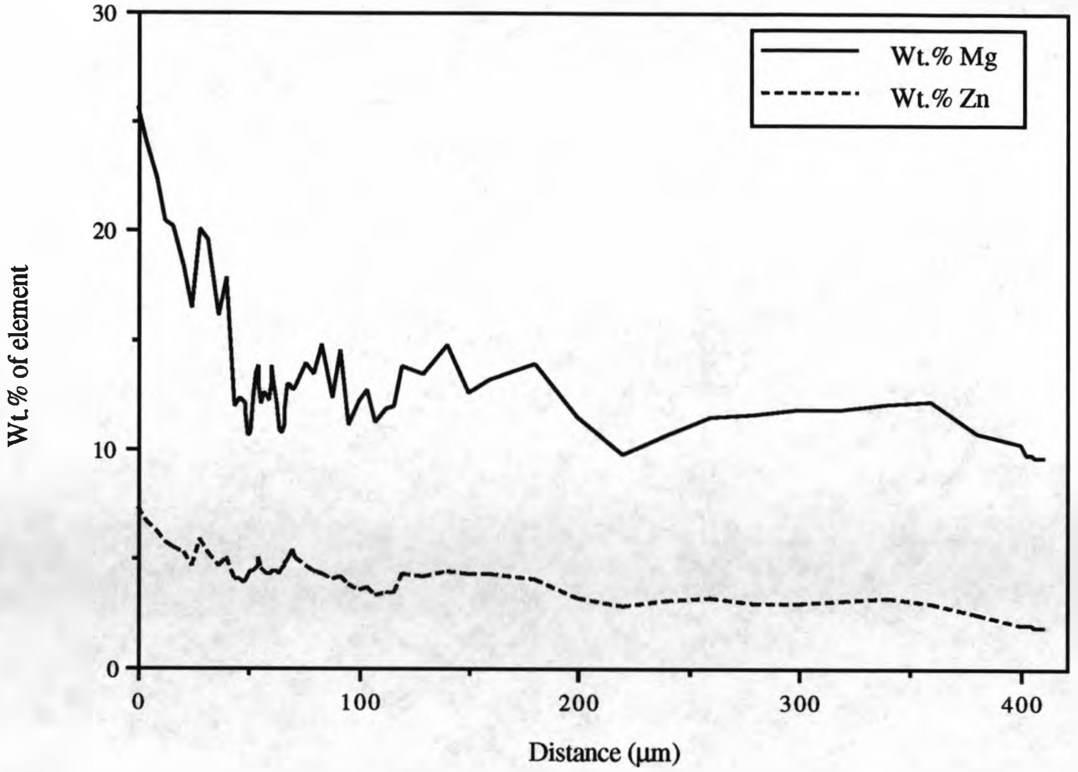

Fig4.33. ZAF corrected WDS depth profile of the composition of LSM 7075 alloy (fusion line at ~ 50 µm and the surface at 410 µm).

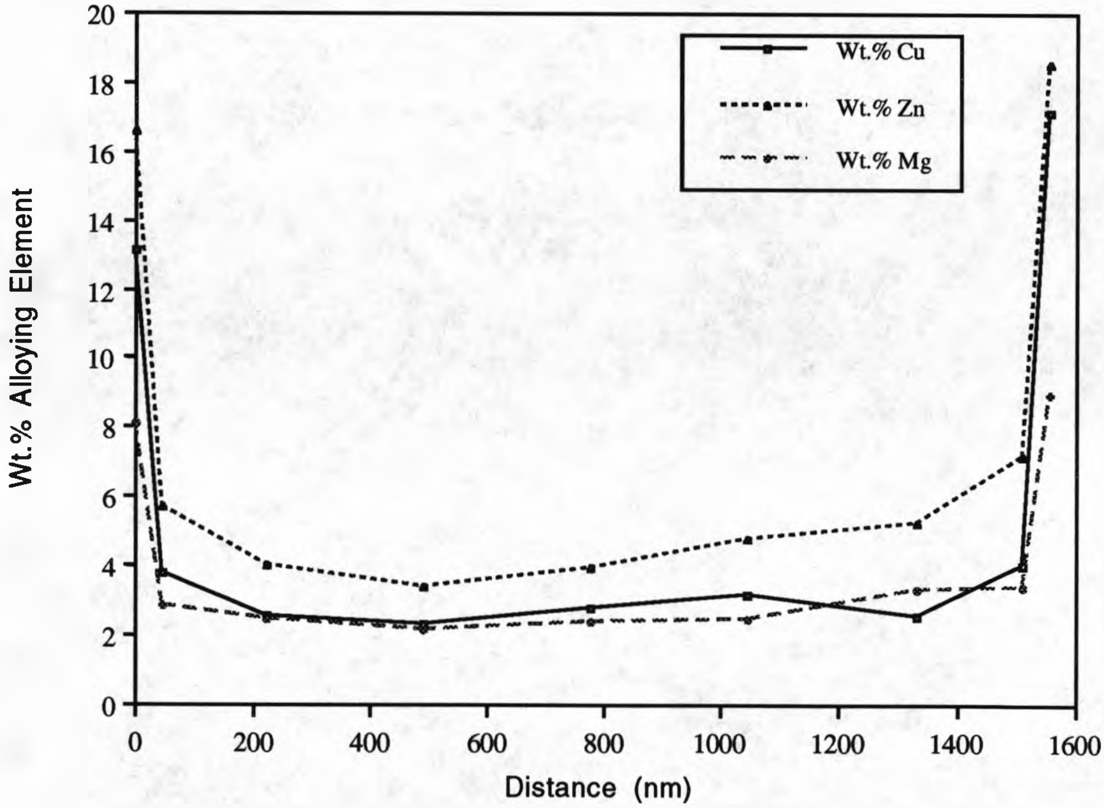

Fig.4.34. Variation in composition across a dendrite in laser surface melted 7075 alloy, analysis by STEM.

(a)

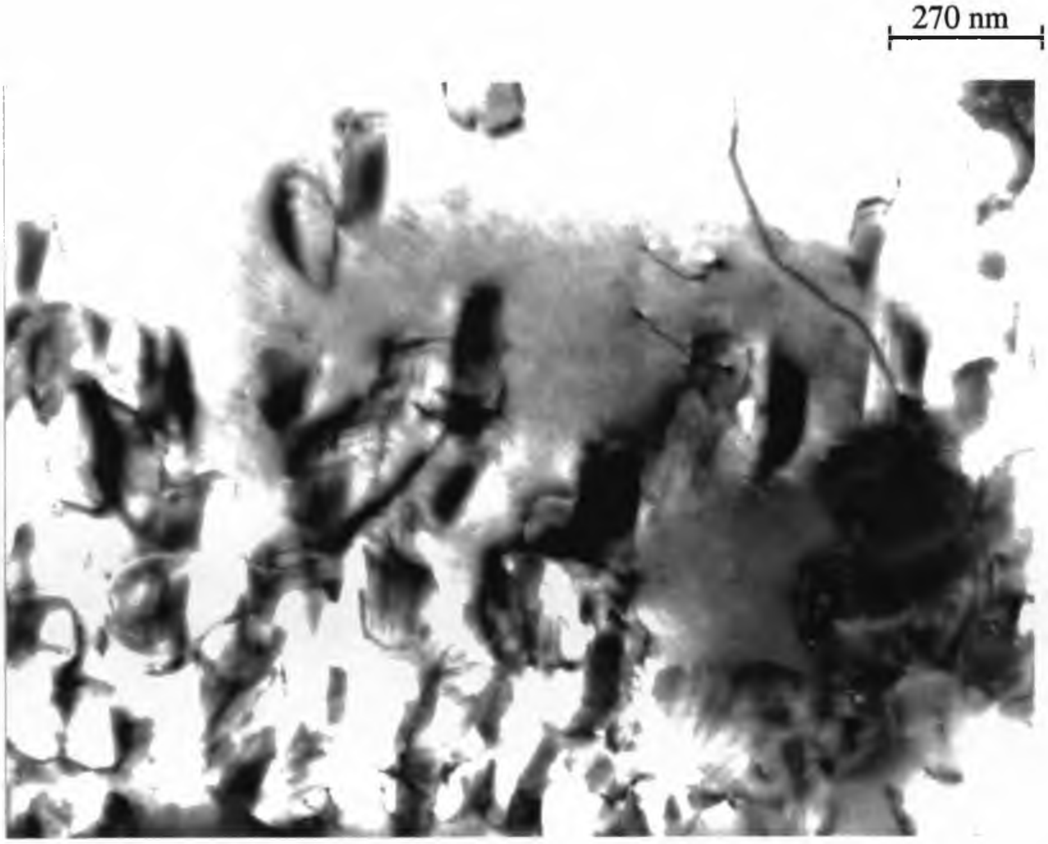

(b)

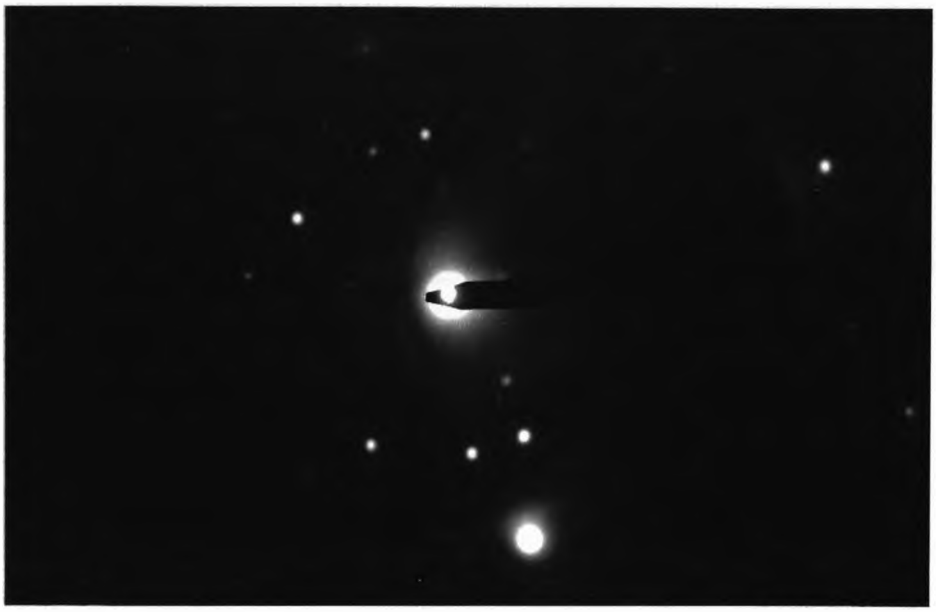

Figure 4.35. (a) TEM micrograph depicting the microstructure of LSM 7075 alloy after 6 months of natural ageing. (b) [112]Al SAD pattern including diffraction from the precipitates shown in (a).

(a)

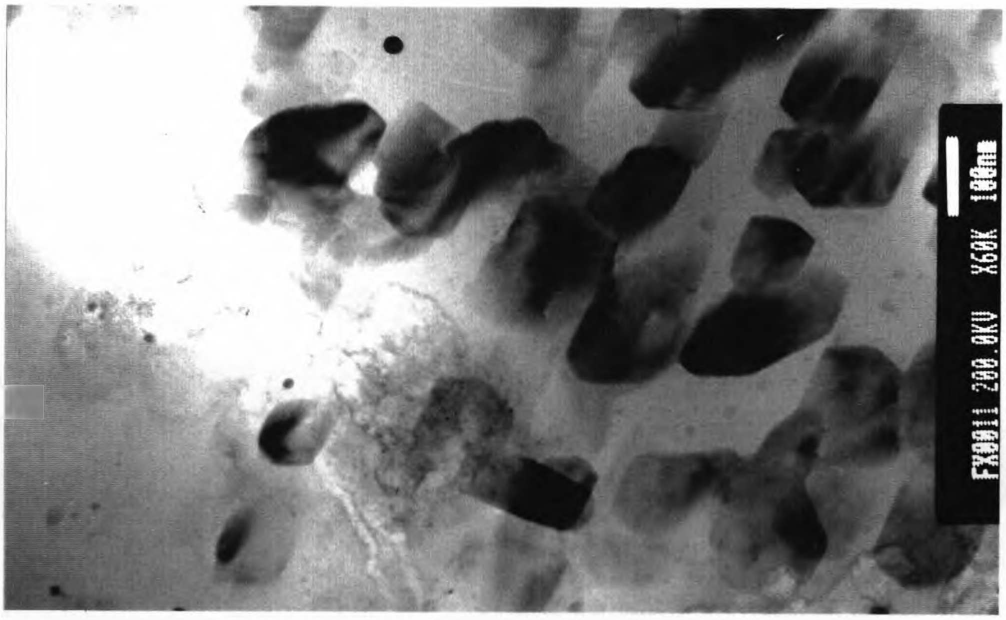

(b)

Figure 4.36. (a) TEM micrograph of LSM 7075 alloy after 12 months of natural ageing. (b) $[011]_{Al}$ SAD pattern from (a) also showing diffraction from the precipitates determined to be orthorhombic, B = $[112]_{ortho}$.

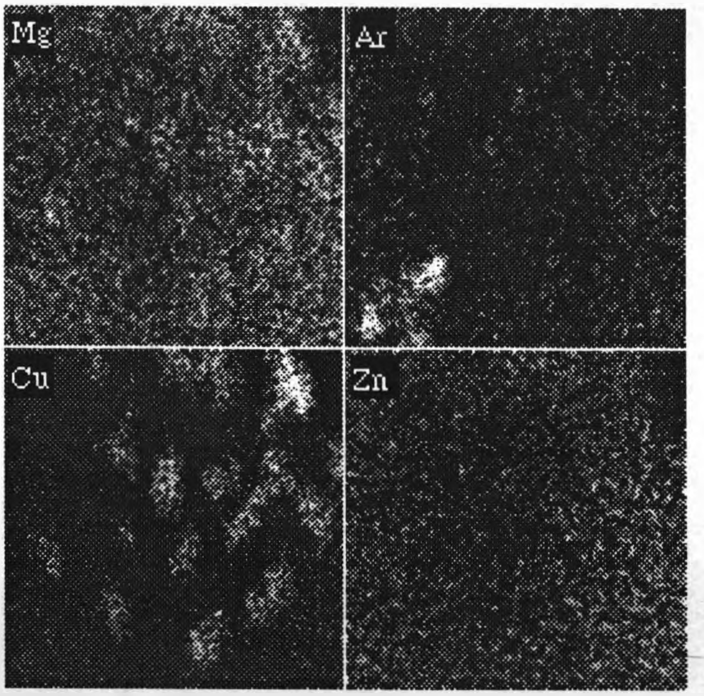

Figure 4.37. X-ray maps obtained from a thin foil sample of LSM 7075 by the STEM technique, showing the solute concentrations in a region where precipitates have formed by natural ageing.

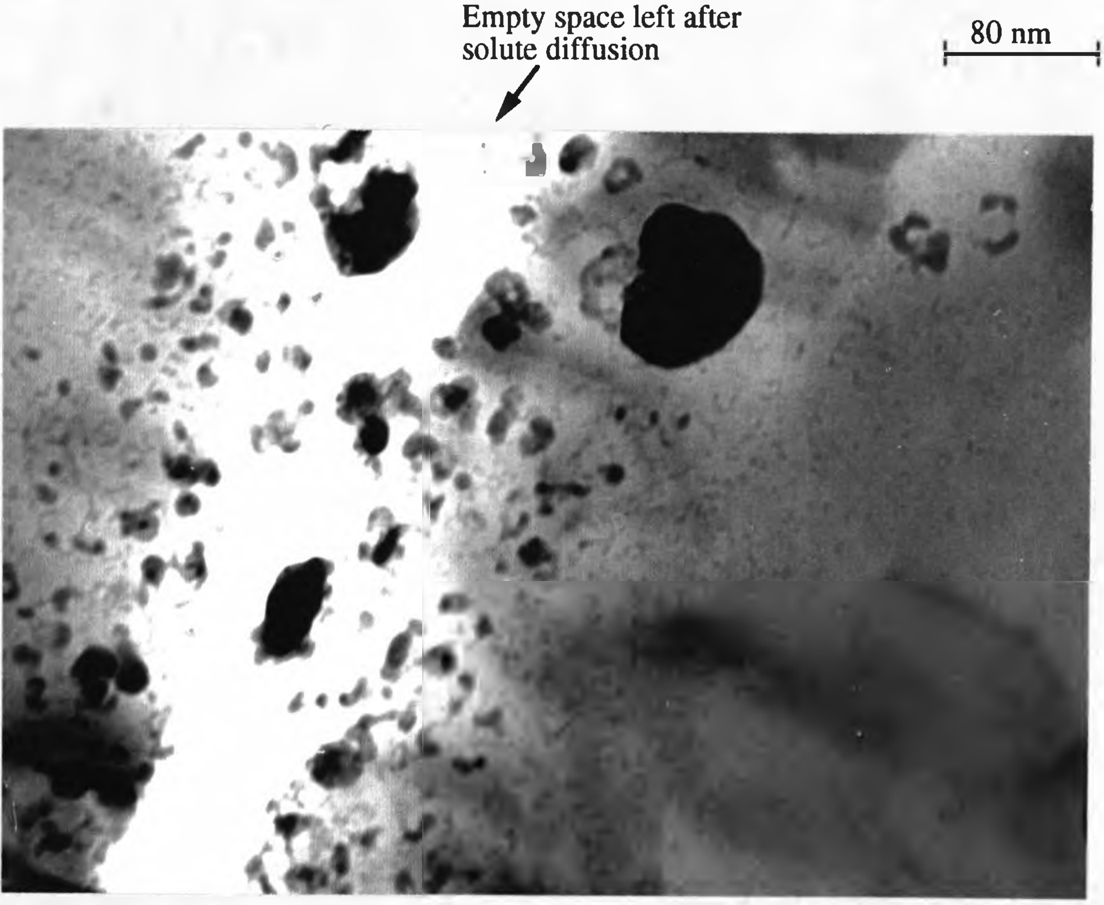

Figure 4.38. TEM micrograph showing evidence of solute diffusion from the interdendritic phase into the Al; this effect coincided with the formation of the P2 precipitates.

4.2. CORROSION PROPERTIES

4.2.1. 2014 Aluminium Alloy

4.2.1.1. Pitting of as-received 2014 T651 aluminium alloy

The resistance to pitting of 2014 T651 alloy measured by potentiodynamic anodic polarization in normal aerated chloride electrolytes was very low. The potential shift, E_{PD}, at the onset of pitting was less than 50 mV in 1M NaCl at 30°C. The free corrosion potential, E_{corr}, was typically ~-730 mV (SCE) in the aerated solutions but was never stable. In deaerated solutions E_{corr} was decreased to ~-750 mV (SCE) and became stable after half an hour of immersion. Irrespective of the nature of the solution the pitting potential, E_{pit}, remained approximately -690 mV (SCE).

Corrosion pits on the surface of the 2014 alloy in the as received condition were irregular deep pits as can be seen in Figure 4.39.

4.2.1.2. Pitting of the laser surface melted 2014 aluminium alloy

The results of the pitting scans carried out in the different chloride solutions for both the as received alloy and the laser surface melted alloy are summarised in Table 4.3. Table 4.3 shows that there was an increase in E_{pit} after laser surface melting. For the 2014 T6 alloy the potential difference, E_{PD}, between the free corrosion potential and the pitting potential was between 10 mV and 50 mV but after laser surface melting the difference was between 50 mV and 200 mV. On the whole, E_{corr} was decreased after LSM and E_{pit} was increased. A typical polarization curve for the surface melted 2014 alloy is shown in Figure 4.40.

A set of results from the measurements of free corrosion potential in aerated 1M NaCl solution against time for the 2014 alloy are shown in Figure 4.41. It is shown that the effect of laser surface melting was to raise the rest potential which is perhaps better described here as the free corrosion potential (E_{corr}). After about 100 hours of immersion E_{corr} for the surface melted alloy had decreased to the same level as the as received alloy. The two alloys then behaved in the same manner for a short time after which E_{corr} for the surface melted alloy decreased a little more to be come more or less steady at a value just less than that for the as received alloy. Studies of the surface after the immersion tests showed that corrosion had been most extensive at the track-track interfaces.

4.2.1.3. Corrosion morphology and distribution

Overall corrosion was observed to occur at four distinct sites on the surface of the LSM alloy. These sites coincide with, the overlap region between successive laser melt tracks, grain boundaries, solute bands and within the cellular dendritic subgrain structure itself. Examples of pitting[1] on the the alloy after laser surface melting are shown in Figure 4.42. During anodic polarization propagation of the pits seemed to spread more easily across the surface of the LSM alloy; pits were shallow rather than deep as in the case of the as received alloy. More significantly, in the timed immersion tests and at high anodic polarization, the corrosion propagated down through the LSM layer and eventually encountered the heat affected zone (HAZ) of the substrate; preferential corrosion along the grain boundaries then occurred. In the worse cases this led to small areas of the LSM layer spalling off. This latter behaviour was more noticeable in the timed immersion tests where corrosion along the track/track interfaces seemed to be the preferred mode of attack (see Figure 4.43).

4.2.1.4. Surface analysis by XPS

Analysis of the surface oxide film on the as received and LSM 2014 aluminium alloy was carried out by XPS. Figures 4.44 and 4.45 show wide spectrum profiles for the as received alloy and the laser surface melted alloy respectively; both were polished and

---

[1] Pitting does not occur in the classical sense, but for want of a better more general word, the term is used here to loosely describe the corrosion morphology seen in the LSM alloys.

left to air oxidise under normal ambient conditions. It was found that a freshly abraded surface of the as received alloy quickly oxidised forming a surface film of aluminium oxide. Analysis of the Cu 2p region revealed no trace of Cu in the surface film. As previously mentioned one of the pretreatments prior to surface melting was to immerse the alloy in 1M NaOH. XPS analysis of the surface after immersion showed that not only had the aluminium been oxidised very heavily but that the oxide contained all the major alloying elements; Cu, Mg, Mn, and Si. The Mg, Mn and Si were present in the oxide as mixed compounds; not necessarily as the respective basic oxides of each element. Peak binding energy data indicated that a complex silicate may have formed involving these three elements.

It has already been shown that after laser surface melting that there was a redistribution of the alloying elements within the melted layer arising from the formation of a different microstructure. Similarly the composition of the surface film after laser surface melting was also different (see Figure 4.45). XPS analysis showed that Mg and Si were present in the oxide as compounds and that Cu was present either in the elemental form or as Cu^+. Ar was also detected in the oxide which was present in the alloy as a result of being absorbed by the resolidifying melt pool from the shrouding gas used during LSM.

4.2.2. 7075 Aluminium Alloy

4.2.2.1. Corrosion of as received 7075 T6 aluminium alloy

The polarization curves for the 7075 alloy in standard 1M NaCl at 30°C are shown in Figure 4.46. The first observation was that there were apparently two breakdown potentials. The next observation was that the second breakdown potential became less noticeable with increasing pretest immersion times. The first breakdown potential was always approximately -800 mV (SCE) but the second breakdown potential seemed to increase slightly with increasing immersion time. When the tests were repeated in deaerated 1M NaCl solution the second breakdown potential was virtually non-existent after only 5 minutes pretest immersion and had completely disappeared for immersion times greater than 10 minutes; the value of the first breakdown potential was unchanged from that measured in the aerated solutions.

Inspection of the surface of some of the samples after potentiostatic polarization at -800 and -760 mV (SCE), just before the two individual breakdown potentials, in deaerated 1M NaCl solution, showed that for the first breakdown potential intergranular corrosion was the mode of attack and for the second it was mainly pitting that occurred. Also, after immersion in the same solution for periods of up to two weeks it was found that whilst the sample had suffered from both intergranular corrosion and pitting corrosion it was the former that was the most severe.

4.2.2.2. Corrosion of the laser surface melted 7075 aluminium alloy

Laser surface melting was found to have little or no effect on the breakdown potential of the 7075 alloy. In aerated 1M NaCl solution the only noticeable effect was that the second breakdown potential was no longer observed. In the deaerated solution the breakdown potential was measured to be between -770 and -790 mV (SCE) and thus moved to a slightly more positive potential than that of the as received alloy. E_{corr} was generally slightly lower than the value for the as received alloy, ~-1000 mV (SCE) compared to ~ 900 - 950 mV. A typical polarization curve for the surface melted 7075 alloy is shown in Figure 4.47.

In addition to the polarization measurements, immersion tests were carried out to monitor the change in free corrosion potential with time. Figure 4.48 shows the results for both the as received alloy and the surface melted alloy. As with the polarization measurements very little difference was found in the corrosion behaviour of the surface melted alloy. Figure 4.48 shows that E_{corr} behaved in more or less the same way for both of the alloy conditions. E_{corr} for the surface melted alloy started at a slightly lower potential but after a few hours the potential of the as received alloy had decreased to a level similar to the surface melted alloy.

4.2.2.3. Corrosion morphology and distribution

On the as received alloy pits were clearly observed to form at second phase particles. However, intergranular corrosion was the main form of attack as can be seen from Figure 4.49. On the surface melted alloy corrosion also occurred preferentially at the grain boundaries, especially at the grain boundaries adjacent to the melt track/melt track interfaces. The interfaces between overlapping melt tracks did show signs of attack but preferential dissolution was not serious.

Whereas in the as-received alloy the corrosion was intergranular and therefore tended to penetrate deep into the sample, the corrosion on the surface melted alloy tended to be more transgranular initially; this can be seen in Figure 4.50. In this micrograph the pit initiated at a grain boundary and the direction of pit propagation was along the cellular dendrites lying parallel to the exposed surface. Pits that formed on immersion tested samples or samples polarised to several hundred millivolts above the breakdown potential penetrated the full depth of the melted layer. Dissolution of the substrate was, however, halted by a change in the direction of the corrosion reaction. When the pits reached the partially melted grains in the HAZ preferential attack along the grain boundaries occurred because of the enhanced size of the precipitate free zone, this is illustrated in Figure 4.51. After sufficiently long periods of time this resulted in regions of the melted layer spalling off and exposing the unaffected substrate which then continued to be attacked in the usual intergranular fashion.

4.2.2.4. Surface analysis by XPS

Qualitative analysis of the oxide of the as-received and surface melted alloys (see Figure 4.52 and Figure 4.53 respectively) showed that there was no fundamental difference in composition of the oxide on the as-received alloy and the LSM alloy.

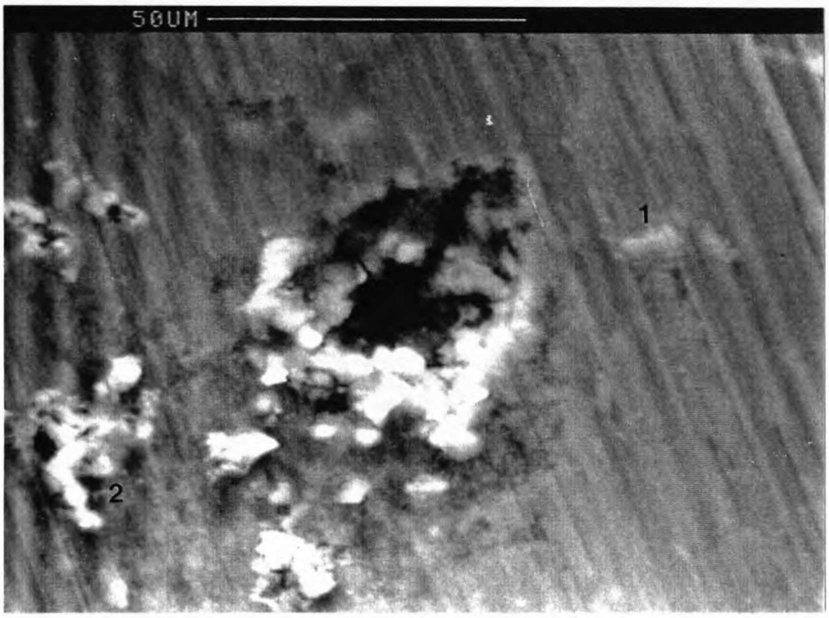

Figure 4.39. SEM micrograph showing a pit on the surface of as-received 2014 alloy. The growth of the pit was accelerated by the presence of second phase particles, marked 1 and 2.

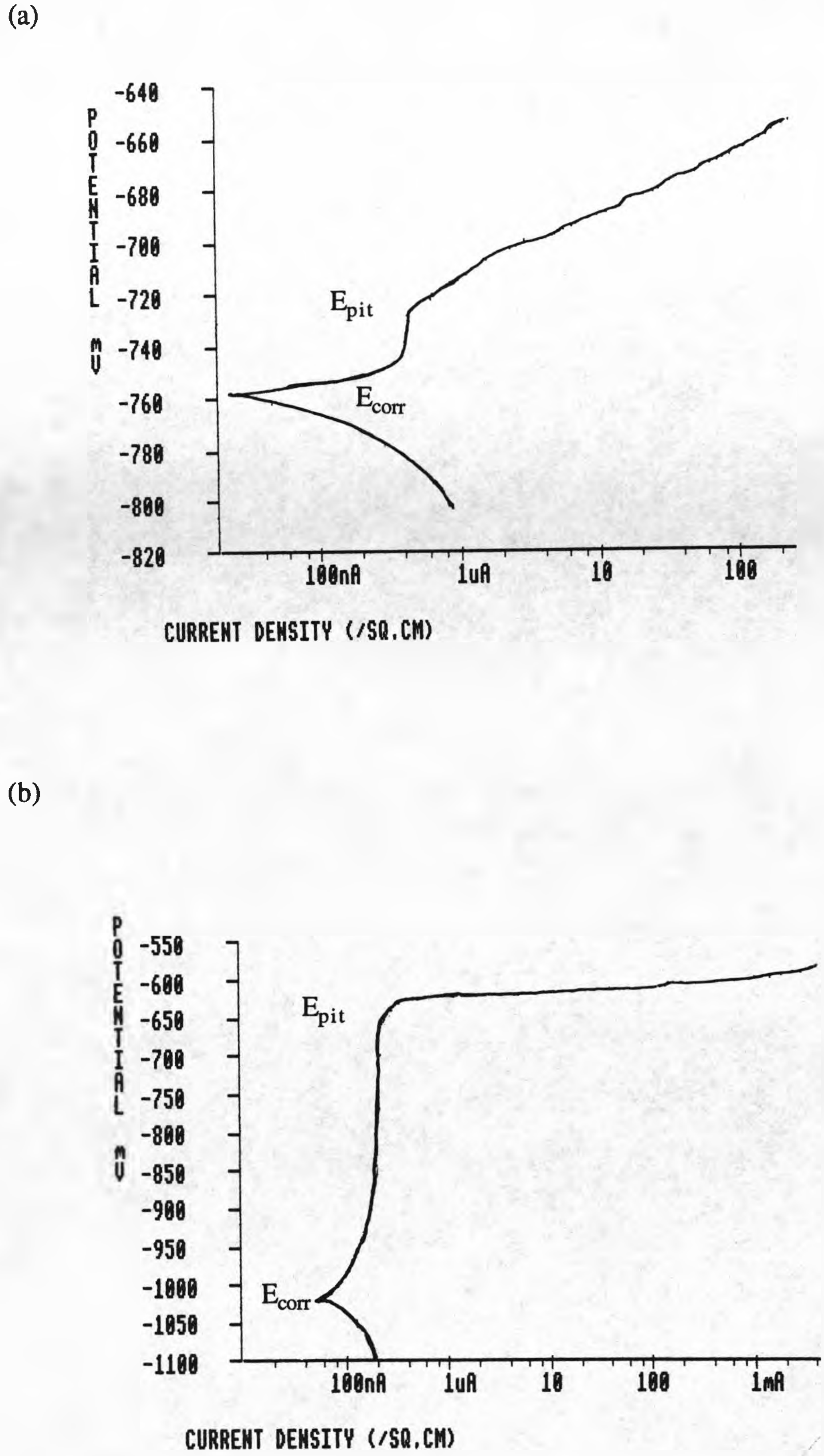

Figure 4.40 Potentiodynamic anodic polarization curves: (a) as-received 2014 alloy; (b) LSM 2014 alloy. Tested in 1 M NaCl, 30 °C, deaerated for 2 hrs with N_2, 10 mV/min. The vertical scale shows the absolute potential versus SCE

Test solution	Alloy	E_{corr} (mV SCE)	E_{pit} (mV SCE)	E_{PD} (mV)
1 M NaCl (30 mV/min)	AR 2014	- 656	- 631	25
	SM 2014	- 599	-	-
	AR 7075	- 817	- 797/- 742	20/75
	SM 7075	- 830	- 815	15
1 M NaCl (deaerated)	AR 2014	- 755	- 700	55
	SM 2014	- 1029	- 617	412
	AR 7075	- 905	- 795	110
	SM 7075	- 999	- 782	217
0.1 M NaCl (deaerated)	AR 2014	- 688	- 638	50
	SM 2014	- 996	- 536	460
	AR 7075	- 901	- 711	190
	SM 7075	- 985	- 720	265
3 % NaCl pH 8 (60 mV/min)	AR 2014	- 687	- 607	80
	SM 2014	- 610	- 530	80
	AR 7075	- 780	- 760/- 670	20/110
	SM 7075	- 784	- 720	64
0.1 M KCl (deaerated)	AR 2014	- 726	- 646	80
	SM 2014	- 781	- 546	235

Table 4.3. Anodic polarization data for the as-received (AR) and LSM (SM) alloys. Potential scan rate = 10 mV/min unless stated otherwise, laser scan velocity = 20 mm/s.

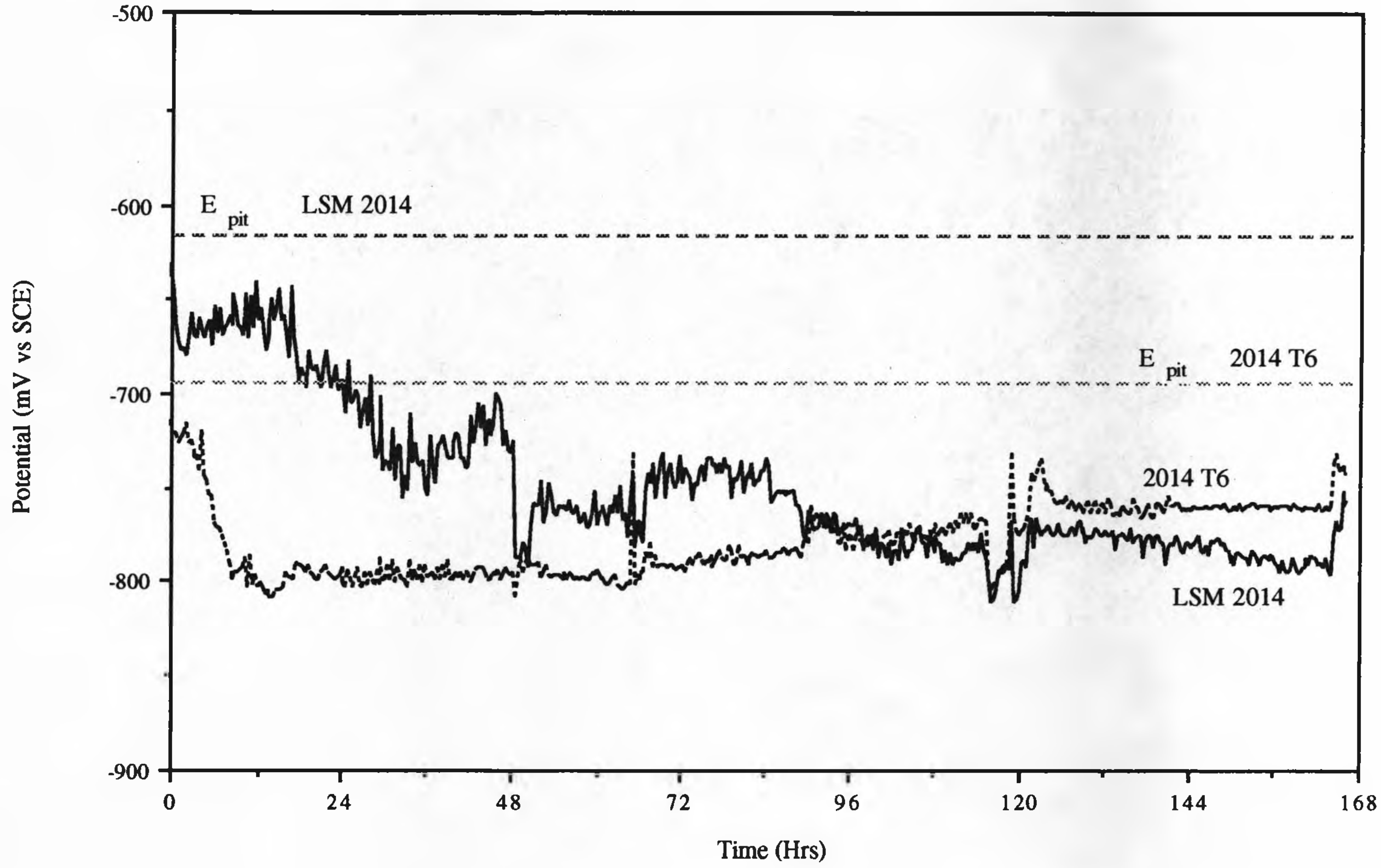

Figure 4.41. Free corrosion potential versus time for the as-received 2014 T6 and LSM 2014 alloys in 1M NaCl at 30 °C.

(a)

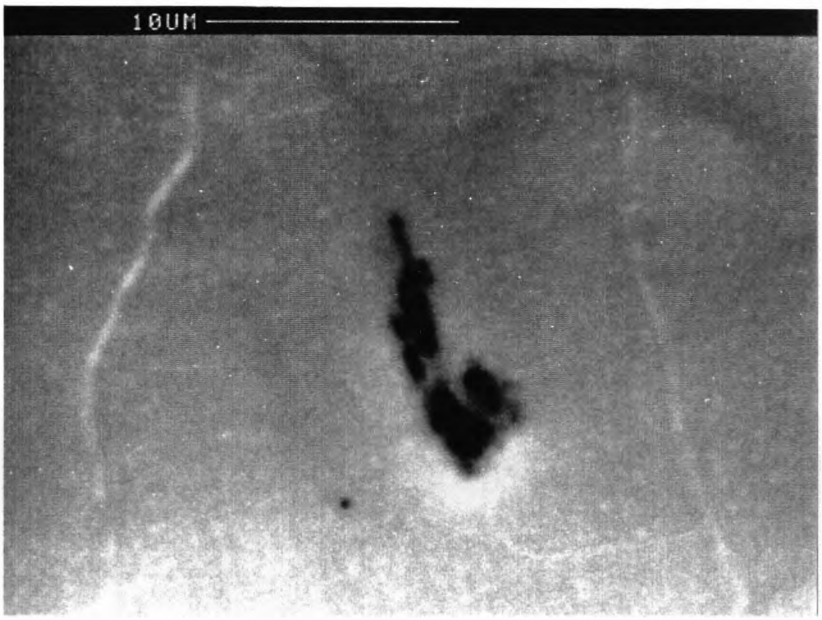

(b)

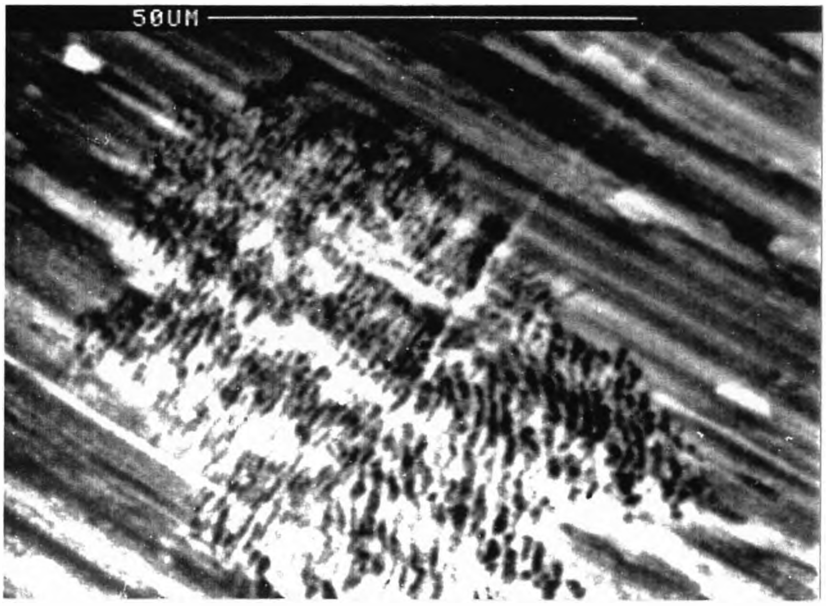

Figure 4.42. SEM micrographs showing two forms of corrosion on the LSM 2014 alloy. (a) Intradendritic corrosion of the α-Al accelerated by the interdendritic phase. (b) Transgranular corrosion nucleated at the grain boundary and spreading by the same mechanism as in (a).

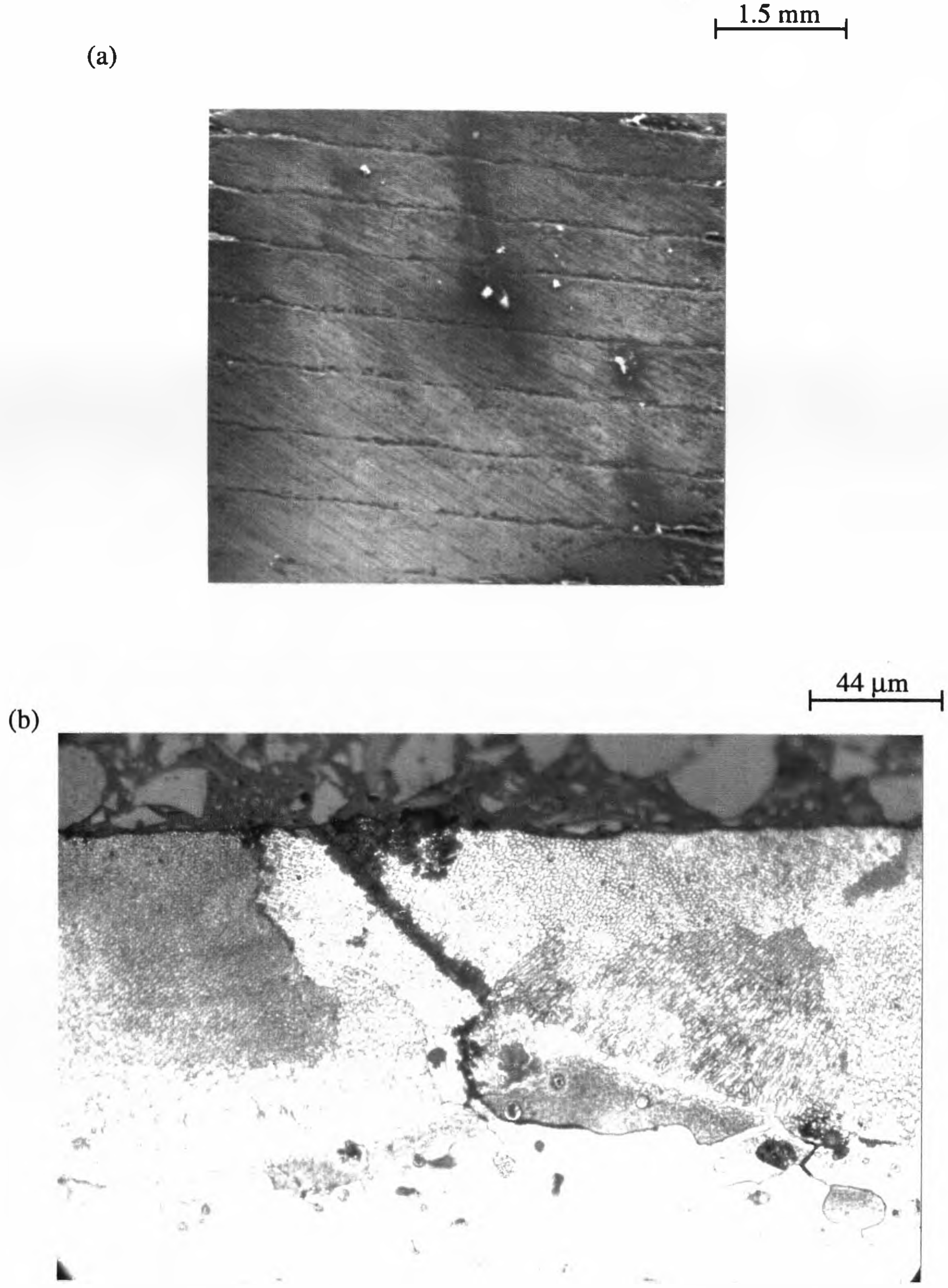

Figure 4.43. Optical micrographs illustrating intertrack corrosion: (a) After anodic polarization in 3 % NaCl pH 8 at 100 mV/min; (b) after immersion in 1 M NaCl for 150 hrs.

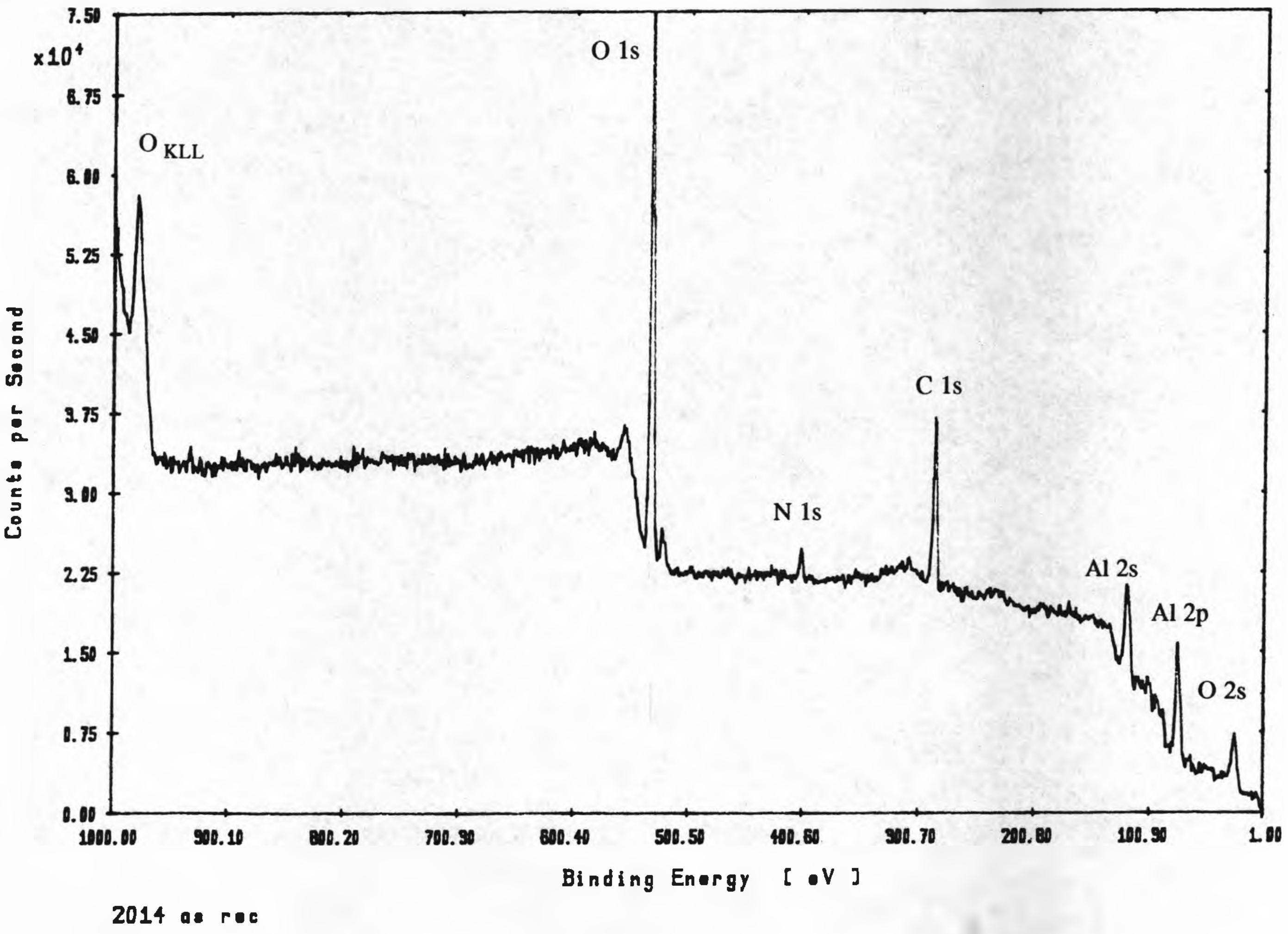

Figure 4.44. XPS wide scan profile for the surface of as-received 2014 alloy. Sample polished and exposed to normal atmospheric conditions.

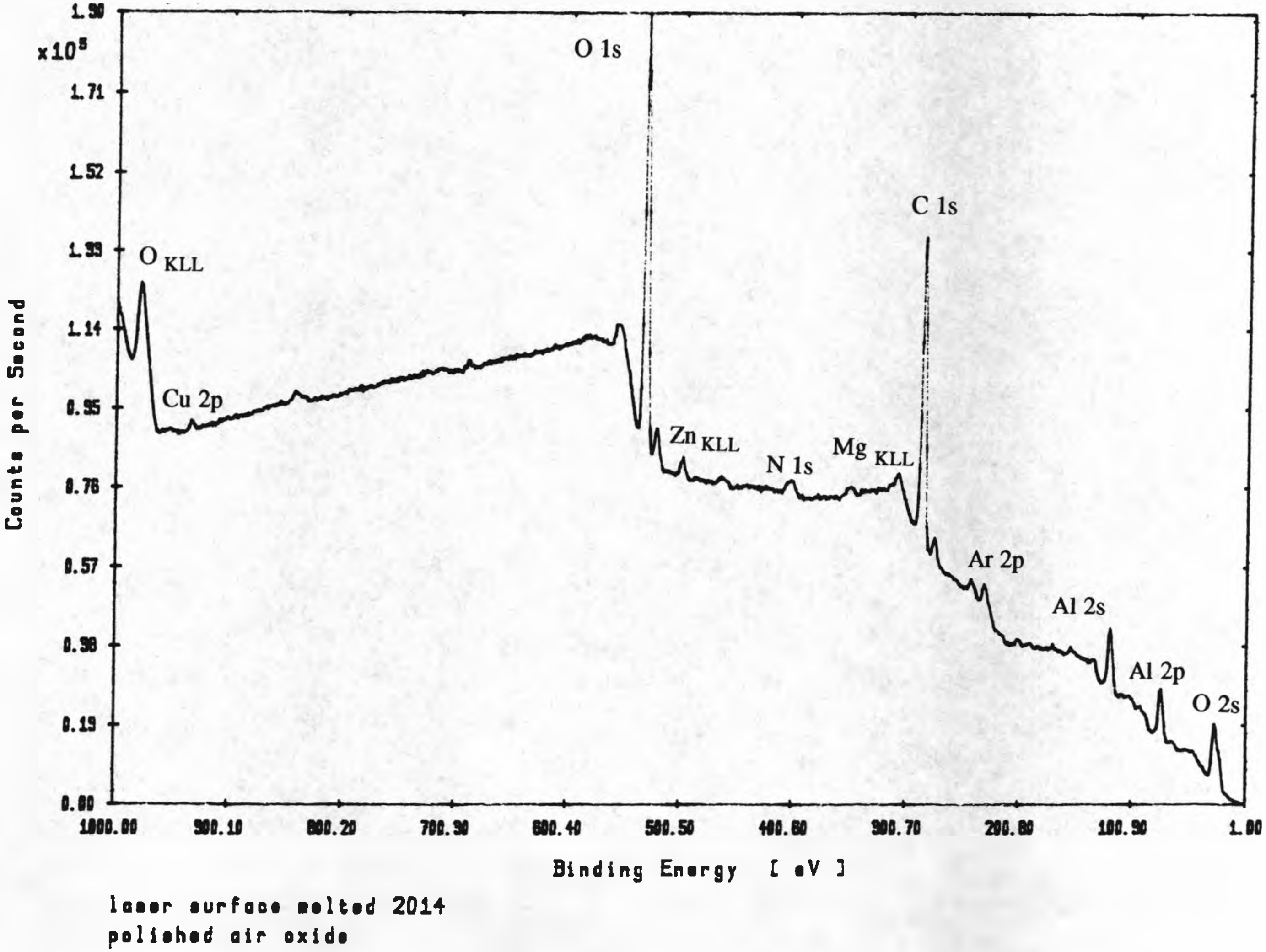

Figure 4.45. XPS wide scan profile for the surface of LSM 2014 alloy. Sample polished and exposed to normal atmospheric conditions.

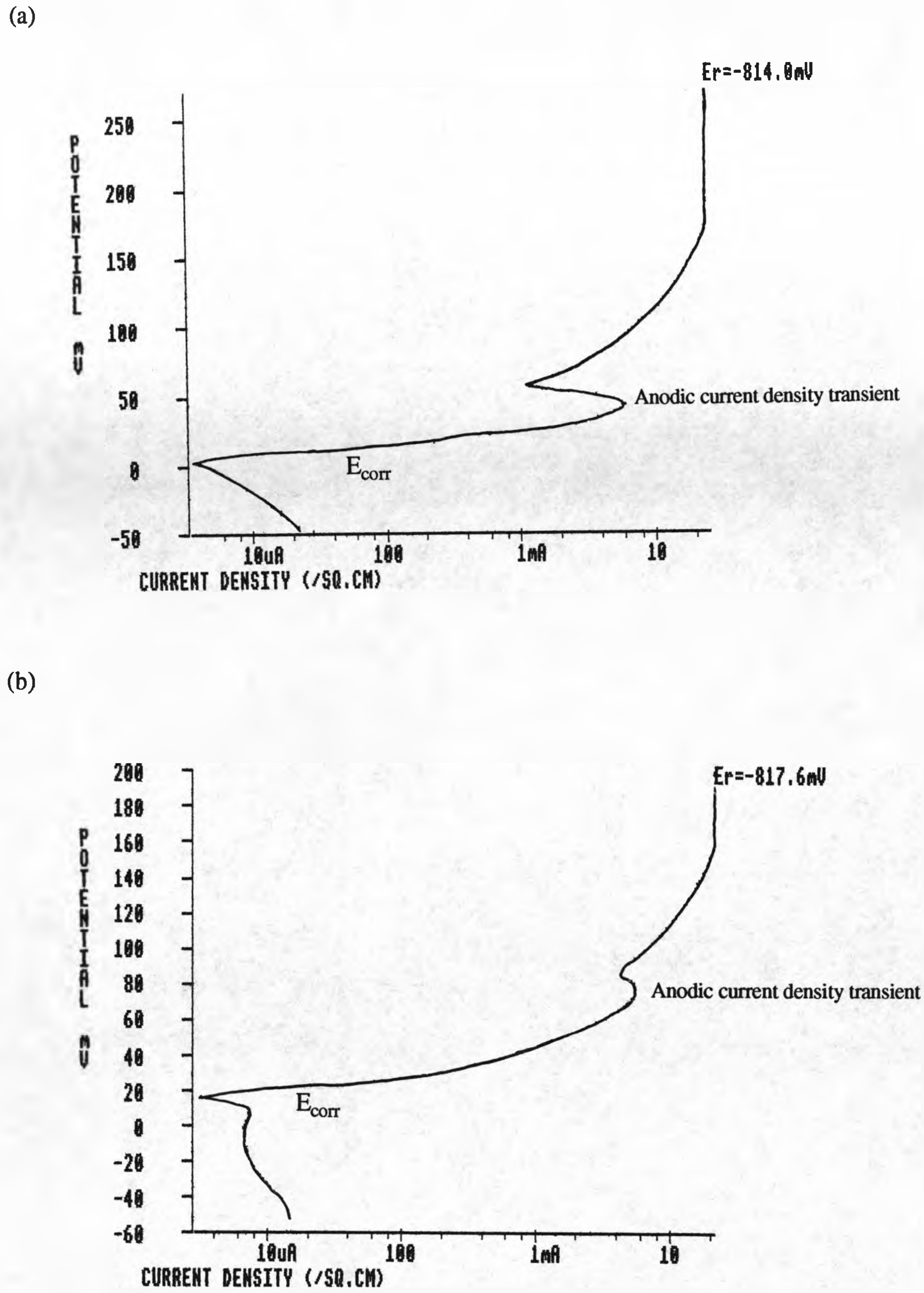

Figure 4.46. Potentiodynamic anodic polarization curves for as-received 7075 alloy; (a) immersed for 5 before testing, (b) immersed for 60 mins before testing.Tested in 1 M NaCl, 30 °C, 30 mV/min. The vertical scale shows the potential difference from E_{corr} (Er)

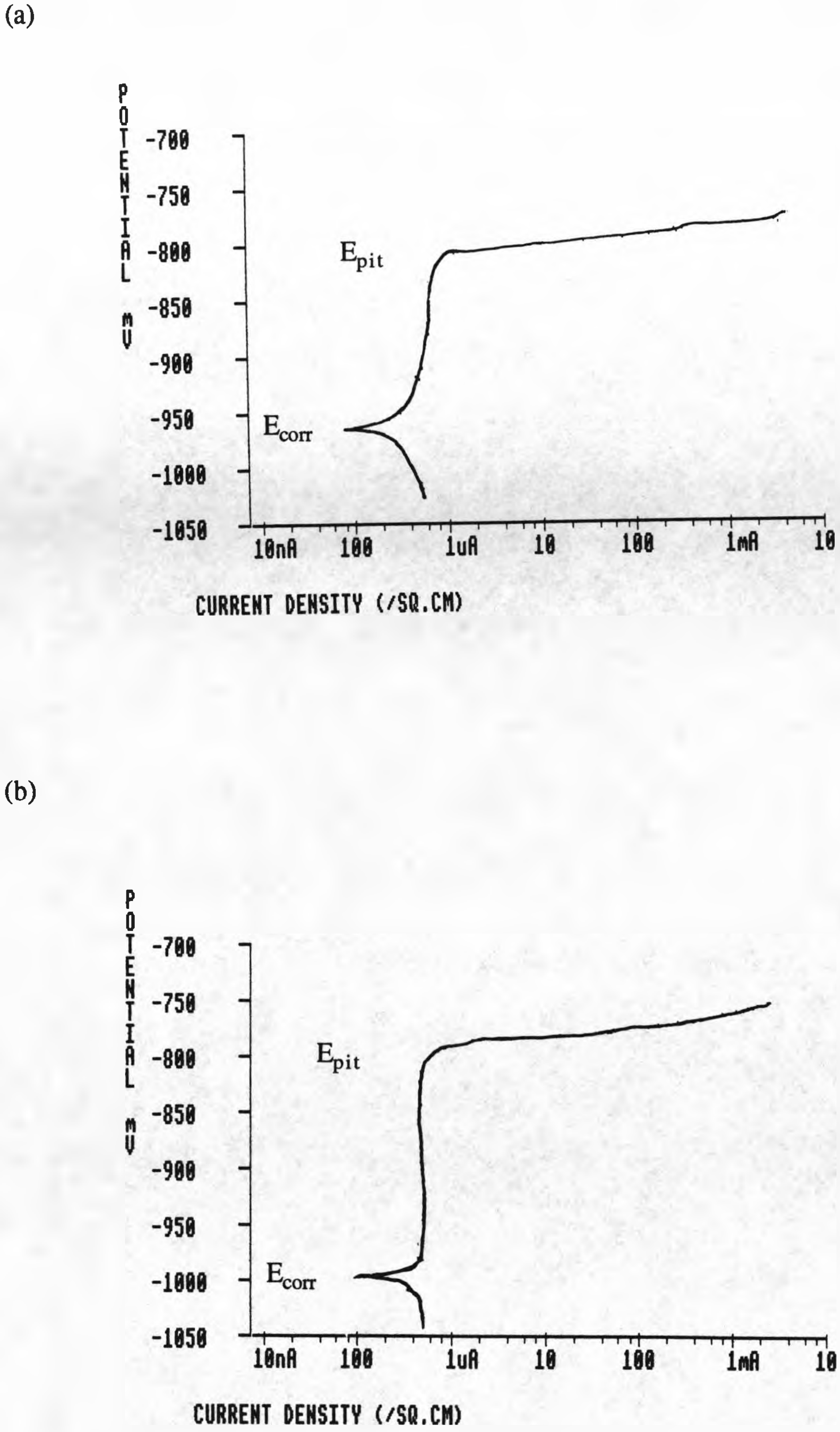

Figure 4.47. Potentiodynamic anodic polarization curves: (a) as-received 7075 alloy; (b) LSM 7075 alloy. Tested in 1 M NaCl, 30 °C, deaerated for 2 hrs with N_2, 10 mV/min. Vertical scale shows the absolute potential versus SCE.

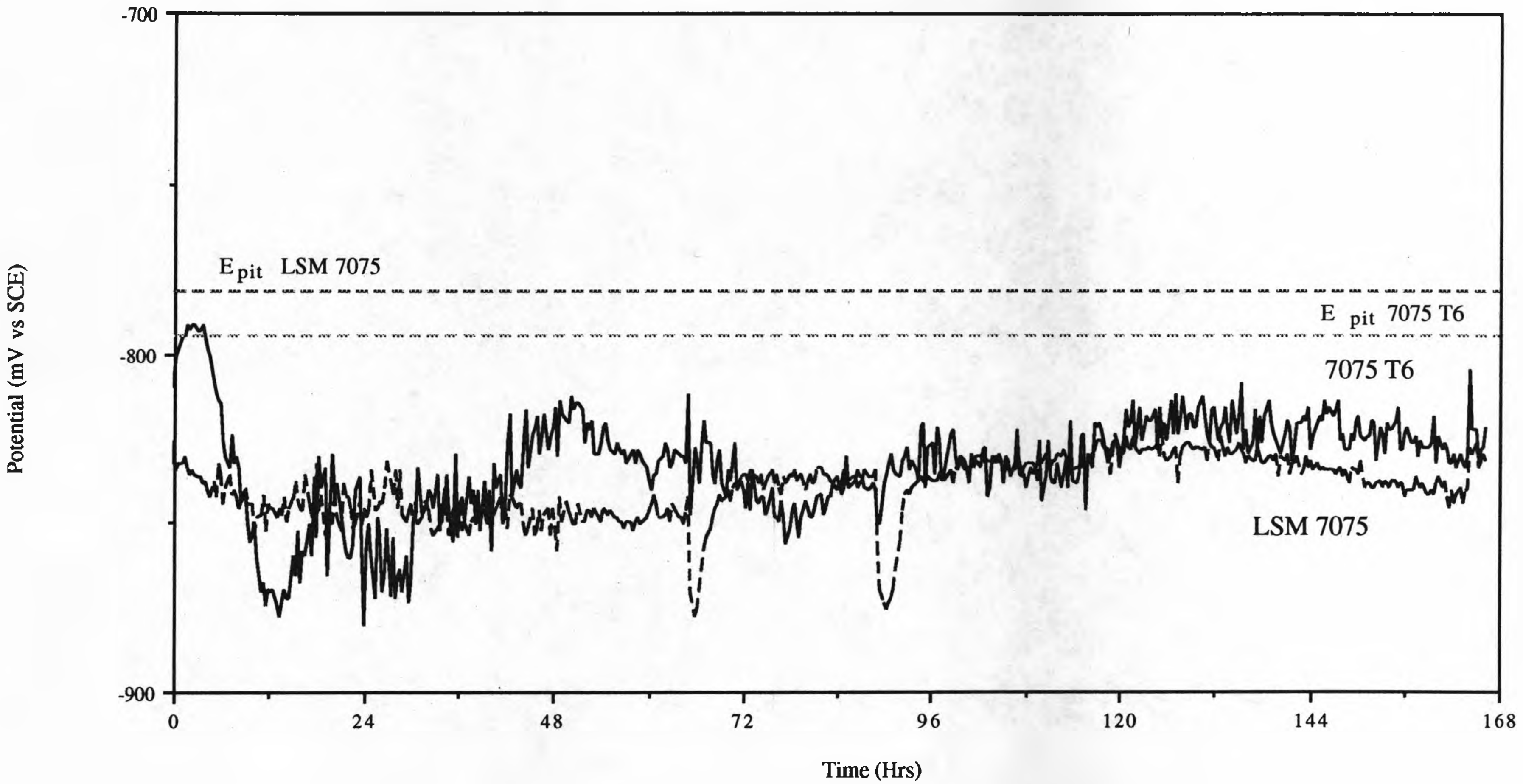

Figure 4.48. Free corrosion potential versus time for the as-received 7075 T6 and LSM 7075 alloys in 1 M NaCl at 30 °C.

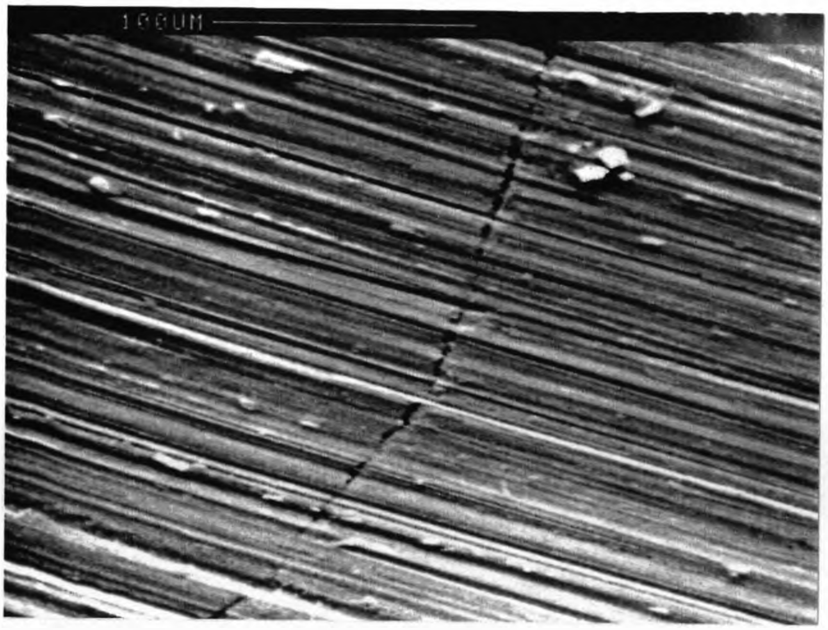

Figure 4.49. SEM micrograph showing evidence of intergranuar corrosion on as-received 7075 alloy.

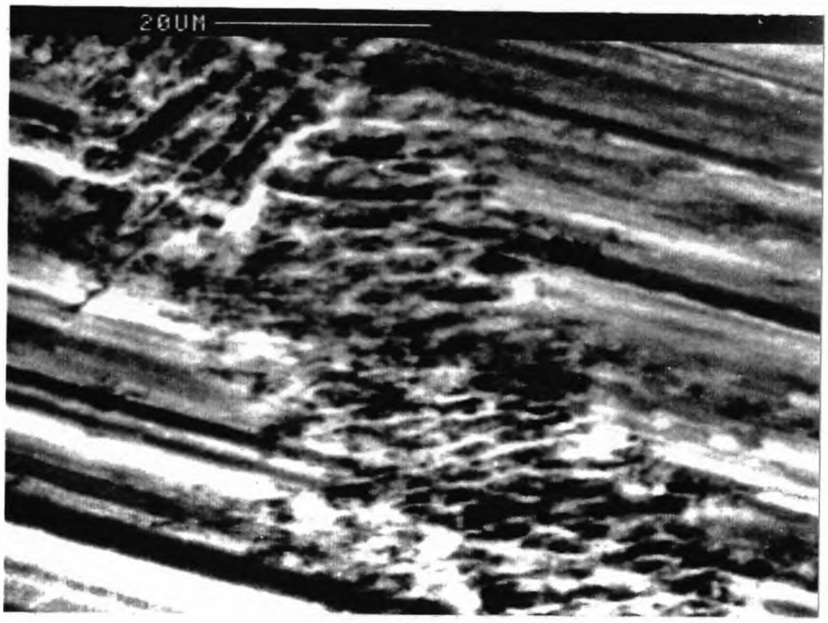

Figure 4.50. SEM micrograph illustrating transgranular corrosion on LSM 7075 alloy, nucleated at a grain boundary.

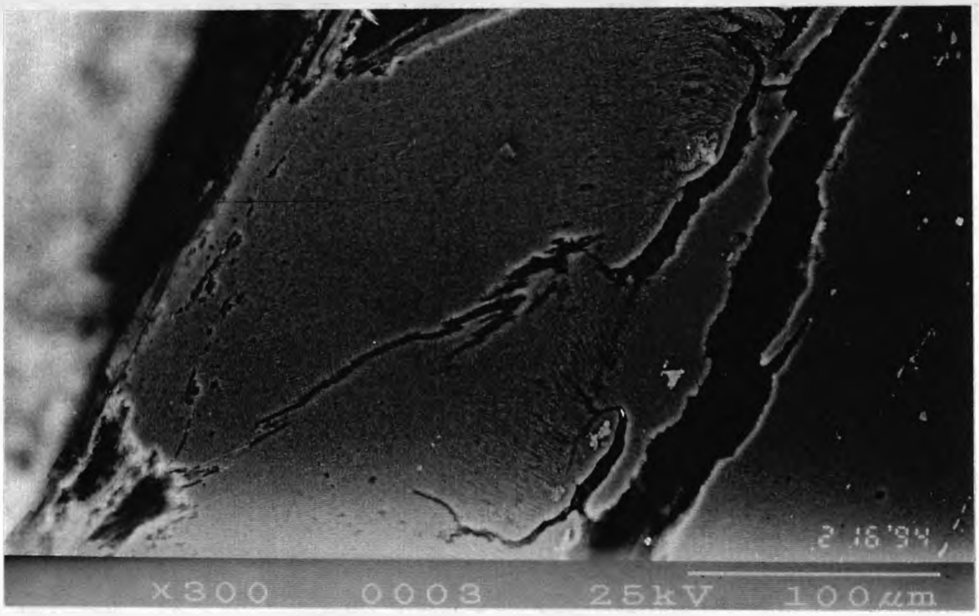

Figure 4.51. SEM micrograph illustrating the severity of corrosion along the grain boundaries in the HAZ of the 7075 alloy substrate once the melted layer had been penetrated; this occurred only during immersion tests and at large anodic polarization potentials.

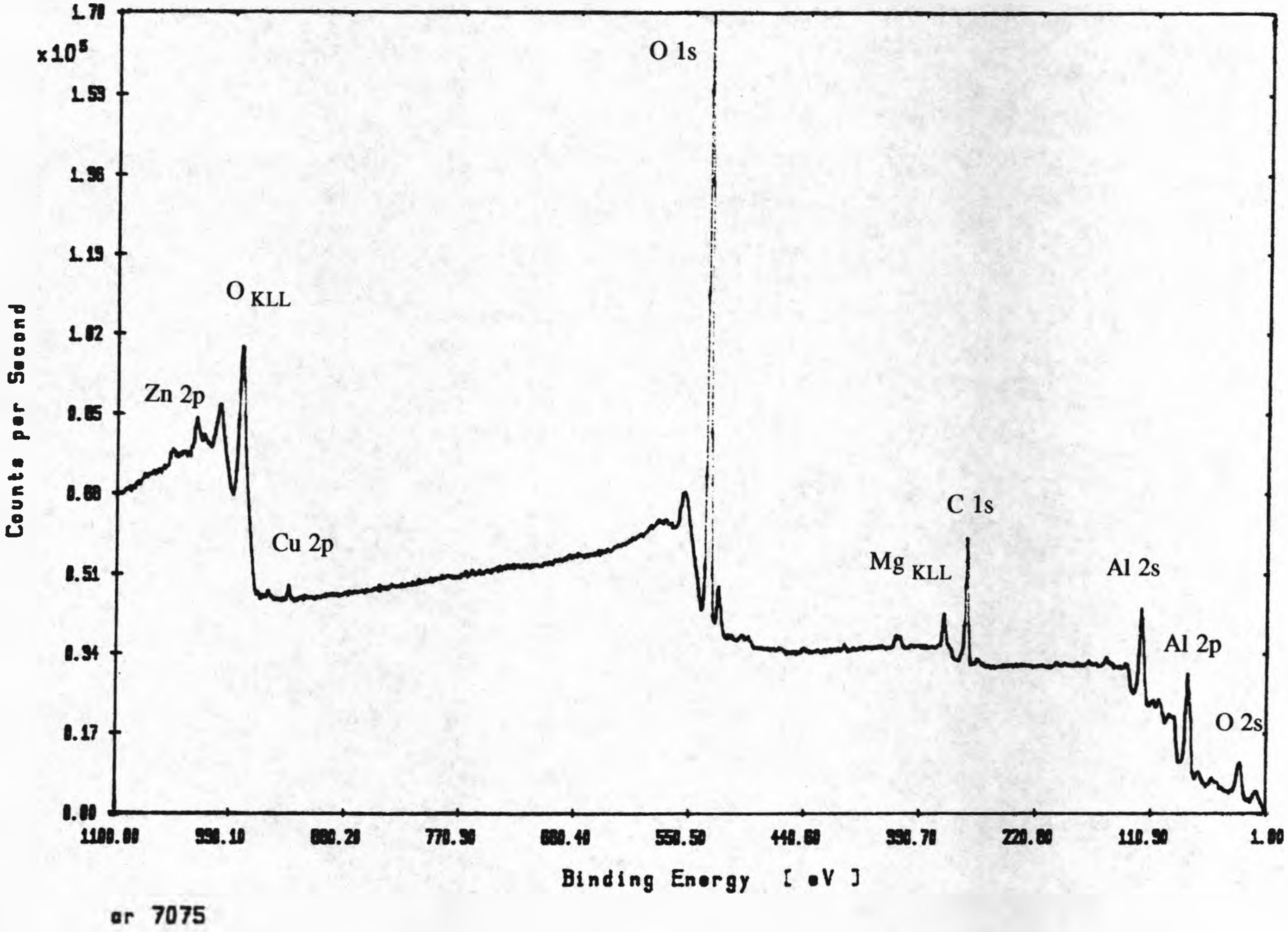

Figure 4.52. XPS wide scan profile for the surface of as-received 7075 alloy. Sample polished and exposed to normal atmospheric conditions.

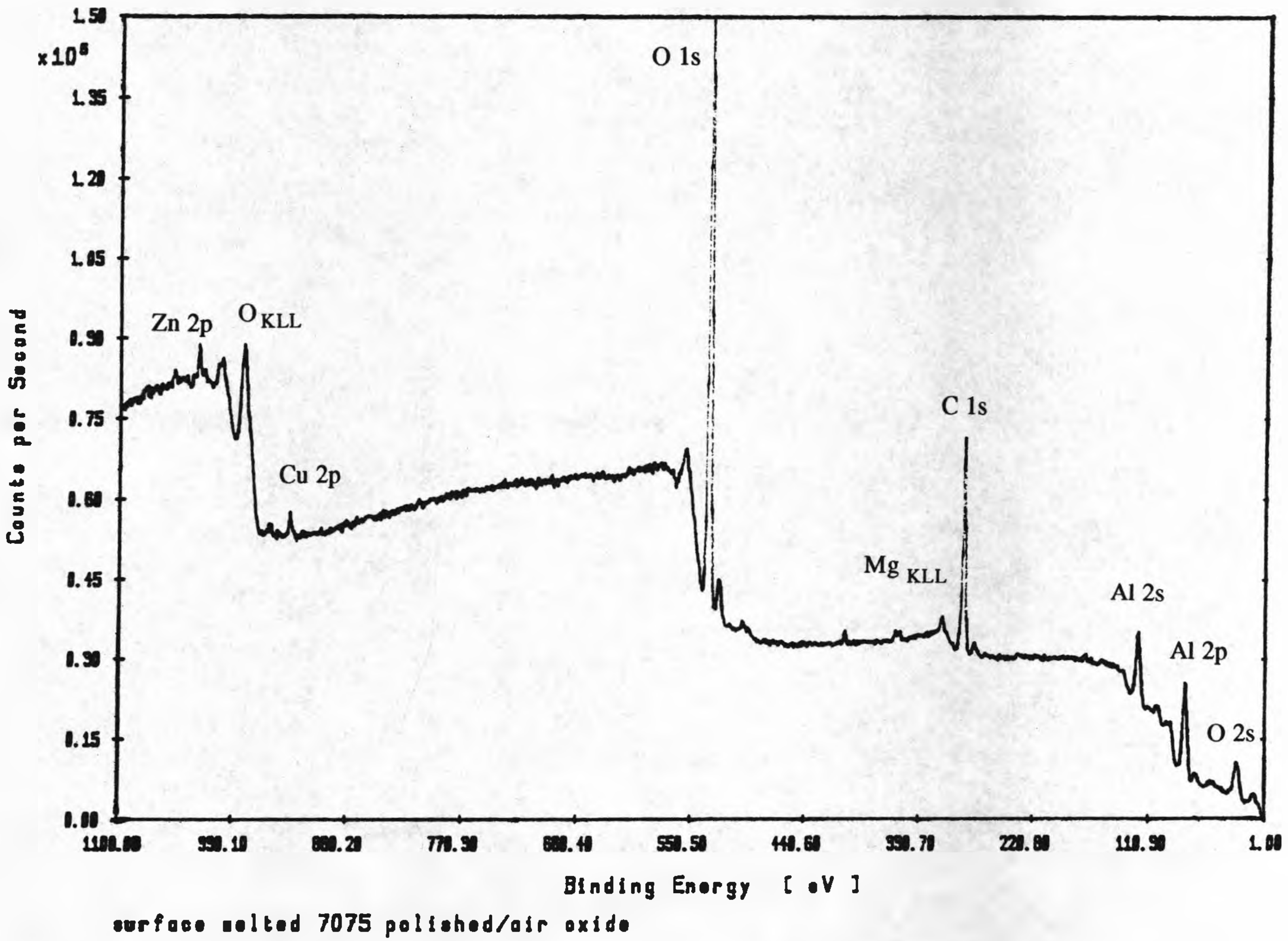

Figure 4.53. XPS wide scan profile for the surface of LSM 7075 alloy. Sample polished and exposed to normal atmospheric conditions.

4.3. MECHANICAL PROPERTIES

4.3.1. Hardness Results

Hardness measurements were carried out to provide an indication of the mechanical properties of the materials. Laser surface melting had the effect of decreasing the hardness of both the 2014 and 7075 alloys. This can be seen in the graphs shown in Figure 4.54 and 4.55. The micro-hardness of the as received 2014 and 7075 alloys was ~ 175 Hv and ~200 Hv respectively, but in the melted layer the hardness had decreased to as low as half of the original value in some areas. Variation of the hardness was observed as the microstructure changed, the lowest values coinciding with the banded structures and just below the surface. The hardness profile in Figure 4.54 also shows the true extent of the HAZ. Studies of the microstructure showed the depth of the HAZ to be of the order of 100 μm but Figure 4.54 demonstrates that the hardness value did not equal the value of the as-received alloy until depths of the order of 1 mm were reached.

4.3.2. Residual Stress Results

The residual tensile stresses were measured in the laser surface melted 2014 alloy for multiple overlapping tracks and for two different surface pretreatments. Both the sodium hydroxide treatment and the sooting were carried out to decrease the reflectivity of the aluminium alloy. Figure 4.56 shows that the surface tensile residual stresses were higher when the alloy was pretreated by immersion in sodium hydroxide solution. From Figure 4.56 it is also possible to see that there was a relationship between laser scan velocity and residual stress; increasing the scan velocity increased the residual stress. It was also found that as scanning velocity was increased to more than 70 mm/s the residual stress started to decrease rapidly.

Figure 4.57 shows the effect of changing the distance between melt tracks on residual stress. It can be seen that as the distance increases, or the percentage of overlap decreases, the residual stress increases. However, it can also be seen that the stress remained below the value for a single melt track (~155 MPa) which was always tensile in the case of these alloys .

The residual stress was also found to vary through the depth of the melted layer. This is shown qualitatively in Figure 4.58 in which the the diffraction angle 2θ is plotted against $\sin^2\psi$, where ψ is the angle of orientation of the sample to the incident radiation. For a uniform stress distribution the plotted curve should be linear but as Figure 4.58 shows the stress distribution was non-linear. Stress measurements were also carried out after successive layer removal and the results are plotted in Figure 4.59. It can be seen that the highest residual stresses were at the fusion boundary where there was a sharp decrease in the HAZ and eventually at 520 μm, just below the HAZ, the stress started to become compressive.

One sample of each of the alloys was heat treated at 100°C in order to study how the residual stresses changed with heating time and the results of this are shown in Figure 4.60. Initially there was an increase in the residual stress in both of the alloys. This was more noticeable in the 2014 alloy which showed a change from ~115 MPa to ~140 MPa but after the first hour the increase stopped and the residual stress then began to decrease. After 4 hrs the residual stress had fallen to ~100 MPa but at the last measurement (~5.5 hrs) the stress had slightly increased again to nearly 110 MPa. For the 7075 alloy the stress levelled off at a constant value of ~135 MPa after nearly 2 hours.

4.3.3. The Effect of Residual Stress on Corrosion Resistance

From Figures 4.61 and 4.62 it can be seen that there was a decrease in pitting potential with increases in residual stress; the effect being as a function of the intertrack distance and laser scan velocity, respectively. However, although the residual stresses seemed to have had a deleterious effect on the pitting potential the actual value remained above that of the as-received materials. A characteristic feature of many of the pits that formed on the surface melted alloy was microcracking. Figure 4.63 shows cracks that occurred at the base of a corrosion pit. It can be clearly seen that cracks have opened up in the centre of the grains parallel to cellular dendrites and not at the grain boundaries. This was taken as an indication that the residual stresses were high enough to induce a form of localised stress corrosion cracking. Other than this there was not a significant amount of preferential corrosion at cracks that have been associated with the residual stress.

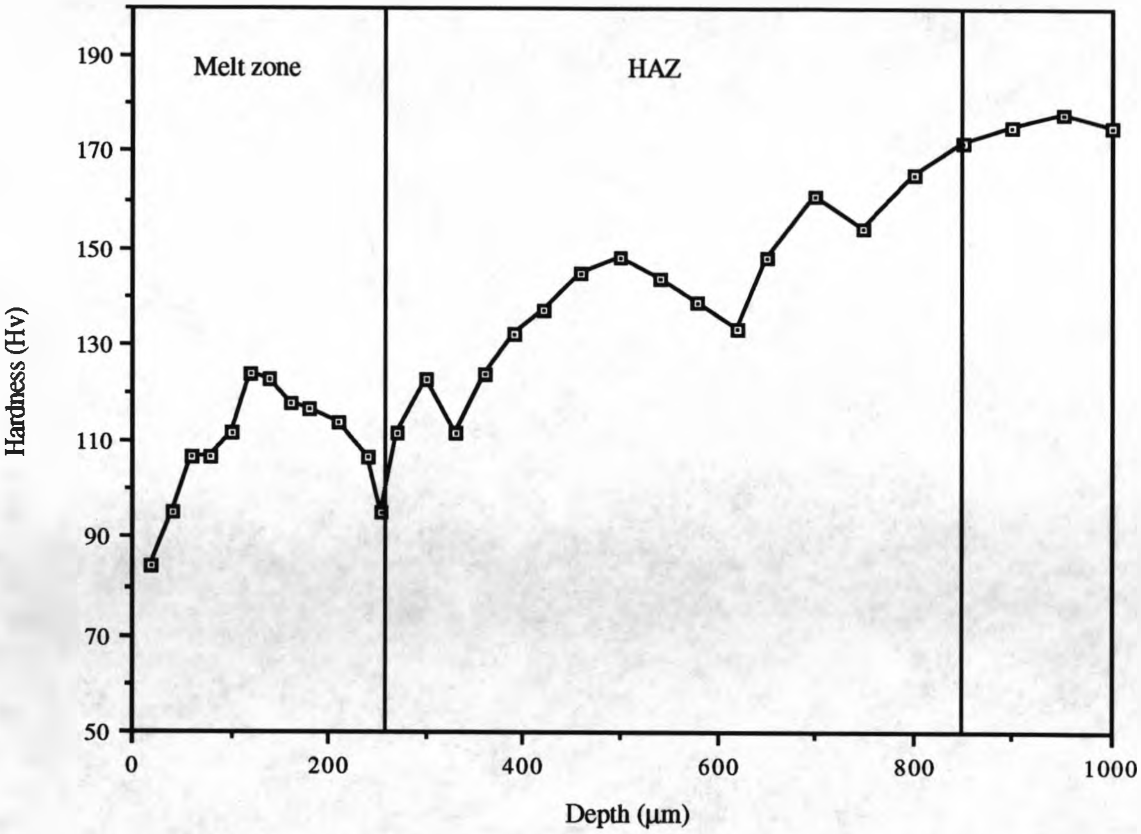

Figure 4.54. Hardness versus depth for LSM 2014 alloy; Vs = 15 mm/s, pretreated with NaOH. The curve shows the true extent of the HAZ.

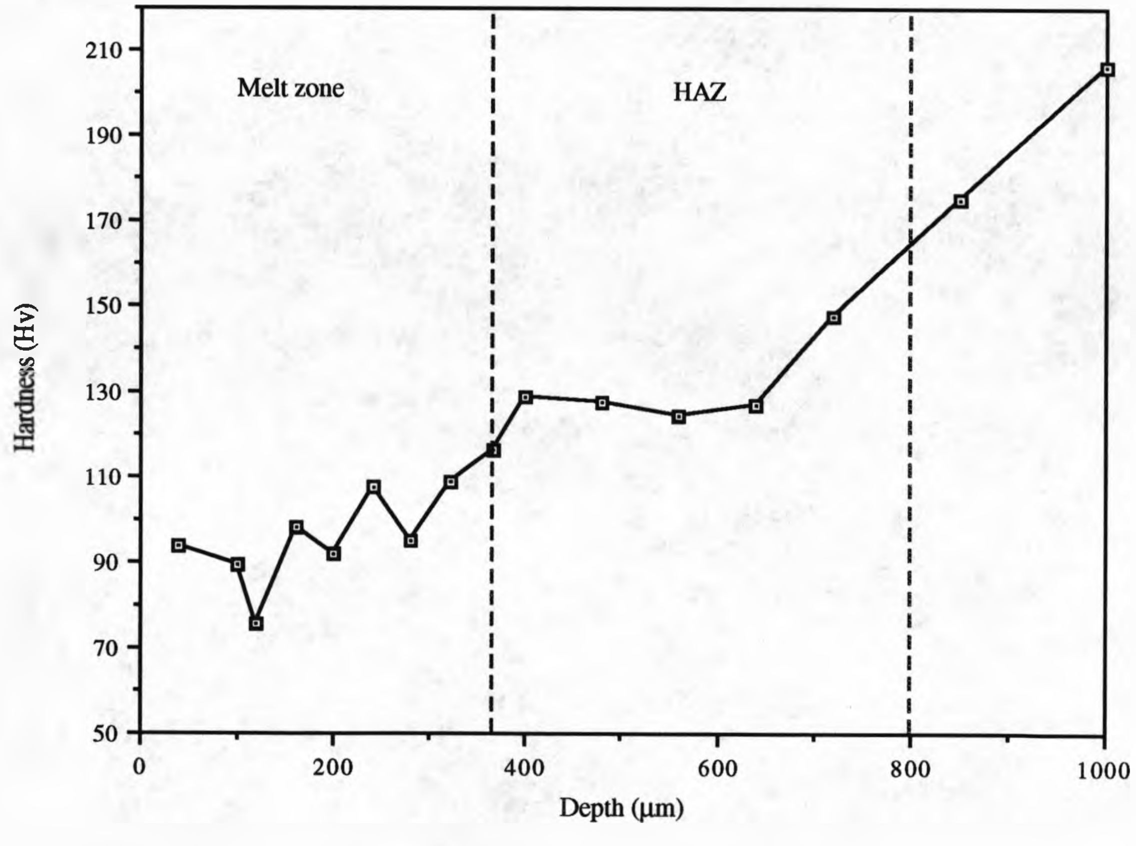

Figure 4.55. Hardness versus depth for LSM 7075 alloy; Vs = 22 mm/s pretreated with NaOH

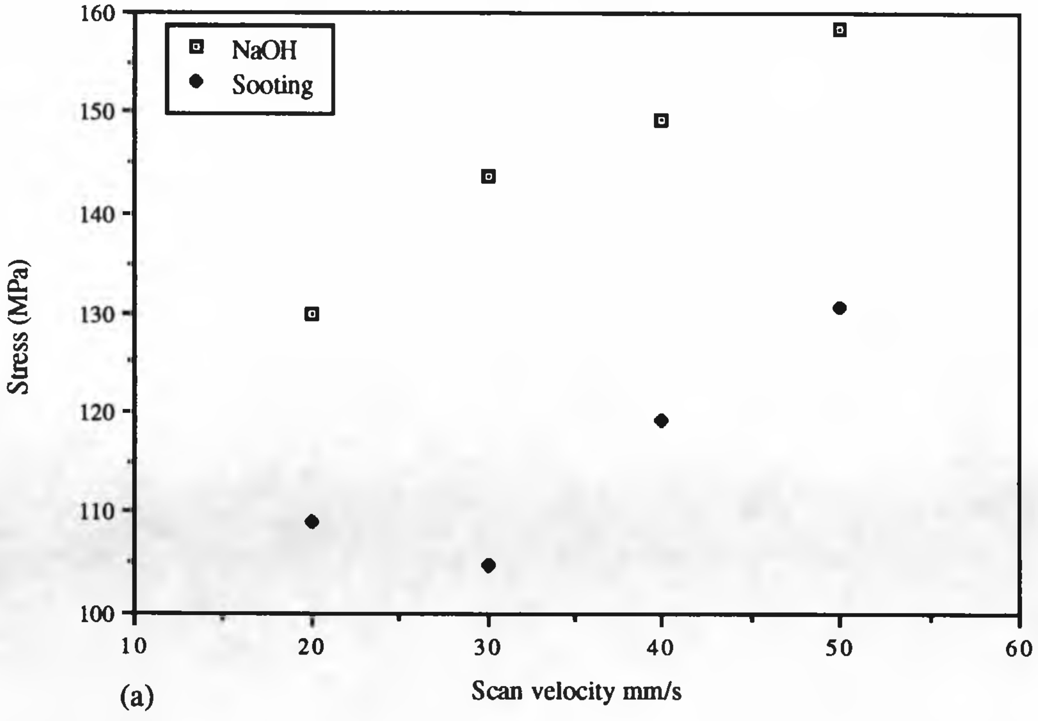

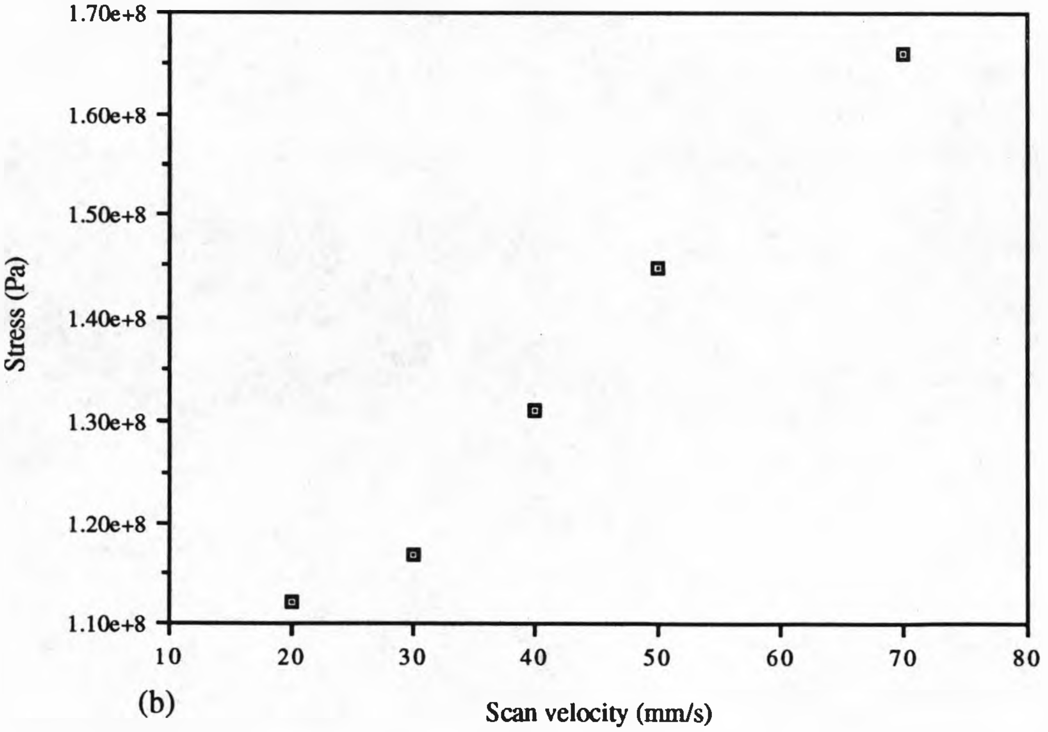

Fig.4.56. The effect of scan velocity on residual stress in laser surface melted aluminium alloys; (a) 2014 with different pre-treatments, (b) 7075 pre-treated by sooting.

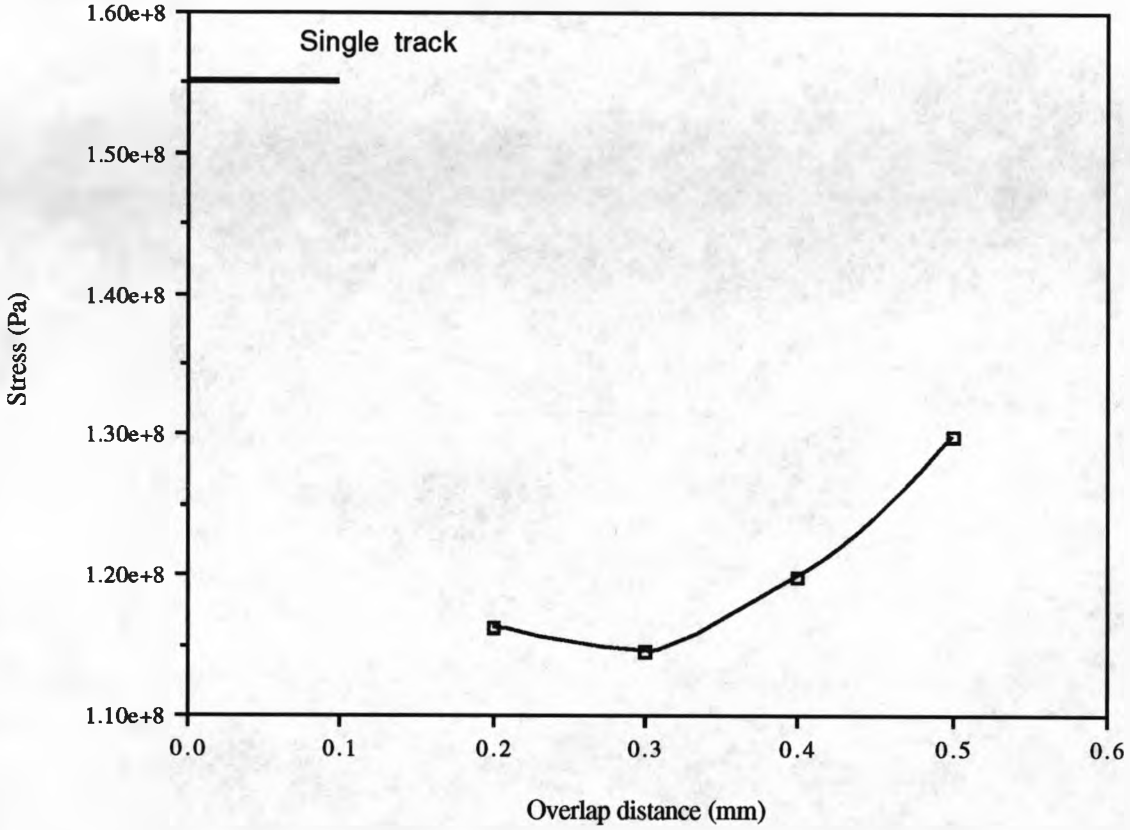

Fig.4.57. The effect of melt track overlap distance on residual stress; 2014 alloy pre-treated with NaOH; laser scan velocity = 20 mm/s.

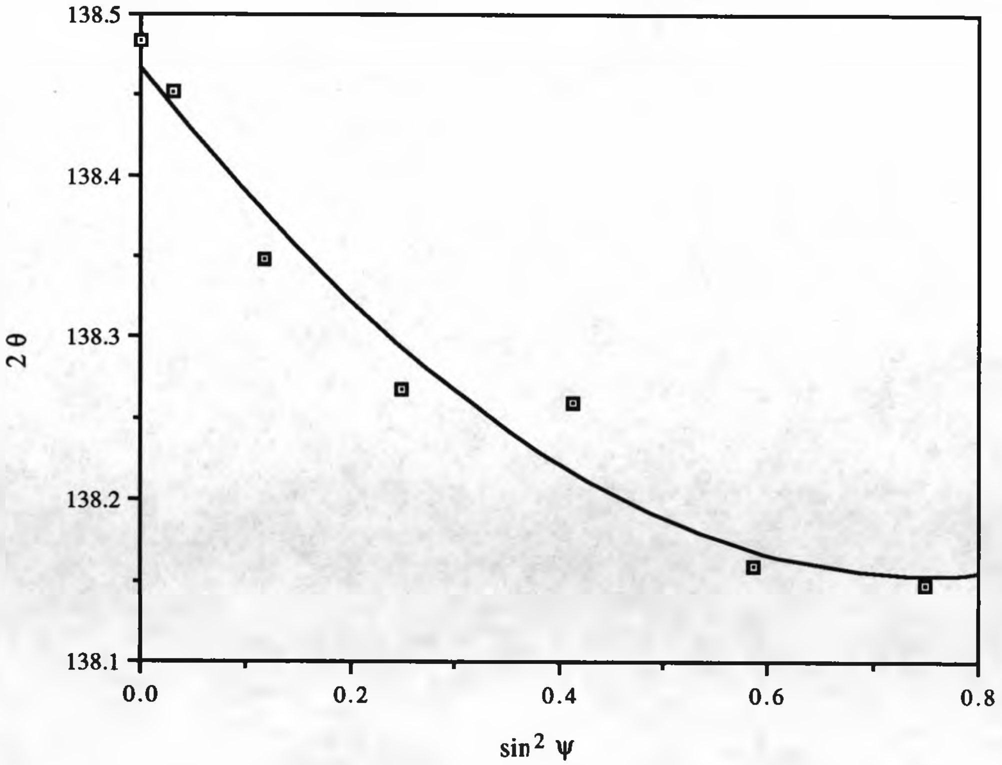

Fig.4.58. Variation of diffraction angle for Al(422) peak with specimen orientation for the LSM 2014 alloy.

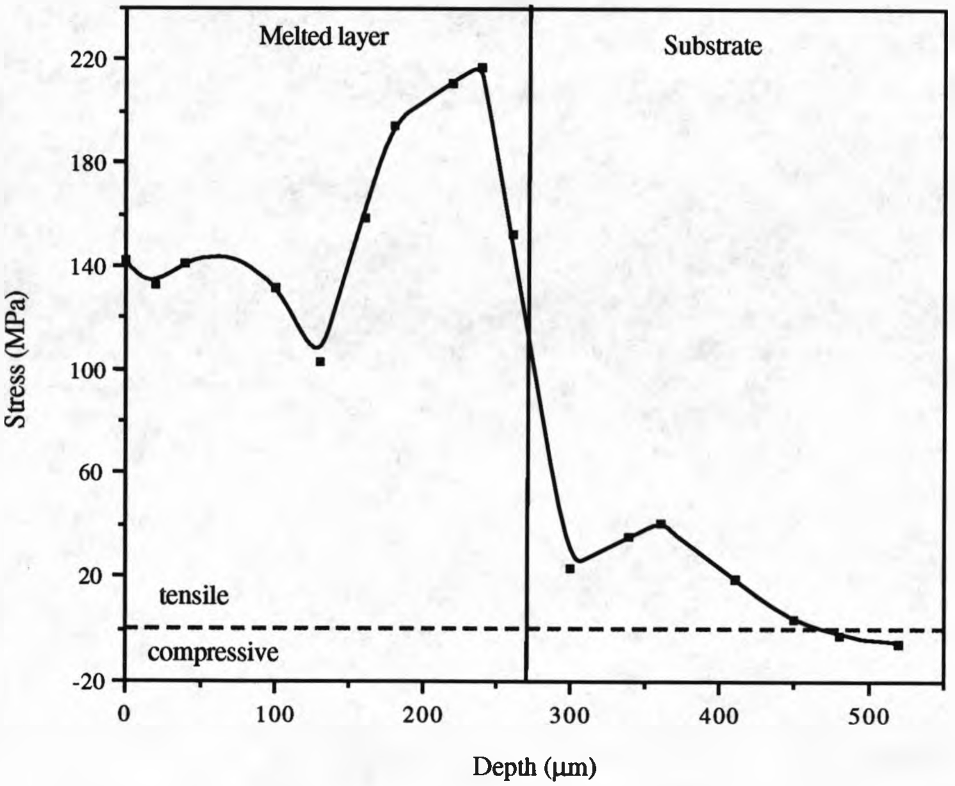

Fig.4.59. Residual stress as a function of depth for LSM 2014 alloy, data corrected for layer removal.

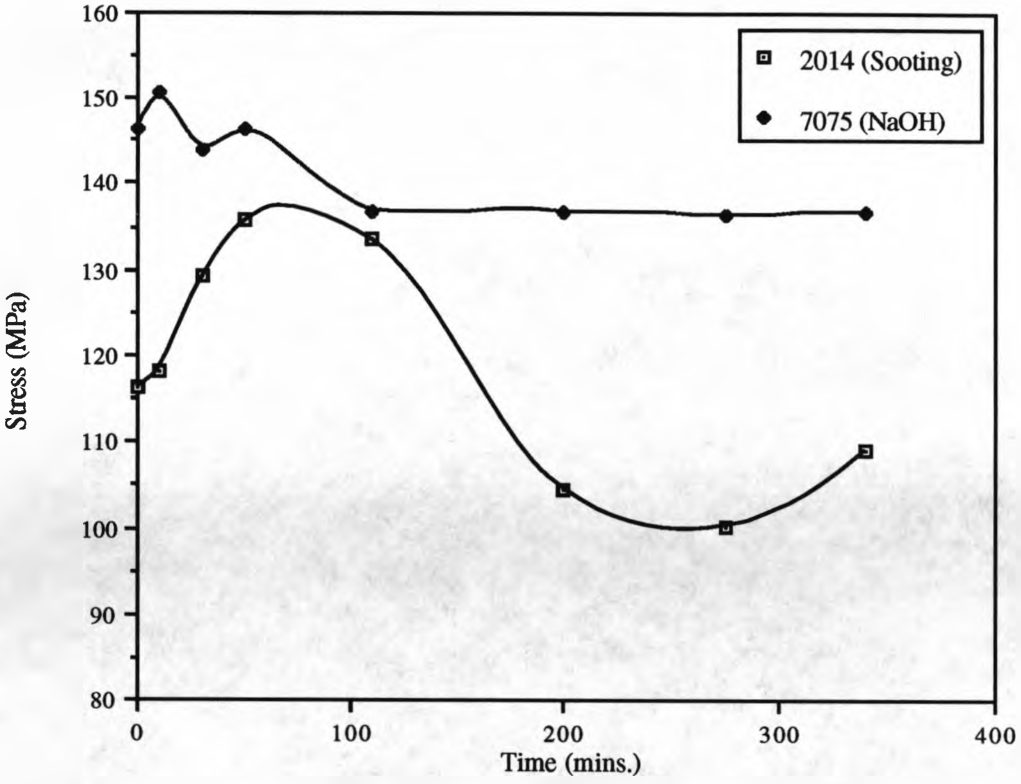

Fig.4.60. The effect of heat treatment time on the residual stress; V=15mm/s, heated at 373K.

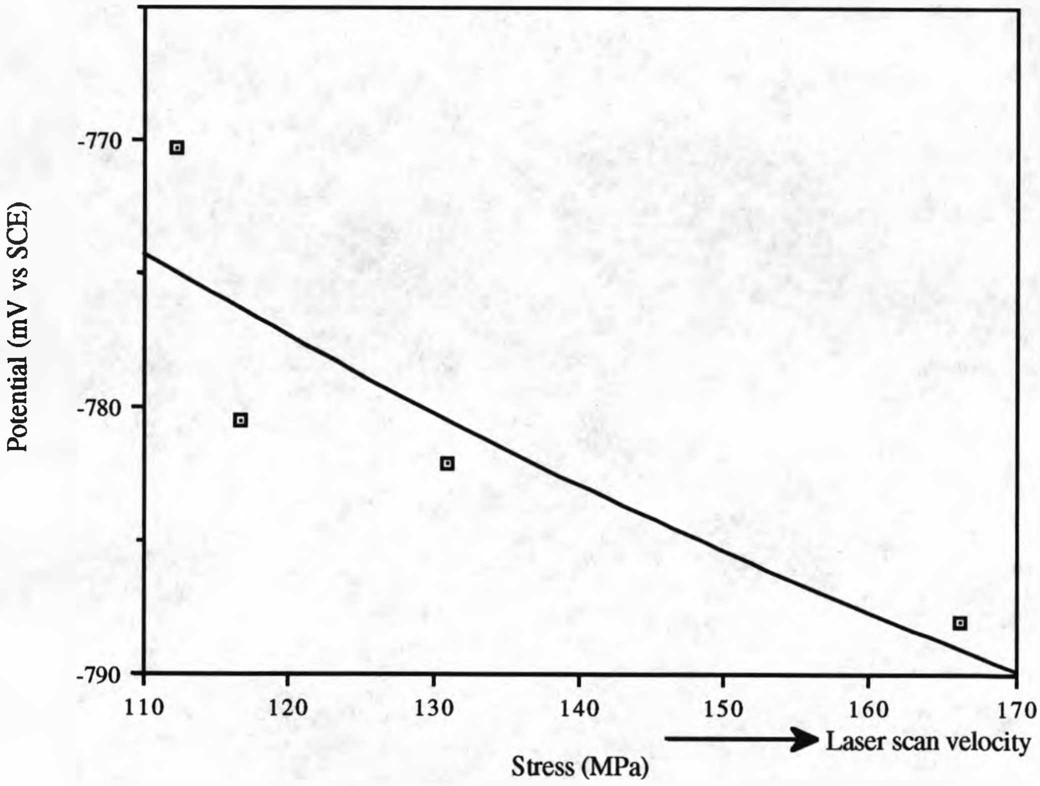

Fig.4.61. The effect of residual stress as a function of laser scan velocity on the pitting potential of 7075; scan 10 mV/min in deaerated 1 M NaCl.

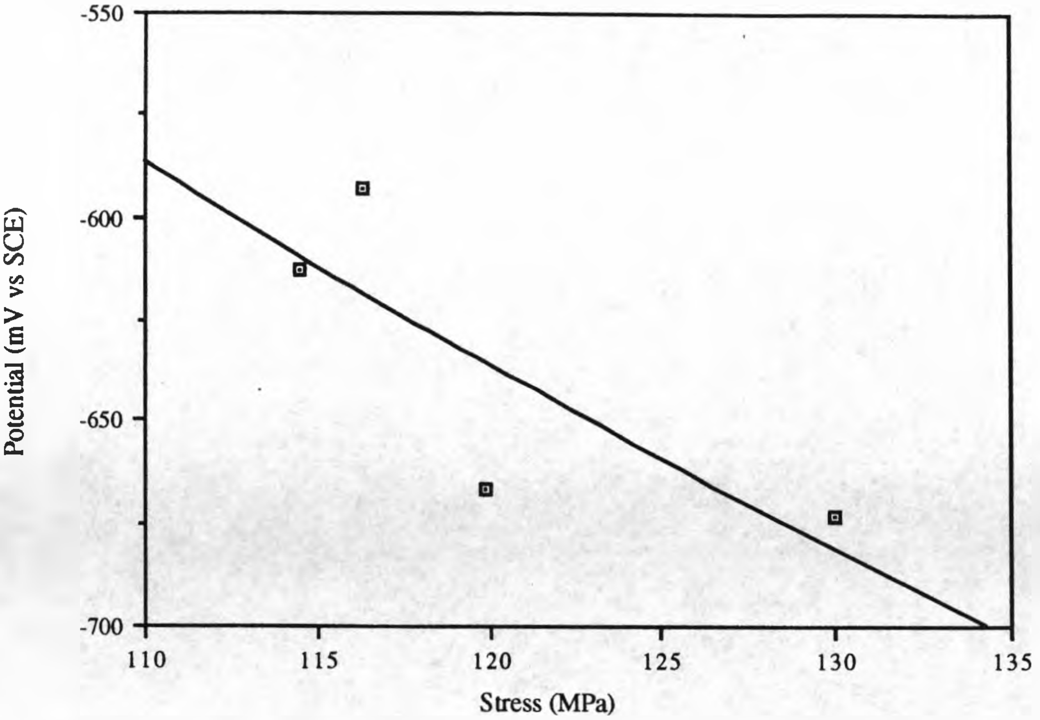

Figure 4.62. Pitting potential versus the residual stress measured as a function of the intertrack distance for LSM 2014 alloy; scanned at 10 mV/min in deaerated 1M NaCl.

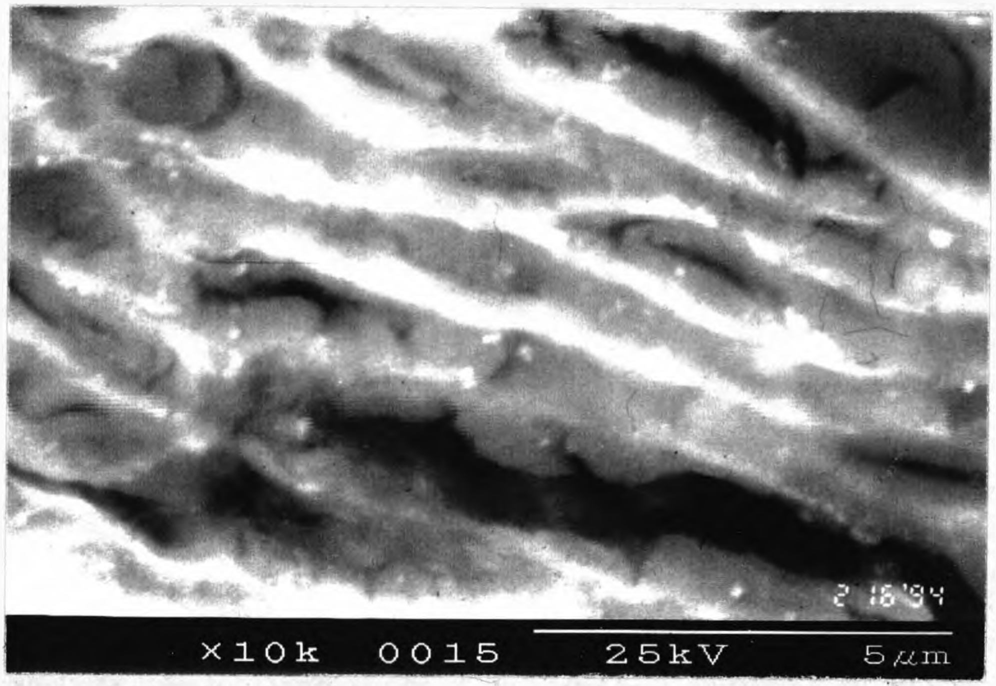

Figure 4.63. SEM micrograph showing microcracks formed during intradendritic corrosion on LSM 2014 alloy.

5. RESULTS OF LASER SURFACE ALLOYING

The results in this section are concerned with the laser surface alloying (LSA) of aluminium alloy substrates with Mo. The preliminary results concerned with the selection of the best way to introduce Mo into the melt pool produced by the laser were given in Chapter 3 section 3.2.2. Hence these results are only concerned with LSA with predeposited plasma sprayed coatings; in particular the 25% Mo- 75% Al coating. The results are presented under the two sub-headings; microstructure and solidification, and corrosion properties.

5.1. MICROSTRUCTURE AND SOLIDIFICATION

5.1.1. Microstructure of the Surface Alloy

The microstructure of the surface alloyed 2014 alloy substrate with the Mo added by the different techniques outlined in section 3.2.2 are shown in Figures 5.1 and 5.2 for comparison with the surface alloyed plasma sprayed coating. The microstructure of the LSA 2014 with the predeposited plasma sprayed coating (2014/Mo) was dendritic, similar to that of the laser surface melted alloys observed in the previous chapter. Figure 5.3 shows the typical microstructure of the surface alloy in cross section. At the limit of the melt depth (~400-500 µm) growth started with a region of planar front solidification. However, unlike in the LSM alloys, the planar front was very small and in some cases very difficult to distinguish from the adjacent partially melted grains in the HAZ of the substrate; this is shown in Figure 5.4. The columnar grains that started to grow at the fusion boundary consisted of cellular dendrites orientated in the general direction of heat flow. Using the same analysis as for the LSM alloys the cooling rates were estimated to be of the order of 10^6 K/s during solidification adjacent to the fusion boundary but increased to be of the order of 10^7 K/s just below the surface. The columnar growth was epitaxial, with some grain boundaries being continuous, from the HAZ in the substrate, through the melt zone to the free surface.

Intermetallic particles were dragged into the melt pool from the top edge of the melted region as shown in Figure 5.5. In addition Figure 5.6 shows that convection in the melt then helped to distribute the micron sized intermetallic particles within the grains. A banded structure was also found in the alloyed layer. The bands were marked out by intermetallic particles lying in arcs parallel to the fusion line as illustrated in Figure 5.7. Some slightly larger intermetallic particles were observed in the HAZ caused by overlapping the laser melt tracks (Figure 5.8).

A more detailed inspection of the microstructure was carried out by TEM and micrographs showing characteristic features of the dendritic structure are presented here. Figure 5.9 shows the basic cellular dendritic structure, however, sub-micron sized intermetallic particles were also nucleated and frozen inside the primary α-Al dendrites; they were not just confined to the interdendritic phase. These intermetallics, shown in Figure 5.10 were found to consist mainly of faceted crystals seemingly randomly orientated within the α-Al, as indicated by the accompanying SAD pattern in Figure 5.10 (b). Examination of the calculated plane spacings from the SAD patterns and the data from the X-ray diffraction scans shown in Figure 5.11 indicated that the faceted particles were similar in structure to the intermetallic $Al_{12}Mo$ and Al_5Mo phases; these results are summarised in Table 5.1. Two other types of intermetallic were identified; a spherical particle shown in Figure 5.12 and a star shaped particle shown in Figure 5.13. No match was made with existing data for the spherical particles. From the SAD pattern shown in Figure 5.13 (b) it was found that the dendritic star crystals had the same structure as the star shaped particles found in some of the laser surface melted 7075 alloy samples, indicating that they were $MgAl_2O_4$.

5.1.2. Composition

It was found that the melt tracks were quite homogeneous and a good degree of mixing was achieved after the LSA treatment. Composition profiles, measured by WDS for Cu and Mo, are shown in Figure 5.14. Each point on the composition profiles represents an area averaged value because the minimum probe size for analysis was about 2 µm.

Even so it can be clearly seen that complete mixing has been achieved to the limit of the melt depth. It is apparent from the graph that the concentration of Mo in Al has been significantly increased as a result of laser surface alloying. The composition profile across an α-Al dendrite obtained by STEM is shown in Figure 5.15. This shows that up to 2.5 wt.% Mo was retained in solid solution, and that the interdendritic phase contained only a slightly higher concentration of Mo. From EDX analysis the star shaped particles shown in Figure 5.13 were found to be oxide particles that were essentially $MgAl_2O_4$ in type but with a significant amount of Mo as well. This is illustrated in Figure 5.16. The faceted precipitate shown in Figure 5.11 was found to have a more complex composition to that of $Al_{12}Mo$ because it also contained Cu and Mg in approximately the same atomic concentrations as Mo.

5.2. CORROSION PROPERTIES

5.2.1. Potentiodynamic Pitting Scans

A typical polarization curve for LSA Mo/2014 in 1M NaCl is shown in Figure 5.17. Table 5.2 shows the average values for E_{corr}, E_{pit}, and E_{PD} in each of the test electrolytes. The figure in the brackets in each row shows the number of tests performed to get the average. The passive current was typically of the order of 0.5 $\mu A/cm^2$ for all of the tests. It is shown that the effect of LSA with Mo was to decrease E_{corr} and increase E_{pit}, compared to -755 mV (SCE) and -700 mV (SCE) respectively for the as-received 2014 alloy, and hence increase the relative potential difference, E_{PD}, required to cause pitting. For corrosion in 1M NaCl it can be seen that as the scanning velocity was increased the pitting resistance decreased. The value of E_{pit} was -617 ± 8 mV (SCE) for all the samples tested but E_{corr} increased with increasing scan velocity, hence E_{PD} decreased. The corrosion resistance of the surface alloy in the 0.1 M chloride solutions was better than in the 1M NaCl solution and E_{pit} increased to -516 ± 10 mV (SCE).

For comparison the as-received plasma sprayed coating and pure Mo were corrosion tested in 0.1M and 1M NaCl. The plasma sprayed coating exhibited no corrosion resistance, with the current rapidly increasing even at low applied potentials. Pure Mo, however, suffered from general corrosion in the 1M NaCl solution. The current increased with potential but very slowly indicating low corrosion rates. In the 0.1M NaCl solution the pure Mo seemed to remain passive over a very large range. At low potentials the surface darkened slightly but the current did not increase until the applied potential was nearly 1V.

5.2.2. The Variation of Free Corrosion Potential with Time

The free corrosion potential, E_{corr}, was monitored for up to 1 week in 1M NaCl and the results are plotted in Figure 5.18 along with the measured pitting potential. It can be seen that E_{corr} stayed below the pitting potential for the majority of time of the test but never attained a steady state value. Inspection of the samples after immersion showed a tendency for preferential attack along the track-track interfaces.

5.2.3. Pit Morphology and Distribution

The pitting behaviour of the LSA 2014/Mo alloy was different to that of the LSM 2014 alloy. During anodic polarization pits were observed to form where intermetallic particles had grouped together; this can be seen in Figure 5.19. The pits grew by the dissolution of the aluminium between the intermetallic particles. Pits did not, however, form preferentially at existing surface defects such as the exposed gas pores shown in Figure 5.20.

5.2.4. X-ray Photoelectron Spectroscopy

The oxide that formed on a freshly abraded surface of the LSA 2014/Mo alloy under normal atmospheric conditions was found to contain Mo. Studies using XPS showed that the Mo in the air formed oxide was in both the metallic state and in one of its oxidation states probably the Mo^{6+} state. After polarization in chloride electrolytes the

XPS data indicated that the oxidation state of the Mo had changed and that the Mo was present in more than one form, as a combination of the Mo^{4+} and Mo^{6+} states forming a complex molybdate or oxide. Mo was not found in the metallic state after polarization.

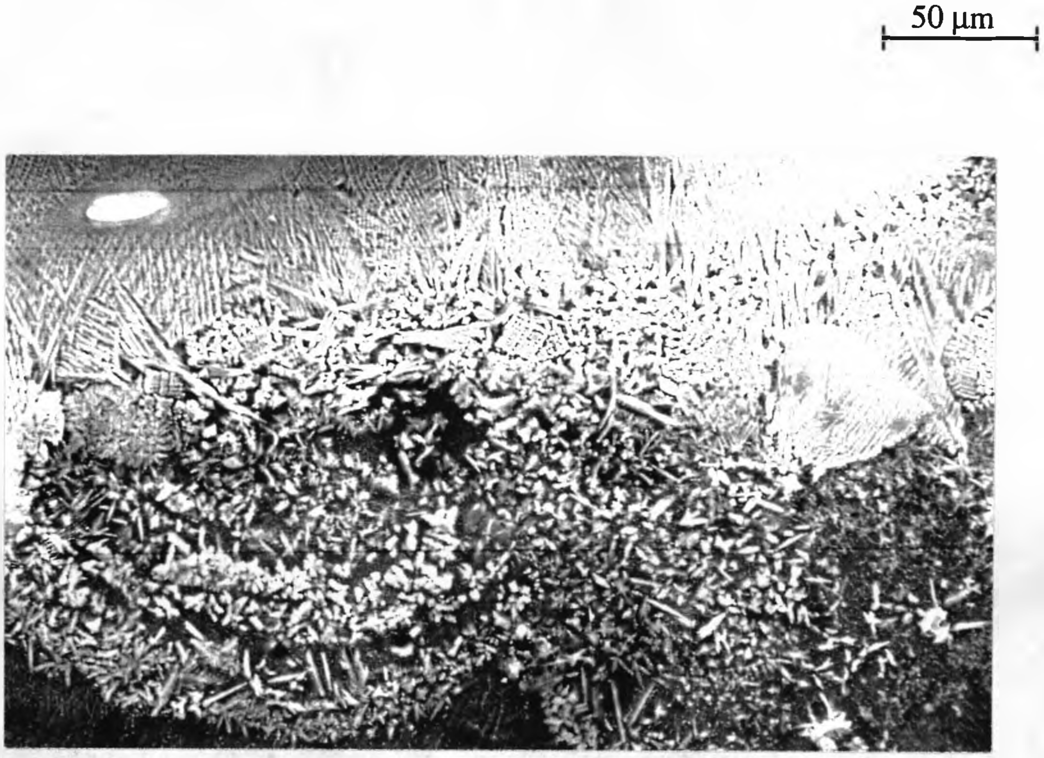

Figure 5.1. SEM micrograph showing the microstructure of a surface alloy obtained via LSA using preplaced powders of Mo and Al on the 2014 alloy.

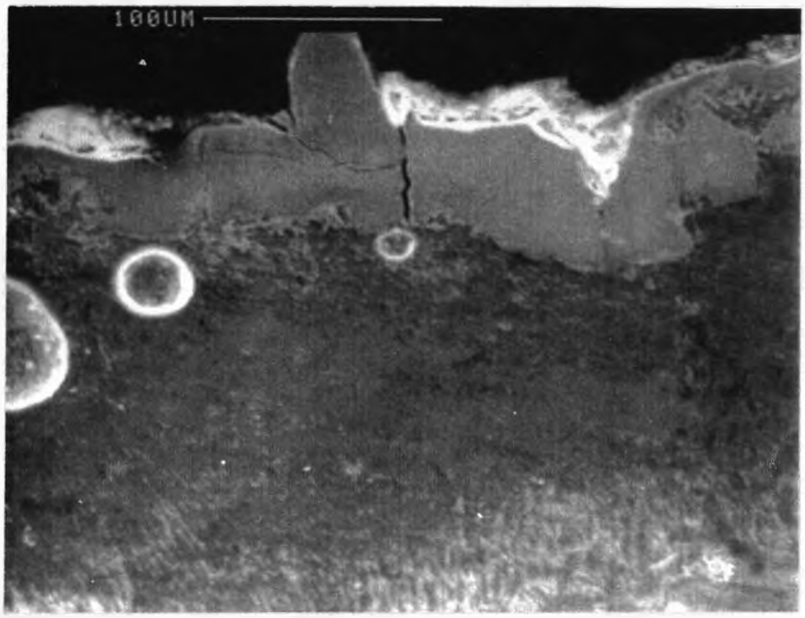

Figure 5.2. SEM micrograph depicting the microstructure of a surface alloy obtained by LSA using a predeposited 75 wt.% Mo - 25 wt.% Al plasma sprayed coating on the 2014 alloy as the substrate material.

Figure 5.3. SEM micrograph showing the microstructure of a surface alloy obtained by LSA using a predeposited 25 wt.% Mo - 75 wt.% Al plasma sprayed coating on the 2014 alloy as the substrate.

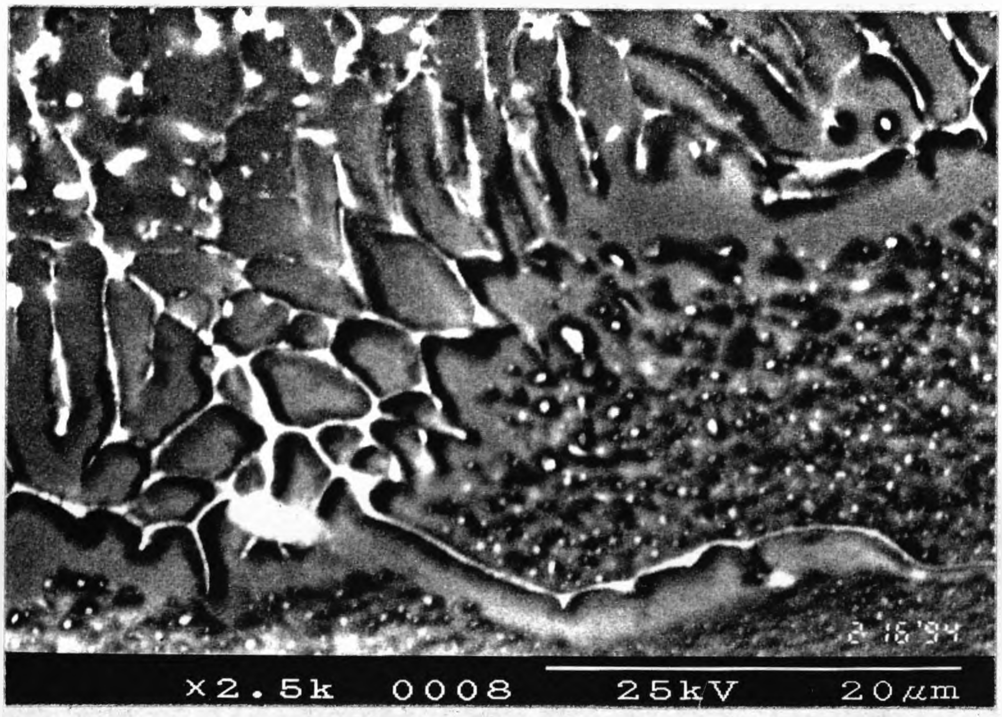

Figure 5.4. Back-scattered electron (BSE) microgaph showing the FBR of the LSA 2014/Mo alloy. There is only a very narrow band of planar front growth at the fusion line.

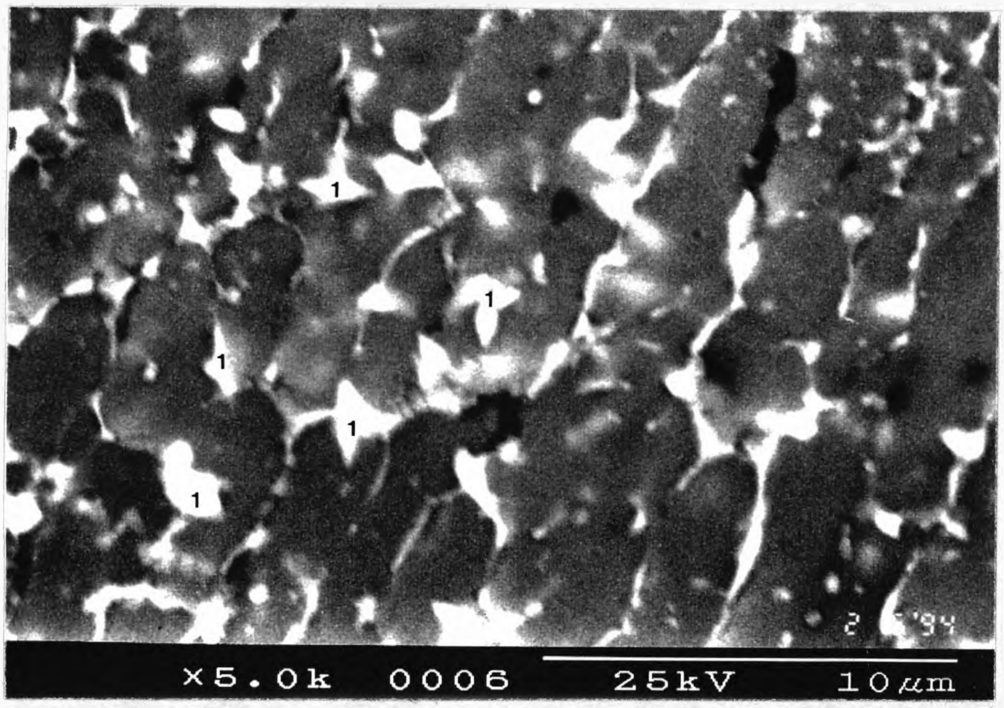

Figure 5.5. BSE micrograph of LSA 2014/Mo taken just below the surface and at the edge of the melt zone. The faceted particles (marked 1) formed under the partially melted plasma sprayed coating and were dragged into the melt pool by convection.

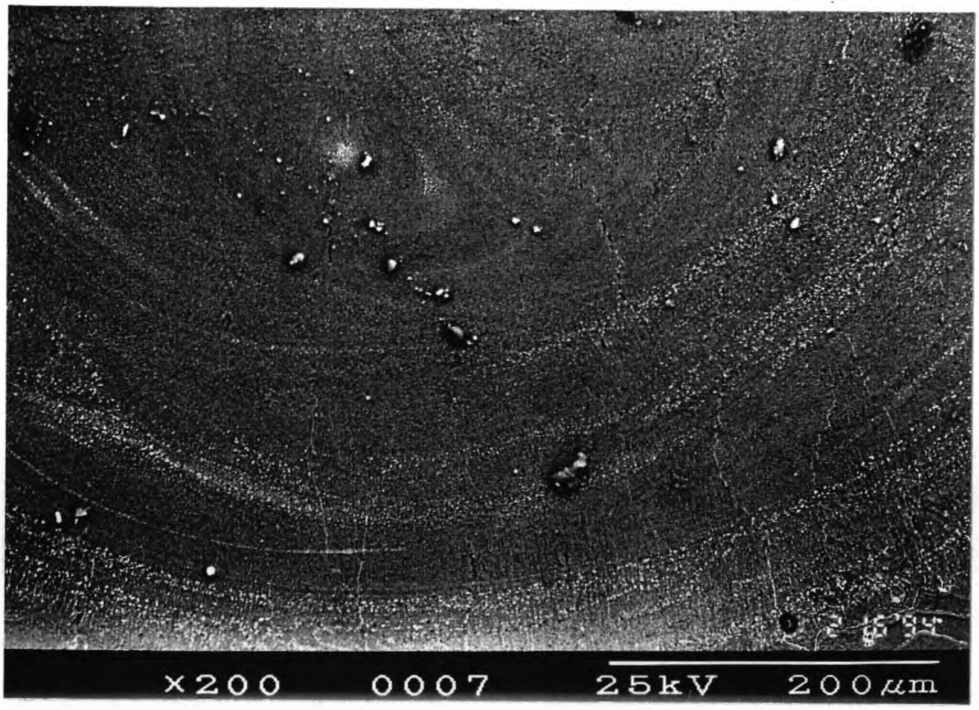

Figure 5.6. BSE micrograph showing the convection contours which are highlighted by the clusters of intermetallic particles.

Figure 5.7. BSE micrograph of the banded structure observed close to the limit of the melt depth in LSA 2014/Mo alloy.

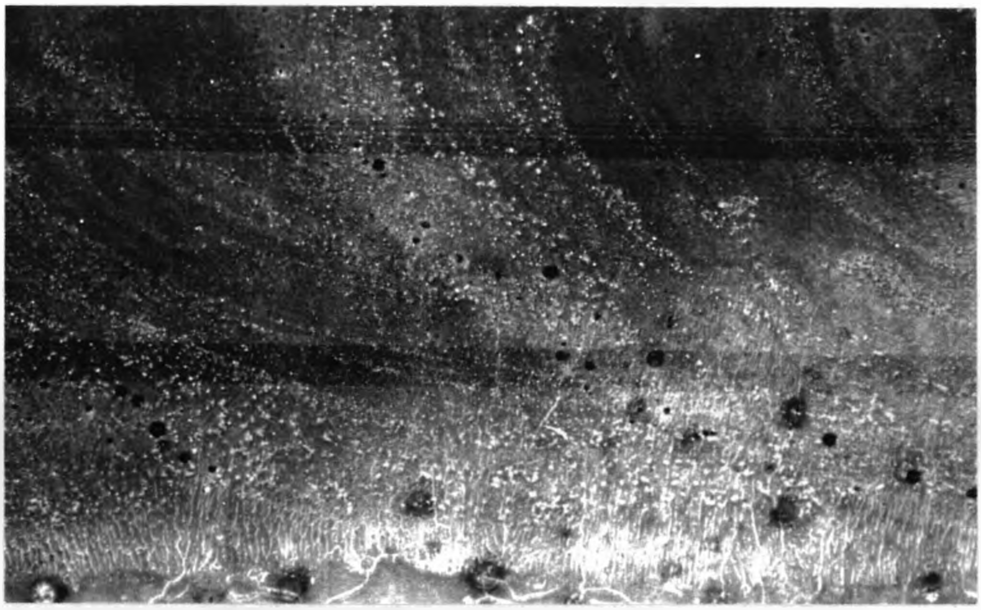

Figure 5.8. SEM micrograph of a transverse (x-z) cross section of the LSA 2014 alloy. Intermetallic particles are concentrated at the track/track interfaces and in the convection contours

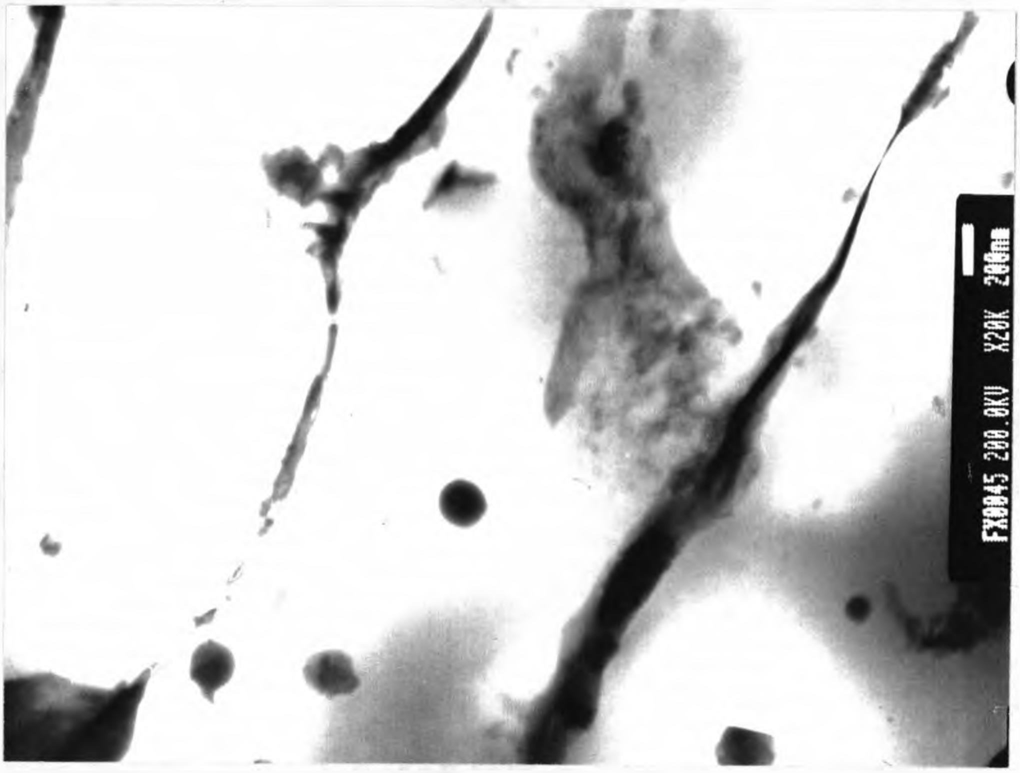

Figure 5.9. TEM micrograph of cellular dendrites in the LSA 2014 alloy. The α-Al contains some trapped intermetallic particles.

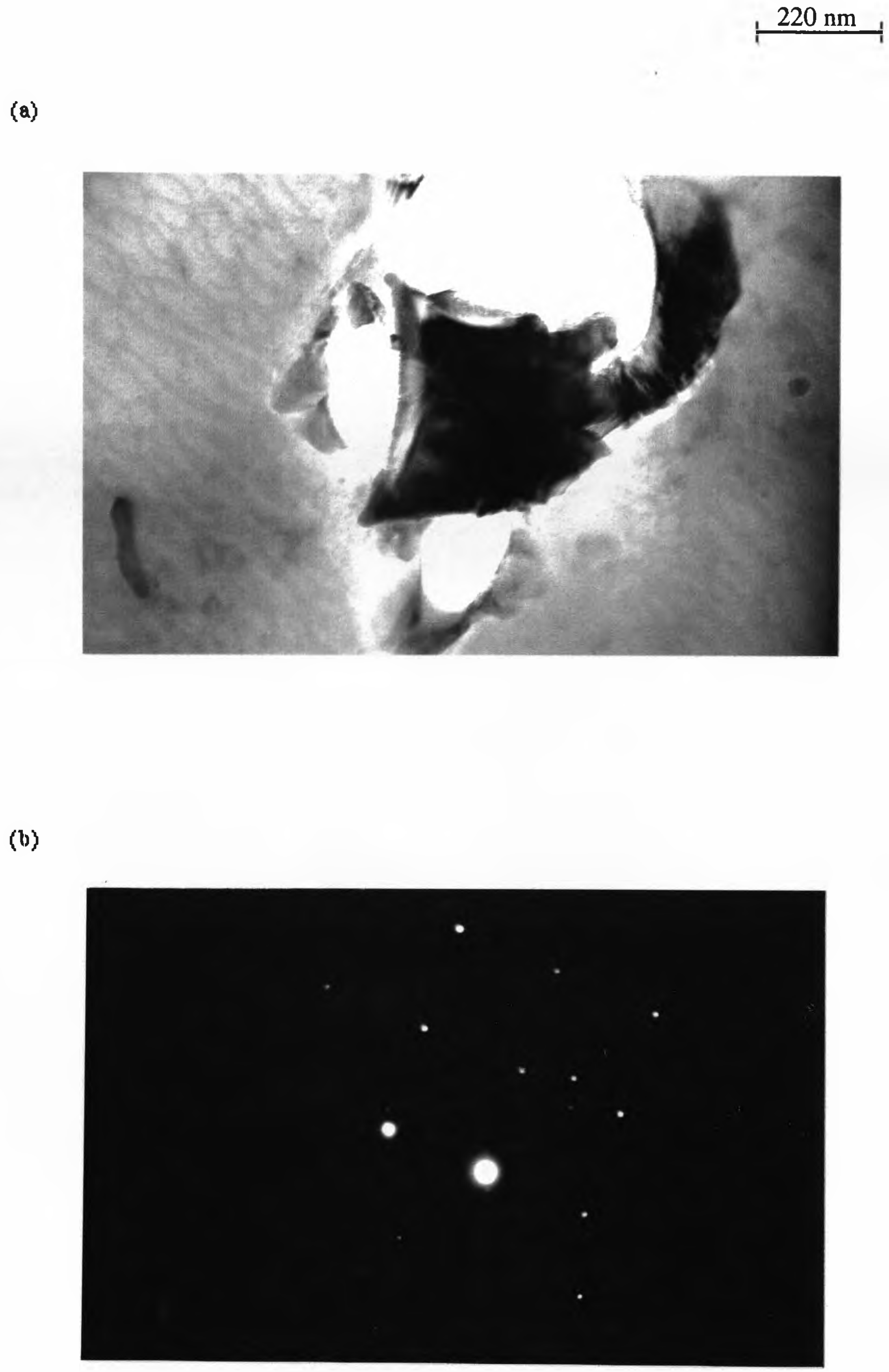

Figure 5.10. (a) TEM bright field image of an angular intermetallic particle found in the surface alloy prepared by LSA with a 25 wt.% Mo plasma sprayed coating. (b) SAD from (a); B = $[\bar{5}\bar{5}2]_{\mathrm{cubic}}$.

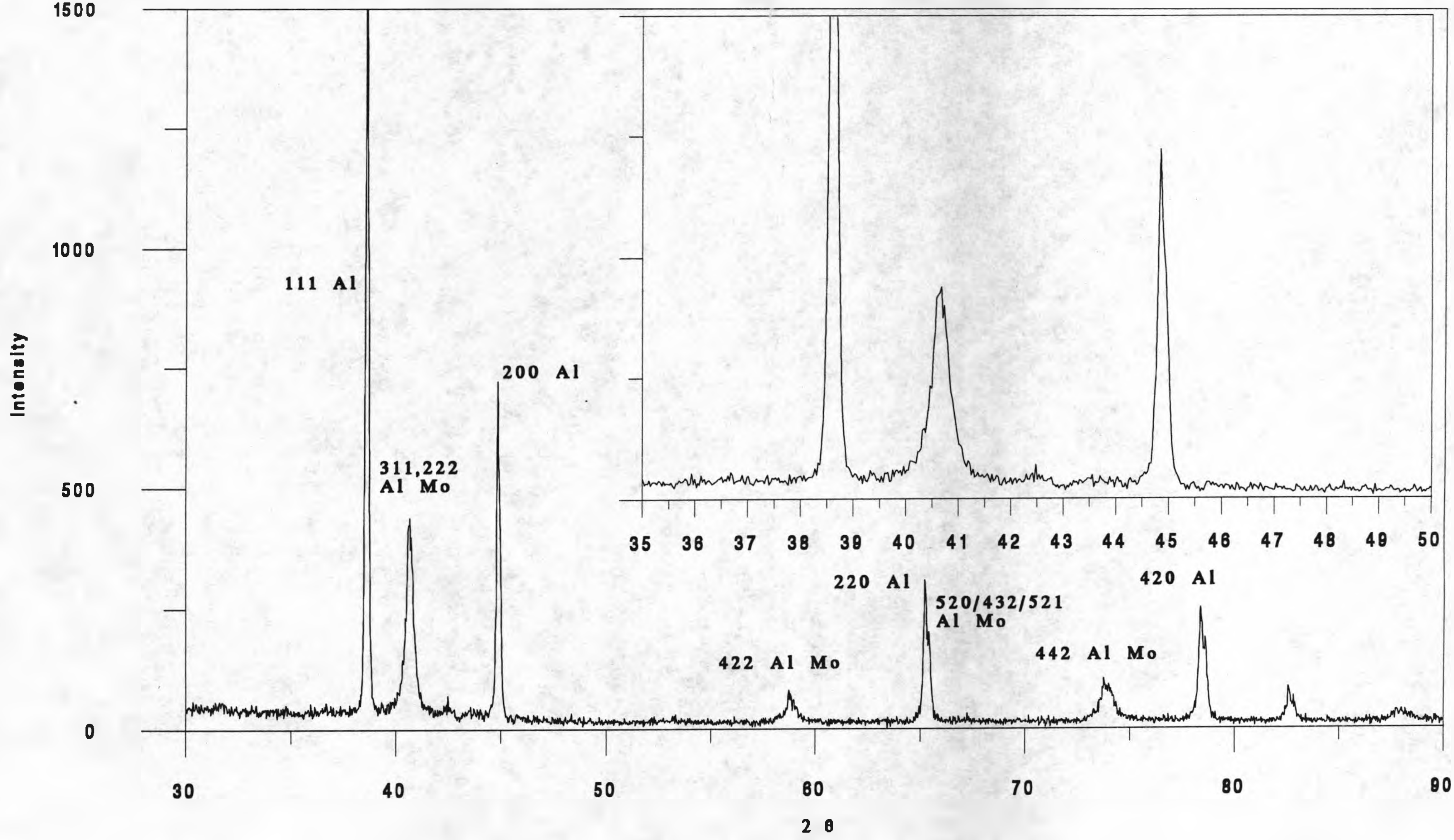

Figure 5.11. X-ray diffraction profile for LSA 2014/Mo alloy.

SAD Pattern	Electron Diffraction		X-ray Diffraction	
	d-spacing (ang.)	(hkl)	d-spacing (ang.)	(hkl)
1. Al [011]	7.4074	100 ($Al_{12}Mo$)	2.3061	311, 222 ($Al_{12}Mo$)
	2.4591	221, 300 ($Al_{12}Mo$)	1.5697	422 ($Al_{12}Mo$)
	2.344	111 (Al)	1.4287	220 (Al)
	2.027	200 (Al)	1.4199	520, 432, 521 ($Al_{12}Mo$)
2.	4.3478	100 (Al_5Mo)	1.2809	442 ($Al_{12}Mo$)
	2.3585	111 (Al_5Mo)	1.2178	420 (Al)

Table 5.1. Electron diffraction data from the two types of angular precipitates observed in the LSA 2014/Mo alloy compared with the X-ray diffraction data, showing the phase with the plane spacings that most closely matched the measured d-spacings.

Figure 5.12. (a) TEM bright field image of some spherical intermetallic particles found in the surface alloy prepared by LSA with a 25 wt.% Mo plasma sprayed coating. (b) SAD from (a); B = $[\bar{1}33]_{Al}$.

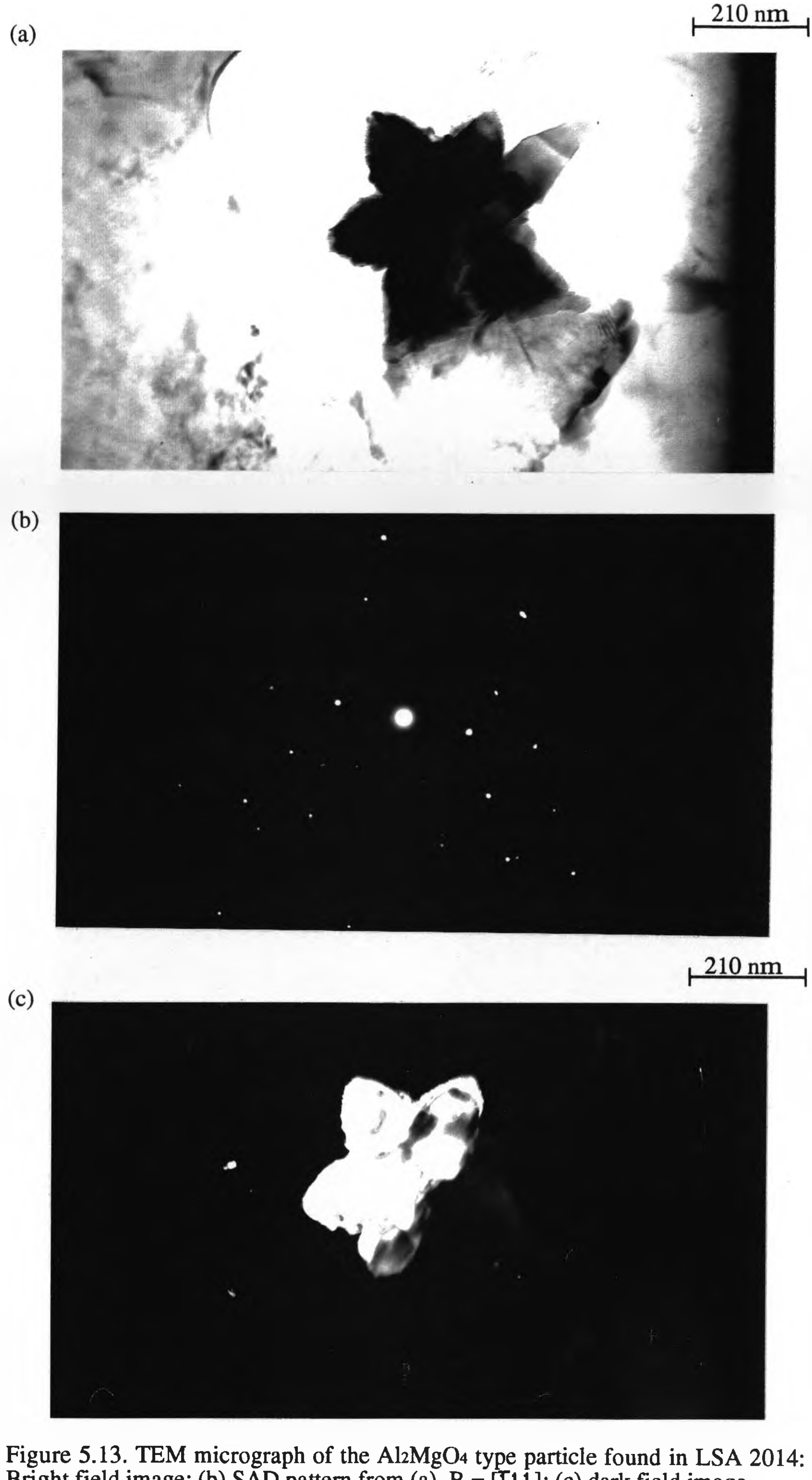

Figure 5.13. TEM micrograph of the Al_2MgO_4 type particle found in LSA 2014: (a) Bright field image; (b) SAD pattern from (a), B = $[\bar{1}11]$; (c) dark field image.

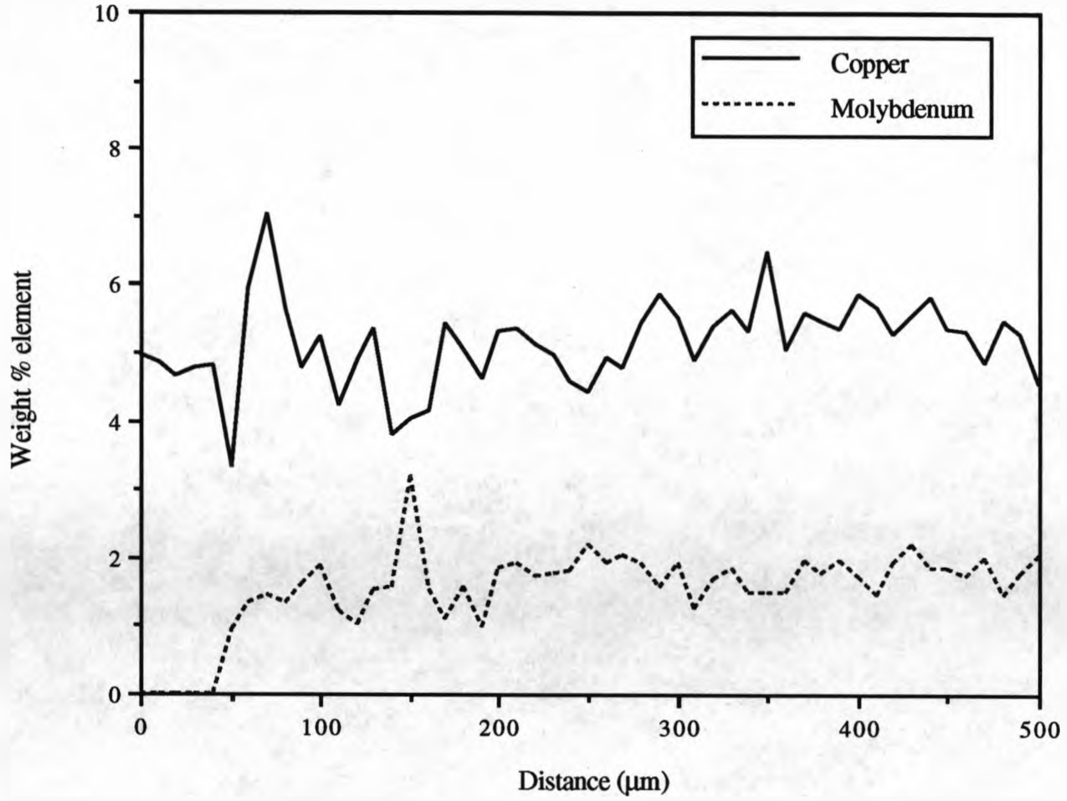

Fig.5.14. ZAF corrected WDS depth profile from substrate (0 µm) to surface (500 µm) for laser surface alloyed 2014 alloy (25%Mo plasma sprayed coating).

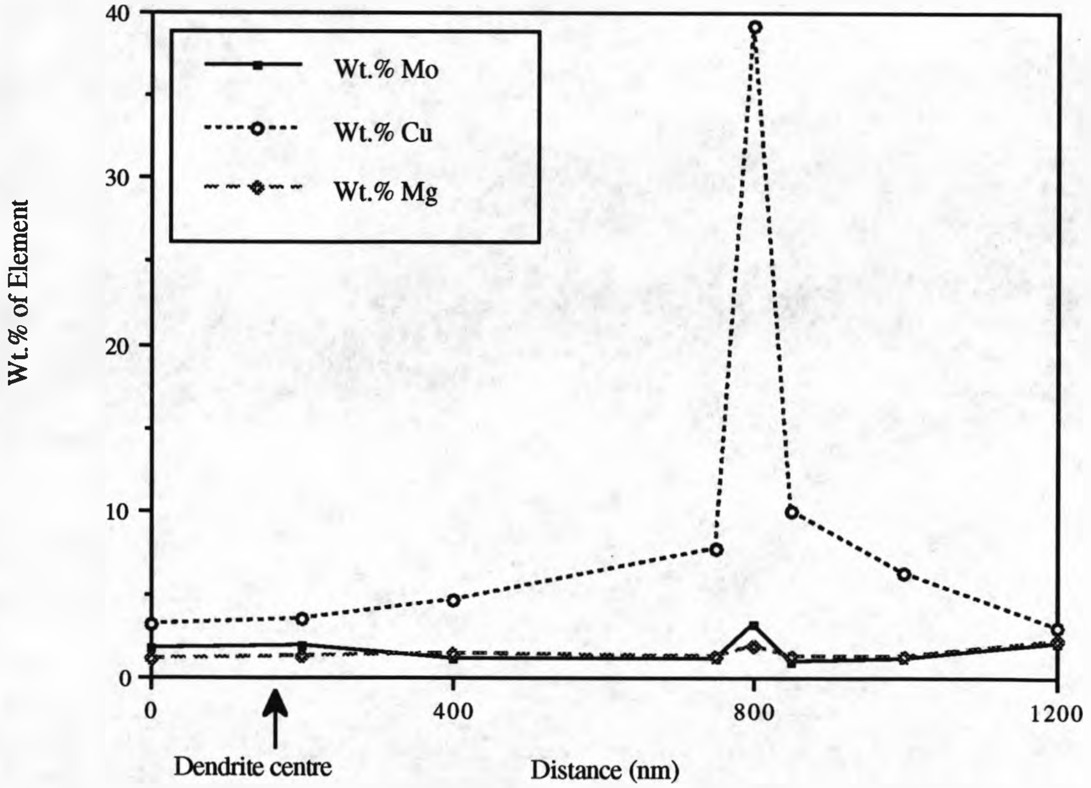

Fig.5.15. EDX composition profile across a dendrite arm in LSA 2014/Mo, V=20mm/s, P=1.5kW; analysis by STEM.

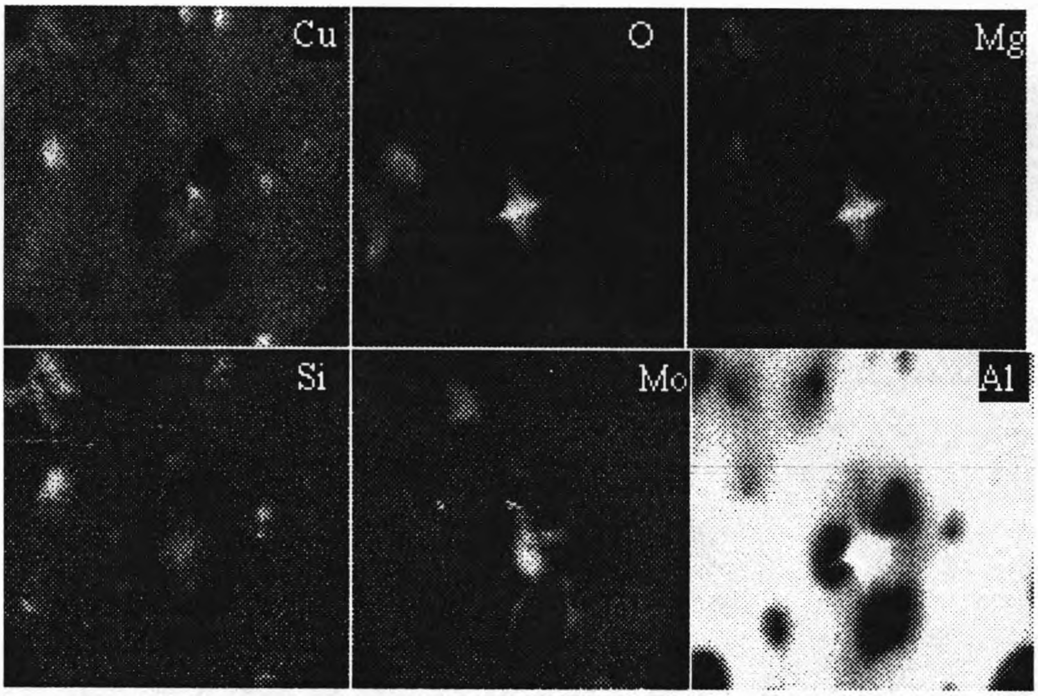

Figure 5.16. X-ray maps of a star shaped particle found in the LSA 2014/Mo alloy. Its composition is similar to the Al_2MgO_4 particles found in LSM 7075 alloy.

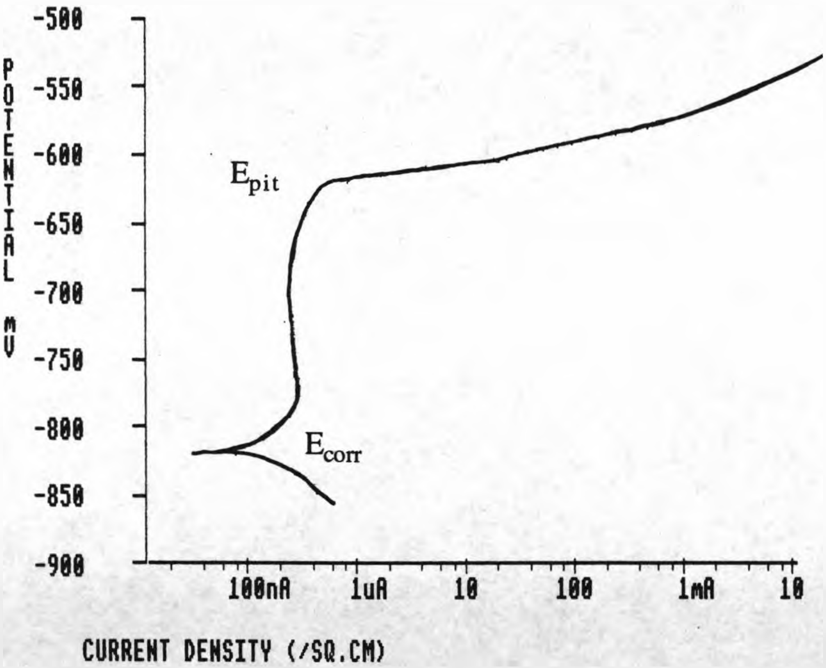

Figure 5.17. Potentiodynamic anodic polarization curve for LSA 2014/Mo alloy. Tested in 1 M NaCl, 30 °C, deaerated for 2 hrs with N_2, 10 mV/min. The vertical scale shows the absolute potential versus SCE.

Test solution	Laser scan velocity (mm/s)	E_{corr} (SCE)	E_{pit} (SCE)	E_{PD}
1 M NaCl	20	- 844	- 614	$230_{(2)}$
	50	- 794	- 624	$170_{(4)}$
	70	- 730	- 612	$118_{(4)}$
0.1 M NaCl	20	- 834	- 519	$315_{(3)}$
0.1 M KCl	20	- 890	- 512	$378_{(5)}$

Table 5.2. Results of potentiodynamic anodic polarization in various deaerated electrolytes scanned at 10 mV/min. The units are in mV.

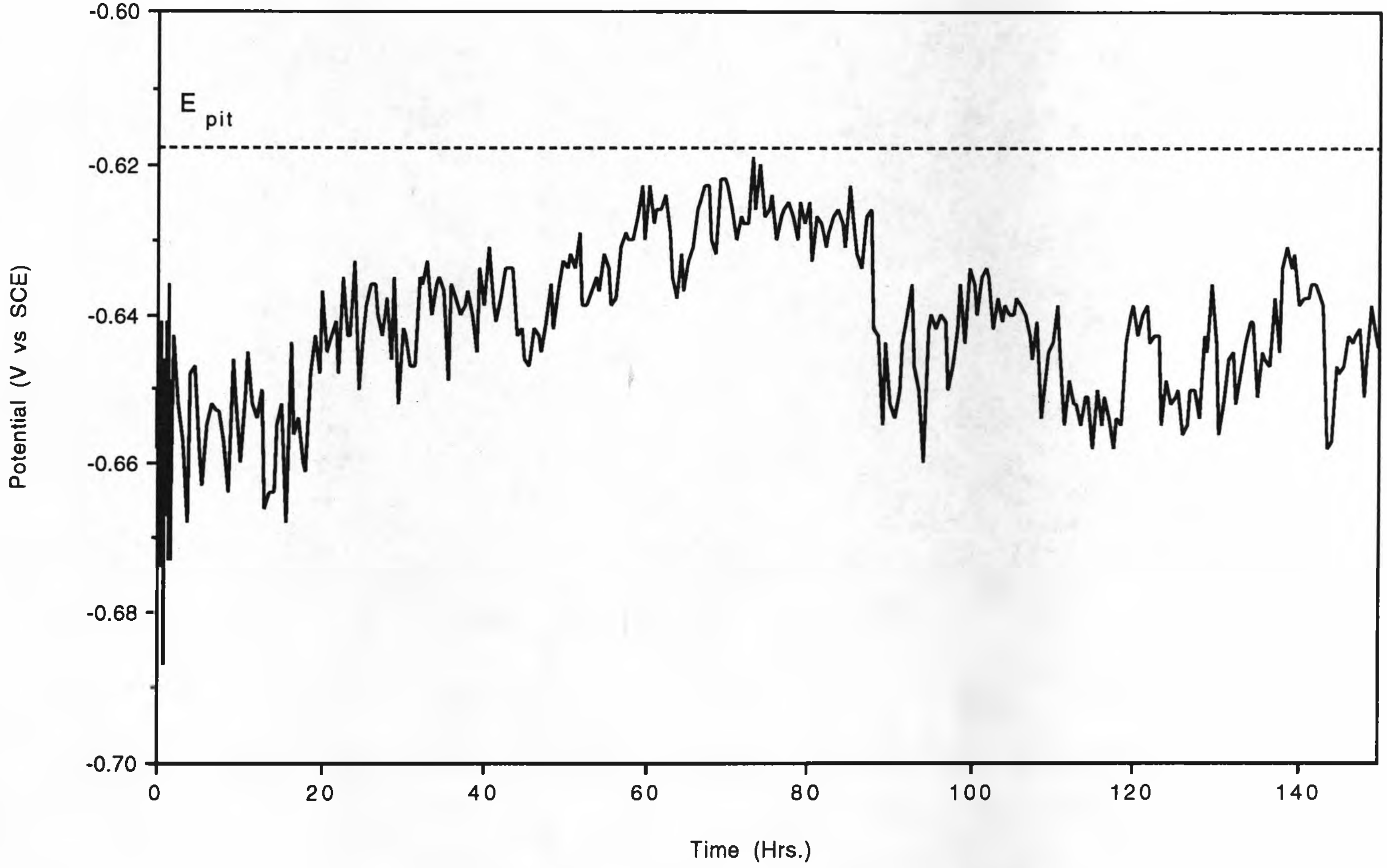

Fig.5.18. Free corrosion potential versus time for laser surface alloyed plasma sprayed 2014 (25%Mo-75%Al, 20mm/s), immersed in 1M NaCl at 30°C.

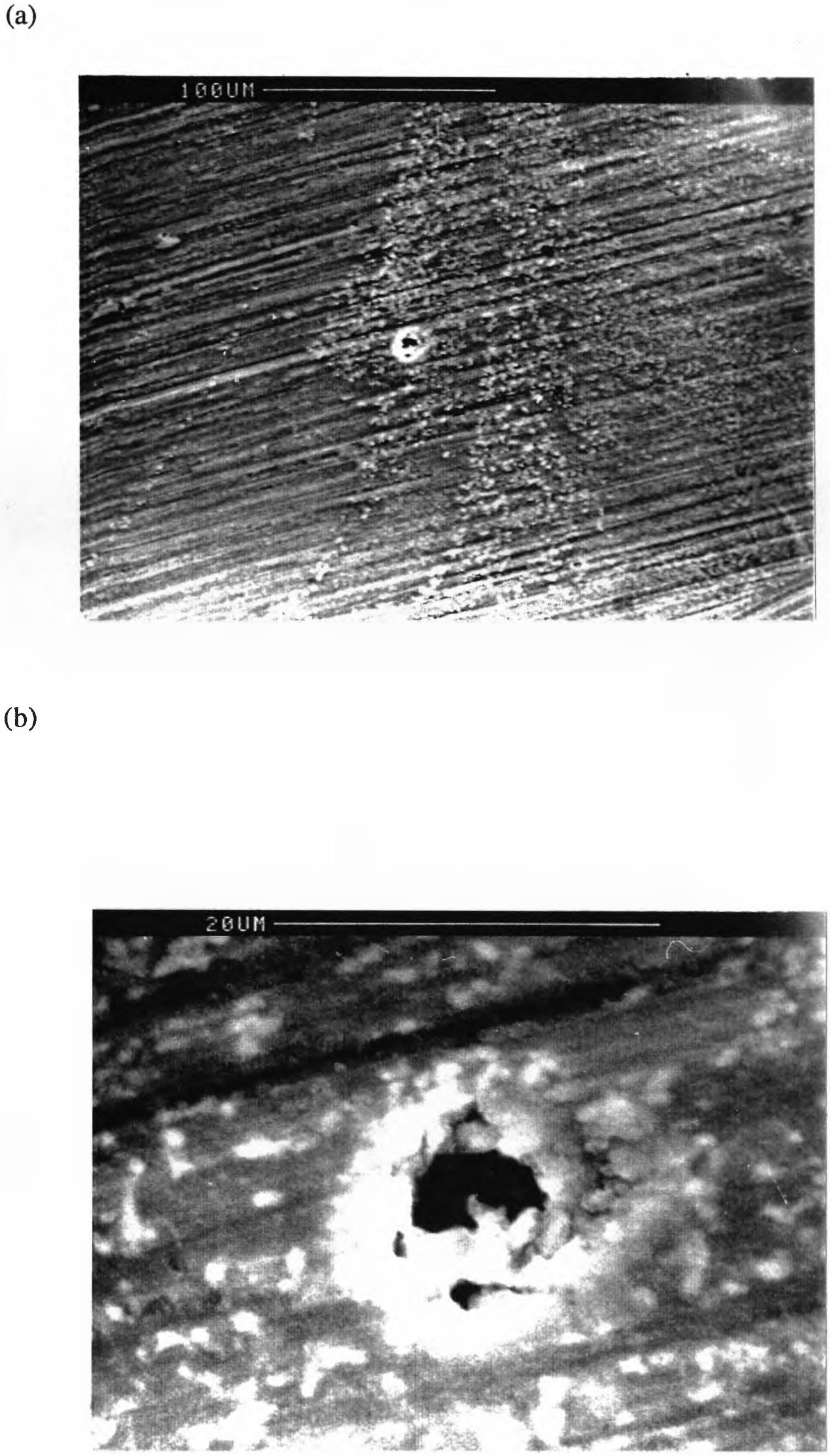

Figure 5.19. (a) SEM micrograph of a corrosion pit formed amidst a cluster of intermetallic particles. (b) As (a) at higher magnification.

Figure 5.20. SEM micrograph of the surface of LSA 2014/Mo alloy showing that corrosion did not occurr preferentially at the exposed gas pores during anodic polarization in 1 M NaCl.

6. DISCUSSION

It was shown in Chapters 4 and 5 that LSM and LSA treatments can increase the pitting resistance of aluminium alloys by producing new surface microstructures. It is the aim of this chapter to elucidate the effect of the new microstructures on the corrosion resistance of the alloys. Discussion of the formation of the melt pool and the microstructures will be made with reference to the solidification theory in the literature. Mechanical properties will be considered especially in terms of the residual stresses and the effects they have on the microstructure and corrosion resistance. The corrosion of the new alloys will be discussed with reference to the general theory of pitting corrosion of aluminium alloys. Furthermore, the reliability of the electrochemical tests used to measure the pitting resistance will be considered with reference to pitting corrosion data for aluminium alloys found in the review.

6.1. MICROSTRUCTURE AND SOLIDIFICATION

It is generally accepted that very high cooling rates can be achieved using lasers, especially with the more recent picosecond pulsed lasers, and it is often claimed that rates of between 10^6-10^{12} K/s are now possible. Within this range of cooling rates it is believed that there is a large number of possible microstructures that can form involving non-equilibrium solidification. The formation of amorphous phases, nanocrystalline metallic glasses and novel microstructural features have all been investigated by laser surface treatment of aluminium alloys. In the present study after both LSM and LSA, except after alloying with preplaced powders, the microstructure of the surface was found to consist of large columnar grains that grew epitaxially from the unmelted substrate alloys. It was estimated that the cooling rates achieved were in the range of 10^5-10^7 K/s and, therefore, the resulting microstructures were similar to other more conventional welding techniques such as tungsten-inert gas (TIG) welding (Kou and Le,1983, and Juarez-Islas, 1991).

6.1.1. The Structure of the Melted Layer

6.1.1.1. Porosity

The gas pores, mainly at the substrate/fusion line interface, in the melted layers are believed to be the result of released hydrogen or from vaporisation of alloying elements. In the case of hydrogen pores the gas may have come from trapped hydrogen in the substrate alloy (Kim and Weinman, 1978). The solubility of hydrogen is several orders of magnitude higher in the liquid than in the solid, so that during solidification the hydrogen is segregated out of the liquid and forms bubbles when its concentration leads to an equilibrium pressure that exceeds 1 atm. Since the solidification rate is higher than the rate at which some of the gas bubbles rise to the surface some of them are caught by the solidification front and become entrapped in the melted layer.

The hydrogen may have resulted from the adsorption of H_2O as, in many cases, the alloys were pretreated by immersion in aqueous NaOH solutions. The H_2O is reduced by Al according to the reaction:

$$2Al + 3H_2O \rightarrow Al_2O_3 + 3H_2(g) \qquad (R1)$$

H_2O may also result from the decomposition of $Al(OH)_3$ that formed during the pretreatment or by oxidation in a humid atmosphere (Nylund and Olefjord, 1991). The decomposition of the hydroxide occurs between 100 °C and 310 °C according to the reaction:

$$Al(OH)_3 \rightarrow AlOOH + H_2O \qquad (R2)$$

Above 310 °C the ALOOH decomposes:

$$2AlOOH \rightarrow Al_2O_3 + H_2O \qquad (R3)$$

and the H_2O is then further reduced according to reaction R1 to give H_2.

6.1.1.2. Dimensions of the melt pool

Figure 6.1 shows the theoretical maximum melt widths for three input powers and it can be seen that the experimentally measured widths for an input power of 1.5 kW are similar to the theoretical melt widths for 500 W. It is clear then that not all of the power was absorbed by the surface. The size of the melt pool is dependent on a number of material and process parameters but for aluminium alloys the initial controlling factor is the surface reflectivity which can be as high as 97% for the wavelength of the CO_2 laser (10.6 μm). In the case of this study the reflectivity was reduced by surface pretreatments but it can be seen from Figure 6.1 that approximately 65 % of the input power was not involved in melting the substrate. However, the theoretical calculations were based on the heat transfer model for a three dimensional moving point heat source (Rosenthal, 1946). This model assumes no melting, no radiant loss, constant thermal properties and a semi-infinite work piece, and is usually only useful for calculating the temperature T at a distance x, y, and z from the moving point heat source. The solution for the model and the equation used in the above calculations is:

$$T - T_0 = \frac{Q}{2\pi k} . e^{\frac{-vx}{2\alpha}} . \frac{e^{\frac{-vR}{2\alpha}}}{R} \qquad (6.1)$$

Where T_0 = initial temperature, Q = absorbed power, k = thermal conductivity, v = traverse speed, α = thermal diffusivity, and $R = (x^2 + y^2 + z^2)^{1/2}$.

By assuming that the equation is valid for melting it is possible to substitute the melting temperature, T_m for $T-T_0$. However, because the melt depth is zero at the maximum melt width and by assuming that no forward melting takes place then, R = y and x = z = 0, see Figure 6.2; rearranging Eqn. 6.1 then allows the melt width to be calculated iteratively using Equation 6.2 given below. Then by assuming that radiant loss was the only factor affecting the heat absorption, it can be deduced from the experimental width measurements that the reflectivity of the surface was still at best no lower than ~ 60 % even after surface pretreatment prior to LSM.

$$\frac{T_m 2\pi k}{Q} = \frac{e^{\frac{-Vy}{2\alpha}}}{y} \tag{6.2}$$

6.1.2. Solidification and Microstructure of Laser Surface Melted Alloys

In the following sections the discussion refers jointly to the results of the 2014 and 7075 aluminium alloys. Where significant differences arise the alloys will be discussed separately. The basic structure of the surface melted layers can be divided into three regions: the planar front solidification region, cellular dendritic growth region, and the banded structure; all of which have associated corrosion problems which will be discussed in a later section. In addition to the as solidified structure, this section also includes a discussion of the phenomenon of ageing which occurs in the 7075 alloy.

6.1.2.1. Planar front solidification

The observed planar front regions were typically only 3-5 μm wide, situated along the fusion boundary, and can be explained as follows. The occurrence of planar front solidification depends on the value of G/R in the stability condition defined by the equation:

$$\frac{G}{R} \geq \frac{-m_L C_S^*(1-k)}{kD_L} \tag{2.4}$$

Where G = temperature gradient, R = solidification rate, m_L = slope of the liquidus,

C^*_S = solid concentration in equilibrium with the liquid concentration C^*_L at the solid/liquid interface, k = partition coefficient = C^*_S/C^*_L, D_L = diffusivity in the liquid. The condition for a planar front to exist is then that G/R must be large. It can been assumed that this condition was satisfied at the limit of the melt depth because there was a very thin band of planar front solidification. Here there must have been a very large temperature gradient across the solid/liquid interface coupled with a very low growth rate at the onset of solidification. There is good support for this assumption in the results of other workers. Lasek et al (1991) suggested that planar front solidification occurs when the temperature gradient is of the order of 10^6 K/m and the solidification rate is below 10^{-3} m/s, and Hegge and De Hosson (1990) calculated that the lower limit of the solidification rate for the stability of a planar front is of the order of 20 μm/s. This second fact accounts for the small width of the observed planar front region. The limiting growth rate is almost immediately exceeded, after solidification has started, due to the fact that spontaneous self quenching from the substrate quickly leads to an increase in the solidification rate and a decrease in the temperature gradient. This can be seen in Figure 6.3 from Katayama et al (1991) which shows the change in growth rate, cooling rate and thermal gradient as a function of melt depth. The change in G/R then leads to a change to dendritic or cellular dendritic growth.

The concentration of Cu in the planar front solidification region in the LSM 2014 alloy decreased at the fusion boundary to approximately 2 wt.% Cu before rising to ~8 wt.% Cu at the end of the planar front. In the work by Munitz (1985) the copper distribution across the fusion boundary for a binary Al-4.5 wt.% Cu alloy was shown to decrease to ~2.75 wt.% Cu in the planar front region and then steadily increase until it reached 4.5 wt.% Cu again. Munitz did not show the composition beyond the planar front region but stated that it saturated at 4.5 wt.% Cu. In his work Munitz calculated the theoretical variation across the fusion boundary using the following equation:

$$C_s(X) = C_0 \cdot \left[1 - (1 - k)\exp\left(\frac{kR}{D_L}X\right)\right] \qquad (6.3)$$

where $C_s(X)$ = solute concentration at a distance X from the fusion line; C_0 = initial solute concentration; k = the equilibrium partition coefficient; R = growth rate; D_L = liquid diffusion coefficient. This equation predicted a Cu concentration of only 0.75 wt.% near to the fusion line for an initial concentration of 4.5 wt.%. Neither the theoretical results nor the experimental results showed an increase above the equilibrium concentration at the end of the planar front region where cellular dendritic growth started. This does not seem reasonable because for an alloy starting with a homogeneous solute concentration there must be a balance of the overall concentration from the unmelted region through the fusion boundary and the remaining resolidified layer. This means that if in the planar front region there is a decrease in the Cu concentration there must be an increase in the concentration above that of the equilibrium value somewhere ahead of the planar front. Due to solute rejection ahead of the planar front causing constitutional undercooling it is reasonable to expect that there would be a solute enriched region marking the end of planar front solidification and the start of a new growth mechanism. In the case where some of the solute in the substrate alloy is incorporated into other phases, such as the $CuAl_2$ precipitate in Al-Cu alloys, the effect would be even greater due to the redissolution of the second phase particle and the subsequent redistribution of the solute. This is in fact what has been found in this work, shown in Figure 4.19, where at the point when planar front solidification gives way to cellular dendritic solidification there was a sharp increase in the Cu concentration.

6.1.2.2. Cellular dendritic growth

There is at present some disagreement as to what is considered to be the difference between cellular growth and cellular dendritic growth. In this study the term cellular dendritic growth has been taken to define the growth of a cellular structure that involves the segregation of alloying elements to the cell boundaries and hence forms a separate phase. Furthermore, true cells grow in the direction of maximum thermal gradient, where as cellular dendrites grow in the crystallographic <100> directions that are most closely aligned with the maximum thermal gradient (Matsunawa et al, 1990). In reality the two directions are very similar because the laser heat source is not stationary so the dendrites are forced to bend round, hence there are deviations from the <100> direction.

Cellular dendritic structures were found to form in both of the commercial aluminium alloys studied in this work. The only observed difference in the two alloys was the point at which cellular dendritic growth stopped. In the 2014 alloy cellular dendrites continued to grow up to the surface of the melted layer, but in the 7075 alloy the cellular dendrites were replaced by a single phase region just below the surface as shown in Figure 4.31. It is thought that the solid solution region was able to solidify because the constitutional supercooling was extremely high due to increased solute saturation in the last of the liquid in the melt pool. The results would also seem to support this because it was found that the surface microstructure consisted of nanocrystalline equiaxed grains that had a comparatively high Mg concentration.

Other workers have previously characterised the structures of binary alloys after laser surface melting of Al-Cu; A.Munitz (1980), A.Munitz (1985), Zimmermann et al (1989), Gill and Kurz (1993), S.C.Gill and W.Kurz (1993(b)), and Al-Fe; Carrard et al (1991), Gremaud et al (1990), Gremaud et al (1991), and reported structures that were very similar to those in this work. Rama and Sekhar (1987) have developed models to account for the various structural changes that occur in the melt depth as a result of variable solidification rates, temperature gradients and cooling rates, and found good agreement with experimental results for LSM on 2024 aluminium alloy.

The cooling rate was estimated by Munitz (1985) using the following equation:

$$\mathrm{DAS} = a.\varepsilon_{av}^{-n} \tag{6.4}$$

where DAS = secondary dendrite arm spacing, a = constant typical of the material, ε_{av} = average cooling rate = RG_L, and n varies between 1/2 and 1/3. This equation has two significant limitations to its use. The first is that it has only reliably been verified for cooling rates below 10^3 K/s and lends doubt to the results that Munitz (1985) has found and which are shown in Figure 6.4. The second is that the cooling rate is derived from the secondary dendrite arm spacing which is a feature that is not seen in the microstructure of the surface melted alloys in the present study or in the microstructures observed by other workers including Munitz (1985). This means that unless a single convention is adopted there will always be discrepancies in cooling rate data. For example, given similar dendrite spacings to those measured in this study the cooling rates calculated by Leech (1989) using the above equation were approximately an order of magnitude lower. For these reasons the cooling in this work rate was calculated using the more common equation from solidification theory shown below (Steen 1991):

$$\frac{1}{GR} = -\frac{C_{L_{max}}\lambda^2}{2m_L D_L} \tag{6.5}$$

where GR = cooling rate, C_{Lmax} = maximum solute concentration in the liquid, λ = cell spacing, m_L = slope of the liquidus, and D_L = diffusivity. However, for cellular dendritic growth to start the following condition must be satisfied:

$$\frac{G}{R} \leq \frac{-m_L C_S^*(1-k)}{kD_L} \tag{6.6}$$

where R = solidification rate and k = equilibrium partition coefficient.

Thus the cooling rate for the onset of dendritic growth $(GR)_{Dend}$ can be calculated according to the following equation:

$$(GR)_{Dend} = R^2\frac{-m_L C_S^*(1-k)}{kD_L} \tag{6.7}$$

Now the local solidification rate at the interface can be found in terms of the laser scan velocity V_s as follows (Gremaud et al, 1990):

$$R = V_s \cos\theta \tag{6.8}$$

where θ is the angle between the laser scanning direction and the orientation of the normal to the solid liquid interface (see Figure 6.5). By assuming that the solute concentration in the solid equals the equilibrium solute concentration for the alloy then $C^*_S = C_{Lmax}$, and by substituting Equation. 6.8 into Equation. 6.7 and combining with Equation. 6.5 it is possible to obtain the following relationship for the cell spacing at the onset of cellular dendritic growth in terms of the laser scan velocity.

$$\frac{1}{\lambda} = \frac{V_s C_{L_{max}} \cos\theta}{D_L}\sqrt{\frac{(1-k)}{2k}} \tag{6.9}$$

Equation 6.9 can then be used as an indication of the structural refinement that would be obtained as a result of laser surface melting, which can have some affect on the corrosion resistance of the alloy. The significance of this will be discussed in more detail later in section 6.3 of this chapter. Equation. 6.9 shows that the cell spacing is inversely proportional to the laser scan velocity and the curve from experimentally determined results plotted against the theoretical curve is shown in Figure 6.6. The values used to obtain the curve were $C_{Lmax} = 0.0456$ wt.%, $\theta = 82^\circ$, $D_L = 1\text{x}10^{-9}$ m²/s, and $k = 0.172$. The experimental points do not lie on the theoretical curve because the terms cos θ and C_L are in fact not constant and k is not equal to the equilibrium value but the non-equilibrium value which is likely to be close to 0.5 - 0.6. The two other discrepancies in Equation. 6.9 can be explained as follows.

The above equations 6.7 and 6.8 can also be used to calculate the angle of growth at the onset of cellular dendritic solidification and it is found that as the laser scan velocity increases θ increases. For example at 400 mm/s, in theory for a Al- 4.56 wt.% Cu binary alloy, cellular dendrites initially grow at 88.7° to the laser scanning direction and at 20 mm/s the angle is 75.4° and hence the relationship between scan velocity and cell spacing moves away from a simple inverse law. The second deviation from the simple inverse relationship arises from the fact that the solute concentration in the melt changes as a consequence of increasing the scan velocity. In Figure 6.7 it can be seen that large second phase particles have melted and resolidified without any uniform distribution of the alloying elements. This effect was noticed for scan velocities greater than 70 mm/s and means that the value of the solute concentration used in Equation. 6.9 is not equal to the equilibrium solute concentration C_{Lmax}. Further to this, an assumption is made that the material is a binary alloy so the value used in the theoretical calculations is about 2 wt.% lower than the maximum solute concentration of the actual alloy. Taking into account these departures from the simple inverse relationship it is still proposed that Equation. 6.9 can be used to predict microstructure refinement after laser surface melting given that further investigation is still required to find the relationship between V_s and θ and the effect that V_s has on the solute concentration in the melt.

6.1.2.3. Solute banding

Equation. 6.6 above can be used to explain the occurrence of planar front solidification, and subsequent cellular, cellular dendritic, and finally dendritic growth. However, it cannot be used to explain other phenomena such as solute banding, segregation, and the formation of non-equilibrium structures. The section that follows discusses the appearance of solute banding with reference to models proposed by other workers.

Current theory has not been able to produce a single reliable model to explain the phenomenon of solute banding. This problem is made more complex by the fact that more than one form of banding exists. In the present study bands were observed to form as concentric contours parallel to the fusion line and lying throughout the melt zone in both of the surface melted alloys, and this is explained it terms of discontinuous supercooling. However a second form of banding was also present in the 7075 alloy which appeared as alternating layers of α-Al and intermetallic particles.

The appearance of the first type of banding was associated with both structural changes and compositional fluctuations. The cellular dendrites were slightly coarser within a band but progressively became more refined as the solidification continued. Now if we consider once again constitutional supercooling, the cellular dendrites grow from the melt at a lower temperature than the equilibrium freezing temperature. However, the solidification rate increases because solute rejection to the melt increases the supercooling and because of the dependence on the laser scanning velocity shown in Equation. 6.8. The result is the rapid evolution of latent heat which then causes an inversion of the supercooling and solidification temporarily halts. Solute diffusion from the solid into the adjacent liquid takes place (Gurev and Stout, 1963), which further increases the solute concentration in the liquid resulting in supercooling once again and growth restarts with a band of solute enriched solid. Banding has recently been reported in 2024 aluminium alloy by Milewski et al (1993) but its occurrence was attributed to fluctuations in the energy absorption from the pulsed laser. This explanation was also given by Davies and Garland (1975) who suggested that variations in the local energy absorption induced changes in growth rate, which in turn produce fluctuations in the composition. It has also been suggested by Copley et al (1978) that the surface tension of the melt is sufficiently high so as to pull the liquid away from the growth front. As the liquid accumulates its mass becomes such that the surface tension can no longer support it and it then falls back onto the old solid/liquid interface and solidifies itself.

It is not likely that the explanations given by Davies and Garland (1975) and Copley et al (1978) for solute banding are responsible for the observed structures in this study. If the energy absorption varied during melting then it would be only natural to find that the melt depth profile varied also. However, the profiles of the melt pools were always smooth so this indicates that the energy absorption was uniform. Also, the Al would have been very fluid at the high temperatures achieved in the melt. It is, therefore, unlikely that the surface tension could pull the liquid away for a sufficiently long enough time as to cause the formation of a new growth front after the collapse of any accumulated melt. However, it has been shown by Antony and Cline (1977) that surface tension effects are responsible for the characteristic surface ripples that are formed after melting and resolidification.

The second form of banding, present only in the 7075 alloy, has been found to be very similar to the kind of banded structures observed by Gremaud et al (1991) and Gill and Kurz (1993) in Al-Fe and Al-Cu alloys, respectively. The banding structures were characterised in terms of the growth rate so for slow growth rates they used the term low-velocity bands and similarly at higher scanning rates, high velocity banding. The low velocity bands were in fact the same as those discussed above but the high velocity bands consisted of a succession of light and dark bands that were parallel to the solid/liquid interface. The dark bands consisted of an ultra-fine cellular dendritic structure, whilst the light bands were said to be a region of planar front solidification. They proposed that the high velocity banded structure occurred at the limit of absolute stability due to the acceleration and deceleration of the local growth rate, according to the graph shown in Figure 6.8, so that the mean growth rate equalled the rate of advance of the isotherms in the liquid. Hence, it was also observed that the growth rate in the individual bands was not constant such that the mean growth rate was not equal to the local growth rate within a light or a dark band. For instance, in a dark band the local growth rate, calculated from primary cell spacing, was about 500 mm/s for V_s=2.0 m/s, whereas the mean growth rate was 700 mm/s. On the other hand the local growth rate within a light band was deduced to be about 17 m/s for the same mean growth rate. Unlike in low-velocity banding, in the high-velocity bands the band spacing was observed to be dependent on velocity with the dark bands decreasing in size with increasing velocity until there was only growth of the light bands.

Even though the second type of banding found in the surface melted 7075 is similar in appearance to the high velocity bands of Gremaud et al (1991) they are not the same. The most obvious difference is the scale of the banded structure. The band width is approximately 5 μm for the LSM 7075 alloy in this work but the high velocity bands in the Al-Fe alloys studied by Gremaud et al (1991) had a spacing of ~200 nm, which is an indication of the higher growth rates in the Al-Fe alloy. The structure was also different because the bands in the 7075 alloy consisted of alternating layers of α-Al and intermetallic and not the ultra-fine cellular dendritic structure reported by Gremaud et al (1991). Therefore, the banded structure in the LSM 7075 grew by planar front solidification of the α-Al with the periodic rapid solidification of the solute enriched liquid that is just in front of the solid/liquid interface (Sperry, 1955). This is similar to the type of microstructure observed by McCafferty et al (1981) for a surface melted Al-1.2 wt.% Mn alloy.

6.1.2.4. Microstructural stability and ageing

The structural stability is very important because the formation of precipitates should mean that the corrosion resistance would be expected to decrease, and therefore it was necessary to study natural ageing. The microstructure of the LSM 2014 alloy was found to be very stable because the intermetallic phase in the interdendritic boundaries is believed to be $CuAl_2$ (Milewski et al, 1993). A very small amount of precipitation of θ'' in the α-Al was observed in thin foils of the LSM 2014 but only after 12 - 18 months. This is in sharp contrast to the work of Noordhuis and De Hosson (1993) who found that a LSM 2024 alloy exhibited signs of precipitation after only 1 week of room temperature ageing. The difference in composition between 2014 and 2024 alloys is small but because 2024 has a higher Mg and lower Si content it is possible that the stability of the structure is lower because of the mutual attraction of Cu and Mg atoms due to the size factor of the respective atoms (Van Lancker, 1967). This means that it is easier for Cu and Mg to form zones and hence begin the nucleation of precipitates.

In thin foil samples of the LSM 7075 alloy, however, it was found that after a period of a few months the microstructure started to change. Firstly there was the appearance of large, 100 nm, intermediate precipitates (P1) that later transformed to a more stable precipitate (P2). Secondly, the interdendritic region started to break up after about a year as the atoms started to diffuse into the α-Al; this occurred at about the same time as the P2 precipitates started to appear. The exact identity of the precipitates is not known but three possible candidates have been proposed. The three possible structures are analogous to η'(Yan et al, 1992), $CuMgAl_2$ and Mg_2Cu (Van Lancker, 1967), which have all been reported as having an orthorhombic structure.

Precipitation can occur as a consequence of interactions between solute atoms and the high quenched in vacancy concentrations and dislocation densities that arise after laser surface melting; the results showed an increase in copper concentration in the precipitates that seemed to have nucleated on or adjacent to dislocations. Nucleation may have been started by the formation of Cu-vacancy pairs (Livak and Papazian, 1984) which then diffuse to dislocations where the vacancies are absorbed and the Cu can form the nucleus because of the lower activation energy barrier (Davies et al, 1994). Once copper starts to concentrate in zones elastic strain energy starts to increase in the surrounding Al matrix because copper has a smaller atomic radius than Al. However, Mg has a larger atomic radius than Al and thus there is an attractive interaction between the Cu and Mg which reduces the elastic strain energy and allows the precipitate to grow (Van Lancker, 1967).

At some stage during the growth of the precipitate a structural transformation occurred and the P1 precipitate changes to the P2 structure. This coincided with the diffusion of material from the interdendritic phase into the Al (see Figure 4.38), which can be taken as evidence that the P2 precipitates grow at the expense of the the interdendritic phase. This would only be possible though if the P2 precipitates were more stable than the precipitates in the interdendritic regions (Porter and Easterling, 1988). Solute diffusion is possibly aided by the presence of dislocation loops, that are just visible in Figure 4.38, which formed as a result of collapsing vacancy clusters. This mechanism has been confirmed by Embury and Nicholson (1965), who have shown that the quenched-in vacancy concentration has a strong effect on the precipitation kinetics in Al-Zn-Mg alloys.

Compositional analysis of the precipitates confirmed the presence of up to 20 wt.% Cu but from this information it was not possible to identify the exact phase. The η' phase is an intermediate precipitate in the $MgZn_2$ formation sequence but its composition may include the MgAlCu phase which is completely miscible in $MgZn_2$ (Wert, 1981). Furthermore, it is also possible that Cu substitutes for Zn in the precipitation sequence of this alloy (Mondolfo, 1976). However, the results also showed that the zinc concentration in the melted layer was reduced because of vaporisation; Figure 6.9 shows that the vapour pressure of zinc is higher than Mg, Al and Cu. The reduced concentration of zinc may then affect the type of precipitate that forms. The X-ray maps in Figure 6.10 show increases in the Cu and Mg concentration in the precipitates but none for Zn. This could then be taken as an indication that the precipitates were possibly $CuMgAl_2$ or Mg_2Cu, which would suggest that the P2 precipitates were not tending toward η' phase formation.

Simulation of the SAD patterns from each of the above phases using Diffract 1.2a on a Macintosh computer produced patterns very similar to the experimentally obtained results. By comparing the plane spacings and considering the composition the most likely candidate for the P2 precipitate is then η' or a transient precipitate leading to this phase. η' has recently been found to have a face centred orthorhombic structure with a = 4.92 Å, b = 8.52 Å, and c = 7.01 Å, and an orientation relationship with the $[\bar{2}0\bar{1}]$, $[\bar{1}\bar{1}\bar{2}]$, and $[\bar{1}0\bar{2}]$ directions being parallel to the [001], [011], and [112] directions in the Al matrix (Yan et al, 1992). Furthermore, the P2 precipitates are similar in appearance to those observed by Davies et al (1994) in a SiC reinforced Al-Zn-Mg-Cu alloy aged at 210 °C for 3/4 hr, which were also identified as η'.

The precipitates mentioned above were not found in bulk samples. Some of the surface melted 7075 alloy was set aside under normal room temperature conditions for over 12 months and TEM thin foils made from these samples contained no evidence of precipitation. It is possible though that after short periods of artificial ageing that these precipitates would be observed and then it would also be possible to study the effect on the corrosion resistance of the surface melted layer.

6.1.3. Solidification and Microstructure of Laser Surface Alloyed Al Alloy Substrates

The following section gives only a brief discussion of the solidification and microstructure of the LSA aluminium alloy substrates because most of the points covered in the discussion of laser surface melting in the previous section also apply here. There were only slight differences in the microstructure of the surface alloyed substrates with the predeposited plasma sprayed coating and the LSM alloys. These differences concerned the size of the initial planar front region at the maximum melt depth, and the precipitation from the melt of intermetallic particles during cellular dendritic growth.

6.1.3.1. Planar front solidification

The microstructures of the LSA layers on the 2014 alloy substrates were shown to be very similar to the microstructure of the LSM alloy. However, the region of planar front solidification was narrower in the LSA alloys. At the maximum melt depth the partially melted grains contained coarsened precipitates bordering the fusion line that were responsible for the nucleation of the interdendritic phase. This then suppressed planar front solidification, which instead started by cellular dendritic growth and was probably assisted by very high supercooling.

6.1.3.2. Cellular dendritic growth

The equilibrium solubility of Mo in Al is very low (~0.08 wt.%) so that on solidification it is rejected from the solidifying liquid very quickly producing large constitutional supercooling and the dendritic structure nucleates. The solute concentration was very even in the melt, which is apparent by the presence of intermetallic particles at the fusion boundary and which is also confirmed by the composition profile in the results (see Figure 5.14). However, Figure 6.11 also seems to show that there was not sufficient time in the melt for the Mo to completely segregate to the interdendritic boundaries. This meant intermetallic particles solidifying at the solid/liquid interface were frozen into the α-Al. Figure 6.11 shows two such cases of this where the nucleation of an intermetallic particle on the cell boundary has interrupted the growth of the interdendritic phase and another is seen to have formed in the centre of the dendrite arm. Both of the intermetallic particles seem to have been nucleated by the presence of the smaller spherical precipitate. In fact all of the angular precipitates were formed on or adjacent to one of the spherical precipitates.

The true identity of the spherical precipitates is not known. Clear electron diffraction could not be obtained in order to index its structure because, as Figure 6.11 shows, in many cases more than one angular precipitate would be nucleated on the spheres. Electron diffraction from the angular precipitates, however, showed similarities with X-ray powder diffraction data (summarised in Table 5.1) which indicated that the intermetallic $Al_{12}Mo$ phase was present in the new surface alloy.

A third form of precipitate was also identified in the results and these were the $MgAl_2O_4$ star shaped particles. Ar gas was used to shroud the surface alloying operation but as already explained for the surface melting if the gas pressure is not sufficiently high then oxygen can be adsorbed and very quickly diffuse into the liquid. However, oxygen may already have been present because the plasma sprayed coatings were very porous. Therefore this makes it very difficult to remove all of the oxygen and explains why the $MgAl_2O_4$ particles were found in all of the surface alloyed samples prepared with predeposited plasma sprayed coatings.

6.2. MECHANICAL PROPERTIES

6.2.1. Hardness measurements

The results showed that the hardness in the melted layer of both of the LSM alloys had decreased compared to that of the unmelted substrates. In addition, the hardness of the LSA 2014/Mo alloy was also lower than the untreated substrate and comparatively lower than the LSM 2014 alloy.

In recent work by Noordhuis and De Hosson (1993) on laser surface melting of 2024 alloy the hardness values in depth profiles were shown to decrease from the surface to the fusion line for laser scan velocities between 10 mm/s and 80 mm/s. Their hardness value for a scanning velocity of 20 mm/s is slightly less than the the average value obtained from the depth profile in this study, and Noordhuis and De Hosson (1993) present no data for the hardness of the substrate alloys so it is not possible to compare the effect of LSM on the hardness. It is interesting to note that they observed precipitation of θ′and possibly S′ phase in the melted layer at scanning velocities between 10 mm/s and 40 mm/s; they also attributed the increases in hardness to the presence of these precipitates. No hardening effects due to precipitation were observed in the present study involving the 2014 alloy which is all but identical to the 2024 alloy except for the fact that 2014 has a higher Si and a slightly lower Mg content. However, other recent work involving the 2024 alloy (Almeida, 1993) has showed that the changes in the hardness following LSM were similar to the LSM 2014 alloy in this study.

The reductions in the hardness values observed in this study are probably due to the fact that the age hardening precipitates are removed from the structure and that the overall grain size is increased in the laser processed surfaces. Therefore the mechanism for strengthening most likely depends on cell boundary-dislocation interactions. It is also possible that solid solution hardening has had some effect on the hardness. However, because of the scale of the microstructure it is likely that the cell boundary-dislocation interactions are the most significant factor.

6.2.2. Residual Stresses

6.2.2.1. The effect of surface pretreatment on residual stress

The residual stresses were measured in laser surface melted 2014 alloy with two different surface pretreatments. Tensile residual stresses were higher when the alloy was pretreated by immersion in sodium hydroxide solution. This may be due to the fact that sooting results in a relatively dense black surface coating and therefore the alloy absorbs more of the peripheral laser energy of the Gaussian distribution and hence a greater proportion of the surrounding substrate material is heated. Therefore, the absorbed heat has a more significant stress relieving affect when area coverage involves multiple laser melt tracks.

6.2.2.2. The effect of laser scan velocity on residual stress

There is good agreement in the results, shown in Figure 4.56, with the work on stainless steels by Lamb et al (1986) who showed that as the scanning velocity is increased the residual stress increases. This arises because as the velocity is increased less of the substrate is melted and the secondary heating effects on the substrate are also smaller. As a result of this the successive melt depths are shallower leading to faster quench rates which in turn result in higher residual stresses. It was also found that as scanning velocity was increased to higher than 70 mm/s the residual stress started to decrease rapidly. This can be attributed to cracking during solidification. The volume contraction during solidification and cooling produces the thermal stresses and these are concentrated in the last liquid that solidifies (Pumphrey and Lyons, 1948). The cracks were found to run along grain boundaries, from the fusion zone to the free surface in the most severe cases, and since the grain boundaries formed through segregation during the competitive growth of the grains the solute rich liquid would have been among the last to solidify.

6.2.2.3. The effect of intertrack distance on residual stress

There are potentially two heat mechanisms for stress relieving the laser surface melted layer. Firstly there is the effect due to substrate heating which is mainly affected by the amount of incident heat energy, secondly there is the part of the prior melt track that lies within the heat affected zone of the overlapping melt track. The results presented in Figure 4.57 show good agreement with the work by Lamb et al (1986) on steels. It was found that as the distance between overlapping tracks increases, or the percentage of overlap decreases, the residual stress increases. This is because the residual stresses are concentrated at the overlaps (Van Brussel and De Hossen, 1993) and therefore by decreasing the overlap distance the heat effect on previous melt tracks is increased, hence a greater degree of stress relief is achieved.

The residual stress in a single track was tensile in the case of these alloys which agrees with the work on plain carbon steels by Van Brussel and De Hossen (1993) and 316 stainless steel by Lamb et al (1986). The stress remains tensile because there are no solid state transformations that can offset the tensile stress built up during solidification. Compressive stresses have been recorded for single tracks on 420 stainless steel (Lamb et al, 1986) and were attributed to the effect of the martensitic transformation. It is expected that if the distance between melt tracks was decreased further then the residual stress would fall away sharply when the prior melt track was situated wholly within the heat affected zone of the overlapping melt track.

6.2.2.4. The effect of heat treatment on residual stress

One sample from each of the alloys was heat treated at 100°C in order to study how the residual stress changed. The results indicated that the stresses were initially increased but the reason for the increase during the initial period of heat treatment is not fully understood at present. The increase is possibly associated with the lattice strain built up during the migration of the solute copper atoms from points of high concentration into the aluminium lattice to form Guinier-Preston (GP) zones. At the temperature chosen for these experiments the GP zones are very stable and for a long time. The ageing characteristics of this alloy suggest that the peak aged condition would not be achieved for many tens of days at the temperature used (Ashby and Jones, 1986), see Figure 6.12. Therefore, the effectiveness of stress relieving at this temperature would be very small. This is reflected in the fact that the stress level shown in Figure 4.60, even though seeming to fall after ~90 minutes, remained at quite a high level (~100 MPa). It is also possible that the overall small decrease in residual stress may be due to the diffusion of the solute atoms from points of high concentration into the surrounding material. It is expected, therefore, that further heat treatment for several days may actually result in a significant decrease in residual stress.

6.2.2.5. Subsurface stresses

Depth profiling was carried out to measure the stress distribution in the melted layer and also to determine the depth at which the stresses became compressive. In the results the subsurface stresses were shown to vary greatly with melt depth. The plot of 2θ against $\sin^2\psi$ in Figure 4.58 indicated that the change in the internal residual stresses did not follow a linear relationship with depth. This is deduced by the fact that the depth of penetration of the incident X-rays is a function of specimen orientation so that if the distribution of stress was uniform throughout the melt depth the resulting graph of 2θ (or d-spacing) versus $\sin^2\psi$ would be a straight line.

However, it was additionally noticed that the residual stresses could be correlated to the hardness values, and that the maximum stress, shown in Figure 4.59, coincided with the minimum hardness which occurred at the maximum melt depth, as shown in Figure 4.54. Furthermore, the experimentally measured stress distribution after layer removal showed that the stresses did not become compressive until depths past the HAZ. This also seems to bear a similarity to the hardness profiles where the hardness values did not equal those of the untreated alloy until several hundred microns past the HAZ.

6.3. CORROSION PROPERTIES

6.3.1. Corrosion of As-received Aluminium Alloys

6.3.1.1. Pitting corrosion of the as-received 2014 alloy

The 2xxx alloys are known to be very susceptible to pitting corrosion because the principal alloying addition is copper which has a recognised detrimental effect on the corrosion resistance of aluminium. The corrosion properties of this group of aluminium alloys has been the subject of extensive research and the results presented in this study show good agreement with the literature.

Urushino and Sugimoto (1979) measured the pitting potential of the 2024 alloy to be in the range of -750 mV to -600 mV (SCE) for different ageing times between 0 and 10 days. E_{pit} for the alloy aged for 2 days was the same as that of the 2014 alloy used in this study, which was aged under the same conditions. They also showed however, that the 2024 and 2017 alloys had two pitting potentials. A lower E_{pit} corresponding to grain boundary corrosion and a second, higher, E_{pit} which marked the onset of grain matrix pitting. This type of behaviour was not observed for the 2014 alloy either by potentiodynamic or potentiostatic conditions in this study. Ambat and Dwarakadasa (1992) have measured E_{pit} for the 2014 alloy to be -705 mV (SCE) in 3.5% NaCl pH 8. They later showed that the effect of increasing the pH was to decrease E_{pit} (Ambat and Dwarakadasa, 1993). They measured E_{pit} for the 2014 alloy in 3.5% NaCl, pH 10 to be -762 mV (SCE) and with a passive current density of 3.5 $\mu A/cm^2$ which is approximately 50 mV lower than the results of this study where the pH is close to a neutral solution for 1 M NaCl.

6.3.1.2. Corrosion of the as-received 7075 alloy

The corrosion resistance of 7075 alloy is known to be better than that of 2014 and other alloys. 7075 contains a smaller amount of copper and has higher amounts of the less noble elements Mg and Zn. This means that precipitates that are strongly cathodic are not likely to form. The higher amounts of Mg and Zn, however, promote the formation of anodic phases.

The potentiodynamic anodic polarization curve for as-received 7075 tested in 1M NaCl, shown in Figure 4.46 in Chapter 4, indicates that the alloy has attempted to passivate because there is an anodic current density transient. It is possible that an unstable film was able to form on the surface for a short time causing the small passivation loop. The breakdown of the film would then lead to immediate pitting. However, potentiostatic tests and subsequent studies of the surface revealed that the two breakdown potentials were associated with firstly intergranular corrosion and secondly grain matrix pitting corrosion. It was also shown that as the pretest immersion time increased the magnitude of the anodic current density transient decreased. This effect has not previously been reported for the 7075 aluminium alloy but similar results were obtained for E_{corr} with a corresponding single breakdown potential by Mansfeld and Fernandes (1993).

A possible explanation for this behaviour is that segregation of Mg and Zn to the grain boundaries during heat treatment causes the formation of a PFZ adjacent to the grain boundaries. This would undoubtedly lead to preferential corrosion at grain boundaries not only because of the galvanic effect but also due to the fact that magnesium has a higher affinity to chlorine, in that it forms stable chlorides more easily, than Al (Cottrell, 1982). There are also small amounts of copper added to the 7075 alloy (up to 3 wt.%) to aid the nucleation of GP zones. In this alloy the zones go on to form the stable η ($MgZn_2$) precipitate and the copper is thought to be retained in solid solution. However, if the copper atoms were to diffuse to the grain boundaries then the grain boundaries would become cathodic to the rest of the grain and thus present a mechanism for preferential attack of the adjacent grain matrix. Several workers have investigated the effect of grain boundary segregation of Cu, Mg, and Zn on the susceptibility to stress-corrosion cracking (SCC) of 7xxx alloys. The results are, however, rather contradictory. For example Shastry et al (1981) found that SCC susceptibility increased with increasing solute segregation in 7075 alloy but Pickens and Langan (1987) showed that for a similar Al-Mg-Zn alloy even though segregation of Mg did occur at grain boundaries it was not a sufficient condition for SCC.

6.3.2. The Corrosion Properties of Laser Surface Melted Alloys

There is to date a very small volume of work reported involving the electrochemical behaviour of laser surface treated aluminium alloys. There has been no work published involving corrosion property measurements of laser surface melted Al-Cu and Al-Zn-Mg alloys. McCafferty et al (1982) found that the pitting potential of an Al-1%Mn alloy in sodium chloride solutions was not improved after laser surface melting, but if anything was made slightly worse. In sodium citrate solutions they noticed an active-passive transition and that the current density was lower at all potentials for the surface melted alloy. Consequently there was an increase in the resistance to uniform corrosion. However, there was no explanation given as to the possible reason for the observed improvements. Opera et al (1985) measured the corrosion current densities of aluminium alloy AL4 in 5% NaCl during anodic potentiodynamic polarization, when the potential equalled E_{corr} + 100 and 200 mV. This alloy contains about 9.5% Si, and the corrosion current density was found to depend on the laser specific energy input (MW/m^2) and the microstructure for laser scanning velocities of 300, 500 and 1300 mm/s; no reference was made to the corrosion resistance of the untreated alloy. They found that for the slow laser scanning speed, 300 mm/s, and hence high specific energy input (> 40 MW/m^2), the corrosion current density was high (~ 20 - 40 mA/cm^2) and they attributed this to a coarser dendritic structure. Conversely for a higher laser scanning speed, 700 mm/s, the corrosion current density decreased to less than 20 mA/cm^2, which they said was due to a more homogeneous structure being formed. However, when the specific energy input was < 20 MW/m^2 (V_s = 1300 mm/s) the current density increased again, up to 160 mA/cm^2, and the structure of the surface melted layer was nonuniform.

In the present study the maximum laser scanning speed used to melt samples for corrosion testing was 70 mm/s. The relationship between the pitting potential of LSM 7075 alloy and residual stress as a function of increasing laser scan velocity was shown in Figure 4.61. The graph implied that as V_s increased E_{pit} decreased but the range over which pitting potential was measured was only between -790 and -770 mV (SCE). Furthermore, the results depicted in Figure 4.61 were not very reproducible. However, for the range of laser scanning velocities investigated E_{pit} was always measured between -790 and -770 mV (SCE). Opera et al (1985) attributed the changes in corrosion properties of LSM AL4 to the changes in the microstructure with increasing V_s. In this present work the morphology of microstructure did not actually change in the range of the laser scanning speeds used and therefore, it is not surprising that there was not a dramatic change in the pitting potential. It is still believed, however, that the laser scanning speed influences the pitting corrosion behaviour due to the presence of the residual stresses, and this will be discussed in section 6.3.4.

6.3.2.1. Corrosion of LSM 2014 alloy

It was shown in Chapter 4 that the anodic pitting potential of 2014 alloy was increased by up to 100 mV (SCE) over that of the as-received alloy. The actual improvement is however best viewed in terms of the applied potential or the passive range, E_{PD}, from E_{corr} to E_{pit}. In the case of the as-received alloy E_{PD} was of the order of 50 mV but after surface melting E_{PD} had increased to as much as 400 mV. The larger value arises from the fact that not only had E_{pit} increased from -700 mV (SCE) to ~-600 mV (SCE) but also because after deaeration E_{corr} had decreased to as low as -1050 mV (SCE). This large decrease was not observed for the as-received alloy in deaerated solutions. The increases in E_{PD} after the LSM treatment are believed to be due to changes in the oxide layer as discussed below.

In Chapter 4 it was also shown that the composition of the oxide film on the laser surface melted alloy was slightly different to that of the as-received alloy. The oxide on the as-received alloy was found to contain only Al whilst that of the surface melted alloy was found to contain traces of all of the major alloying elements. It is not fully understood as to how the changed oxide composition has affected the pitting resistance of the alloy. By incorporating some of the alloying elements into its structure the oxide film may have been more resilient. The oxide film may also have been more even due to the finer microstructure. With the absence of large second phase particles the oxide may have had fewer pre-existing thin areas and therefore it would have been more resistant. However, the copper in the oxide film was apparently in the elemental form and therefore according to accepted belief should have had a detrimental effect on the corrosion resistance. Unfortunately XPS techniques do not give information on the distribution of the elements in the oxide other than through carrying out depth profiling which was not a part of the present study.

McCafferty et al (1982) showed by Auger spectroscopy that the oxide formed on the surface after laser melting was essentially that of pure aluminium. The laser melted surface contained decreased concentrations of the alloying elements Mn, Fe, and Si compared to the unmelted surface. They explained this by comparing the surface tension data of the liquids of the individual elements and noting that Mn, Fe, and Si were not surface active relative to Al. Virtanen and Bohni (1993), however, found that their results suggested the composition was different for Al- 12 wt.% Si and Al- 17 wt.% Si alloys after laser melting and probably due to an increased Si content. They said that the Si in solid solution may have been increased after surface melting with the laser and that this Si could then have been incorporated in the oxide film. In addition, they also showed that in the high Si alloy (Al- 17 wt.% Si) that the heterogeneity of the surface was much larger and that the oxide formed on the interface regions of overlapping laser passes was less resistant to pitting. The observations in the present study are, therefore, similar to those of Virtanen and Bohni (1993).

A further consideration is that because Cu was found in the oxide after LSM the pH of zero charge, pH_{pzc}, of the oxide may have been reduced. Natishan et al (1986) have shown that the pH_{pzc} of the oxide of Cu is lower than that of Al. Therefore, Cu may have been able to increase the pitting potential of LSM 2014 by being incorporated into the structure of the oxide film.

6.3.2.2. Corrosion of LSM 7075 alloy

Differences in the corrosion properties have been shown to exist between laser surface melted 2014 and 7075 alloys. The effect of surface melting on the corrosion properties of the 7075 alloy was that the second breakdown potential, seen during the testing of the as-received alloy, was eliminated. The pitting potential of the surface melted 7075 alloy in 1M NaCl was also only slightly different to that of the initial pitting potential of the as-received alloy, and there was only a decrease in E_{corr} of ~50 mV in deaerated 1M NaCl solutions. The XPS profiles in Figures 4.52 and 4.53 also showed that the surface oxide on the 7075 alloy was apparently unchanged after LSM, so the actual corrosion mechanisms of anion adsorption on, reaction with, and subsequent thinning of the oxide layer may not have changed either. In which case the small differences that were noticed may only be due to a more even oxide film after LSM.

It was suggested in section 6.3.1.2 that the second breakdown potential, which existed for short immersion times when the as-received 7075 alloy was polarised in the chloride electrolytes, was caused by the onset of pitting corrosion in the grain matrix, and this was due to the presence of second phase particles. In the surface melted alloys the second breakdown potential was absent and this can be explained as follows. The result of surface melting was that the second phase particles were dissolved and the alloying elements were redistributed to the cellular dendritic boundaries and grain boundaries during solidification. The refined structure of the grain matrix might then have been more corrosion resistant than the grain structure of the untreated alloy. However, the overall increase in corrosion resistance was not significantly large. This effect might be due to an increase in the zinc content of the α-Al which might have offset slightly the beneficial effect of having a refined grain structure (Ramadan et al, 1992 and McCafferty et al, 1993). Furthermore, in the surface melted alloy the grain boundaries contained higher amounts of Mg and Zn than in the as-received condition and therefore it is possible that the susceptibility to grain boundary corrosion was increased after LSM. The segregation to the grain boundaries occurred because the grains solidified epitaxially by cellular dendritic growth, and the grain boundaries formed as a result of the competitive growth of opposing cellular dendrites. The corrosion reaction, if one were to occur, would then be controlled by the potential difference between the grain matrix and the grain boundary phase. In the as-received alloy pitting is initiated in the grain matrix because of the potential difference between the anodic $MgZn_2$ particles and the Al solid solution. Analysis of the composition of the interdendritic phase and hence the grain boundary phase showed that it was not consistent with being $MgZn_2$. Any slight decrease in the potential difference between the grain boundary and the matrix would then account for an increase in the corrosion resistance, assuming of course that intergranular corrosion was the preferred mechanism.

6.3.3. Corrosion Morphology and Distribution in the LSM Alloys

It was mentioned in the results, section 4.2.1.3, that there were four distinct regions where localised corrosion (loosely defined as pitting) occurred on the laser surface melted 2014 alloy. These were at the melt track overlaps, grain boundaries, solute bands, and within the cellular dendrites. After the initial nucleation of the individual pitting events the mechanism for propagation was essentially the same for each of the regions and can be attributed to local potential differences because of the change in composition. The distinguishing factors between the pits were their size and occurrence. Generally the intradendritic pits were initially very small and they grew laterally across the surface by dissolution of the Al. The grain boundary pits were really just an extension of this in that pitting was nucleated at the grain boundaries but propagation was again lateral as opposed to penetrative. These two forms of pitting were the most common and are believed to be the first that nucleated in the anodic potentiodynamic pitting scans.

The third form of pitting was not at first obvious and was not revealed until the samples were polished and etched after the corrosion tests. These were pits that formed at the solute bands and again were caused by localised galvanic corrosion. They were characterised by the fact that not only did they spread across the surface due to the cellular dendritic structure but also down into the melted layer along the contour of the band. These pits were only found to occur though if the pitting scans were performed up to potentials much higher than the pitting potential so that at potentials close to E_{pit} they resembled the more common interdendritic pits.

The last form of pitting, which was observed at the track overlaps, was not really observed at low potentials in the pitting scans but was quite severe at much higher potentials. Also this form of attack seemed to be more severe after long immersion times. Examination of the cross sections showed that even though interdendritic pits had formed on samples used for immersion tests it was the intertrack form of attack that was the most severe. A possible explanation for this is that initially pitting nucleated at the interdendritic sites but as the attack progressed the corrosion products which formed on the surface effectively sealed off these sites. The preferred mode of attack then switched to the track overlaps and the pit morphology, being deeper rather than more spread out, gave rise to suitable conditions for the autocatalytic propagation of these pits as oxygen became depleted. The reason that this was not more predominant in the pitting scans could then be due to the fact that removal of the corrosion products from the surface allowed the other pits to grow preferentially. Gas formation could have been responsible for scouring the surface and hence ensuring that the interdendritic type of pits were always exposed. However, pitting along the track interfaces was also found to be dependent on the applied potential because at very high potentials the corrosion at these sites was so severe as to cause furrowed grooves along the length of the interface. In this case pits apparently also nucleated by the blocky particles formed in the adjacent HAZ of the melted layer. This can be seen in Figure 6.13 which shows the dissolution of the aluminium matrix around second phase particles in the HAZ adjacent to a track-track interface. Coalescence of the pits and the simultaneous corrosion of the planar front region resulted in the formation of the grooves that were clearly visible to the naked eye.

In the case of the LSM 7075 alloy, studies of the surface after polarization showed that localised corrosion had a tendency to occur at the grain boundaries. Fewer sites were found in the grain matrix than in the surface melted 2014 alloy but where they had formed they had the same morphological characteristics as those on the 2014 alloy. There did not seem to be a propensity for pitting to nucleate on the the solute bands which is probably due to the fact that the compositional changes associated with the banding were not as severe as in the 2014 alloy.

6.3.4. The Effect of Residual Stress in the LSM Alloys on Corrosion Resistance

It was stated in the results (also shown in Figure 6.7) that the residual stresses were capable of causing solidification cracking along grain boundaries and hot tearing in the region of the fusion boundary. These cracks have an obvious effect on the corrosion resistance in that they provide sites for crevice corrosion which can be accelerated by the grain boundary phase. Not all of the grain boundaries, however, exhibited cracking but it is safe to assume that these grain boundaries are under the effect of the residual stresses. Therefore, in a corrosive environment it would be reasonable to expect that preferential corrosion occurred at the grain boundaries due to the effect of residual stresses as well as any compositional effects. In actual fact this was only observed in the 7075 alloy where pitting on the surface melted alloy was generally initiated at grain boundaries. In addition to this the increase in pitting potential of the LSM 7075 alloy was found to be quite poor when compared to that of the LSM 214 alloy. Previously this difference was explained in terms of the composition of the phases at the grain boundaries. An additional effect that may also account for poor corrosion resistance is that of dislocations and their effect on the susceptibility to SCC. The high quenched in vacancy concentration results in the formation of dislocations which when adjacent to grain boundaries can assist in the SCC mechanism (Jacobs, 1966) brought about by the residual stress. Recently it was shown by Talianker and Cina (1989) that the susceptibility to SCC was primarily determined by the presence of dislocations adjacent to grain boundaries and not the structure and composition of grain boundary precipitates.

The preferential attack at grain boundaries was less severe in the LSM 2014 alloy when compared to the grain matrix corrosion. However, the residual stress may still have had a subtle effect on the corrosion mechanism. It has already been shown (Figure 4.63) that pitting corrosion caused the dissolution of the α-Al along the dendrite arms in the grain matrix, and that the Al in the dendrite arms at the bottom of the pits contained ultra fine cracks which are believed to be caused as a result of the residual stresses. Now if we consider the above explanation for grain boundary SCC then it can also be applied to the dendritic corrosion. TEM studies have shown qualitatively that there is a large dislocation density in the α-Al after LSM. If the assumption is made that the interdendritic boundaries behave similarly to grain boundaries in the presence of a high dislocation density, then it can be further assumed that the residual stresses may cause a very localised form of SCC within the cellular dendrites. As microcracking has been observed in the corrosion pits this seems to be a good explanation of the effect of residual stress on the corrosion resistance of the LSM alloys. Furthermore, Hemsworth et al (1969) found that cracking occurred along cell boundaries as well as grain boundaries which would seem to support the above explanation.

The results also show that the maximum residual stresses are encountered at the FBR so that corrosion along grain boundaries in the HAZ is accelerated by the high stress and exfoliation type corrosion can occur, similar to that observed by Onoro and Ranninger (1993) in gas tungsten arc (GTA) welded 2017 and 7015 Al alloys tested in chloride solutions.

It is possible that if the residual stresses were eliminated or made to be compressive then further increases in the pitting resistance over those already observed could be obtained. Hoordhuis and De Hosson recently showed that the surface stresses of a LSM 2024 alloy could be made compressive by shot peening for as little as 60 seconds.

6.3.5. Corrosion of Laser Surface Alloyed 2014 Alloy Substrate and Mo

In this section the results for the corrosion of the LSA 2014 alloy with the predeposited 25 wt.% Mo- 75 wt.% Al plasma sprayed coating (LSA 2014/Mo) will be discussed with reference to results obtained by workers using other non-equilibrium techniques.

The anodic pitting potential was increased after the LSA treatment (see Table 5.2). From the results it has been assumed that the Mo present in both the α-Al and the oxide film of the surface alloyed layer was responsible for the increase. In the 0.1 NaCl solution the pitting potential was found to be ~-520 mV (SCE) which is comparable to the work of Natishan et al (1986) who reported a pitting potential of -560 mV for an alloy containing 4 at.% Mo ion implanted into pure Al, though no data was presented for E_{corr}. However, Moshier et al (1986) did observe similar values of E_{corr} (-930 mV (SCE) in deaerated 0.1 N KCl) to those in this study (-890 mV (SCE) in 0.1 M KCl) for an Al-6 a/o Mo ion implanted alloy but reported a pitting potential of -210 mV (SCE).

The Mo in solid solution has the effect of raising the free corrosion potential of the Al, which in turn should decrease the rate of galvanic dissolution at cathodic second phase particles such as $CuAl_2$. The presence of Mo rich intermetallic particles, however, caused pitting to occur and thus prevented the true pitting potential of the Al-Mo solid solution from being measured. Similar behaviour has been reported by Davis et al (1990) who found that pits spontaneously formed at intermetallic particles in heat treated Al-Mo but is in contrast to the work of Shaw et al (1991) who showed that the presence of intermetallic particles in Al-W alloys prepared by magnetron sputter deposition had only a minor effect on the corrosion resistance of the alloys.

It is evident from the results that the presence of the Mo has increased the corrosion resistance of the aluminium alloy. At the present time, however, it is not possible to determine whether the Mo has been incorporated in the oxide as part of the Al_2O_3 structure or as an intermediate layer between the metal surface and the outer oxide layer. It is possible that the Mo could exist in the oxide either in the metallic state or in one of its oxidation states. Its effect on the corrosion resistance could then be one of strengthening the oxide structure as observed by Davis et al (1991) so that anodic dissolution is retarded, or if Mo were present in the oxide film as MoO_4^{-2} it could possibly behave as an effective barrier against the diffusion of chloride ions to the alloy surface (Moshier et al 1989)). In this study it has been shown that the oxide that forms in air contains the Mo^{6+} ion and further consideration of the Al 2p peaks indicates that the oxide may be $Al_2(MoO_4)_3$ when compared to the work of Moshier et al (1989). It was also shown that after polarization in chloride electrolytes that the Mo in the film had been oxidised to more than just one state, possibly containing the Mo^{4+} ion. This then seems to support the findings of Moshier et al who said that as the potential was increased the amount of Mo^{6+} decreased and the amount of hydrated Mo compound increased. They proposed that breakdown occurs when the hydration of the film reaches such an extent that the molybdate ion is so severely depleted as to allow the ingress of the chloride ion to the metal surface.

Urquidi and MacDonald (1985) have used a solute-vacancy interaction model to explain the increase in breakdown potential when Mo^{6+} is present in passive films on stainless steels. It may also be possible to apply the model to the present work where Mo^{6+} was found in the oxide film. The model assumes that Mo^{6+} can form complexes with the negatively charged cation vacancies in the oxide film. This means there would be a decrease in the free cation vacancy concentration by reducing the flux of these vacancies from the film/solution interface to the metal/film interface. This phenomenon then leads to an increase in the breakdown potential. Urquidi and MacDonald (1985) also showed that the model predicts that the induction time for the onset of pitting at any given applied potential was increased due to the presence of Mo^{6+}. This can then be used to explain why the potential in the immersion tests was quite stable indicating good corrosion resistance.

Since pitting is believed to be initiated by the adsorption of an anion at the oxide/solution interface the presence of Mo may also affect the pitting resistance by decreasing the pH_{zch} of the oxide film on the alloy (Natishan et al, 1988). Cl^- ions will only adsorb, however, when the surface has a net positive charge (i.e. when the local surface pH < pH_{zch}). By decreasing the pH_{zch} of the oxide it means that the potential must be increased to a higher value before the local pH at the surface falls below the pH_{zch}, and Cl^- can be adsorbed. This can be further coupled with the findings of Davis et al (1991) that the oxide dissolution is affected by the presence of Mo because the value of pH_{zch} for metal oxides is related to their solubility as shown in Figure 6.14 (Szklarska-Smialowska, 1992). Therefore, if the characteristics of the oxide film were still the same as aluminium oxide but with a lower pH_{zch} due to the Mo being present, then the oxide solubility would also be decreased for the same reason. Hence, if oxide thinning plays a role in pit initiation, the beneficial effect of Mo in raising E_{pit} may be related to the decreased dissolution rate of the oxide.

6.3.6. The Corrosion Testing Technique and Experimental Errors

The validity of applying the criterion proposed by Hoar and Mears (1966) for the selection of passive alloys (see chapter 2 page 30) to aluminium alloy systems will be discussed in this section with particular reference to the two types of behaviour observed in the anodic pitting scans and the immersion tests.

Figure 6.15 shows the change in E_{corr} with time for LSM 2014 and LSA 2014/Mo with the corresponding experimentally measured values of E_{pit}. According to the theory of Hoar and Mears (1966) pitting will not occur so long as the free corrosion potential does not exceed the pitting potential. Comparison of the curves of E_{corr} shown in Figure 6.15 with the theory depicted by Figure 2.15 would lead to the conclusion that the alloys under observation had suffered pitting corrosion. However, E_{corr} in both cases never actually increased above E_{pit} so the alloys should not have pitted according to Hoar and Mears (1966). Studies of the surfaces after immersion for 150 hrs, however, showed that the alloys had pitted extensively. Therefore, from these observations it is apparent that there is a short fall in one or both of the testing procedures.

If we first consider the immersion tests then it can be said that the interpretation of the results according to Hoar and Mears (1966) represents a true indication of the corrosion behaviour of the alloys in an aggressive environment. This is then verified by the fact that the E_{corr} versus time plots show pitting behaviour and that pits are found in the surface after immersion testing. Now, confusion arises because the anodic polarization curves demonstrate that the alloys can be passive over quite a large range of potentials and that they have a specific pitting potential. However, this raises the question as to what is meant by the pitting potential when measured by anodic polarization. This can be answered as follows. During anodic polarization starting at $E \leq E_{corr}$ an artificial oxide film is grown on the surface of the alloy, as in anodising, and this occurs at very low current densities. This occurs because at the initially lower potentials the interfacial pH is in the near neutral region at which the hydroxide ion is not soluble. The result is that $Al(OH)_3$ is precipitated on to the surface (Ambat and Dwarakadasa, 1993). However, as the potential increases to more noble values dissolution of the oxide occurs simultaneously, due to the formation of soluble chloride salts of Al (Lorking and Mayne, 1961 and Mazhar et al, 1986) and a reduction in the local interfacial pH (Silcock, 1959 and Ambat and Dwarakadasa, 1992). On further polarization a potential may be reached at which the rate of dissolution is greater than the rate of formation. At this point the current density starts to increase. At first the increase is very slow and is not noticed on the scale of polarization diagrams where the current density is often plotted on log axes. Eventually a potential is reached where the film thickness is such that Cl^- can be adsorbed directly on to the metal surface. Then, due to the high potential the interfacial pH drops to low values at which the metal dissolution is accelerated (Ambat and Dwarakadasa, 1992). This is then identified by the characteristic increase in the current density. Thus the two types of test demonstrate different types of behaviour because the samples tested by immersion for long periods of time have a significantly thinner protective oxide film to start with.

Another significant factor is that deaerating the solution has the known effect of decreasing E_{corr} and hence increasing the passive range. This then raises the question whether it would be more valid to carry out corrosion tests in normal aerated solutions. If so this would then also eliminate experimental errors which arise as a consequence of insufficient deaeration when using gases such as N_2. It has been shown that the free corrosion potential varies as a result of residual O_2 being present in chloride solutions deaerated with N_2 (Shaw et al, 1990). Using the present experimental procedures it would be very difficult to guarantee that the N_2 concentration was the same for each test. This could then account for the spread in the experimental results where even though the value of E_{pit} remained fairly constant the value of E_{PD} was very changeable, for a given alloy and set of conditions, because the measured value of E_{corr} was not constant. However, for alloys that start to pit at potentials close to E_{corr}, for example the LSM 7075 alloy, it is more advantageous to deaerate the solutions because it can be more clearly seen at what point breakdown occurs.

Hence, the use of anodic polarization scans is a convenient way of ranking aluminium alloys by their ability to form a protective oxide layer, the potential range over which the layer is effective, and by the value of their pitting potentials. Then if further information is required immersion tests can be carried out.

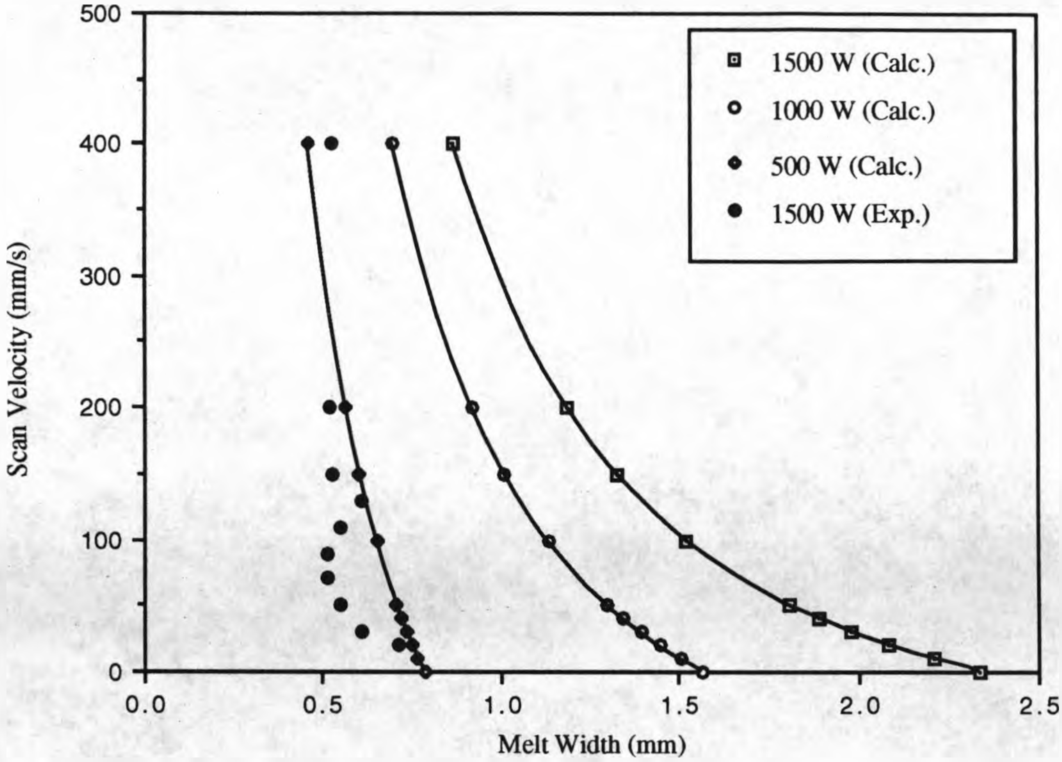

Figure 6.1. Graph showing the experimentally measured melt widths versus laser scan velocity for an output power of 1.5 kW, compared to the values calculated in theory using Equation 6.2.

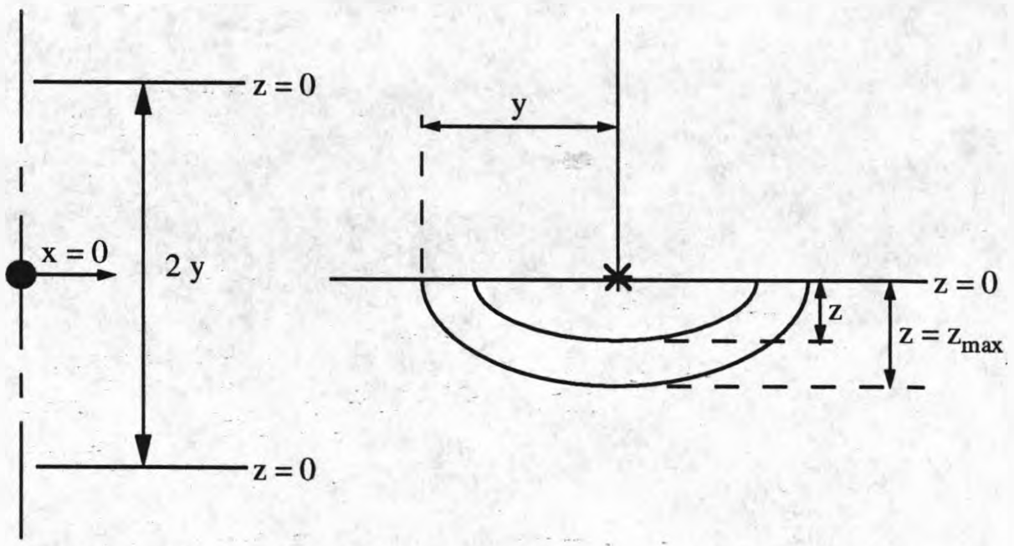

Figure 6.2. Schematic diagram of the heat input for a three dimensional moving point source given by Equation 6.1, when $T - T_0 = T_m$ at $z = x = 0$.

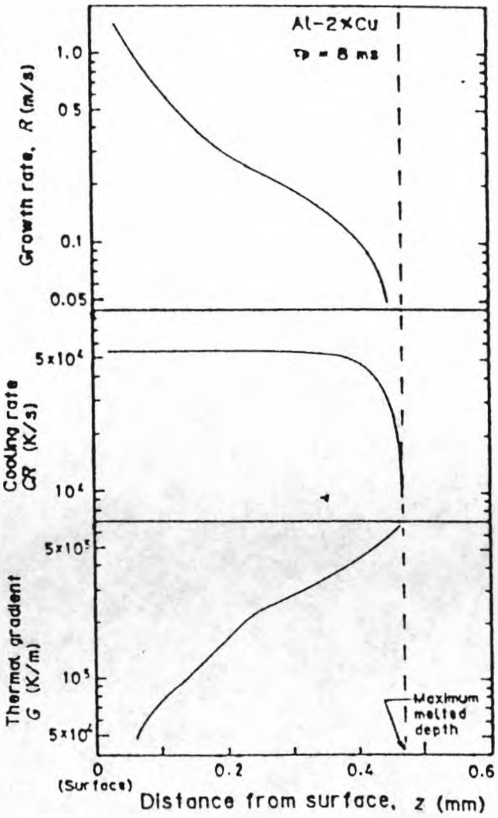

Figure 6.3. The growth rate, cooling rate and temperature gradient at the liquidus temperature from the maximum melt depth to the surface for a laser melted Al - 2 wt.% Cu alloy, from Kataymama et al (1991).

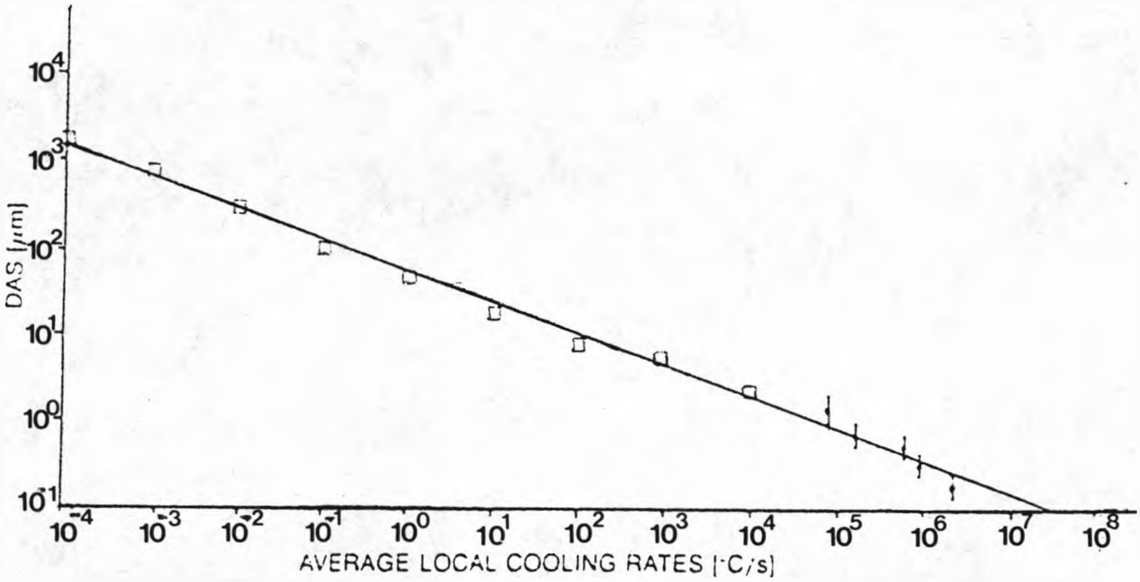

Figure 6.4. Plot of the secondary dendrite arm spacing versus the cooling rate from the work of Munitz (1985).

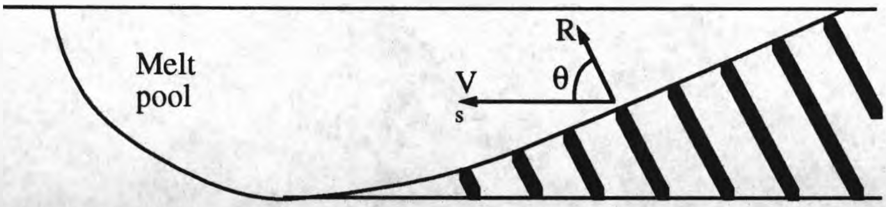

Figure 6.5. Schematic diagram of the laser melt pool showing the relationship between the laser scan velocity, Vs, and the the growth rate, R.

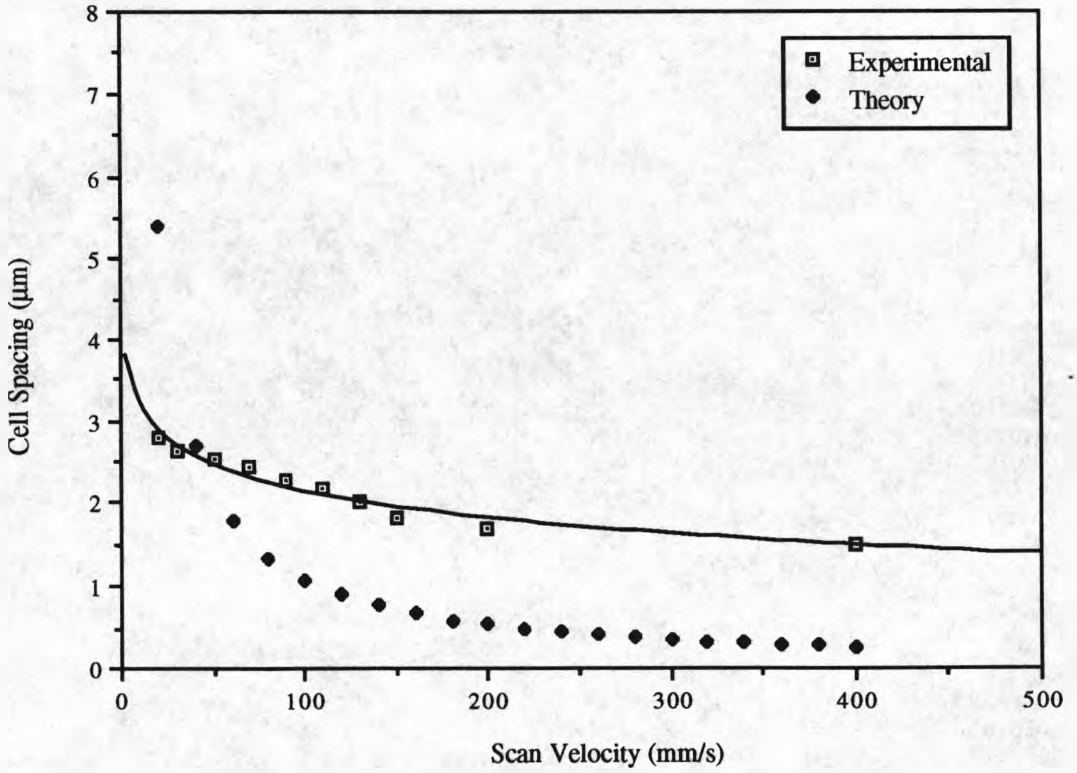

Figure 6.6. Plot of the measured cellular dendrite arm spacing at the maximum melt depth versus laser scan velocity for LSM 2014, compared to the theoretical spacings given by Equation 6.9.

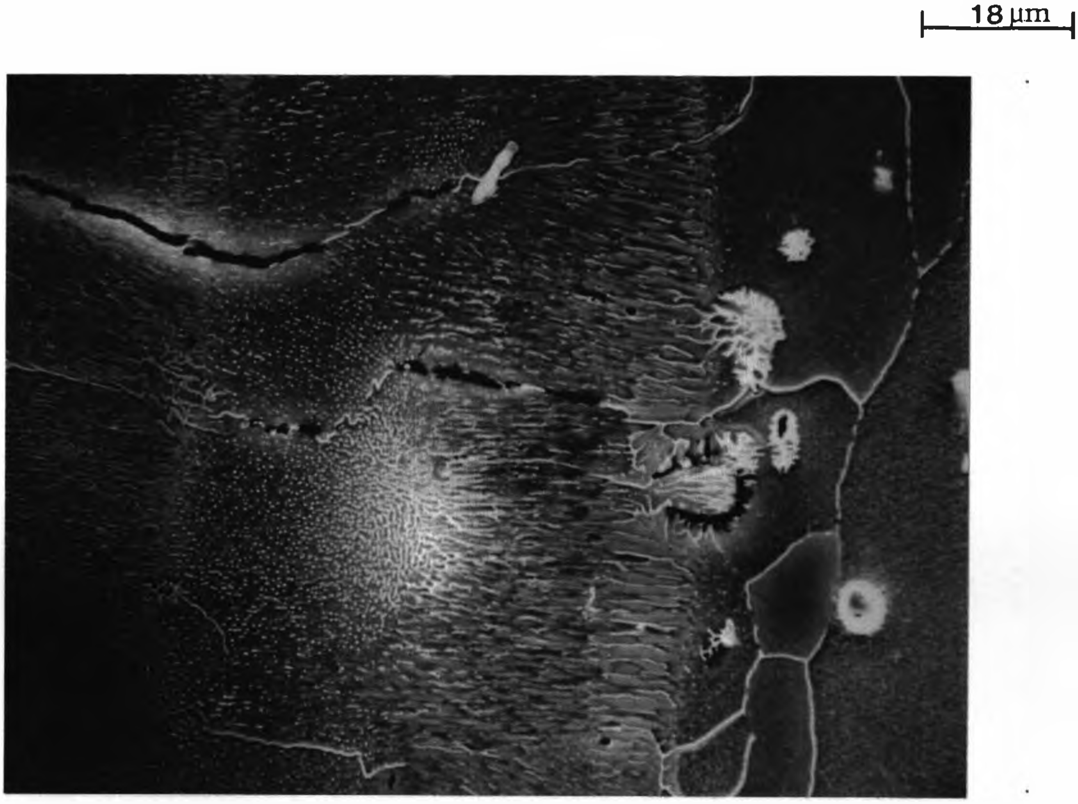

Figure 6.7. SEM micrograph showing a region of the melt zone where a previous second phase particle was melted but there was insufficient time in the melt for the complete redistribution of the solute atoms.

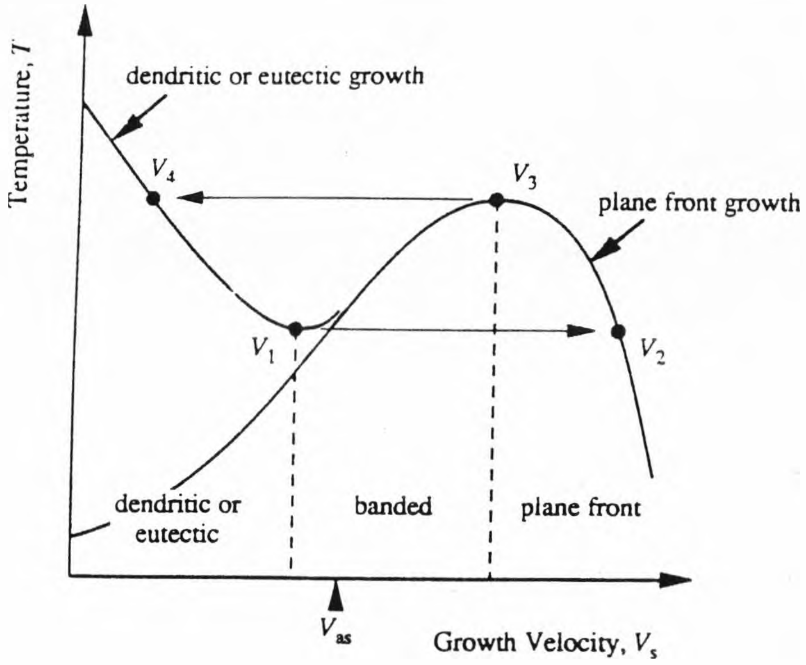

Figure 6.8. Schematic diagram to illustrate the model for banding proposed by Carrard et al (1992).

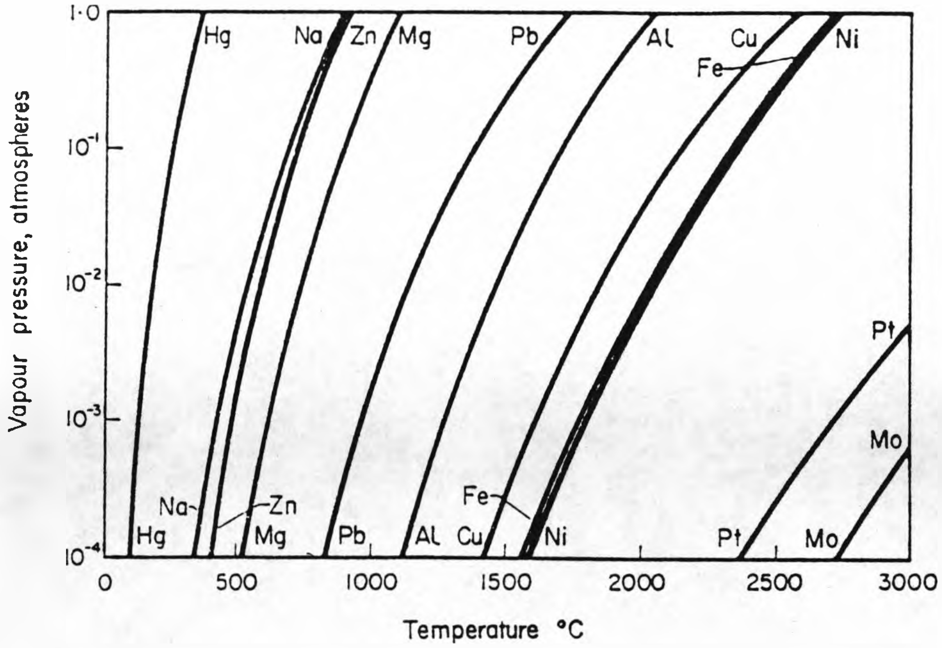

Figure 6.9. Vapour pressure for various metals as a function of temperature (Cottrell, 1982).

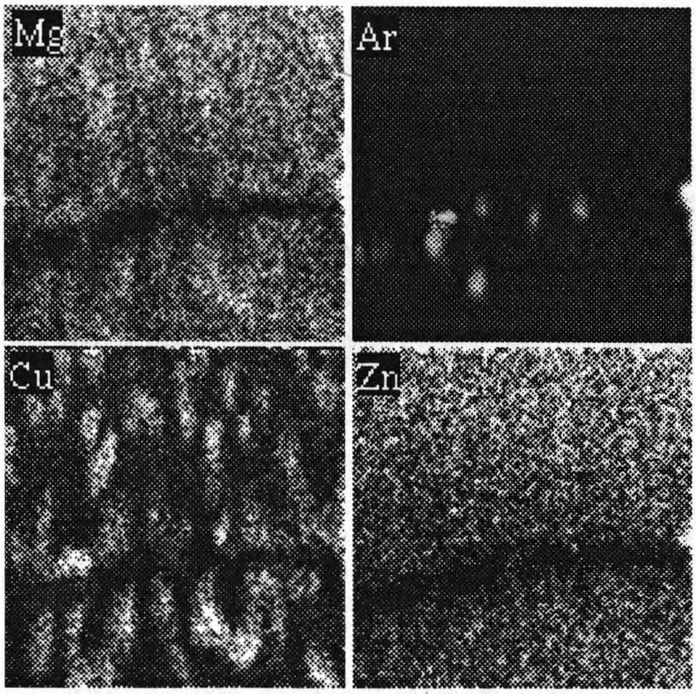

Figure 6.10. X-ray maps from the P2 precipitates in naturally aged LSM 7075 alloy.

Figure 6.11. TEM micrograph showing how intermetallic particles were frozen into the cellular dendrites in LSA 2014/Mo alloy. It is possible that the larger particle (1) was nucleated by the spherical particle (2).

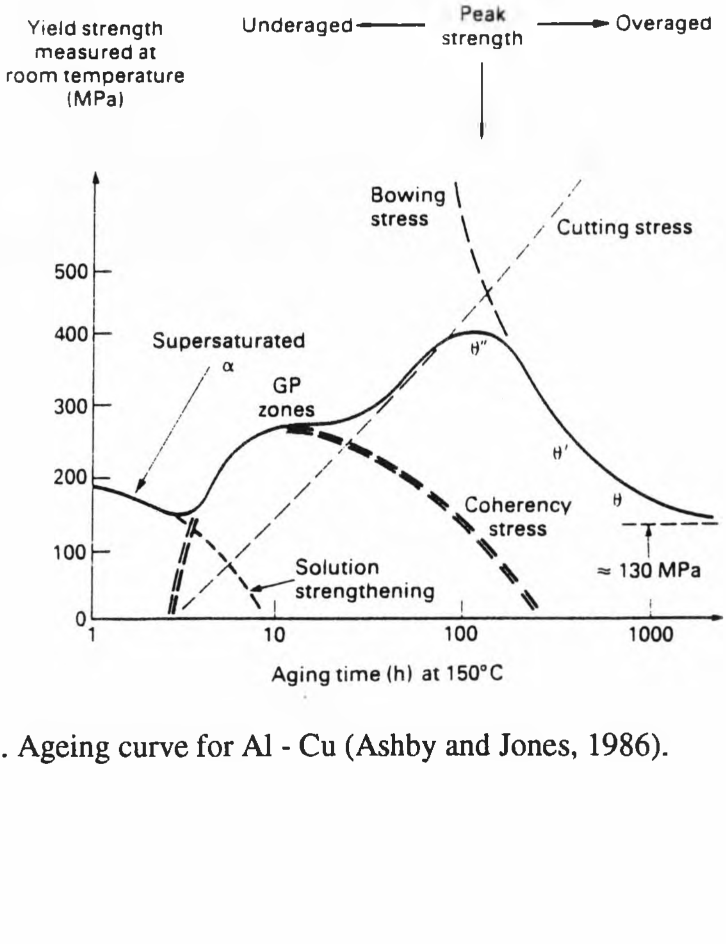

Figure 6.12. Ageing curve for Al - Cu (Ashby and Jones, 1986).

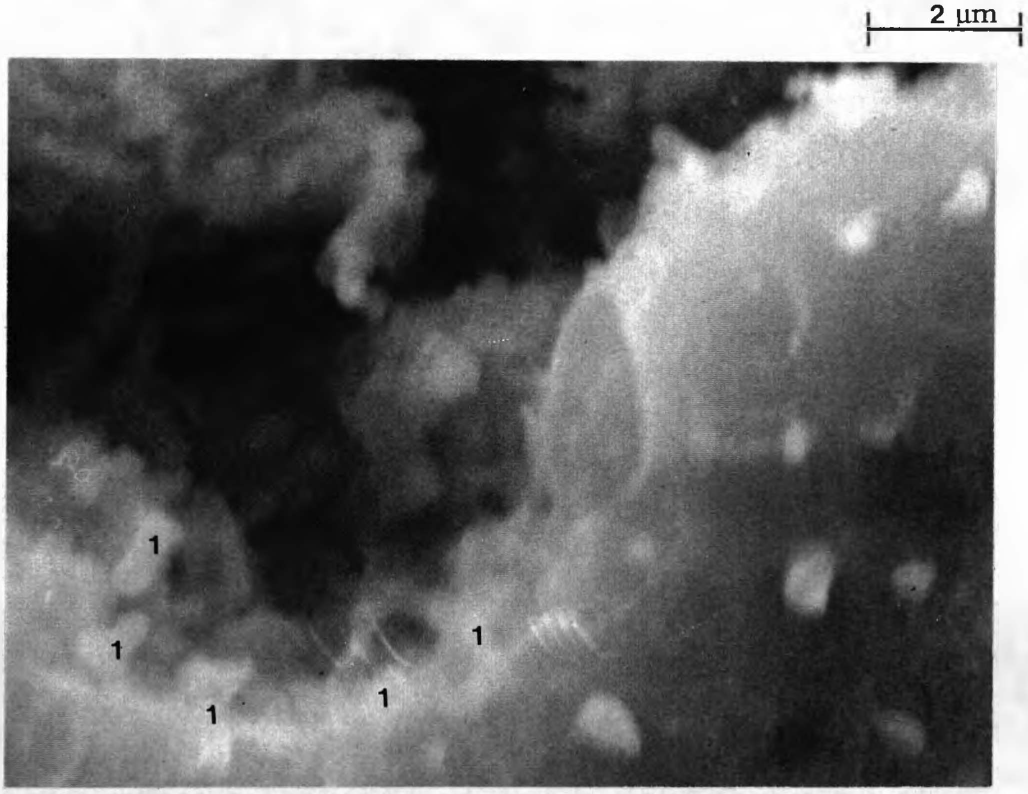

Figure 6.13. SEM micrograph showing that dissolution of the α-Al surrounding the second phase particles (marked 1) has taken place during anodic polarization in chloride electrolytes. The paricles formed in the HAZ and FBR of overlapping melt tracks.

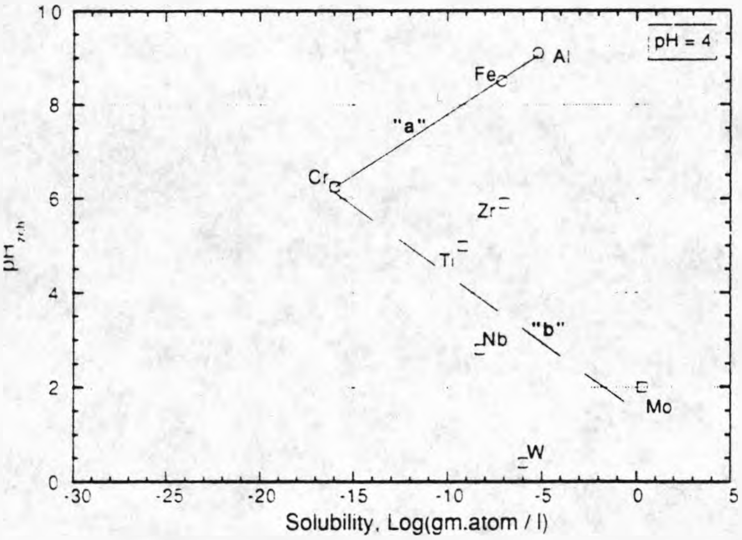

Figure 6.14. pH of zero charge for the hydrated oxide of various metals versus the solubility of the oxide in solution at pH 4. Line "a" represents metal oxides that are soluble in acid solutions, and line "b" is for metal oxides that are stable in acid solutions (Szklarska-Smialowska, 1992).

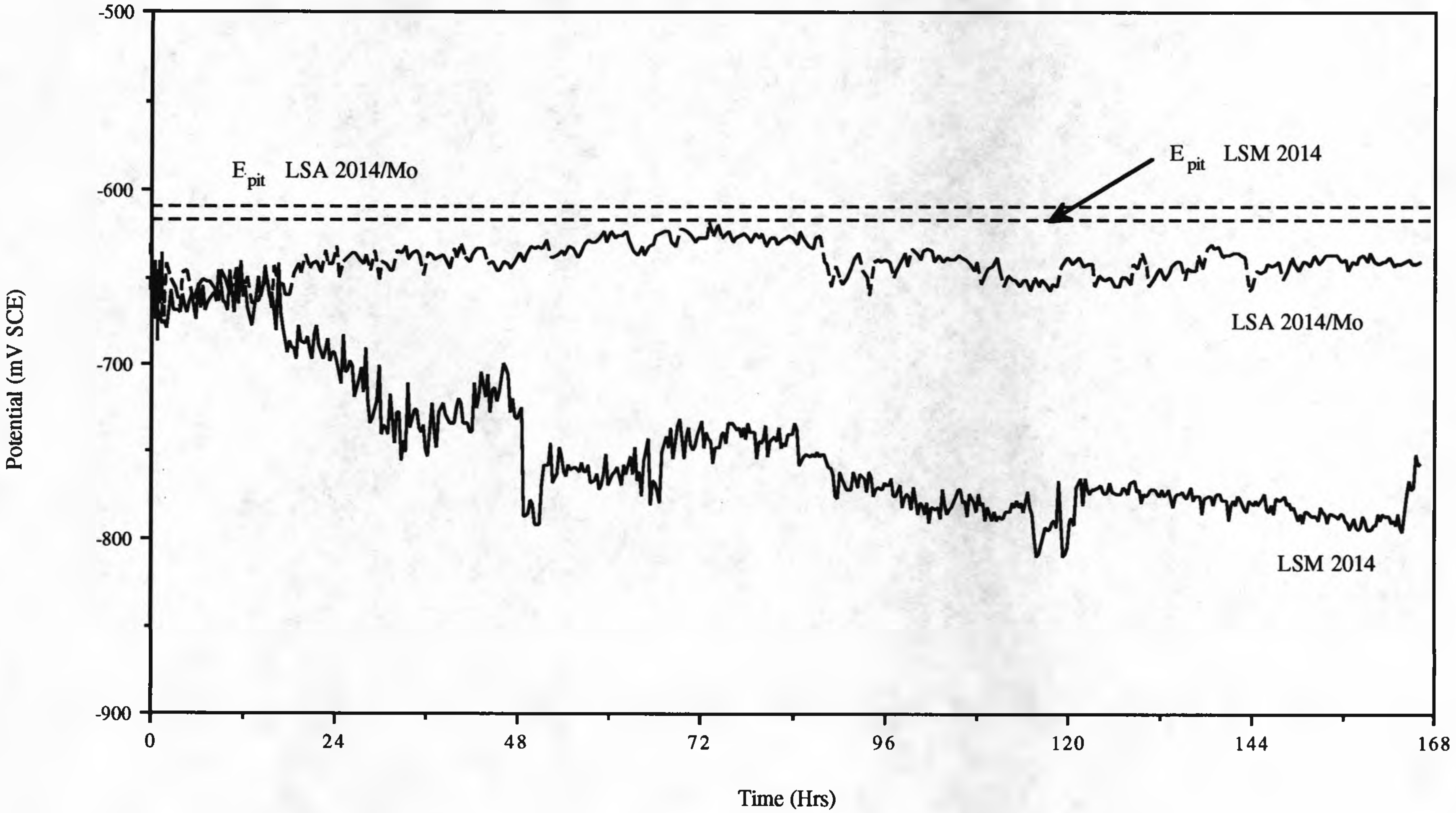

Figure 6.15. Free corrosion potential versus time for LSM 2014 and LSA 2014/Mo

7. CONCLUSIONS

7.1. LASER SURFACE MELTING

1. 2014 and 7075 Al alloys were surface melted with a 1.5 kW CO_2 laser. Laser melt tracks with uniform melt depth and minimum porosity were obtained when, the surface was pretreated by immersion in NaOH solutions and then subsequently melted at laser scanning velocities greater than 12 mm/s.

2. The microstructure of the resolidified layers consisted of columnar grains that had grown epitaxially from the substrate alloys. Solidification commenced with a region of planar front growth that was approximately 3 - 5 μm wide, and proceeded with cellular dendritic growth in the main body of the melt pool.

3. A characteristic feature of the surface melted layers was solute banding. In both of the alloys concentric bands were formed in the microstructure when, during solidification, there were momentary halts of the advancing solid/liquid interface. The almost instantaneous restart of solidification resulted in a band of solute enriched solid and a slight coarsening of the cellular dendritic structure. A second form of banding was observed in the LSM 7075 alloy that consisted of alternating layers of α-Al, solidified by planar front growth, and an intermetallic phase. This second form of banding occurred because the local growth rate exceeded the limit of absolute stability.

4. Transmission electron microscopy, with scanning electron attachment for EDX analysis, showed that the cellular dendritic structure consisted of dendrite arms of α-Al and a compact interdendritic region formed from many very small precipitates. The main interdendritic phase in the 2014 alloy was found to be θ - phase ($CuAl_2$); the interdendritic phase in the LSM 7075 alloy could not be identified.

5. The structure of the LSM 2014 alloy was found to be stable over the period of this project. However, the LSM 7075 alloy underwent a phase transformation after 6

months, from initial LSM, in TEM thin foil samples stored at room temperature. After a further 6 months the structure had changed to α-Al containing precipitates that have been shown to be similar to the η'- $MgZn_2$ phase. Solute diffusion was also shown to occur simultaneously with the precipitation reaction, resulting in holes being left in the interdendritic regions, and is believed to have aided the growth of the precipitates.

6. For laser scanning velocities greater than 70 mm/s cracks appeared in the resolidified layers. These cracks were initiated in the fusion boundary region and propagated towards the free surface. The occurrence of cracking was attributed to the presence of high residual stresses, accumulated during rapid solidification, that exceeded the yield stress.

7. The residual stresses were measured by X-ray diffraction and it was found that the stress increased with increasing laser scan velocity and decreased with increasing melt track overlap. From depth profiling it was also found that the highest stresses coincided with the fusion boundary region, where it was also found that there was a minimum in the hardness value.

8. Anodic potentiodynamic polarisation in chloride electrolytes revealed that in the case of the 2014 alloy corrosion resistance was increased, in so much as the potential required to cause appreciable pit propagation, E_{pit}, was of the order of 100 mV higher after laser surface melting. In deaerated electrolytes E_{corr} was decreased after LSM, which had the overall effect of increasing the passive range of the alloy. This effect is believed to be the result of a more homogeneous oxide on the surface of the 2014 alloy after LSM.

9. In the 7075 alloy E_{pit} was not increased appreciably after LSM but there was a decrease in E_{corr}, thus slightly increasing the passive range. The most noticeable change was the elimination of the anodic current density transient that was observed for the as-received alloy. The occurrence of two breakdown potentials in the as-received alloy was attributed to, first the onset of grain boundary corrosion which was then followed

by an anodic current density transient which was accompanied by grain matrix pitting.

10. The effect of the residual stresses in the LSM layers on the corrosion resistance was that they caused a type of localised stress corrosion cracking within the cellular dendritic microstructure. Also, because the stress was a maximum at the FBR, when the corrosion reaction reached the fusion line large intergranular cracks appeared in the HAZ that often resulted in areas of the LSM layers spalling off.

7.2. LASER SURFACE ALLOYING

11. After LSA with Mo into the 2014 alloy microstructures similar to the LSM 2014 alloy were achieved by choosing processing parameters that gave satisfactory LSM layers. As a result of the rapid solidification, the solid solubility of Mo in the α-Al dendrites was increased to nearly 2 wt.% Mo compared to the equilibrium concentration of only 0.08 wt.% Mo.

12. $Al_{12}Mo$ intermetallic particles were present in the alloyed layer and clustered on the convection contours, whilst much smaller precipitates were able to form within the cellular dendritic structure. The intermetallic phase accounted for the majority of the Mo in the new surface alloy. Oxide particles similar to Al_2MgO_4, but containing Mo, were also found in all the surface alloy samples, and it is thought that they were due to the presence of oxygen in the voids of the predeposited plasma sprayed coatings.

13. The corrosion resistance of the 2014 alloy was improved after LSA resulting in an increase in E_{pit} of over 100 mV and upto 400 mV. Pits were observed to form in the proximity of the intermetallic particle clusters, which is believed to be the reason why the increases in E_{pit} were small, given that similar increases were obtained from the LSM treatment.

14. The shift in E_{pit} to more noble values is believed to be due to the presence of Mo in the surface oxide film. XPS analysis showed that Mo was present in the air formed

oxide, most probably in the Mo^{6+} state, and that after polarization in chloride electrolytes a more complex oxide formed, that possibly also contained Mo^{4+}.

8. SUGGESTIONS FOR FUTURE WORK

The work presented in this thesis has been concerned with the characterisation of the microstructure and corrosion properties of laser surface melted and laser surface alloyed aluminium alloys. A link between the microstructure of the as-laser processed layers and the corrosion properties has been made in each of the above cases. Limitations to the improvement of the corrosion resistance of these alloys by LSM and LSA have arisen because of few key microstructural effects.

Firstly, there is the problem of overlapping laser melt tracks. After LSM treatments preferential attack occurs during corrosion because of the change in composition across the track/track interfaces, and because of the transformation of the interdendritic phase to form globular particles. Therefore, it is suggested that if greater area coverage could be achieved, by either using a more powerful laser with a more defocussed beam or by using a type of oscillating mirror arrangement to focus the laser, then the corrosion resistance may be increased by having fewer overlaps. Secondly, there are the problems associated with the formation of intermetallic phases. The LSM alloys were preferentially attacked within the cellular dendritic structures due to the interdendritic phases, and the LSA alloy suffered pitting corrosion because of clusters of intermetallic particles. It may be possible to minimize these effects if a greater percentage of the solute atoms were retained in solid solution with the Al by increasing the cooling rates. This would be achieved by increasing the laser scan velocity. However, it was also shown in this work that increasing the scan velocity increased the residual stress, which was also shown to have a deleterious effect on the corrosion resistance. Therefore, it is suggested that preheating the substrates prior to laser processing may lead to a reduction in the residual stress. Furthermore, in the case of LSA the formation of intermetallic particles may possibly be avoided if a lower Mo concentration were to be used in the predeposited plasma sprayed coating, or by depositing thin layers.

As far as the characterisation of the microstructures is concerned, this work has covered the as-laser processed condition of the LSM and LSA alloys. However, it has also been shown that thin foil samples from the LSM 7075 alloy exhibit natural ageing. Future work may, therefore, involve an investigation of the effect of heat treatment on the microstructure of the bulk LSM samples. This could then also include, an investigation of the effect heat treatment on the residual stress, and the corrosion resistance of the laser processed alloys.

APPENDIX A1. THE THEORY OF RESIDUAL STRESS MEASUREMENT BY X-RAY DIFFRACTION

A1.1 STRESS-STRAIN RELATIONS (Barrett and Massalski, 1987)

According to the theory of elasticity, Hooke's law states that the stress, σ_x, is related to the strain, ε_x, by the modulus of elasticity, E.

$$\sigma_x = E\varepsilon_x \tag{A1.1}$$

As a result of the stress in the x direction there is a linear strain in that direction. However, there is also a strain in the transverse directions which is related to the strain in the x direction by Poisson's ratio, υ. Thus:

$$\varepsilon_y = \varepsilon_z = -\nu \cdot \varepsilon_x = -\frac{\nu\sigma_x}{E} \tag{A1.2}$$

Now, if we consider a sphere of unit volume under the action of stresses, then it will deform to an ellipsoid. If the three principal stresses σ_1, σ_2, and σ_3 are taken to be parallel to the orthogonal axes x, y, and z then the equation for the strain ellipsoid can be written as

$$\frac{x^2}{\varepsilon_1} + \frac{y^2}{\varepsilon_2} + \frac{z^2}{\varepsilon_3} = 1 \tag{A1.3}$$

Any point on the surface of the ellipsoid represents a normal strain, whose magnitude and direction are given by $\varepsilon_{\phi\psi}$, as shown by Figure A1.1, which can be determined in terms of the principal strains ε_1, ε_2, and ε_3 as

$$\varepsilon_{\phi\varphi} = \varepsilon_1\alpha_1^2 + \varepsilon_2\alpha_2^2 + \varepsilon_3\alpha_3^2 \tag{A1.4}$$

where:

$$\alpha_1 = \cos\phi \sin\varphi$$
$$\alpha_2 = \sin\phi \sin\varphi$$
$$\alpha_3 = \cos\varphi = \left(1 - \sin^2\varphi\right)^{1/2}$$

Similarly the stress is given by

$$\sigma_{\phi\varphi} = \sigma_1\alpha_1^2 + \sigma_2\alpha_2^2 + \sigma_3\alpha_3^2 \tag{A1.5}$$

The stress cannot be measured directly and therefore needs to be related to the strain measurements. Hooke's law states that the strain along any principal direction is due to the stress acting along that axis, plus the superimposed strains from the Poisson effect of principal stresses acting along the other axes. Thus:

$$\begin{aligned}\varepsilon_1 &= \frac{1}{E}[\sigma_1 - \nu(\sigma_2 + \sigma_3)]\\ \varepsilon_2 &= \frac{1}{E}[\sigma_2 - \nu(\sigma_1 + \sigma_3)]\\ \varepsilon_3 &= \frac{1}{E}[\sigma_3 - \nu(\sigma_1 + \sigma_2)]\end{aligned} \tag{A1.6}$$

Substituting these values into Equation A1.4 then gives the strain in any direction ϕ, ψ within a body related to the principal stress. Thus the general strain equation is given by:

$$\varepsilon_{\phi\varphi} = \frac{1+\nu}{E}\left(\sigma_1\alpha_1^2 + \sigma_2\alpha_2^2 + \sigma_3\alpha_3^2\right) - \frac{\nu}{E}(\sigma_1 + \sigma_2 + \sigma_3) \qquad \text{(A1.7)}$$

A1.2 X-RAY STRESS ANALYSIS RELATED TO THE STRAIN EQUATION

X-ray stress measurements are confined to the surface, therefore, by assuming plane stress conditions, $\sigma_3 = 0$, then Equation A1.7 can be simplified to

$$\varepsilon_{\phi\varphi} = \frac{1+\nu}{E}\left(\sigma_1\alpha_1^2 + \sigma_2\alpha_2^2\right) - \frac{\nu}{E}(\sigma_1 + \sigma_2) \qquad \text{(A1.8)}$$

It must be noted that due to the Poisson effect, even though σ_3 is zero, there will always be a strain ε_3, as shown in Figure A1.2. Substituting for α_1 and α_2 in Equation A1.8 gives

$$\varepsilon_{\phi\varphi} = \frac{1+\nu}{E}\left(\sigma_1\cos^2\phi + \sigma_2\sin^2\phi\right)\sin^2\varphi - \frac{\nu}{E}(\sigma_1 + \sigma_2) \qquad \text{(A1.9)}$$

However, when $\psi = 90°$ the surface stress component, σ_ϕ, is given by

$$\sigma_\phi = \sigma_1\cos^2\phi + \sigma_2\sin^2\phi \qquad \text{(A1.10)}$$

and hence:

$$\varepsilon_{\phi\varphi} = \frac{1+\nu}{E}\cdot\sigma_\phi\sin^2\varphi - \frac{\nu}{E}(\sigma_1 + \sigma_2) \qquad \text{(A1.11)}$$

This is the basic equation relating lattice strains to stresses used in the X-ray diffraction technique for measuring stresses. It may be used to measure the surface stress σ_ϕ in any direction on the surface of the specimen.

The simplest measurements are made when the surface stress component to be determined is placed in the plane of rotation of the goniometer table. In this case two measurements of the lattice plane spacings for a given of hkl planes are required for stress calculations; one at $\psi = 0^\circ$ and the second at $\psi = 45^\circ$. This is illustrated in Figure A1.3. The measured strain is always parallel to the bisector of the angle between the incident and diffracted beams and, therefore, the stress is determined in the ϕ direction on the surface. It can thus be seen that the relationship between the strain normal to the specimen surface, $\varepsilon_\perp$, and the lattice plane spacing, $d_\perp$, is

$$\varepsilon_\perp = \varepsilon_{\phi\varphi} = \frac{d_\perp - d_0}{d_0} = \frac{\Delta d}{d_0} \tag{A1.12}$$

where d_0 = interplanar spacing in the unstressed condition.

However when $\psi = 0^\circ$, Equation A1.11 can be written as

$$\varepsilon_\perp = -\frac{\nu}{E}\sigma_1 \tag{A1.13}$$

for a single principal stress.

Now considering the situation when $\psi = 45^\circ$ then

$$\varepsilon_{\phi\varphi} = \frac{d_\varphi - d_0}{d_0} \tag{A1.14}$$

which gives an expression for the stress by equating Equation A1.12 with A1.14, combining with Equation A1.13 and then substituting in Equation A1.11. Thus:

$$\sigma_\phi = \frac{d_\varphi - d_\perp}{d_0}\left(\frac{E}{1+\nu}\right)\frac{1}{\sin^2\varphi} = K\cdot\left(\frac{d_\varphi - d_\perp}{d_0}\right) \tag{A1.15}$$

The term d_0 can be substituted by $d_\perp$ without appreciable error so the final expression for the surface stress in a single direction is given by:

$$\sigma_\phi = K\cdot\left(\frac{d_\varphi - d_\perp}{d_\perp}\right) \tag{A1.16}$$

A1.3 THE RELATION BETWEEN DIFFRACTION ANGLE AND THE STRESS EQUATION

X-ray diffraction involves measuring the angular position, θ, of the diffracted beam for a set of hkl planes. Therefore it is more convenient to express the stress equation in terms of θ instead of interplanar spacings.

Diffraction from a set of crystal planes will occur when Bragg's law is satisfied:

$$n\lambda = 2d\sin\theta \tag{A1.17}$$

where:

n = integer

λ = wavelength of X-ray beam

Differentiating Bragg's law with respect to θ gives

$$\frac{\Delta d}{d} = -\cot\theta\cdot\left(\frac{\Delta 2\theta}{2}\right) \tag{A1.18}$$

Combining Equations A1.16 and A1.18 gives

$$\sigma_{\phi} = K \cdot \frac{\cot\theta}{2} \cdot \left(2\theta_{\perp} - 2\theta_{\varphi}\right) \cdot \frac{\pi}{180} \qquad \text{(A1.19)}$$

Thus the final equation for stress in terms of diffraction angle 2θ becomes

$$\sigma_{\phi} = K' \cdot \Delta 2\theta \qquad \text{(A1.20)}$$

where K´ is the stress concentration factor.

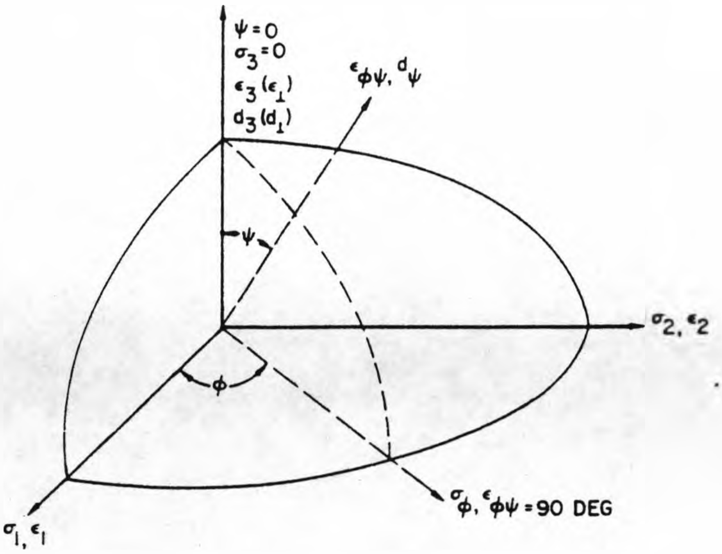

Figure A1.1. Schematic diagram illustrating ellipsoids of stress and strain with units used in X-ray diffraction stress analysis.

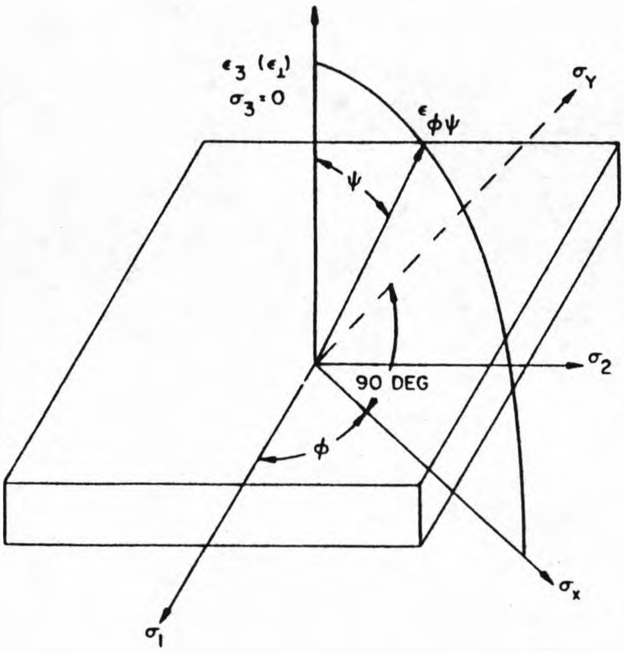

Figure A1.2. Stress in a biaxial system where $\varepsilon_3 \neq 0$.

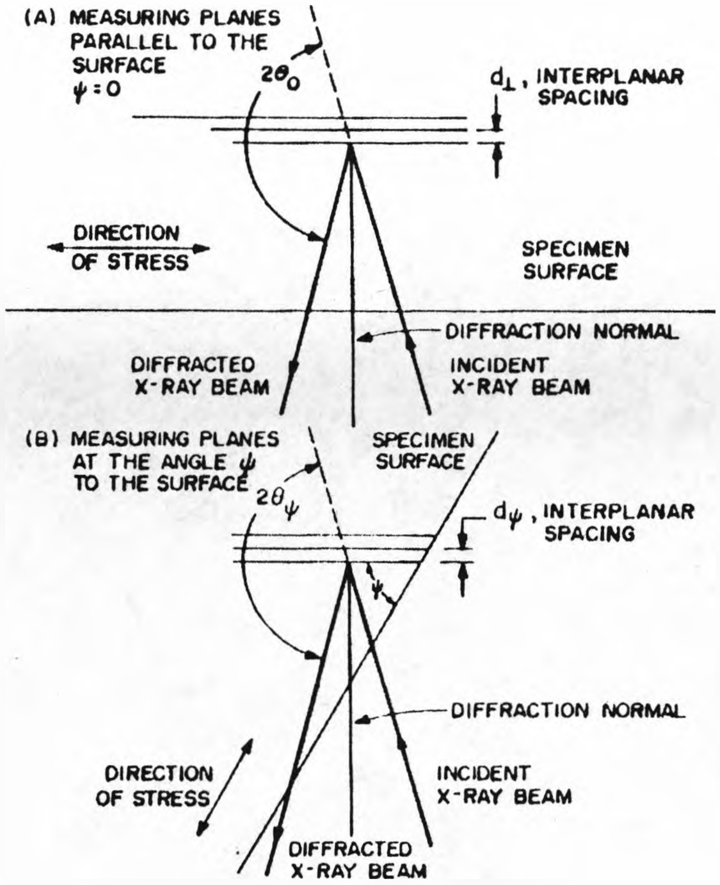

Figure A1.3. Schematic diagram illustrating the orientation of measured (hkl) planes with respect to the specimen surface: (A) specimen at $\psi = 0°$; (B) specimen rotated through $\psi°$.

A.Almeida, 1993, Private communication, unpublished work.

J.A.Alonso and J.M.Lopez, 1986, Mater.Let., 4, p.316.

R.Ambat and E.S.Dwarakadasa, 1992, Corr.Sci., 33, No.5, p.681.

R.Ambat and E.S.Dwarakadasa, 1993, Brit.Corr.J., 28, No.2, p.142.

T.R.Antony and H.E.Cline, 1977, J.Appl.Phys., 48, p.3888

M.F.Ashby and D.R.H.Jones, 1986, Engineering Materials 2, Pergamon Press, Oxford, U.K.

G.Beck and T.Ericsson, 1986, Proc.Residual Stresses in Science and Technology, Vol.1, Garmisch-Partenkirchen, FRG, p.27.

P.L.Bonora, M.Bassoli, P.L.De Anna, G.Battaglin, G.Della Mea, P.Mazzoldi and A.Miotello, 1980, Electrochimica Acta, 25, p.1497.

M.J.Bozack and R.D.Beshears, 1993, Corr.Sci., 34, No.4, p.631.

B.A.Van Brussel and J.Th.M. De Hossen, 1993, Mat.Sci.Eng., A161, p.83.

M.Carrard, M.Gremaud and M.Pierantoni, 1991, Scripta Metall.Mat., 25, p.925.

M.Carrard, M.Gremaud, M.Zimmermann and W.Kurz, 1992, Acta Metall.Mater., 40, p.983.

W.M.Carroll, M.Murphy and C.B.Breslin, 1993, Corr.Sci., 34, No.9, p.1495.

T.W.Clyne and G.J.Davies, 1978, Metal Science, 12, p.233.

S.M.Copley, D.Beck, O.Esqivel and M.Bass, 1978, AIP Conf.Proc, No.50, Am.Inst.Phys., NY, USA, p.161.

A.Cottrell, 1982, An Introduction to Metallurgy, 2nd Edn, Arnold, London, U.K., p.83.

A.G.Crooks and E.Hornbogen, 1989, Metall.Technik, 43, No.10, p.954.

B.D.Cullity, 1978, Elements of X-ray Diffraction, 2nd Edn., Addison-Wesley, Massach., Calif., USA.

D.K.Das, A.G.Paradkar and R.S.Mishra, 1992, Scripta Metall.Mater., 26, p.1211.

C.H.J.Davies, N.Raghunathan and T.Sheppards, 1994, Acta Metall.Mater., 42, No.1, p.309.

G.J.Davies and J.G.Garland, 1975, Int.Met.Reviews, 20, p.83.

G.D.Davis, W.C.Moshier, T.L.Fritz and G.O.Cote, 1990, J.Electrochem.Soc., 137, p.422.

G.D.Davis, W.C.Moshier, G.G.Long and D.R.Black, 1991, J.Electrochem.Soc., 138, p.3194.

C.W.Draper and J.M.Poate, 1985, Int. Metals Reviews, 30, No.2, p.85.
J.D.Embury and R.B.Nicholson, 1965, Acta Metall., 13, p.403.

U.R.Evans and T.P.Hoar, 1932, Proc.Roy.Soc.(A), 137, p.343.

R.T.Foley, 1986, Corrosion, 42, No.5, p.277.

M.G.Fontana, 1987, Corrosion Engineering, 3rd Edn., McGraw-Hill, New York, USA.

G.S.Frankel, R.C.Newman, C.V.Jahnes and M.A.Russak, 1993, J.Electrochem.Soc., 140, No.8, p.2192.

G.S.Frankel, M.A.Russak, C.V.Jahnes, M.Mirzamaani and V.A.Brusic, 1989, J.Electrochem.Soc., 136, No.4, p.1243.

E.Gaffet, J.M.Pelletier and S.Bonnet-Jobez, 1989, Acta Metall., 37, No.12, p.3205.

S.C.Gill and W.Kurz, 1993, Acta Metall.Mater., 41, No.12, p.3563.

S.C.Gill and W.Kurz (b), 1993, Mat.Sci.Eng., A173, p.335.

S.C.Gill, M.Zimmermann and W.Kurz, 1992, Acta Metall.Mater., 40, No.11, p.2895.

L.Gjonnes, 1991, Micron and Microsc.Acta, 22, No.1-2, p.123.

M.Gremaud, M.Carrard and W.Kurz, 1990, Acta Metall.Mater., 38, No.12, p.2587.

M.Gremaud, M.Carrard and W.Kurz, 1991, Acta Metall.Mater., 39, No.7, p.1431.

A.K.Gupta, A.K.Jena and M.C.Chaturvedi, 1987, Mater.Sci.Tech, 3, p.1012.

H.S.Gurev and R.D.Stout, 1963, Weld.J., 42, p.298.

P.L.Hagans and R.L.Yates, 1989, Environmental Degradation of Ion and Laser Beam Treated Surfaces, Eds. G.S.Was and K.S.Grabowski, The Minerals,Metals and Materials Soc., p.215.

H.J.Hegge and J.Th.M.De Hosson, 1990, Scripta Metall. Mat., 24, p.593.

H.J.Hegge and J.Th.M.De Hosson, 1991, J.Mater.Sci., 26, p.711.

B.Hemsworth, T.Boniszewski and N.F.Eaton, 1969, Met.Constr. and Brit.Weld.J., 1, No.2, p.5.

T.P.Hoar, 1970, J.Electrochem.Soc. 117, No.1, p.17C.

T.P.Hoar and D.C.Mears, 1966, Proc.Roy.Soc. Series A, 294, p.486.

A.Houndri, S.Polymenis, Y.Chryssoulakis and D.Pantelis, 1992, Metall.Trans.A, 23A, p.1801.

W.Hubler and G.Wranglen, 1964, Proc.4th Scandanavian Corrosion Cong., p.60.

A.J.Jacobs, 1966, Met.Prog., 5, p.80.
A.K.Jain, V.N.Kulkarni and D.K.Sood, 1981, Thin Solid Films, 86, p.1.

S.Jobez, J.M.Pelletier and A.B.Vannes, 1990, Key Eng.Mater.,46-47, p.317.

S.Jobez, J.M.Pelletier, A.B.Vannes and P.F.Gobin, 1988, Proc.XXII Int. Metallurgy Congress: Inovation for Quality I, Bologne, Italy, p.377.

N.Jost and C.Rasche, 1990, Proc.European Conf. on Laser Treatment of Materials (ECLAT 3), Erlangen, FRG; eds. H.W.Bergmann and R.Kupfer, Sprechsaal Publ.Grp., Germany, p.485.

N.Jost and H.Haddenhorst, 1991, J.Mater.Sci.Let., 10, p.913.

J.A.Juarez-Islas, 1991, J.Mater.Sci., 26, p.5004.

G.Kaech and W.Epprecht, 1978, Scripta Metall., 12, p.493.

S.Katayama, H.Muraki, H.Simidzu and A.Matsunawa, 1991, Proc.ICALEO (1991), p.352.

C.Kim and L.S.Weinman, 1978, Scripta Metall.Mat., 12, p.57.

J.Kruger, 1988, Int.Mater.Revs., 33, No.3, p.113.

S.Kou and Y.Le, 1983, Metall.Trans.A, 14A, p.2245.

M.Lamb, D.R.F.West and W.M.Steen, 1986, Mat.Sci.Tech., 2, p.974.

M.Van Lancker, 1967, Metallurgy of Aluminium Alloys, Chapman and Hall, London, pp. 63-169.

J.Lasek, P.Bartuska and V.Synecek, 1992, 3rd Int.Conf. on Aluminium Alloys, Trondheim, Norway, 22-26 June.

J.Lasek, P.Bartuska, V.Synecek, and M.Simerska, 1991, Laser in Engineering, 1, p.111.

P.W.Leech, 1989, Thin Solid Films, 177, p.133.

R.Li, M.G.S.Ferreira, A.Almeida, R.Vilar, K.Watkins and W.Steen, 1993, "Localised Corrosion of Laser Surface Alloyed 7175-T7351 Aluminium Alloy with Chromium", European Symp. on Modifications of Passive Films, February, Paris, France.

R.J.Livak and J.M.Papazian, 1984, Scripta Metall.Mat., 18, p.483.

K.F.Lorking and J.E.O.Mayne, 1961, J.Appl.Chem., 11, p.170.

U.Luft, H.W.Bergmann and B.L.Mordike, 1987, Laser Treatment of Materials, ed. B.L.Mordike, DGM Informationsgesellschaft mbH, Oberursel, Germany, p.147.

F.Mansfeld and J.C.S.Fernandes, 1993, Corr.Sci., 34, No.12, p.2105.

A.Matsunawa, S.Katayama and H.Simidzu, 1990, Trans.Jap.Weld.Res.Inst., 19, No.1, p.67.

A.A.Mazhar, W.A.Badawy and M.M.Abou-Romia, 1986, Surf.Coat.Tech., 29, p.335.

E.McCafferty, P.G.Moore and G.T.Peace, 1982, J.Electrochem.Soc., 129, No.1, p.9.

E.McCafferty, P.M.Natishan and G.K.Hubler, 1993, Corr.Sci., 35, No.1-4, p.239.

E.McCafferty, E.G.Shafrin and J.A.McKay, 1981, Surf.Tech., 14, p.219.

J.O.Milewski, G.K.Lewis and J.E.Wittig, 1993, Weld.Res.Supp., July, p.341-s

L.F.Mondolfo, 1976, Aluminium Alloys, Butterworths, London.

P.G.Moore, E.McCafferty and L.S.Weinman, 1977, Reports NRL Progress, Nov., p.9.

W.C.Moshier, G.D.Davis, J.S.Ahearn and H.F.Hough, 1986, J.Electrochem.Soc., 133, p.1063.

W.C.Moshier, G.D.Davis, G.O.Cote, 1989, J.Electrochem.Soc., 136, p.356.

A.Munitz, 1980, Metall.Trans.B, 11B, p.563.

A.Munitz, 1985, Metall.Trans.B, 16B, p.149.

P.M.Natishan, E.McCafferty and G.K.Hubler, 1986, J.Electrochem.Soc., 133, p.1061.

P.M.Natishan, E.McCafferty and G.K.Hubler, 1988, J.Electrochem.Soc., 135, p.321.

P.M.Natishan, E.McCafferty and G.K.Hubler, 1991, Corr.Sci., 32, No.7, p.721.

J.Noordhuis and J.Th.M.De Hosson, 1993, Acta.Metall.Mater., 41, No.7, p.1989.

A.Nylund and I.Olefjord, 1991, Mat.Sci.Eng., A134, p.1225.

J.Onoro and C.Ranninger, 1993, Brit.Corr.J., 28, No.2, p.137.

B.K.Opera, V.M.Andriyakhin, V.I.Volgin and V.V.Bandurkin, 1985, Prot.Met. (USSR), 21, No.1, p.74.

J.M.Pelletier, L.Renaud and F.Fouquet, 1991, Mater.Sci.Eng., A134, p.1283.

P.Petrov and D.Dimitroff, 1993, Vacuum, 44, No.8, p.857.

J.R.Pickens and T.J.Langan, 1987, Metall.Trans.A, 18A, p.1735.

M.Pierantoni and E.Blank, 1990, Key Eng.Mater., 46-47, p.355.

M.Pierantoni, M.Gremaud, P.Magnin, D.Stoll and W.Kurz, 1992, Acta Metall. Mater., 40, No.7, 1637.

M.Pilloz, J.M.Pelletier and A.B.Vannes, 1992, J.Mater.Sci., 27, p.1240.

I.J.Polmear, 1989, Light Alloys, Edward Arnold, London, pp.18 - 141.

D.A.Porter and K.E.Easterling, 1988, Phase Transformations in Metals and Alloys, VNR international, Wokingham, UK, pp.208 - 308.

W.I.Pumphrey and J.V.Lyons, 1948, J.Inst.Met., 74, p.439.

R.M.Ramadan, S.W.Sharkawy and M.A.El-Zeky, 1992, Scripta Metall.Mater., 27, p.821.

K.V.Rama and J.A.Sekhar, 1987, Acta Metall., 35, No.1, p.81.

P.Reznicek, M.Holmanova and O.Honzik, 1989, Aluminium, 65, p.1259.

D.M.Roessler, 1986, The Industrial Laser Handbook, Eds. D.Belforte and M.Levitt, Laser Focus, Littleton MA,USA, p. 16.

A.Roosz, I.Teleszky, F.Boros and G.Buza, 1993, Mater.Sci.Eng., A173, p.351.

D.Rosenthal, 1946, Trans. ASME, p. 849.

W.F.Savage and A.H.Aronson, 1966, Weld.Res.Suppl., 45, p.85-s.

J.C.Schuster and H.Ipser, 1991, Metall.Trans.A, 22A, p.1729.

J.C.Scully, 1983, The Fundamentals of Corrosion 2nd Edition, Pergamon, Oxford, pp.56-130.

J.R.Scully, T.O.Knight, R.G.Buchheit and D.E.Peebles, 1993, Corr.Sci., 35, No.1-4, p.185.

C.R.Shastry, M.Levy and A.Joshi, 1981, Corr.Sci, 21, No.9, p.673.

B.A.Shaw, G.D.Davis, T.L.Fritz and K.A.Olver, 1990, J.Electrochem.Soc, 137, No.1, p.359.

B.A.Shaw, G.D.Davis, T.L.Fritz, B.J.Rees and W.C.Moshier, 1991, J.Electrochem.Soc., 138, No.11, p.3288.

B.A.Shaw, T.L.Fritz, G.D.Davis and W.C.Moshier, 1990, J.Electrochem.Soc., 137, No.4, p.1317.

J.M.Silcock, 1959-60, J.Inst.Metals, 88, p.357.

J.M.Silcock, 1960-61, J.Inst.Metals, 89, p.203.

H.Simidzu, S.Katayama and A.Matsunawa, 1990, Proc.ICALEO (1990), p.492.

Z.Szklarska-Smialowska, 1992, Corr.Sci., 33, No.8, p.1193.

A.Solina, M.De Sanctis, L.Paganini, A.Blarasin and S.Quaranta, 1984, J.Heat Treating, 3, No.3, p.193.

P.R.Sperry, 1955, J.Metals, 7, p.145.

W.M.Steen, 1986, The Industrial Laser Handbook, Eds. D.Belforte and M.Levitt, Laser Focus, Littleton MA,USA, p. 158

W.M.Steen, 1991, Laser Materials Processing, Springer-Verlag, London, p.155.

W.M.Steen and K.G.Watkins, 1992, "Coating by Laser Surface Treatment", 3rd Int.Symp.on High Temperature Corrosion and Protection of Materials, J.De Physique IV, Colloq.9, p.581.

V.Synecek, B.Major, P.Bartuska, J.Lasek and M.Simerska, 1992, Z.Metallkd., 83, p.246.

T.Takeda, K.Adachi and H.Hisada, 1992, Proc. LAMP'92, Nagaoka, Japan, p.795.

M.Talianker and B.Cina, 1989, Metall.Trans.A, 20A, p.1989.

K.R.Tretheway and J.Chamberlain, 1988, Corrosion, Longman Scientific and Technical, Harlow, UK, pp.61-106.

M.Urquidi and D.MacDonald, 1985, J.Electrochem.Soc., 132, No.3, p.555.

K.Urushino and K.Sugimoto,1979, Corr.Sci., 19, p.225.

S.Virtanen and H.Bohni, 1993, "Effect of Laser Surface Remelting on Passivity and its Breakdown of Al-Si Alloys", European Symp. on Modifications of Passive Films, February, Paris, France.

R.Volz, 1991, Proc. ICALEO (1991), p.389.

J.A.Wert, 1981, Scripta Metall.Mater., 15, p.445.

T.I.Wu and J.K.Wu, 1992, Scripta Metall.Mater., 27, p.875.

J.Yan, L.Chunzhi and Y.Minggao, 1992, J.Mater.Sci., 27, p.197.

M.Yasuda, F.Weinerg and D.Tromans, 1990(a), J.Electrochem.Soc., 137, No.12, p.3708.

M.Yasuda, F.Weinerg and D.Tromans, 1990(b), J.Electrochem.Soc., 137, No.12, p.3716.

L.Yulong, H.Jiandong, L.Jianshe and L.Jian, 1991, Process.Adv.Mater., 1, p.193.

M.Zimmermann, M.Carrard and Kurz, 1989, Acta Metall., 37, No.12, p.3305.

".......life for the majority of the population is an unlovely struggle against unfair odds, culminating in a cheap funeral."

Memoirs Of An Infantry Officer
by
Siegfried Sassoon

128